Graduate School ETD Form 9
(Revised 12/07)

PURDUE UNIVERSITY
GRADUATE SCHOOL
Thesis/Dissertation Acceptance

This is to certify that the thesis/dissertation prepared

By Changwook Jeong

Entitled
Landauer Approach to Thermoelectrics

For the degree of Doctor of Philosophy

Is approved by the final examining committee:

MARK S. LUNDSTROM
Chair

MUHAMMAD A. ALAM

SUPRIYO DATTA

YONG P. CHEN

To the best of my knowledge and as understood by the student in the *Research Integrity and Copyright Disclaimer (Graduate School Form 20)*, this thesis/dissertation adheres to the provisions of Purdue University's "Policy on Integrity in Research" and the use of copyrighted material.

Approved by Major Professor(s): MARK S. LUNDSTROM

Approved by: M. R. Melloch 06-25-2012
Head of the Graduate Program Date

Graduate School Form 20
(Revised 9/10)

PURDUE UNIVERSITY
GRADUATE SCHOOL

Research Integrity and Copyright Disclaimer

Title of Thesis/Dissertation:
Landauer Approach to Thermoelectrics

For the degree of Doctor of Philosophy

I certify that in the preparation of this thesis, I have observed the provisions of *Purdue University Executive Memorandum No. C-22,* September 6, 1991, *Policy on Integrity in Research.**

Further, I certify that this work is free of plagiarism and all materials appearing in this thesis/dissertation have been properly quoted and attributed.

I certify that all copyrighted material incorporated into this thesis/dissertation is in compliance with the United States' copyright law and that I have received written permission from the copyright owners for my use of their work, which is beyond the scope of the law. I agree to indemnify and save harmless Purdue University from any and all claims that may be asserted or that may arise from any copyright violation.

Changwook Jeong
Printed Name and Signature of Candidate

06-25-2012
Date (month/day/year)

*Located at http://www.purdue.edu/policies/pages/teach_res_outreach/c_22.html

LANDAUER APPROACH TO THERMOELECTRICS

A Dissertation

Submitted to the Faculty

of

Purdue University

by

Changwook Jeong

In Partial Fulfillment of the

Requirements for the Degree

of

Doctor of Philosophy

August, 2012

Purdue University

West Lafayette, Indiana

ACKNOWLEDGMENTS

First and foremost, I would like to express my deepest appreciation to my thesis advisor, Prof. Mark S. Lundstrom who made the whole achievements reported here possible. He introduced me to many exciting fields and gave me every opportunity to co-work and discuss with top researchers in the field. He also taught me how to approach a difficult problem in a simple, but elegant way. I specially thank him for warm encouragement and support through various stages of my graduate life. His insights and attitudes are an excellent example of a great scientist, and will benefit my whole life - not only professionally, but also, more importantly, personally.

I also sincerely thank my co-advisor, Prof. Muhammad A. Alam, for providing me the opportunity to learn and work with him. I would have never reached the level of achievement without his continued encouragement and motivation during the graphene project. His clarity of thinking and critical thinking skills helped me to look into the problems from a totally different perspective.

I acknowledge Prof. Supriyo Datta for providing insightful suggestions to my research problems. I have been very fortunate to receive academic guidance and to take his classes when I first started the research. His simple, but unified perspective that can applied to many transport problems helped me understand the basis of nano-electronics such as current flow and energy exchange.

I would like to thank Prof. Dimitiri Antoniadis at MIT, Dr. Rama Venkatasubramanian at RTI, Prof. Gehard Klimeck, Prof. Alejandro Strachan, Prof. Ali Shakouri, Prof. Eric Pop at UIUC, and Dr. Natalio Mingo at CEA-Grenoble for extensive discussion and

collaborations. I also thank Prof. Yong Chen for being in my advisory committee and for giving useful comments on my research.

It was a great joy to work in the Purdue computational electronics group, and I remain indebted to my former and current colleagues, Dr. Jesse Maassen, Dr. Raseong Kim, Dr. Shuaib Salamat, Dr. Yang Liu, Dr. Himadri Pal, Dr. Tony Low, Dr. Lutfe Siddiqui, Dr. Pradeep R Nair, Dr. Siyuranga O. Koswatta, Dr. Neophytos Neophytou, Dr. Mathieu Luisier, Yunfei Gao, Xufeng Wang, Nicholas Vargo, Dionsis Berdebes, Dr. Sunhee Lee, Seokmin Hong, Dr. Honghyun Park, Dr. Hoon Ryu, Dr. Sebastian Steiger, Dr. Abhijeet Paul, Ankit Jain, Biswajit Ray, James Moore, Mohammad Ryyan Khan, Ruiyi Chen, Supreme Das, Md.Masuduzzaman, Sourabh Dongaonkar, Dr. Ahmad E. Islam, Dr. Dhanoop Varghese, Dr. Jonghyun Go, and Dr. Abu Naser Zainuddin for their help and support. I also thank Cheryl Haines and Vicki Johnson for their support on travel, meeting arrangements, and many administrative issues.

I remain indebted to Dr. Kinam Kim, Dr. Hongsik Jeong, Dr. Gitae Jeong, Dr. Gwanhyeob Koh, and Dr. Sujin Ahn, who encouraged to start new journey at Purdue and enriched my experience at Samsung.

Finally, I owe more than words can describe to my family: my parents, my brother, and my fiancée, Sunyoung Hwang, Hyebin Jeong, and Seyeon Jeong. This work is dedicated to them.

Many thanks to all the agencies that funded this work and to Purdue NCN, the MARCO Focus Center on Materials, Structures and Devices for the computational resources and wonderful support that they have provided through all these years.

TABLE OF CONTENTS

Page

LIST OF TABLES....vii
LIST OF FIGURES....viii
ABSTRACT.... xx
1. INTRODUCTION 1
  1.1 A Brief History of Thermoelectrics....1
  1.2 Thermoelectric Physics....2
    1.2.1 Thermoelectric Effects.... 2
    1.2.2 Thermoelectric Energy Conversion and Applications.... 4
    1.2.3 Figure of Merit and the Coefficient of Performance 6
  1.3 Thermoelectric Research....8
    1.3.1 Bismuth Telluride Alloys: 1950s - 1990s.... 8
    1.3.2 Beyond Bismuth Telluride: after 1990s.... 9
    1.3.3 Evaluation of Thermoelectric Devices.... .12
  1.4 Nanocomposites Thermoelectrics.... 13
    1.4.1 Motivation for Nanocomposite Thermoelectrics.... 13
    1.4.2 Key Experimental Accomplishments 14
    1.4.3 Manufacturing Processes and Materials Properties 17
    1.4.4 Electron and Phonon Transport 21
    1.4.5 Modeling Nanocomposite TE materials 22
  1.5 Thesis Outline....24
  1.6 List of Associated Publications.... 27
2. LANDAUER VS. BOLTZMANN APPROACH FOR ELECTRONS 29
  2.1 Introduction....30
  2.2 Approach....32
  2.3 Results....36
  2.4 Discussion....41
  2.5 Summary and Conclusion....48
3. LANDAUER VS. BOLTZMANN APPROACH FOR PHONONS 49
  3.1 Introduction....49
  3.2 Approach....51
  3.3 Results....56
  3.4 Discussion....62
  3.5 Summary and Conclusion....67

Page

4. THERMAL CONDUCTIVITY OF BULK AND THIN-FILM SILICON: A LANDAUER APPROACH 68
  4.1 Introduction........ 68
  4.2 Approach........ 70
  4.3 Bulk Thermal Conductivity........ 73
  4.4 In-Plane and Cross-Plane Thermal Conductivity for Thin Films........ 76
  4.5 Discussion........ 81
  4.6 Summary and Conclusion........ 84
5. ON THE BEST BANDSTRUCTURE FOR THERMOELECTRIC PERFORMANCE: A LANDAUER PERSPECTIVE 85
  5.1 Introduction........ 85
  5.2 Approach........ 89
  5.3 Single Energy Case 91
  5.4 One-dimensional Analysis........ 92
  5.5 Three-dimensional Analysis: Constant Mean-free-path........ 94
  5.6 The Mahan and Sofo Upper Limit........ 101
  5.7 Role of Scattering........ 103
  5.8 High Valley Degeneracy........ 104
  5.9 Distorted Density of States........ 107
  5.10 Summary........ 113
6. EXPLORATION OF POWER FACTOR ENGINEERING APPROACHES 115
  6.1 Introduction........ 115
  6.2 Molecules, Graphene, and Composite Energy Bands........ 116
  6.3 Cross-Plane Superlattice Peltier cooler........ 118
  6.4 Conclusions........ 119
7. GRAPHENE AS A TRANSPARENT CONDUCTOR........ 120
  7.1 Introduction........ 120
  7.2 Approach........ 123
  7.3 Results........ 126
  7.4 Discussion........ 129
  7.5 Conclusions........ 134
8. CONCULSIONS AND FUTURE WORK 135
LIST OF REFERENCES 140
A. ON ELECTRONIC STRUCTURE ENGINEERING AND THERMOELECTRIC PERFORMANCE 165
  A.1 Introduction........ 165
  A.2 Approaches........ 166
  A.3 Results........ 168

Page

A.4 Discussion……………………..………………………………..............170
A.5 Summary and Conclusion……………………..……………………….178

B. COMPUTATIONAL STUDY OF THE ELECTRONIC PERFORMANCE OF CROSS-PLANE SUPERLATTICE PELTIER DEVICES 179

B.1 Introduction………………...………..……….......…………….............179
B.2 Approach………………...……..………………………………............180
B.3 Results and Discussion……………..…………………….……............181
B.3.1. Hetero-junction and Single barrier 181
B.3.2. Multi Barriers 184
B.4 Conclusions……………………......…..…………………………............185

C. NUMBER OF CONDUCTING CHANNELS FOR 1D, 2D, AND 3D..................... 186

D. DIFFUSIVE MISMATCH MODEL FROM LANDAUER APPROACH................ 188

E. MODELING APPROACH FOR NANOCOMPOSITES 190

E.1 Introduction……………………..…………………………...................190
E.2 Generating the Physical Structure……………………….……..….............191
E.3 Modeling Electron Transport……………………..…....……….............193

F. THE MAXIMUM POWER CONDITION AND THE MAXIMUM EFFICIENCY CONDITION 196

G. THE EFFECT OF ANISOTROPIC BAND.. 199

VITA 201

LIST OF TABLES

Table Page

1.1 Summary of fabrication techniques for TE materials……………………………….18

2.1 Analytic “density-of-modes” and full band NEGF-TB simulation. 40

2.2 Summary of parameters used in Figure 2.6. 44

LIST OF FIGURES

Figure Page

1.1 The schematic diagram of (a) one level picture and TE devices for (b) power generation, and (c) refrigeration. The TE device is composed of p-type and n-type conductors connected electrically in series and thermally in parallel. The solid red and blue lines at the contacts in (b) denotes Fermi-Dirac distribution. The solid circles and arrows denote electrons and the direction of electron flow.. 5

1.2 The maximum ZT vs. total κ . The dashed line: PF = 40 μW/m^{2}K^2, T=300K; Conventional semiconductors used in IC industry (open diamonds): a1) Si 300K [1,2], a2) Si 1275K [1], a3) Ge 300K [3], a4) GaAs 300K [4]; bulk TE materials used in TE devices (open triangles): b1) p-Bi_2Te_3 300K [5], b2) p-$Bi_xSb_{2-x}Te_3$ 300K [6], b3) n-$Si_{80}Ge_{20}$ 1275K [7], b4) PbTe 300K [8]); nanostructured materials fabricated by thin films processing (filled circle): c1) Si nanowire (NW) 300K [9], c2) Si NW 200K [10], c3) Bi_2Te_3/Sb_2Te_3 superlattice (SL) 300K [11], c4) PbTe/PbSeTe quantum dot (QD) SL 300K [12] , c5) PbTe/PbSeTe QD SL 575K [13]; electronic structure engineered bulk materials (open star): d1) Tl-PbTe 773K [8]; partially filled skutterudites (filled square): d2) n-$Yb_xCo_4Sb_{12}$ 600K [14]; bulk nanostructured materials fabricated by thermal processing (filled inverse triangles): e1) p-$Na_{1-x}Pb_mSb_yTe_{2+m}$ 650K [15], e2) p-Pb_xSn_{1-x}Te-PbS 642K [16], e3) n-$AgPb_mSbTe_{m+2}$ 800K [17], e4) PbSbTe 700K [18], e5) p-PbTe-SrTe 800K [19]; and powder metallurgy (filled triangles): f1) p-Bi_2Te_3 300K [20], f2) p-$Bi_xSb_{2-x}Te_3$ 475K [6], f3) n-$Si_{80}Ge_{20}$ 1275K [7], f4) Si 1275K [1], f5) n-LaTe 1273K [21], f6) n-$Yb_xCo_4Sb_{12+y}$ 800K [22]. Note that the report of ZT ~ 3.5 (c5) in Ref. [13] turned out to be an error due to inaccurate carrier concentration measurements. Examination of the Hall samples used in Ref. [13] indicated incorrect contact geometries, with pressed indium contacts that were large relative to the sample size and inset from the edges[23] 16

1.3 Schematic diagram of a potential barrier used for modeling a grain boundary where E_B is a barrier height and L_G is grain size. 21

Figure Page

2.1 (a) Comparison of the density of modes, $M\left(E\right)$, computed by 3 different approaches for Germanium (Ge): NEGF-TB model, Effective Mass Approximation (EMA), and counting bands. The *M(E)* from counting bands (dashed line) is on top of *M(E)* from the NEFG-TB model. (b) Illustration of bands counting method for specific dispersion relation for Ge. Dotted line is guide to eye. 38

2.2 Full band calculations of the density of states (*DOS*) and the density of modes (*M*) for Ge, GaAs, and Bi_2Te_3. The midgap is located at E = 0. The inset in Fig. 2.2(b) shows *M(E)* near the conduction band edge for GaAs. 39

2.3 Comparison of fitting based on parabolic dispersion relation with fitting based on Kane dispersion relation. Non-parabolicity parameter α used for GaAs is 0.64^{71}. Above 1eV, *L* valleys contribute to the density of modes in addition to Γ valley. 41

2.4 Calculated Seebeck coefficients (S) using eqn. (2.2) and experiments as a function of reduced Fermi level ($\eta_F = \left(E_F - E_C\right)/k_BT$). We assumed that scattering rate ($1/\tau$) is proportional to the density-of-states, i.e. phonon scattering is dominant. The reduction of Seebeck coefficient around $\eta_F = -2$ for Bi_2Te_3 is attributed to the bipolar conduction due to its relatively small bandgap (0.162 eV). 42

2.5 Comparison of the simulated and experimentally measured *S*, *G,* and κ for Bi_2Te_3 assuming a constant mean-free-path, $\lambda_0 = 18, 4$ nm for conduction and valence bands. Thermal conductivity is the sum of the electronic and lattice thermal conductivity. Used parameters are listed in Table 2. 43

2.6 Calculated and measured PF and ZT as function of the Fermi level. Used parameters are listed in Table 2. 45

2.7 Comparison of EMA with full-band calculation for Ge. On the *y* axis, Seebeck coefficient (*S*), electrical conductivity (*G*) and thermal conductivity by electron(κ_e) are plotted from 0 to 400 μV/K , 0 to 4×10^6 $\Omega^{-1}m^{-1}$, and 0 to 40 W m^{-1} K^{-1}. 46

2.8 Energy dispersion relation showing the lowest (a) conduction bands and (b) valence bands of GaAs. (y axis ranges from E_C (or E_V) to E_C (or E_V) + $5k_BT$ because $-\partial f_0/\partial E$ spread about $5k_BT$.) Each red dot represents a conducting channels for positive moving electrons at specific energy for an electron moving with a positive velocity. In the valence bands, most of the

Figure Page

bands (especially heavy holes) have at least two conducting channels per energy....47

3.1 Phonon dispersion along the high symmetry lines and phonon density of states for (a) Si and (b) Bi_2Te_3. (c) Specific heat per volume of Si (Inset) and Bi_2Te_3 . The solid and dashed lines are for the results of calculation and experiments. 58

3.2 (a) Illustration of bands counting method for specific dispersion relation for Si. Dotted line is guide to eye. (b) Number of phonon modes of Si and Bi_2Te_3 . The dashed and dashed-dot lines are the results obtained from the Debye model with the fitted sound velocities of 1.74×10^5 cm/s and 5.32×10^5 cm/s for Si and Bi_2Te_3, respectively. 59

3.3 Ballistic thermal conductance per area of Si and Bi_2Te_3 . Insets: lattice thermal conductivity of Si and Bi_2Te_3 . The solid line and symbols are calculated and experimental values, respectively. 60

3.4 Extracted average mean-free-path of Si and Bi_2Te_3 by taking the ratio of experimental thermal conductivity to ballistic thermal conductance per area. 61

3.5 Comparison of Debye temperature for the specific heat (Θ_D) and Debye temperature for thermal conductivity (Θ_M) normalized by maximum Θ_D. (b) Debye model vs. full dispersion for Bi_2Te_3 . Red and green solid lines are full band results of number of phonon modes (M_{ph}) and density of states (D_{ph}) in arbitrary units. The dashed-dot and dashed lines are results from Debye approximation at low frequency for M_{ph} and D_{ph} 64

3.6 Specific heat calculation and (b) extracted average mean-free-path of Bi_2Te_3 for Debye models and full band results. Insets of Fig. 6(a) and Fig. 6(b) are thermal conductivity calculation and spectral mean-free-path for backscattering, respectively. Solid lines: full band results; Dashed and dashed dot lines: Debye approximation. 65

3.7 (a) number of phonon conducting modes (M_{ph}) and Eq. (3.7f) at 300 K, (b) number of electron conducting modes (M_{el}) calculated from full band electronic structure and Eq. (3.7e) at 300 K. For horizontal axis, $\varepsilon = E_{el} - E_C$ for number of electron conducting modes and $\varepsilon = E_{el} - E_F$ for a electron "window function" assuming $E_F = E_C$ which is a typical condition for optimum performance. 66

Figure Page

4.1 (a) For bulk Si, energy-resolved number of conducting channels (M_{ph}), window function (W_{ph}), and the mean-free-path for backscattering (λ_{ph}) are plotted at 300 K. Note that the entire spectrum of M_{ph} participates in conduction since W_{ph} is almost constant. The mean-free-path shows that low-energy acoustic phonons have long λ_{ph} since they don't suffer a lot from umklapp scattering. The spectral λ_{ph} are calculated based on the relaxation time approximation for umklapp scattering,[24] point defect scattering,[25] and crystalline boundary scattering.[26] (b) The thermal conductivity κ_{ph} (left axis) and the average MFP $\langle\langle\lambda_{ph}\rangle\rangle$ (right axis) are plotted as a function of temperature. Experimental results are obtained from Ref. [26]. Good agreement between calculation and experiment is observed. 74

4.2 The cumulative thermal conductivity, κ_{ph} , as a function of energy is plotted for diffusive (scattering) and ballistic (no scattering) cases. For the ballistic case, all energy channels equally contribute to κ_{ph}. With scattering, low-energy channels mainly contribute to κ_{ph} because high-energy phonons have very short mean-free-paths. 75

4.3 We plot the computed cumulative thermal conductivity (κ_{ph}) as a function of the mean-free-path (MFP) for backscattering (λ_{ph}) using three different phonon dispersion models: full phonon dispersion, a sine-type dispersion, and a Debye model. The computed results are compared to the MD simulations obtained from Ref. [[27]]. The MD simulation is plotted while taking into account the difference between a conventional MFP for scattering (l_{ph}) and the MFP for backscattering, i.e. $\lambda_{ph} = (4/3)l_{ph}$. Our results with full phonon dispersion (solid line) is in good agreement with the recent MD simulations,[27] which showed ~50% of the heat conduction is attributed to phonons with MFP > ~1 μm. The MFP distribution is not correctly predicted by a simple sine-type dispersion model (dotted line) or a Debye model (dashed line). Inset: Computed thermal conductivity κ_{ph} vs. temperature is plotted for the three phonon dispersion models and is compared to experiment.[26] Note that regardless of the phonon dispersion model used, we can fit well the experimental data by adjusting scattering parameters..................78

Figure Page

4.4 Thermal conductivity (κ_{ph}) vs. silicon layer thickness at room temperature is plotted. In-plane experimental data [28–31] and calculations are shown by open squares and by blue lines, respectively. For our calculations, a surface roughness of 0.5 *nm* is used, which is a typical value for SOI wafers. We assume that the point defect scattering rate for SOI wafer is 2× larger than that of bulk Si. The results with the point defects (blue solid line) give a better fit for thicker Si layers. The cross-plane experimental data [32] and calculations are shown by filled circle and by red lines, respectively. It is assumed that the $M_{ph}(\omega)$ for the thin film is the same as that for bulk Si... 79

4.5 Along the in-plane (in) and the cross-plane (cross) transport directions, $\lambda_{50\%}$ and $\langle\langle\lambda_{ph}\rangle\rangle_{eff}$ are plotted as a function of the thickness of the thin Si films at room temperature. Here, $\lambda_{50\%}$ is the mean-free-path (MFP) at which the cumulative thermal conductivity (κ_{ph}) is equal to 50%, and the average MFP, $\langle\langle\lambda_{ph}\rangle\rangle_{eff}$, is obtained from Eq. (4.3d). The cross-plane direction displays about 2× smaller $\lambda_{50\%}$ and $\langle\langle\lambda_{ph}\rangle\rangle_{eff}$ than the in-plane direction. $\langle\langle\lambda_{ph}\rangle\rangle_{eff}$ is always less than $\lambda_{50\%}$ since $\langle\langle\lambda_{ph}\rangle\rangle_{eff}$ places too much emphasis on the high energy modes with very small MFPs. Note that for the in-plane direction, about 50% of the heat conduction is carried by phonons with a mean-free-path greater than the thickness of the thin film when the thickness is smaller than ~0.2 μm (blue symbol). 81

5.1. The maximum *ZT* vs. total κ . Conventional semiconductors used in IC industry (circle): Si 300K,[1,2] Ge 300K,[3] GaAs 300K [4]; bulk TE materials used in TE devices (triangles): Bi_2Te_3 300K,[5] $Bi_xSb_{2-x}Te_3$ 300K,[6] $Si_{80}Ge_{20}$ 1275K,[7] PbTe 300K [8]; nano-engineered materials (square): Si nanowire (NW) 300K,[9] Si NW 200K,[10] Bi_2Te_3/Sb_2Te_3 superlattice (SL) 300K,[11] PbTe/PbSeTe quantum dot (QD) SL 300K,[12] Tl-PbTe 773K,[8] $Na_{1-x}Pb_mSb_yTe_{2+m}$ 650K,[15] Pb_xSn_{1-x}Te-PbS 642K,[16] $AgPb_mSbTe_{m+2}$ 800K,[17] PbSbTe 700K,[18] p-PbTe-SrTe 800K,[19] Bi_2Te_3 300K,[20] $Bi_xSb_{2-x}Te_3$ 475K,[6] n-$Si_{80}Ge_{20}$ 1275K,[7] Si 1275K,[1] n-LaTe 1273K,[21] n-$Yb_xCo_4Sb_{12+y}$ 800K.[22] The dashed line is the *ZT* that would be obtained if the power factor of each material were the same as that of silicon. 87

5.2 (a) The 1D dispersion, $E(k) = 2t_0(1 - \cos k_x a)$ with two different bandwidth (BW) of a dispersion, ~0.1 (dashed line) and ~0.6 eV (solid line). k_x is

Figure Page

displayed in the units of π/a. (b) The corresponding the density-of-states, $D(E)$, in the units of $eV^{-1}nm^{-1}$ and (c) the number of conducting channels, $M(E)$, which represent the number of states that participate in transport at a given energy E. Note that although the $D(E)$ goes to infinity, $M(E)$ remains bounded independent of bandwidth. 93

5.3 (a,c) The 3D density-of-states, $D(E)$, for the narrow and the broad bandwidth (BW) bands. (b,d) The number of conducting channels, $M(E)$, for the narrow and the broad BW bands. Full-band calculations (solid line) are compared to effective mass approximation (EMA, dashed line). Based on the EMA, $D(E)=m_e\sqrt{2m_e(E-E_C)}/2\pi^2\hbar^3$ and $M(E)=m_e(E-E_C)/2\pi\hbar^2$, where E_C is the band edge. Fitted effective masses (m_e) at the bottom of band are $m_e=m_0$ for the broad band and $m_e=10m_0$ for the narrow band, where m_0 is the electron rest mass. It is seen that the $D(E)$ and the $M(E)$ obtained from parabolic band assumption (dashed line) match well the full-band TB results (solid line) only at the bottom of the band. Dotted line is the arbitrarily normalized ” window function”, $W=(-\partial f_0/\partial E)$, where f_0 is Fermi-Dirac distributions. For horizontal axis, $\varepsilon=E-E_C$ for $D(E)$ and $M(E)$ and $\varepsilon=E-E_F$ for $W=(-\partial f_0/\partial E)$ where E_F is the Fermi level. We assumes $E_C=E_F$ which is a typical condition for optimum performance.......... 95

5.4 Efficiency normalized by Carnot efficiency η_C (upper panel) and power for (a) zero lattice thermal conductivity, $\kappa_{ph}=0$, and (b) a finite lattice thermal conductivity, $\kappa_{ph}=0.5$ W/m-K are plotted as a function of the bandwidth (BW). Efficiency and power are evaluated from two different perspectives. Solid line: condition for the maximum thermoelectric efficiency. Dashed line: condition for the maximum power that a thermoelectric generator delivers to a load. The load resistance and the location of the Fermi level are co-optimized in order to extract the maximum efficiency or the maximum power output. 97

5.5 For zero lattice thermal conductivity ($\kappa_{ph}=0$), (a) *ZT*, (b) the power factor (PF) and the Lorenz number (*L*), and (c) the Seebeck coefficient (S), the

Figure Page

electrical conductivity (σ) and the electronic thermal conductivity (κ_{el}) are plotted. The units of PF, *L*, *S*, σ, and κ_{el} in the plots are 10^{-6}W/m-K^2, $(k_B/q)^2$, 10^{-3}V/K, $1/\Omega$-m, and 5×10^{-5}W/m-K , respectively. For each value of the BW, we found the optimal location of the Fermi level to maximize *ZT*. As the BW decreases, the highest *ZT* (i.e. efficiency) is obtained for a delta-function like narrow band. This result occurs mainly because as the BW approaches zero, κ_{el} approaches zero and therefore the *L* approaches zero. Note that the maximum PF still appears at a moderate BW............ 99

5.6. For a finite lattice thermal conductivity (κ_{ph} = 0.5 W/m-K), (a) the *ZT*, (b) the power factor (PF) and the Lorenz number (*L*), and (c) the Seebeck coefficient (S), the electrical conductivity (σ) and the electronic thermal conductivity (κ_{el}) are plotted. The units of PF, *L*, *S*, σ, and κ_{el} in the plots are 10^{-3}W/m-K^2, $(k_B/q)^2$, 10^{-4}V/K, $10^4/\Omega$-m, and 10^{-1}W/m-K , respectively. For each value of the BW, we found the optimal location of the Fermi level to maximize *ZT*. In contrast with the case of $\kappa_{ph}=0$, the highest *ZT* occurs for the moderate BW mainly because of the BW dependence of the power factor. Since the BW has a rather small effect on *S*, the strong variation of σ vs. BW explains the shape of the power factor vs. BW. The optimum BW for σ occurs when the width of the Fermi window matches the width of $M(E)$.. 100

5.7 For a finite lattice thermal conductivity (κ_{ph} = 0.5 W/m-K), the *ZT* (solid line) and its upper limit, κ_0/κ_{ph} (dashed line), are plotted as a function of bandwidth (BW). For each assumed bandwidth, the optimal location of the Fermi level is determined to maximize *ZT*. Here a constant mean-free-path is assumed. It can be seen that $ZT \le \kappa_0/\kappa_{ph}$ is always true and the ZT approaches its upper limit for the narrowest BW. 102

5.8 (a) The computed power factor vs. valley degeneracy is plotted. (b) The power factor (PF), (c) S, and (d) σ are plotted as a function of Fermi level for three cases of $N_V=1$, 6, and 12. Symbols represent values at optimal Fermi level. It can be seen that PF of multi-valley semiconductor is improved and that the enhancement is attributed to the increase of σ. 105

Figure Page

5.9 (a) Density-of-states ($D(E)$), (b) number of conduction channels ($M(E)$), (c) mean-free-path (MFP) for backscattering ($\lambda(E)$), and (d) $M(E)\lambda(E)$ are plotted for three cases of three cases of $N_V = 1$, 6, and 12. Symbols represent values at optimal Fermi level. $M(E)$ and $\lambda(E)$ are higher for the multiple valley case because $M(E) \propto \upsilon(E)D(E)$ and $\lambda(E) \propto \upsilon(E)\tau(E)$. Since the transport distribution is proportional to $M(E)\lambda(E)$, it is considerably higher for the multiple valley case. 107

5.10 (a) For constant mean-free-path (MFP), the power factor (PF) vs. ΔE_C for a material with lower band and upper band, where ΔE_C is the band-offset. Lower band is isotropic single valley with an effective mass of m_0 and upper band has an effective mass of $10m_0$. Note that PFs for single valley with an effective mass of m_0 and $11m_0$ are 1.25×10^{-3} W/mT^2 and 1.38×10^{-2} W/mT^2, respectively. Upper band with heavy effective mass produces higher performance regardless of ΔE_C in comparison to the power factor of a single valley and best performance is obtained when $\Delta E_C = 0$. (b - d) The PF, Seebeck coefficient (*S*), and electrical conductivity (σ) vs. Fermi level for three cases of $\Delta E_C = 0$, 5 , and $10k_BT$. Comparing to the case of single valley, it is found that a significant increase in σ lead to improved power factor. Non-monotonic Seebeck coefficient behavior (Fig. 5.10c) maintains large *S* at the degenerate limit. Symbols represent values at optimal Fermi level. ……... 109

5.11 (a) Density-of-states ($D(E)$), number of conduction channels ($M(E)$), mean-free-path (MFP) for backscattering ($\lambda(E)$), and $M(E)\lambda(E)$ vs. Fermi level are plotted for three cases of $\Delta E_C = 0$, 5 , and $10k_BT$ for constant MFP. Since MFP is constant, the sharp increase of $D(E)$ leads to a sharp increase of $M(E)$ and TDFs (i.e. $M(E)\lambda(E)$). The resulting strong energy dependence of $M(E)\lambda(E)$ produces non-monotonic Seebeck coefficient behavior. Symbols represent values at optimal Fermi level. ….. 110

5.12 (a) The power factor (PF) vs. ΔE_C for a material with lower band and upper band, where ΔE_C is the band-offset. Lower band is isotropic single valley with an effective mass of m_0 and upper band has an effective mass of $10m_0$. Red circles represent the PF for a single valley. The improved PF is obtained for $\Delta E_C >\sim 10k_BT$. (b - d) The PF, Seebeck coefficient (*S*), and electrical conductivity (σ) vs. Fermi level for three cases of $\Delta E_C = 5$, 10, and $15 k_B T$. It can be seen that non-monotonic Seebeck coefficient behavior (Fig. 5.9c) improves S at the degenerate limit. As ΔE_C becomes large, σ at optimal Femi level continues to increase. Therefore, the enhanced power factor is obtained when ΔE_C is larger than about $10 k_B T$. 111

5.13 Density-of-states ($D(E)$), number of conduction channels ($M(E)$), mean-free-path (MFP) for backscattering ($\lambda(E)$), and $M(E)\lambda(E)$ vs. Fermi level are plotted for three cases of $\Delta E_C = 5$, 10, and $15 k_B T$. The MFP is decreased when upper bands are available. As a result, $M(E)\lambda(E)$ is reduced. The resulting sharp decrease of $M(E)\lambda(E)$ produces non-monotonic Seebeck coefficient behavior... 112

6.1 (a) The number of conducting channels (M_{el}) for (a) a BPDT vs. a CSW molecules. Engineering the transmission is done by putting side group in the CSW molecule, which creates very sharp Fano resonance. (b) a graphene vs. a graphene superlattice (GR GL). A transmission gap is created by making a periodic graphene PN junction electrostatically. (c) Al content of 0 vs. 0.28 of $Al_xGa_{1-x}As$ alloy. x = 0.28 is the optimal Al content for maximum *ZT*. All three examples seek to achieve a sharp $M_{el}(E)$. (d) the S vs. E_F for GaAs (x=0 in $Al_xGa_{1-x}As$), Bi_2Te_3, ideal molecule which has a delta-function like M_{el}, CSW molecule, a graphene, a graphene SL and composite bands (x=0.28, $Al_xGa_{1-x}As$). For a given Fermi level, the 3D bulk results have a somewhat higher S than the ideal single level molecule because in 3D, energy states are spread-out. (e) *ZT* at 300K with respect to Al composition in $Al_xGa_{1-x}As$. At each x, E_F is selected to maximize *ZT*. The M_{el} is computed from effective mass approximation. The electron mean-free-path is calculated based on the measured mobility. The 10x improvement in *ZT* is achieved at x=0.28. As shown in Fig. 3c, the band-splitting between a lower band (Gamma) and a upper band (L) is 5~ 7 k_BT and the $M_{el}(E)$ for L band is 20 times steeper than the Gamma band at x=0.28. 117

6.2 Schematic diagrams of test structures and corresponding power factor (PF) are plotted for (a,d) single barrier, (b,e) multi-barriers-1: superlattice (SL) contacts, and (c,f) multi-barriers-2. Barrier is $In_{0.52}Al_{0.48}As$. Grayed box represents contact (cnt), where energy relaxation scattering time is assumed to be 50 fs. Solid circle denotes injected electrons from emitter contact. emitter: bulk $In_{0.53}Ga_{0.47}As$ with 0.044 m_0, barrier: $In_{0.52}Al_{0.48}As$ with 0.075 m_0, barrier height: 0.51 eV. (d-f) The dashed-dot is the result of bulk $In_{0.53}Ga_{0.47}As$ and dashed line the result of $In_{0.52}Al_{0.48}As$. Red circle symbols in (d-f) denote maximum PF of single barrier device in (d). 118

Figure Page

7.1. Transmittance as a function of sheet resistance (R_S) for polycrystalline graphene grown by chemical vapor deposition (CVD) method,[252] the networks of carbon nanotubes (CNT) [249] and nanowires (NW),[250] ITO,[252] and a hybrid of poly-graphene and NW mesh. The dashed lines are guide to eye. The best reported data are selected from literatures. The data for the hybrid are computed based on the following parameters: the R_S of a single crystalline graphene ~ 30 Ω/sq, the ratio of inter-grain resistance to intra-grain resistance ~ 63, the percentage of high-resistance grain boundary (P_{GB}) = 35%, and geometric aperture of 99% (an average distance between NWs of ~ 10 μm, a line width of 100 nm, and a height of 100 nm) for metal NW mesh with bulk Ag conductivity being assumed. The value in the bracket represents the number of layers for poly-graphene or the hybrid..... 122

7.2 (a) Five microstructures generated by Voronoi tessellation for use of finite difference method: uniform square grain (square), uniform hexagonal grain (hex1), perturbed hexagonal grain with normal size distribution (hex2), and random grains with normal size distribution (rand1) and with log-normal size distribution (rand2). The percentage of high-resistance grain boundary is 50%. High- and low- resistance grain boundary are shown by red and by blue line. A grain is shown by white and has about 200 nodes per grain. A schematic diagram for one-model is also shown to explain how the one-node model represents one grain. The sheet resistance across low-resistance grain boundary and the sheet resistance across high resistance grain boundary are denoted as R_{lo} and R_{hi}, respectively. (b) Grain size distributions are shown for perturbed hexagonal grain and two random grains. (c) the normalized conductance vs. sample length for five different microstructures (symbols) and one-node model (solid , dashed, and dashed-dot line) for three different percentage of high-resistance GB (P_{GB} = 20%, 50%, and 80%). Inset: the dependence of the conductance exponent, n, on the sample length, i.e. $G \propto (L_C)^n$ 125

7.3 For a long sample (L_C ~ 100× average grain size), the dependence of the sheet conductance on the percentage of high-resistance grain boundary (P_{GB}) is plotted. Inset: the computed results for grain size dependence is compared to experiments. [253] 127

7.4 The schematic figures to interpret the resistance of poly-graphene as a percolation problem defined by high and low resistance grain boundaries (GB). High-resistance and low-resistance GBs are shown by red and blue line. (a) $P_{GB} = 0\%$ (b) $P_{GB} \sim 60\%$ (c) the concept of 'percolation-doping':

Figure Page

doping the polycrystalline graphene by a sparse random mesh of metal NW. Metal NW is represented by black solid line. All arrows indicate current stream…. 129

7.5 For a hybrid of polycrystalline graphene (poly GR) and nanowires (NW) mesh, the sheet conductance vs. the percentage of high-resistance grain boundary (P_{GB}) for two different contact resistance (R_C) are plotted as a function of NW density (ρ_{NW}). At $\rho_{NW} = 100\%$, average distance between NWs is ~10 μm and $\rho_{NW} = 0\%$ represents poly GR. Inset: the normalized standard deviation (NSD) is plotted........ 131

7.6. (a) A polycrystalline graphene sample with perturbed hexagonal grain for $P_{GB} = 35\%$. High-resistance and low-resistance grain boundaries (GB) are shown by red and blue line, respectively. (d) hybrid polycrystalline graphene – network of metal NW (gray solid line). (b, c, e, f) Corresponding potential profile are plotted for comparison. All potential data are normalized. The contact resistance between graphene and metal NW is assumed to be $200\,\Omega \cdot \mu m$. (g) The simulated transmittance vs. wavelength data for regular grating structures with a period of 5 and 10 μm, a line width of 100 nm, and a height of 100 nm. The average transmittance for the TE and TM mode are considered here........ 133

A.1 For graphene and a graphene SL (a) the transmission (b) the S vs. E_F characteristics........ 169

A.2 For a BPDT molecule and a CSW molecule, (a) the transmission (b) the S vs. E_F 170

A.3 The results for graphene, graphene SL, and a single molecule are compared with common *TE* semiconductors. 171

A.4 Comparison of the results for Gaussian shaped and Lorentzian shaped transmission with respect to standard deviation (σ).. 172

A.5 Calculation of *ZT* for GaAs (x=0 in $Al_xGa_{1-x}As$) with best fitted λ_0 and Eq. 9 is compared to experimental results [4]. 173

A.6 (a) optimum *S*, *G*, and *K* (b) *PF* and *ZT* with respect to Al composition........ 174

Figure Page

A.7 *S*, *G* and *PF* vs. Fermi level for Al composition of (a) 0, (b) 0.17, (c) 0.28 and (d) 0.42. 175

A.8 Density-of -states at (a) x=0.17 and (b) x=0.28. 176

A.9 (a) calculation of maximum *PF* for the simple two band model which is normalized by the maximum *PF* obtained for one band case. (b) *S* vs. E_F characteristics at maximum *PF* condition. 177

A.10 *S* vs. E_F characteristics (a) with the band splitting kept at $5k_BT$ (b) with m_2^*/m_1^* kept at 10. 177

B.1. Schematic diagrams of test structure of numerical experiments. (a) hetero-junction, (b) single barrier (c) multi-barriers-1: SL contacts and (d) multi-barriers-2. Barrier is $In_{0.52}Al_{0.48}As$. Grayed box represents contact (cnt), where energy relaxation scattering time is assumed to be 50 fs. Solid circle denotes injected electrons from emitter contact. emitter: bulk $In_{0.53}Ga_{0.47}As$ with 0.044 m_0, barrier: $In_{0.52}Al_{0.48}As$ with 0.075 m_0, barrier height, Φ_B: 0.51 eV. 181

B.2. Transmission results: (a) semi-classical (blue) for hetero-junction vs. QM calculation for hetero-junction (red) and single barrier (light blue). Barrier thickness is 200 Å (b) single barrier. Barrier thickness: 6, 21, 70, 100 Å (c) multi-barriers-1 (no. of barriers in SL contacts): 1, 2, 4, 10, and (d) multi-barriers-2 (no. of barriers in device region): 1, 2, 4, 10. The dashed dot is bulk $In_{0.53}Ga_{0.47}As$ and dashed line is $In_{0.52}Al_{0.48}As$. Insets: (a) contour plot of transmission at hetero junction as a function of longitudinal energy (x-axis) and transverse energy (y-axis), (b-d) transmission (y-axis) vs. total energy (x-axis, in *eV*) plot when transverse energy is zero. 183

B.3. *S* vs. *G* trade-off: (a) dashed dot is bulk $In_{0.53}Ga_{0.47}As$, dashed line is $In_{0.52}Al_{0.48}As$ and semiclassical results for hetero-junction, red solid line is NEMO calculation for hetero-junction, and light blue line is NEMO calculation for single barrier with barrier thickness of 200 Å (b) single barrier. Barrier thickness: 6, 21, 70, 100 Å (c) multi-barriers-1, no. of barriers in SL cnts + a single barrier device: 1, 2, 4, 10, and (d) multi-barriers-2, no. of barriers in device region: 1, 2, 4, 10. The dashed dot is bulk $In_{0.53}Ga_{0.47}As$ and dashed line is $In_{0.52}Al_{0.48}As$. 184

Figure Page

B.4. (a) PF vs. E_F results: dashed dot is bulk $In_{0.53}Ga_{0.47}As$, dashed line is $In_{0.52}Al_{0.48}As$ and semi-classical results for hetero-junction, red solid line is NEMO calculation for hetero-junction, and light blue line is NEMO calculation for single barrier with barrier thickness of 200 Å (b) maximum PF (PF_{max}) of single barrier with respect to barrier thickness: 6, 21, 70, 100 Å (c) PF_{max} of multi barriers - 1, no. of barriers in SL cnts + a single barrier device: 1, 2, 4, 10, and (d) PF_{max} of multi barriers-2, no. of barriers in device region: 1, 2, 4, 10. The dashed dot and dashed lines in (b)-(d) represents PF_{max} of bulk $In_{0.53}Ga_{0.47}As$ and $In_{0.52}Al_{0.48}As$ in (a), respectively. Square symbols in (c) and (d) denotes PF_{max} of corresponding single barrier device in (b). 185

E.1 (a) the Voronoi diagram of a random set of points in the plane shown by red dots (all points lie within the image), (b)-(e) 2D microstructure generated by Voronoi tessellation. The number probability of HAGBs (shown by black solid line) for (b), (c), (d), and (e) are 25, 50, 75, and 100%, respectively. In this study, microstructure with 50% HAGBs is used – i.e. (c).. 192

E.2 (a) schematic diagram of 2D finite difference mesh ($N \times N$ grids, $N = 100$, grid size = 1 nm). (b) grid points around element (i, j). 195

ABSTRACT

Jeong, Changwook. Ph.D., Purdue University, August 2012. Landauer Approach to Thermoelectrics. Major Professors: Mark S. Lundstrom and Muhammad A. Alam.

Many efforts have been made to search for materials that maximize the thermoelectric (TE) figure of merit, *ZT*, but for decades, the improvement has been limited because of the interdependent material parameters that determine *ZT*. Recently, several breakthroughs have been reported by applying nanotechnology. To further enhance *ZT*, a clear understanding of electronic and thermal transport is necessary. The objectives of this thesis are: 1) to evaluate the electronic and thermal performance with a Landauer approach using full band electronic bandstructure and a full dispersion description of phonons, 2) to show how the Landauer treatment gives new insights to the understanding of thermoelectrics, and 3) to discuss possibilities for enhancing TE performance. We first present a Landauer approach for computing TE parameters using a full band electronic bandstructure. The full band results are related to the more common effective mass formalism. Next, a full dispersion description of phonons is used to calculate the thermal conductivities of bulk and thin films using a Landauer approach. It is shown that simplified dispersion models for phonons should be used with caution and that the Landauer approach provides a relatively simple (but accurate) technique to treat phonon transport from the ballistic to diffusive regimes. We also address the question of how to engineer the electronic structure to enhance the performance of a thermoelectric material by re-visiting from a Landauer perspective the question of what bandstructure produces the best thermoelectric device performance. Next, we explore the possibilities of increasing *ZT* through multi-barrier structures, quantum engineered graphene and molecules, high valley degeneracy, or by distorting the density-of-states. Finally, we shift our attention to nanocomposite thermoelectric materials and discuss a new approach to model nanocomposite TE devices. Using polycrystalline graphene as a testbed of our

model, we study how grain boundaries affect the electronic performance of large-area polycrystalline graphene and propose the new approach of ‘percolation-doping by nanowires’ to beat the transparency-conductivity constraints.

1. INTRODUCTION

As the world's demand for energy increases, the availability for sustainable energy sources has become one of the biggest concerns regarding our future. Solar, wind, and fuel cell technologies have promised environmentally friendly and energy efficient power generation solutions. In addition to these technologies, the use of thermoelectric (TE) power generation to utilize waste heat in various situations such as vehicles, industrial process and homes could be an effective and reliable energy source. Also, the need for thermoelectric cooling in electronics where traditional convection based cooling technology is not viable, is significant. With increasing energy prices and TE technology developments, the field of thermoelectrics has recently received a lot of attention. In Section 1.1, a brief history of thermoelectricity is presented. Section 1.2 addresses essential physics of thermoelectrics, the principles of thermoelectric energy conversion, and the key parameters that determine the device performance and applications. Section 1.3 provides a review of thermoelectric research from the 1950s - 1990s and summarizes recent achievements as well. Finally, the organization of the thesis and a list of associated publications are presented in Sections 1.4 and 1.5, respectively.

1.1 A Brief History of Thermoelectrics

Early 19th century scientists, Thomas Seebeck and Jean Peltier, discovered two phenomena that are the basis for today's TE industry. In 1821, Seebeck found that when a junction of two dissimilar conductors is placed in a temperature gradient, it produces a current, and the current deflects a magnetic compass placed next to it. Peltier, on the other hand, announced in 1833 that the temperature changes across a junction of two dissimilar metals when current flows. In 1838, Lenz explained that heat is either emitted or absorbed at the junction of the materials depending on the direction of current flow. It took a few more decades for William Thomson to understand thermodynamically that both phenomena were different manifestations of the same underlying physics and predict the Kevlin (Thomson) relations. He also discovered a third TE effect, the Thomson effect. In 1911, Altenkirch created a satisfactory theory of thermoelectricity for refrigeration and power generation by introducing the figure of merit, Z. In 1931, Onsager proved rigorously Thomson's findings in a thermodynamic sense and set the stage for further studies.

It was only after 1950s' advancements in semiconductor technology, however, that practical TE devices became feasible; the idea to use thermoelectrics as refrigerators was suggested by Ioffe [33]. With modern techniques, TE modules are now produced to deliver efficient solid state heat-pumping for both cooling and heating, as well as to generate DC power in various circumstances such as space probe and automobiles. New uses and markets for thermoelectrics continue to be developed.

1.2 Thermoelectric Physics

1.2.1 Thermoelectric Effects

The conventional, basic theory of thermoelectricity is covered in many textbooks. In this section, we use a single level model with the Landauer transport theory to explain the Seebeck and Peltier effects and other related phenomena based on Refs. [26, 27]. According to the Landauer formalism, electrical current (I) and heat current (I_q) for a single level model (Fig. 1.1) are expressed as

$$I = \frac{2q}{h}\bar{T}\left(f_1 - f_2\right), \tag{1.1a}$$

$$I_q = -\frac{2\left(E - E_{F1}\right)}{h}\bar{T}\left(f_1 - f_2\right), \tag{1.1b}$$

where h is the Planck constant, $\bar{T}$ is the transmission across the device, E is the energy level of single energy channel, E_{F1} and E_{F2} are the Fermi levels of the two contacts, and f_1 and f_2 are equilibrium Fermi-Dirac distributions for the contacts. Both electrical and heat currents are assumed to be positive along the direction from contact 2 to contact 1. The driving force of current flow is the difference in Fermi-Dirac distributions of contact 1 and contact 2, which can be created by either the voltage difference (ΔV) or the temperature difference (ΔT) between the contacts. In an open-circuit with a temperature gradient, current flow is zero when $f_1 = f_2$. Therefore, the following condition should be met:

$$\frac{E - E_{F1}}{T_1} = \frac{E - E_{F2}}{T_2} = -\frac{E_{F1} - E_{F2}}{T_1 - T_2}. \tag{1.2}$$

Hence, the Seebeck coefficient (S) is expressed in the linear response regime as

$$S \equiv \frac{\Delta V}{\Delta T} = \frac{\left(E_{F1} - E_{F2}\right)/q}{T_1 - T_2} = -\frac{E - E_F}{qT}. \tag{1.3}$$

From Eq. (1.1b), the rate of heat generation (+) or absorption (-), I_q at the junction when electrical current flows from is expressed as

$$I_q = -\frac{I}{q}\left(E - E_F\right), \tag{1.4a}$$

the Peltier coefficient (Π) is

$$\Pi \equiv \frac{I_q}{I} = -\frac{\left(E - E_{F1}\right)}{q}. \tag{1.4b}$$

From Eqs. (1.3) and (1.5), the Kelvin relation arises naturally as

$$\Pi = ST. \tag{1.4c}$$

In 1855, a few decades after the discovery of these effects, William Thomson developed a unifying theory using thermodynamics arguments. The Thomson effect is that heat can be generated or absorbed by a homogeneous conductor if an electric current is passing through it and a temperature gradient is present at the same time. The total energy flux carried by phonons and electrons:

$$Q = \Pi I + IV - \kappa \frac{dT}{dx}, \tag{1.5}$$

where κ is lattice thermal conductivity. The negative x-derivative of the energy flux gives the net energy accumulation, i.e. the rate of heating per unit length:

$$-\frac{dQ}{dx} = -I\frac{d\Pi}{dx} - I\frac{dV}{dx} + \frac{d}{dx}\left(\kappa \frac{dT}{dx}\right), \tag{1.6a}$$

where we assumed that the electric current is constant. Using

$$I = G\frac{dV}{dx} + SG\frac{dT}{dx}, \tag{1.6b}$$

for the gradient of the potential in Eq. (1.6a) gives:

$$-\frac{dQ}{dx} = -\tau I\frac{dT}{dx} - \frac{I^2}{G} + \frac{d}{dx}\left(\kappa\frac{dT}{dx}\right), \tag{1.6c}$$

where the first term is the Thomson effect and the Thomson coefficients (τ) is given by

$$\tau = \frac{d\Pi}{dT} - S, \tag{1.7}$$

with $S \equiv SG/G$. From Eq. (1.4c), the Thomson coefficients is obtained to be

$$\tau = T\frac{dS}{dT}. \tag{1.8}$$

Thermoelectric effects we discussed in this section can be applied to energy conversion between heat and electricity such as refrigeration and power generation. In the following section, we review the basic principles of refrigeration and power generation.

1.2.2 Thermoelectric Energy Conversion and Applications

Figure 1.1 shows schematic representations of TE devices and one level pictures for (b) power generation, and (c) refrigeration. The TE device is composed of two conductors, which are p-type and n-type conductors connected electrically in series and thermally in parallel. When there is a temperature difference as shown in Fig. 1.1(b), a voltage difference is generated. Electrons in N-type conductors move from the hot contacts to the cold contacts, whereas electrons in P-type conductors move from the cold to the hot contacts because of $f_{cold} < f_{hot}$ in N-type and $f_{cold} > f_{hot}$ in P-type at the channel energy level. When the current flows in Fig. 1.1(c) by applying a bias, cooling occurs at the top contact. Electrons always flow from high E_F to low E_F and therefore electrons should absorb energy from the contacts in the middle (i.e. top contact). Cooling and generation capacities can be increased by segmenting (or cascading) multiple TE devices [36].

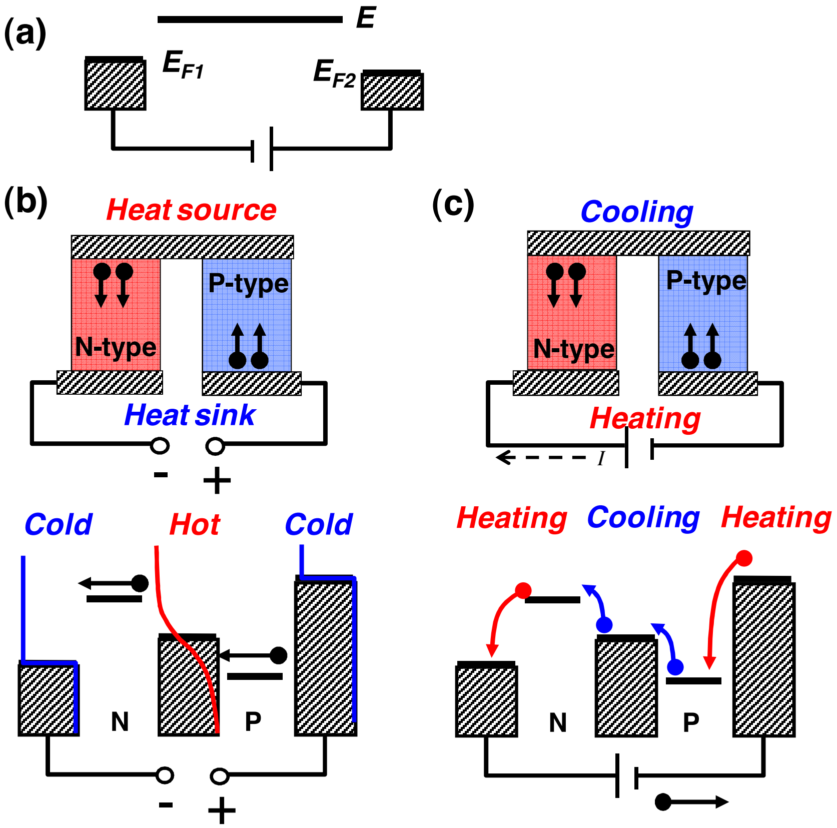

Fig. 1.1 The schematic diagram of (a) one level picture and TE devices for (b) power generation, and (c) refrigeration. The TE device is composed of p-type and n-type conductors connected electrically in series and thermally in parallel. The solid red and blue lines at the contacts in (b) denotes Fermi-Dirac distribution. The solid circles and arrows denote electrons and the direction of electron flow.

Numerous applications of thermoelectric devices have been proposed and used. Thermoelectric technology, however, has low efficiency, and therefore has been limited to niche markets where high reliability, less maintenance, and small size are more important than magnitude of energy output. For example, TE devices have been used in all deep space probe missions to provide onboard power to space probes and have demonstrated high reliability [37]. Remote power units are another example [38]. In addition, TE devices have several cooling applications such as picnic cooler, laser diode cooling, cooling for lasers, microprocessor cooling, car seat and steering cooling as well as heating, ventilation and air-conditioning (HVAC) of vehicles. TE devices are being explored for waste heat recovery in vehicle, industry, power plant and incinerators [31, 32], which will help alleviate the global energy and environmental problems because it does not need to burn additional fossil fuel [38]. New possibilities such as on-chip cooling [41–43] and cryogenic refrigeration [44] are also being explored.

Estimated worldwide production of thermoelectric devices in 2008 was around 25 million units [38]. In 2009, the world market for commercial TE power generation and TE cooling were \$30-50 M/yr and \$200-250M/yr, respectively [45]. The technology has tremendous growth potential and is in accelerated development world-wide. HVAC applications of TE devices alone are estimated to save 4.5 Billion gals/year of fuel in US, and reduce the green house gases by 69.5 million metric tons of CO_2 per year [46]. TE power generation from waste heat has also a large potential in the industrial sector. The industrial sector consumes 31% of the world's energy. Much like vehicular energy, as much as 60% of energy converted to power is wasted [46]. Therefore, with increasing energy prices and TE technology developments, thermoelectrics could become competitive for industrial waste heat recovery in the near future.

The challenge to increasing applications and market size is to enhance efficiency of thermoelectric energy conversion. The efficiency is expressed by the figure of merit, ZT. The figure of merit is still smaller than the value required to compete with the conventional method, $ZT > 3$ [47]. The details of ZT will be discussed in the following section.

1.2.3 Figure of Merit and the Coefficient of Performance

The thermoelectric figure of merit, $ZT = S^2\sigma T/\kappa$, is defined as follows. Consider the n-type conductor in Fig. 1.1(b). When the current flows through the conductor, electrons carry heat from the top to the bottom cooling the top junction. When there is a temperature difference, ΔT, then heat flows back from the hot side to the cold side. There is another heat source, Joule heating, which occurs due to the conductor's finite resistance. We assume that half of the Joule heating passes to the hot side while the other half transfers to the cold side [33]. Then the total heat current cooling at the top junction becomes

$$I_q = \Pi I - \kappa\Delta T - \frac{I^2R}{2}, \tag{1.9}$$

where *R* is the conductor's resistance. In Eq. (1.9), the first term is the Peltier cooling, the second term is the heat back flow, and the last term is the half of the total Joule heating. The I_q in Eq. (1.9) should be maximized to maximize cooling, and the optimum current, $\hat{I}$, is obtained as

$$\frac{dI_q}{dI} = \Pi I - IR = 0, \tag{1.10a}$$

$$\hat{I} = \Pi / R, \tag{1.10b}$$

and the maximum I_q becomes

$$I_{q,\max} = \frac{\Pi^2}{2R} - \kappa \Delta T. \tag{1.11}$$

The maximum cooling occurs when $I_{q,\max} = 0$ so that ΔT is maximized. Then the maximum temperature difference between the hot and cold side becomes

$$\Delta T_{\max} = \Pi^2 / 2R\kappa. \tag{1.12}$$

From the Kelvin relation in Eq. (1.6) and $\sigma = 1/R$, the *ZT* is defined as

$$\Delta T_{\max} = \left(\frac{S^2 \sigma T}{\kappa} \right) \frac{T}{2} \equiv \left(ZT \right) \frac{T}{2}. \tag{1.13}$$

It can be seen that *ZT* determins the maximum possible temperature difference in cooling devices. Alternatively, $ZT = 2\Delta T_{\max} / T$ [48].

The *ZT* is related to the efficiencies of the thermoelectric refrigerator or heat engine. For the refrigerator, the efficiency is defined as the rate of heat removed from the cold side to the input power. The maximum possible efficiency is called the coefficient of performance (COP), and it is expressed in terms of *ZT* as [33]

$$\mathrm{COP} = \frac{T_c}{T_h - T_c} \frac{\sqrt{1 + ZT_m} - T_h / T_c}{\sqrt{1 + ZT_m} + 1}, \tag{1.14}$$

where T_h is the temperature at the hot side, T_c is the temperature at the cold side, and $T_m = \left(T_h + T_c \right) / 2$. Note that as $ZT_m \to \infty$ in Eq. (1.14), the COP approaches the Carnot limit, $T_c/(T_h - T_c)$. The efficiency of a heat engine is the generated power divided by the heat flow from the hot source, and the maximum efficiency ($\eta_{\max}$) is found as [33]

$$\eta_{\max} = \frac{T_h - T_c}{T_h} \frac{\sqrt{1 + ZT_m} - 1}{\sqrt{1 + ZT_m} + T_c/T_h} . \tag{1.15}$$

Similarly, as $ZT_m \rightarrow \infty$, Eq. (1.15) gives the Carnot efficiency of $(T_h - T_c)/T_h$. Therefore, *ZT* should be maximized to obtain high efficiency. Note that as discussed in Appendix F, the efficiency under the maximum power output condition is also crucial parameter.

Cooling and generation capacities can be increased by segmentating multiple TE devices [36]. It was shown that materials with dissimilar compatibility factors cannot be combined by segmentation into an efficient thermoelectric generator [49], where the compatibility factor (*s*) is defined as, $s = \left(\sqrt{1 + ZT_m} - 1\right)/ST_m$. Therefore, in such segmented TE devices, control of the compatibility factor in addition to *ZT* is essential for efficient operation of a thermoelectric device, and thus will facilitate rational materials selection, device design, and the engineering of functionally graded materials.

In the next section, we review important breakthroughs in thermoelectric researches over the past 6 decades and discuss why they have been successful. Other approaches that are being explored to further increase the performance are also reviewed.

1.3 Thermoelectric Research

1.3.1 Bismuth Telluride Alloys: 1950s - 1990s

In the 1950s, when the basic understanding of TE materials became established, the field of thermoelectric advanced rapidly after Ioffe's observation that doped semiconductor are good TE materials [33]. Bismuth Telluride (Bi_2Te_3) was discovered and commercialized. It was the launch of TE industry. In addition to Bi_2Te_3, Lead Telluride (PbTe) and Bismuth Antimony (Bi-Sb) alloys were the best TE materials for refrigeration during the 1950s and 1960s.

The key factors that make Bi_2Te_3 a good thermoelectric material are a low lattice thermal conductivity and high power factors. The formation of solid solutions with iso-structural compounds such as Bi_2Te_3 - Sb_2Te_3 - Bi_2Se_3, Bi-Sb, PbTe-SnTe, InSb-GaSb, Si-Ge increases the phonon scattering rate (alloy scattering) due to atomic mass and volume fluctuations. In addition, the high atomic mass is also related to the low sound velocity. These two factors lead to a low lattice thermal conductivity regardless of relatively large specific heat. For good electronic performance, higher Seebeck coefficients and higher mobility at reasonable doping levels is important. Because Bi_2Te_3 has six valleys in both the conduction and valence bands [2, 35], this allows higher S and σ at the optimum power factor [45]. We will explain the TE performance of Bi_2Te_3 in more detail in Chapter 3.

Over the following three decades 1960-1990, only incremental enhancements in *ZT* were made, and therefore the field received little attention with Bi_2Te_3 remaining the best TE material. Nevertheless, thermoelectrics proved to be competitive in niche applications such as NASA's deep probe mission, laboratory equipment, and medical applications where the unique features of TE devices such as reliability, small size and precise temperature control are more important than cost and efficiency.

1.3.2 Beyond Bismuth Telluride: after 1990s

Stimulated by strong support from the US Department of Defense in the early 1990s, the research community was encouraged to see if the development in material science and nanotechnology can enhance the TE performance. As a result, various type of approaches were taken to develop new TE materials beyond bulk Bi_2Te_3. The most recent efforts to improve ZTs are to combine reducing lattice thermal conductivity such as nanocomposites with power factor enhancement by density of states engineering.

Although the revival of interest in thermoelectrics in the early 1990s was stimulated by the predictions that independent control of S and σ is possible by nanostructuring [42, 43] , recent experimental reports of high ZT [10,12, 44–49] are attributed to suppressing the thermal conductivity, κ. The κ is the sum of the electronic contribution, κ_e , and the lattice thermal conductivity, κ_l . In semiconductors, heat transport tends to be more dominated by the lattice, so κ_l plays a critical role in thermoelectric performance. It has been reported experimentally [58] and theoretically [51, 52] that κ_l can decrease by a few orders of magnitude in lower dimensional devices due to phonon confinement and increased boundary scattering. Phonon transport can be further suppressed by embedding nanoparticles in semiconductors [61]. Reducing κ_l is an effective way to increase *ZT* provided it does not degrade the electronic properties significantly. More detailed review of recent achievements in thermal conductivity reduction in bulk nanocomposite and nanostructured material will be given in Sec 1.4.

Power Factor Engineering. In addition to the enhancements in nanostructures by improving the phonon part (κ_l), there have been continuing efforts to increase the *ZT* of bulk materials because many thermoelectric applications require materials in large quantity. Another way to increase the *ZT* is improving the electronic part (power factor, $S^2\sigma$) and now the question of whether the electronic performance can be enhanced are being asked [8,62,63].

Engineering DOS. Significant improvement in *S* have been predicted and reported for several different materials. For example, an enhanced *S* has been achieved by engineering the density-of-states (DOS) in bulk Tl-PbTe [8], LAST $[(PbTe)_{1-x}(AgSbTe_2)_x]$ system [64], and $La_{3-x}Te_4$ [65]. The goal of DOS-engineering is to create resonant states of impurity in the conduction or valence bands, although most of impurity atoms introduce states in the band gap. In addition, giant Seebeck coefficients have been predicted for nanostructured graphene [66] as well as for appropriately engineered molecules [67]. These examples all seek to enhance performance by achieving a shaply-peaked DOS around a narrow band of energy. Bandstructure engineering could also be achived by controlling strain of the sample. This approach has been very successful for enhancing the electronic performance of nano-transistors and is currently being explored to enhance TE performance [68–71]. DOS and strain engineering are similar because strain can adjust the location of the upper valleys with heavy mass and large valley degeneracies to maximize performance, in which the upper valleys play a role like resonant states. More details of DOS engineering to increase the performance will be discussed in Appendix A.

Energy Filtering. The energy filtering effect has been proposed to improve the power factor. The principle is to introduce an energy barrier (or any type of scattering center) that can preferentially scatter low energy electrons to increase the Seebeck coefficient while maintaining good conductivity through high energy electrons. Theoretical calculation showed significant increases in ZT (as large as 100%) for perpendicular transport in superlattice. This is because the increase in mean carrier energy by energy filtering allows larger carrier density (heavier doping) while maintaining the same scattering rate by ionized impurity scattering process [72]. Experimentally, researchers have shown S can be increased by filtering out low energy electrons [73–75], but an improvement in power factors has been limited. These energy filtering effects could play a role in NC materials because the nanograin boundaries act energy barriers.

Phonon Drag. The phonon drag effect is another way to achieve large S. The phonon drag Seebeck effect is the result of strong electron-phonon interactions. The phonon drag Seebeck effect occurs in the following way. The temperature gradient: 1) transfers momentum from phonon to electron by electron-phonon scattering, 2) which leads to larger electron flow to cold side, so that 3) a larger voltage is developed to make current flow zero in a open circuit condition, resulting in large Seebeck coefficients. When other phonon scattering mechanisms are more dominant than electron-phonon scattering, phonon momentum is relaxed through the dominant phonon scattering process so that phonon drag effect is negligible. Therefore, the phonon drag Seebeck effect is small for highly doped material (i.e., larger electron densities and phonon scattering by impurities.), high temperature (i.e., strong Umklapp scattering), and materials with low Debye temperature (i.e., strong Umklapp scattering). At normal operating temperature, therefore, the phonon drag effect is hard to observe under high doping conditions, which is usually the optimum condition. In low-dimensional structures, it is theoretically reported that the phonon-drag effect cannot improve the performance, although phonon-drag effect is enhanced [76]. Recent experiments, however, suggest that the phonon-drag effect is enhanced to improve ZT in lower dimensions due to the modification of phonon modes [11, 69].

Attempts to search for new low temperature TE devices have been made because the ZT below room temperature becomes even less competitive. Strongly correlated electron systems are being pursued because giant Seebeck coefficients are observed in systems such as Kondo impurity systems, Kondo lattice systems, Kondo insulators, high critical transition temperature (T_C) superconductors, and transition metal oxides [78] . As an example, $FeSb_2$ exhibits more than an order of magnitude increase in *S* and *PF* than conventions TE materials at low temperature, though its physical origin still needs to be understood [36, 71, 72]. In the transition-metal oxides such as $Na_xCo_2O_4$, enhancement in S is attributed to spin entropy due to strong electron-electron interaction [81].

As a new device concept, a thermionic device has been proposed and examined for refrigeration and power generation [48,82–85]. In thermionic devices, energy is transported by ballistic electrons injected over a potential barrier, whereas energy is transported by diffusive carriers in thermoelectric devices. No clear experimental evidence of improved cooling performance, however, has been demonstrated.

1.3.3 Evaluation of Thermoelectric Devices

Electrical conductivity (carrier concentration, mobility) measurements are relatively easy and well developed in the semiconductor industry even for thin films. A variety of methods are used such as the four-point probe method, van der Pauw technique, and Hall measurements [86]. In the measurement of Seebeck coefficients, errors related to the sample dimensions are not present by definition. The key challenge is to determine correct temperature gradient across the sample. Among the individual parameters in the figure of merit, it is thermal conductivity that is the most difficult to measure with relatively high accuracy because both errors in determining the sample dimensions and temperature gradient are present. In particular, samples with low thermal conductivity are harder to measure because the heat loss can easily occur through other paths of low thermal resistivity such as leads and surrounding gas flow. The 3ω method is currently regarded as the best method available, though it requires careful sample preparation [87]. Measurement of intrinsic thermal properties of low dimensional nanostructure such as nanowires and nanotubes with good accuracy are even more difficult with conventional method because of small sample size and large influence of thermal contact resistance. A special microdevice for thermal property measurements, therefore, was proposed [58]. Another technique that is widely used to directly obtain ZT of the bulk or thin film TE device is the Harman method or Z meter [88]. The Harman method utilizes the difference of response time of voltage developed by Joule effects and Peltier-Seebeck effects to applied current. Information from this technique should be compared to the measurements of the individual parameters [88–90].

1.4 Nanocomposites Thermoelectrics

Nanocomposite materials are currently receiving a lot of attention due to reports of increased *ZT* in materials systems that are easy to fabricate and possess good mechanical strength [20,27,91,92]. In this section, we review the field of nanocomposite (NC) thermoelectric materials. Nanocomposite materials encompass a large variety of systems, such as 1D, 2D, 3D crystalline materials, and amorphous materials made of dissimilar components and mixed at the nanometer scale. For thermoelectric (TE) applications, however, the term nanocomposite usually refers to two types of bulk nanostructured materials [27]: 1) materials with nanoparticles in a matrix (host) and 2) polycrystalline materials consisting of nanosized grains where neighboring grains could be different materials or the same materials. Topics surveyed in this review include: 1) the motivation for NCs, 2) key experimental accomplishments, 3) materials fabrication and properties, 4) electron and phonon transport, and 5) modeling approaches. Finally, we discuss challenges and what needs to be done in order to understand, model, and design NCs for TE applications. This section provides the background for Chapter 7 where our modeling approach and some initial results are discussed.

1.4.1 Motivation for Nanocomposite Thermoelectrics

Increasing the TE figure of merit (FOM), $ZT_L = S^2\sigma T_L/\kappa$, involves increasing the power factor ($PF = S^2\sigma$) or decreasing the thermal conductivity (κ), or both.

Nanocomposites have clearly demonstrated the ability to decrease thermal conductivity without significant adverse effects on the electrical performance [21, 83–85]. There are also reports of enhanced Seebeck coefficient at a constant conductivity [9, 67]. Consequently, there is significant promise that with proper design, nanocomposite TE materials could achieve very substantial enhancements in performance.

Theoretical studies of thermal conductivity in superlattices and random nanostructures indicated that the primary cause of low lattice thermal conductivity is not a special, periodic geometry or a perfect interface, but the presence of interfaces with high density [84, 86]. Understanding of how thermal conductivity was reduced while not lowering electrical conductivity in the NCs, however, requires the spectral analysis of electron and phonon transport as we will discuss in Chap. 2, 3, and 4.

The selective scattering of electrons and phonons in the NCs is possible mainly because the electrons that contribute to σ have larger wavelengths than the phonons that contribute to κ_{ph} and interfaces are coherent or semi-coherent. First, the difference in wavelength spectrums for electrons and phonons makes it possible to introduce scattering center that strongly affect phonons and weakly affect electrons to achieve a phonon glass and electron crystal (PEGC) [94]. On top of that, the presence of interfaces and nanograins with a proper size can effectively scatter mid - to long - wavelength phonons, which are less scattered by alloy scattering thereby making it possible to achieve lower thermal conductivity than corresponding bulk samples. Second, coherent or semi-coherent interfaces increase scattering for phonons more than for electrons. This is due to the fact that local strain at semi-coherent or coherent boundaries effectively increases the scattering cross-section for phonons, while the coherent boundaries do not degrade electron flow significantly [20, 53, 88].

1.4.2 Key Experimental Accomplishments

Researchers have fabricated a type of bulk nanostructured materials with a simple fabrication processes such as thermal processing and powder metallurgy methods. In several material systems, such thermal processing methods have succeeded in obtaining ZTs as high as 2.2 at 800 K [94]. The powder metallurgy method has been applied to many bulk materials such as BiSbTe alloy [96,97], Si/Ge alloy [98,99], and skutterudites [22,100] with the ZT greater than 1. Recent achievements by thermal processing and by powder metallurgy are well discussed in Ref. [20] and [101], respectively. Figure 1.2 shows the maximum ZT vs. total thermal conductivity for recent nanostructured TE devices. The results for conventional TE bulk materials have also been included for comparison. It can be seen that recent enhancements in ZTs are mostly due to thermal conductivity reduction, while maintaining or not degrading much the power factor (PF). Thermal conductivity in the NCs is usually less temperature dependent comparing to the corresponding bulk materials because the phonon scattering rate by interfaces becomes more important than Umklapp scattering. Due to a large degradation in electrical conductivity, however, all groups have not succeeded in making NCs with high ZT due to large degradation in electrical conductivity. Lan et al., [101] argued that this could be due to contamination by oxygen, moisture, and other environmental factor during the fabrication process.

To further enhance the ZT, the question of whether the numerator of the ZT, the PF, can be enhanced is now being asked. Some successes have been reported with composite bands [8] and with nanocomposites [18]. Their results are labeled as "PF increase" in Fig. 1.2. Currently, work on combining the concept of composite bands with NCs is underway [101]. Another strategy to increase the electronic performance is the use of energy filtering. Since grain boundaries can act as a potential barrier, the NCs expect to see the energy filtering effect – i.e., the Seebeck coefficient increase at the same carrier concentration. The experimental demonstration of the effect is, however, rare. There have been reports in which a ZT increase results from enhancement of Seebeck coefficients by the energy filtering effect, not from increase in σ/κ ratio [67, 95, 96]. It was reported that the Seebeck coefficient of PbTe thin films increases as the grain size decreases, while the σ/κ ratio keep decreasing [103]. The Seebeck coefficient vs. concentration was examined for PbTe thin films on different substrates, and it was observed that the S at the same concentration depended on the substrates [102]. It was argued that this occurs due to the different properties of grain boundaries which were determined by process condition and substrate.

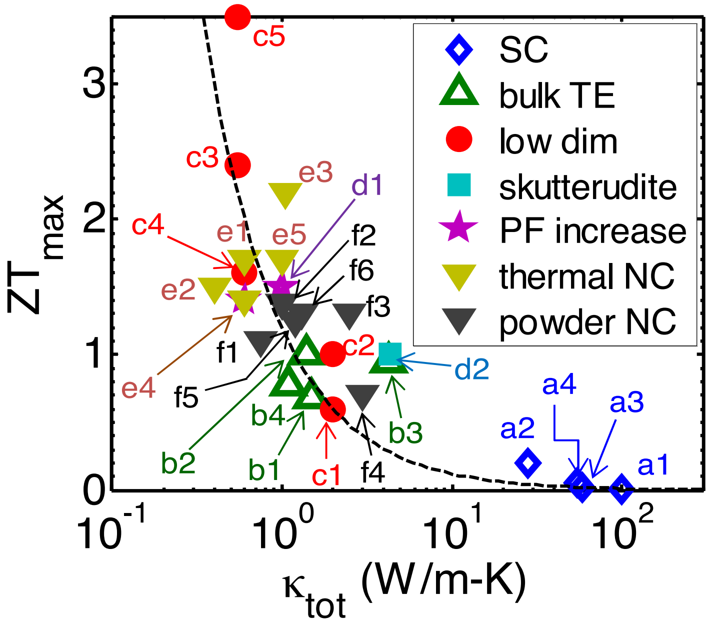

Figure 1.2. The maximum ZT vs. total κ. The dashed line: PF = 40 $\mu W/m^2K^2$, T=300K; Conventional semiconductors used in IC industry (open diamonds): a1) Si 300K [1,2], a2) Si 1275K [1], a3) Ge 300K [3], a4) GaAs 300K [4]; bulk TE materials used in TE devices (open triangles): b1) p-Bi_2Te_3 300K [5], b2) p-$Bi_xSb_{2-x}Te_3$ 300K [6], b3) n-$Si_{80}Ge_{20}$ 1275K [7], b4) PbTe 300K [8]); nanostructured materials fabricated by thin films processing (filled circle): c1) Si nanowire (NW) 300K [9], c2) Si NW 200K [10], c3) Bi_2Te_3/Sb_2Te_3 superlattice (SL) 300K [11], c4) PbTe/PbSeTe quantum dot (QD) SL 300K [12] , c5) PbTe/PbSeTe QD SL 575K [13]; electronic structure engineered bulk materials (open star): d1) Tl-PbTe 773K [8]; partially filled skutterudites (filled square): d2) n-$Yb_xCo_4Sb_{12}$ 600K [14]; bulk nanostructured materials fabricated by thermal processing (filled inverse triangles): e1) p-$Na_{1-x}Pb_mSb_yTe_{2+m}$ 650K [15], e2) p-$Pb_xSn_{1-x}Te$-PbS 642K [16], e3) n-$AgPb_mSbTe_{m+2}$ 800K [17], e4) PbSbTe 700K [18], e5) p-PbTe-SrTe 800K [19]; and powder metallurgy (filled triangles): f1) p-Bi_2Te_3 300K [20], f2) p-$Bi_xSb_{2-x}Te_3$ 475K [6], f3) n-$Si_{80}Ge_{20}$ 1275K [7], f4) Si 1275K [1], f5) n-LaTe 1273K [21], f6) n-$Yb_xCo_4Sb_{12+y}$ 800K [22]. Note that the report of ZT ~ 3.5 (c5) in Ref. [13] turned out to be an error due to inaccurate carrier concentration measurements. Examination of the Hall samples used in Ref. [13] indicated incorrect contact geometries, with pressed indium contacts that were large relative to the sample size and inset from the edges [23].

Using fine particles with low conductivities and coarse particles with high conductivities, Zhao et al. [104] experimentally studied the effect of mixed grain sizes on TE performance for Bi_2Te_3 and showed the possibility of use of percolative transport to boost TE performance. It was seen that there was an optimum fraction of fine particles for maximum ZT and PF. They qualitatively attributed the characteristics to the percolative transport. They, however, found that σ/κ ratio decreases with weight fraction of fine particles because electrical conductivity is more rapidly decreasing with fine particles. So the main benefit came from the increase in Seebeck coefficient. The Seebeck coefficient at the same concentration was increased in comparison to bulk Bi_2Te_3, which was attributed to energy filtering effects by introducing fine particles – i.e. more potential barriers. This experiment is hard to explain by conventional modeling approaches.

To date, nanocomposite design has been empirical - based on trial and error [92, 98, 99]. This is because our understanding of how grain boundaries scatter electrons and phonons is incomplete, and because grain and GB statistics are only known for specific instances. As a result, there is no physical model that can predict the performance of nanocomposites as a function of grain properties and GB statistics. There is, therefore, a critical need to develop a physics-based modeling approach and computational tools for the rational design of nanocomposite thermoelectric materials and devices. Such an approach must begin by modeling the manufacturing processes used to produce nanocomposite materials, which we discuss next.

1.4.3 Manufacturing Processes and Materials Properties

Cost-effective synthesis methods for TE devices are essential factors that drive current research. A variety of materials and synthesis methods have been proposed to introduce high density interfaces in bulk samples with relatively simple fabrication processes. Key features of the main techniques to prepare nanocomposite TE materials are summarized in Table 1.1 and compared to thin film processing methods [21, 100, 101]. There are several requirements for the synthesis method [27]: 1) it should be a bulk process in which preparation conditions can easily be tuned for maximum ZT and 2) thermodynamical stability is important. The two main approaches currently taken for developing NC TE materials are reported to produce stable NCs with high ZTs. For example, thermal stability tests on SiGe NCs shows no change in the thermal conductivity during a period of 1 year at 1275 K under vacuum [1].

Table 1.1.

Summary of fabrication techniques for TE materials

	Thin film processing	**Thermal processing**	**Powder metallurgy**
technique	• Sputtering • vapor deposition • molecular beam epitaxy • liquid phase epitaxy • atomic layer deposition	• zone-metling • Czochralski • Bridgman	• grinding, ball milling • wet chemical process • hot pressing • sintering (ex. SPS)
Pros	• small consumption of materials • high quality samples • low temperature process	• high quality samples • good thermodynamics and crystallographic control	• mechanical strength • low temperature process • low cost mass production • little phase diagram knowledge • overdoping beyond solubility limit
Cons	• need good phase diagram knowledge • high cost, slow • characterization	• need good phase diagram knowledge • brittle • high doping difficult	• highly dense samples difficult • poor crystallographic control

The first approach for producing nanocomposite TE materials is based on nanograin (or nanoparticle) formation from melts by thermal processing. The nanoscale grains are self-formed by either nucleation and growth mechanisms or spinodal decomposition (phase separation process without a nucleation step) or the so-called " matrix encapsulation" technique. In the process, properties like grain size can be adjusted by tuning the process condition such as cooling profile [17, 21, 102]. Though thermal processing has several advantages such as high quality samples without pores, the method needs good phase diagram knowledge, and the samples tend to be brittle due to microcracks [20].

The second method uses powder metallurgy (usually by ball milling + sintering process) to create nanograins. Nanosized crystalline powders of the chosen compound are prepared by grinding and ball milling or wet chemistry processing, then followed by hot pressing or sintering into bulk objects. More recently, spark plasma sintering (SPS) process has been widely adopted to achieve fast densification with minimal grain growth in a short sintering time [107]. The nanosized grains formed by thermal processing described above are usually nanoparticles in a matrix. This approach, however, creates extensive interfaces between the compacted nanoparticles. The challenge, therefore, is to obtain highly dense samples because it is hard to completely remove oxides or organics at interfaces which are used in the sample preparation (grinding, milling or wet chemistry) [21, 91]. The benefits of this method are a relatively low cost process, more choices of materials, better mechanical properties, and improved isotropy [20].

These efforts to develop the NCs fall into several approaches of tailored microstructural and interfacial control: (a) a polycrystalline microstructure with reduced grain size, (b) preferential alignment of grains along favorable transport directions, (c) nanocoated grains, (d) embedded nanoinclusions, and (f) lamellar/multilayer structures. Although each class could be realized by different choice of materials, it is important to find the best microstructure for a given properties of grain and grain boundaries to understand electrical and thermal transport in NCs. This can be only done by modeling studies but current modeling approaches cannot answer this question as will be discussed in next section.

The size of nanoparticles in a host and nanograins in polycrystalline range from several nanometers to several microns, although nanometer sized inclusions are usually observed inside micrometer sized grain for samples with high ZT [92]. It has been reported that grain boundaries between the host grain and the self-formed nanoparticles inside the host grain are semi-coherent or coherent GBs [85, 103, 104], which are regarded as ideal interfaces to only suppress phonon transport. The NCs by power metallurgy, however, have achieved high ZT with random GBs between grains [101]. The microstructures as grain size and GBs and their properties are analyzed using a variety of measurement techniques [85, 105] depending on the scale of the microstructure of interest, the type of properties required, and local availability of the techniques. Analysis techniques include: 1) optical microscopy and scanning electron microscopy (SEM) for coarse scale observation, 2) transmission electron micrograph (TEM) or high resolution TEM (HRTEM) for high-magnification observation, 3) X-ray diffraction (XRD) pattern for the crystallographic structure and preferred orientation in polycrystalline or powdered bulk samples, and 4) electron backscattered diffraction (EBSD) for information about crystallographic structure and strain in a SEM or TEM in nanosized grains. The resulting 2D statistics about grain and GB for limited samples, however, are insufficient to predict the true 3D characteristics [113]. Although a number of methods are recently employed to investigate 3D microstructure [114], the 3D observations for NCs are not reported yet to our knowledge.

Correlation between microstructure and bulk NCs are empirical partly due to the fact that the study of local properties of microstructure and its relation to bulk properties are rare for NCs. Recent scanning tunneling microscopy (STM) measurement of electrical resistivity of a single GB showed that high angle GB (HAGB, or random GB) have almost universal resistivity and about 20 times greater resistivity than low angle GB (LAGB or coherent GB) of which resistivity is similar to grain itself [115,116]. Corresponding thermal conductivity measurements with sub-100 nm resolution are done for devices such as carbon nanotubes with scanning thermal microscopy (SThM) and scanning thermoreflectance microscopy [117]. Thermal conductance measurements at grain boundaries have not been reported, although the importance of GB scattering on thermal conductivity reduction was illustrated by indirect measurement for polycrystalline thin films with micrometer resolution [117]. Spatial measurement of the Seebeck coefficient with nanometer resolution was done in semiconductor p-n junctions using scanning thermoelectric microprobe (SThEM) [118]. Studies of such local electrical and thermal properties for NCs are rare, but there is a report of local probing of the Seebeck coefficient for NCs with micrometer resolution [119].

1.4.4 Electron and Phonon Transport

Understanding electron and phonon transport across interfaces is an essential prerequisite to modeling and controlling the overall properties of the polycrystalline structures. Electronic and thermal transport across grain boundaries have been great concerns for electronic materials. In 1970, Seto developed the first quantitative model for the electron transport in polycrystalline materials [120]. The model he suggested is charge-trapping model in which a GB is modeled as a potential barrier (Fig 1.3). This model is now widely accepted. In addition, the Mayadas-Shatzkes models [121] have been used to interpret experiments performed on polycrystalline films in terms of averaged reflectivity of GBs [108, 115]. For nanocomposite TE materials, similar approaches have been taken in which GBs are modeled as a symmetric Schottky barrier, a single barrier and a multi barriers [92, 98, 99].

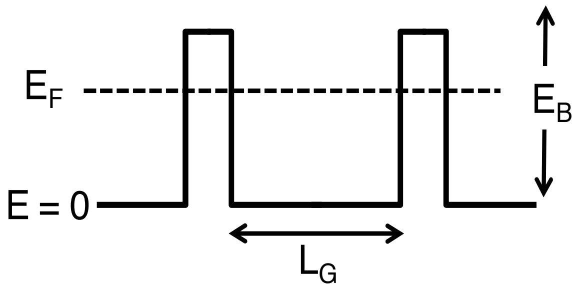

Figure 1.3. Schematic diagram of a potential barrier used for modeling a grain boundary where E_B is a barrier height and L_G is grain size.

The acoustic mismatch model (AMM) and the diffusive mismatch model (DMM) have been used to estimate the thermal boundary resistance [123]. The AMM is limited to smooth surfaces and the low temperature regime because it assumes specular scattering, while the DMM provides good agreement at above room temperature. The key assumption of the DMM is that the phonons suffer from diffusive and elastic scattering at the interface with transmission coefficient from material 1 to 2 given as [123]

$$T_{1\to 2}(\omega) = \sum_j \upsilon_{2,j} D_{2,j} \Bigg/ \left(\sum_j \upsilon_{1,j} D_{1,j} + \sum_j \upsilon_{2,j} D_{2,j} \right) \quad , \tag{5.1}$$

where j is the phonon mode, υ_j the phonon velocity, and D_j the phonon density of states. Starting from a Landauer approach with the same assumption, we can show that the transmission is equivalent to $T_{1\to 2}(\omega) = M_2(\omega) / \left(M_1(\omega) + M_2(\omega) \right)$, as derived in Appendix D. Note that $T_{1\to 2}(\omega)$ is 1/2 for interfaces between same materials in the DMM.

The 2D analysis of microstructures has been done for NCs, so 3D observations for NCs are necessary for improved understanding of the mechanisms governing the properties and formation of interfaces. The experimental measurement of local electrical and thermal properties at the interface will be required to clearly understand thermoelectric properties of interfaces as well as bulk NCs. In the next section, we will review the conventional approach to model transport properties of NCs.

1.4.5 Modeling Nanocomposite TE materials

We first review general approaches to model thermoelectric transport. To treat the bulk materials, techniques like percolation theory, effective medium theory, and drift-diffusion equations have been used. A study of thermoelectric properties of two components systems was done in the effective medium context and showed that the figure of merit can never exceed the largest value of that of any component [124], although power factor enhancement was predicted for a specific types of mixtures [125]. A percolation study of two component systems have also been done and showed a difference between results from effective medium theory and percolative transport, without demonstrating improved performance [119, 120]. The general drift-diffusion equations including thermoelectric effects [128] have been also used to analyze internal cooling and thermal responses in devices such as deep submicron MOSFET [129], bipolar devices [130], and hetrojunction bipolar transistor (HBT) [131]. Recent modeling efforts to understand the electronic and thermal properties are done with a variety of techniques with emphasis on microscopic modeling which include: 1) Boltzmann transport equation (BTE) for electrons [92, 98, 99, 125, 126] and phonons [134], 2) Monte Carlo (MC) simulations [135], 3) Molecular dynamics (MD) simulations [136], 4) modified effective medium theory [137], and 5) non-equilibrium Green's function (NEGF) method [138], which we also used to examine the electronic performance of cross-plane superlattice devices. Another recent example of modeling $Si_{1-x}Ge_x$ NCs was done by Bera et al. [139]. They have implemented a BTE approach for both electron and phonon transport with the relaxation time approximation.

While nanocomposites materials are beginning to yield promising results of ZT > 1, most of the improvements come from low thermal conductivity, without corresponding enhancement in electronic performance. Researchers have been so far trying to suppress the long wavelength phonons that contribute significantly to the thermal conduction, but are not affected by point defect and alloy scattering. This was achieved by introducing high-density interfaces with a larger characteristic length than that of a point defect, which doesn't affect much electron flow due to the difference in wavelength spectrum between electrons and phonons. A few achievements in electronic part have been experimentally reported [18].

To simulate electronic properties, the BTE has been used with relaxation time approximation (RTA). The shape of GBs was modeled as rectangular potential barriers [105] or was calculated by solving Poisson equations [92, 99, 125, 126]. Then, the scattering rate was calculated using the Fermi golden rule in the Born approximation [92, 125], transmission formalism [98, 99], and the partial wave technique [133]. For the electronic dispersion relations, parabolic band or Kane model is usually used. Although results from these model are in a good agreement with experiments, the models require several fitting parameters, such as the GB potential and constants related to screening and depletion at the GBs in addition to average grain size (l_{GB}).

These existing models, however, do not consider several factors that may be important to understand the electronic transport for NCs, such as shapes of grains, 3D distribution of the GBs, types of GBs and associated properties, and quantum mechanical effects such as tunneling through thin GBs and the confinement effect of nanometer sized grain. Morevoer, energy relaxation hasn't been considered in previous studies, but it is important to take it into account to properly treat energy filtering effect as we discussed in Sec. 1.4.4.

For phonon transport in NCs, the phonon BTE [134] and MC simulations [127, 128] have been used to evaluate the geometrical effect on thermal conductivity with an assumption of average phonon mean-free-paths and periodic boundary conditions. The Rayleigh scattering model [73], acoustic Mie scattering model [140], and a standard boundary scattering rate, $\tau_{GB}^{-1} = \upsilon_s / l_{GB}$ in the Debye model [99] were used to calculate the thermal conductivity for NCs with the phonon BTE. A modified effective medium theory, which takes interfaces into account, was also proposed [137] and used [106] to analytically calculate the thermal conductivity. As pointed out in Ref. [27], existing models are insufficient to investigate a desirable type of interface to selectively scatter phonons and the effect of size distribution of nanoparticles.

The limitations of current models are partly due to the fact that the models ignore the statistics of grains and GBs and associated properties as well as their configurations in 3D. Therefore, microstructure-aware modeling informed by associated properties is required. Existing models for NCs haven't employed the DMM to predict the phonon scattering rate or MFP at interfaces, although the charge trapping model was generally used for electrical properties. Theoretical efforts to predict electrical and thermal properties at interface should continue with experimental efforts.

1.5 Thesis Outline

As discussed in the previous section, *ZT* can be increased by improving the electronic part (increasing the power factor) or the phonon part (decreasing κ_l). In the first two chapters, we set the theorectical framework to evaluate the electronic (Chapter 2) and thermal (Chapter 3) performance of bulk diffusive samples with a Landauer approach using full band electronic bandstructure and a full dispersion description of phonons. Then, we extend the Landauer approach to understand the physics of ballistic and quasi-ballistic thermal conduction and to explain the reduced κ_l of thin films (Chapter 4). In the following two chapters, we explore the possibilities to enhance the electronic performance of thermoelectric devices. In Chapter 5, we revisit the question of what bandstructure produces the best thermoelectric performance and discuss the prospects of increasing *ZT* through high valley degeneracy or by distorting the density-of-states from a Landauer perspective. In Chapter 6, we examine electronic performance for several different materials such as molecules and graphene. In Chapter 7, we shift our attention to nanocomposite thermoelectric materials and develop computational framework for modeling the electronic performance of the polycrystalline materials with realistic statistics of grain and grain boundaries. Note that all the symbols and abbreviations are defined and consistent within each chapter. A brief summary of the discussions of each chapter is listed below.

In Chapter 2, using a full band description of electronic bandstructure, the Landauer approach to diffusive transport is mathematically related to the solution of the Boltzmann transport equation, and expressions for the thermoelectric parameters in both formalisms are presented. Quantum mechanical and semiclassical techniques to obtain from a full description of the bandstructure, $E(k)$, the density of modes in the Landauer approach or the transport distribution in the Boltzmann solution are compared and thermoelectric transport coefficients are evaluated. Several example calculations for representative bulk materials are presented, and the full band results are related to the more common effective mass formalism. Finally, given a full $E(k)$ for a crystal, a procedure to extract an accurate, effective mass level description is presented.

In Chapter 3, using a full dispersion description of phonons and a full band description of electronic bandstructure, both the electronic and thermal performance for Si and Bi_2Te_3 thermoelectric materials are examined using a Landauer approach. The relation of classical kinetic theory to the Landauer approach for phonon transport is clarified. The use of simplified dispersion models is discussed and it is shown that a simple effective mass (parabolic dispersion) works well for electrons but a simple Debye model (linear dispersion) for phonons should be used with caution. A technique to extract a well-defined average phonon mean-free-path from the measured thermal conductivity and given phonon-dispersion is presented. We show that this mean-free-path has strong physical significance and explain why it differs greatly from commonly-used estimates.

In Chapter 4, the question of what fraction of the total heat flow is transported by phonons with different mean-free-paths is addressed using a Landauer approach with a full dispersion description of phonons to evaluate the thermal conductivities of bulk and thin film silicon. For bulk Si, the results reproduce those of a recent molecular dynamic treatment showing that about 50% of the heat conduction is carried by phonons with a mean-free-path greater than about one micrometer. For the in-plane thermal conductivity of thin Si films, we find that about 50% of the heat is carried by phonons with mean-free-paths shorter than in the bulk. When the film thickness is smaller than ~0.2 μm, 50% of the heat is carried by phonons with mean-free-paths longer than the film thickness. The cross-plane thermal conductivity of thin-films, where quasi-ballistic phonon transport becomes important, is also examined. For ballistic transport, the results reduce to the well-known Casimir limit (i.e., the blackbody radiation law for phonons) [141]. These results shed light on phonon transport in bulk and thin-film silicon and demonstrate that the Landauer approach provides a relatively simple but accurate technique to treat phonon transport from the ballistic to diffusive regimes.

In Chapter 5, the question of what bandstructure produces the best thermoelectric device performance is revisited from a Landauer perspective. We find that a delta-function transport distribution function (TDF) results in operation at the Mahan-Sofo upper limit for the thermoelectric figure-of-merit, *ZT*. We show, however, the upper limit itself depends on the bandwidth (BW) of the dispersion, and therefore a finite BW dispersion produces a higher *ZT* when the lattice thermal conductivity is finite. Including a realistic model for scattering profoundly changes the results. Instead of a narrow band, we find that a broad BW is best. The prospects of increasing *ZT* through high valley degeneracy or by distorting the density-of-states are discussed from a Landauer perspective. We conclude that while there is no simple answer to the question of what bandstructure produces the best thermoelectric performance, the important considerations can be expressed in terms of three parameters derived from the bandstructure – the density-of-states, the number of channels, and the mean-free-path.

In Chapter 6, we address the question of how to engineer the electronic structure to enhance the performance of a thermoelectric material. We examines electronic TE performance for several different materials. It was shown that most materials, even those for which giant Seebeck coefficients have been predicted, display a similar monotonic behavior of S vs. E_F that is expected from conventional thermoelectric theory. Using III-V alloy semiconductors as a model system, we demonstrated a promise of composite energy bands because of the non-monotonic S behavior, which maintains high S at high carrier densities resulting in high PF. Our findings show quantitatively how barriers in cross-plane superlattices degrade the electrical performance, (i.e., power factor) due to quantum mechanical effects, and that PF of multi barrier structures is no better than a single barrier TE device.

In Chapter 7, we shift our attention to nanocomposite thermoelectric materials and a new approach to model nanocomposite (NC) TE devices is discussed. As a testbed of our model, recent experimental work on polycrystalline graphene is used. How grain boundaries affect the electronic performance of large-area polycrystalline graphene is investigated. We also demonstrate that a composite based on poly-crystalline graphene and a sub-percolating network of metallic nanowires offers a simple and effective route to reduced resistance while maintaining high transmittance. This new approach of 'percolation-doping by nanowires' has the potential to beat the transparency-conductivity constraints of existing materials and may be suitable for broad applications in photovoltaics, flexible electronics, and displays.

Finally, in Chapter 8, we summarize the thesis and suggest a few possible directions for future research.

1.6 List of Associated Publications

The following publications are associated with the work reported in this thesis.

Chapter 2

- **C. Jeong**, R. Kim, M. Luisier, S. Datta, and M. S. Lundstrom, "On Landauer versus Boltzmann and full band versus effective mass evaluation of thermoelectric transport coefficients," *J. Appl. Phys.,* 107, 023707 (2010).

- M. Lundstrom and **C. Jeong**, "Near-equilibrium Transport: Fundamentals and Applications," (Lectures from nanoscience: A Lecture notes series), World Scientific Pub, to appear in 2012

Chapter 3:

- **C. Jeong**, S. Datta, and M. S. Lundstrom, "Landauer vs. Boltzmann and Full Dispersion vs. Debye Model Evaluation of Lattice Thermal Conductivity," *J. Appl. Phys.,* 109, 073718-8 (2011)
- M. Lundstrom and **C. Jeong**, "Near-equilibrium Transport: Fundamentals and Applications," (Lectures from nanoscience: A Lecture notes series), World Scientific Pub, to appear in 2012

Chapter 4:

- **C. Jeong**, S. Datta, and M. S. Lundstrom, "Thermal Conductivity of Bulk and Thin-Film Silicon: A Landauer Approach," *J. Appl. Phys*., 111, 093708 (2012).

Chapter 5:

- **C. Jeong**, R. Kim, and M. S. Lundstrom, "On the Best Bandstructure for Thermoelectric Performance: A Landauer Perspective," *J. Appl. Phys*. 111, 113707 (2012).

Chapter 6:

- **C. Jeong**, and M. S. Lundstrom, "On Electronic Structure Engineering and Thermoelectric Performance," *J. Elec. Mater*., 40, 738-743 (2011)
- **C. Jeong**, Gerhard Klimeck, and M. S. Lundstrom, "Computational Study of the Electronic Performance of Cross-Plane Superlattice Peltier Devices," *Mater. Res. Soc. Proc*., 1314, DOI:10.1557/opl.2011.509 (2011)

Chapter 7:

- **C. Jeong**, Pradeep Nair, Mohammad Khan, Mark Lundstrom, and Ashraf Alam, "Prospects for Nanowire-doped Polycrystalline Graphene Films for Ultratransparent, Highly Conductive Electrodes," *Nano Lett.*, 11, 5020, (2011).

Other publications during the academic program (not discussed in this thesis):

- **C. Jeong**, D.A. Antoniadis, and M.S. Lundstrom, "On Backscattering and Mobility in Nanoscale Silicon MOSFETs," *IEEE Trans. Electron Devices*, vol. 56, no. 11, pp. 2762-2769, Nov. 2009.
- **C. Jeong**, and M. S. Lundstrom, "Analysis of Thermal Conduatanc of Ballistic Point Contacts," *Appl. Phys. Lett.* 100, 233109 (2012).
- R. Kim, **C. Jeong**, and M. S. Lundstrom, "On momentum conservation and thermionic emission cooling," *J. Appl. Phys.* **107**, 054502 (2010).
- A. Paul, S. Salamat, **C. Jeong,** G. Klimeck, and M. S. Lundstrom, "An Efficient Algorithm to Calculate Intrinsic Thermoelectric parameters based on Landauer Approach," *J. Comp. Elect.* **11**, 56–66 (2012)
- R.Chen, S. R. Das, **C. Jeong**, D. B. Janes, M. A. Alam, "Exclusive Electrical Determination of High-Resistance Grain-Boundaries in poly-Graphene," presented at the 2012 Deveice Research Conference (DRC).

2. LANDAUER VS. BOLTZMANN APPROACH FOR ELECTRONS

The contents of Chapter 2 have been extracted and revised from the following publication: C. Jeong, R. Kim, M. Luisier, S. Datta, and M. Lundstrom, "On Landauer vs. Boltzmann and Full Band vs. Effective Mass Evaluation of Thermoelectric Transport Coefficients," *J. Appl. Phys.*, 107, 023707 (2010).

In this chapter, using a full band description of electronic bandstructure, the Landauer approach to diffusive transport is mathematically related to the solution of the Boltzmann transport equation, and expressions for the thermoelectric parameters in both formalisms are presented. Quantum mechanical and semiclassical techniques to obtain from a full description of the bandstructure, $E(k)$, the density of modes in the Landauer approach or the transport distribution in the Boltzmann solution are compared and thermoelectric transport coefficients are evaluated. Several example calculations for representative bulk materials are presented, and the full band results are related to the more common effective mass formalism. Finally, given a full $E(k)$ for a crystal, a procedure to extract an accurate, effective mass level description is presented.

2.1 Introduction

Much experimental and theoretical effort has been directed at improving the thermoelectric (TE) figure of merit, $ZT = S^2GT/K$, where T is the temperature, S is the Seebeck coefficient, G is the electrical conductance, and K is the thermal conductance, which is the sum of the electronic contribution, K_e, and the lattice thermal conductance, K_l. Careful tradeoffs are needed to obtain high ZT. Recent experimental reports of high ZT[9,11,52–57] are attributed to suppressing the lattice thermal conductivity, and now the question of whether the electronic performance can be enhanced is being asked[8,62,63]. New materials[36,52,142–144], new structures (e.g. nanowires[50,145–154], quantum wells[51,53,155], superlattices[12,41,62,63,68,74,145,156–159], and nanocomposites [54,55,160–162]), and strain engineering[68–71], which has been so successful for enhancing the electronic performance of nanotransistors, are all being explored. To address these opportunities, thermoelectric coefficients must be related to an accurate description of the electronic structure of the material.

Thermoelectric parameters are usually evaluated by solving the Boltzmann Transport Equation (BTE)[163]. For low temperature thermoelectrics in mesoscopic structures, the Landauer approach is commonly used[164,165]. The Landauer approach applies to high temperature diffusive samples as well, and it provides an alternative formulation that can be insightful[166]. One objectives for this chapter are to discuss the mathematical relation between the Landauer and Boltzmann approaches when using a full description of the electronic bandstructure and to relate the full band calculations to effective mass level descriptions

In both the Landauer and Boltzmann approaches the thermoelectric parameters are related to the electronic structure of the material. The effective mass approach is widely-used to analyze experiments and to design devices. For more complex materials, full band treatments (*ab initio* or empirical tight binding) have been used [142,167–176]. It is still not clear, however, exactly how full band treatments relate to effective mass level treatments – especially for complex bandstructures. Another objective of this chapter is to discuss the evaluation of thermoelectric parameters from a full band perspective and to show that the results are easily related to an effective mass level description.

The chapter is organized as follows. In Sec. 2.2, we present a brief summary of the Landauer formalism and relate it to the more common approach that begins with the BTE. We also present two methods for evaluating the transport distribution in the Landauer approach from a full band description of the electronic structure. In Sec. 2.3, tight binding simulation results are presented for the conduction and valence bands of germanium (Ge), gallium arsenide (GaAs), and bismuth telluride (Bi_2Te_3). The results are discussed within the Landauer framework in Sec. 2.4, as is the relation of the rigorous approach to the effective mass approach. Our conclusions are summarized in Sec. 2.5.

2.2 Approach

The Landauer formalism in the linear response regime gives the electrical conductance, Seebeck coefficient, and the thermal conductance for zero electric current as[177,178]

$$G = \left(2q^2/h\right)I_0 \qquad [1/\Omega] \tag{2.1}$$

$$S = \left[k_B/\left(-q\right)\right]\frac{I_1}{I_0} \qquad [\mathrm{V/K}] \tag{2.2}$$

$$K_e = \left(T_L 2k_B^2/h\right)\left\{I_2 - I_1^2/I_0\right\} \ [\mathrm{W/K}], \tag{2.3}$$

where

$$I_j = \int_{-\infty}^{+\infty}\left(\frac{E-E_F}{k_B T_L}\right)^j \bar{T}(E)\left(-\frac{\partial f_0}{\partial E}\right)dE\,, \tag{2.4}$$

with

$$\bar{T}(E) = T(E)M(E)\,, \tag{2.5}$$

being the transmission[165], and $M(E)$ the density of modes[179]. For a conductor of length, L, and mean-free-path for backscattering, $\langle\langle\lambda(E)\rangle\rangle$,

$$T(E) = \langle\langle\lambda(E)\rangle\rangle/L \tag{2.6}$$

in the diffusive limit[179]. For some common scattering mechanisms, $\langle\langle\lambda(E)\rangle\rangle$ can be expressed in power law form as $\langle\langle\lambda(E)\rangle\rangle = \lambda_0\left(E/k_B T\right)^r$, where λ_0 is a constant, E is the kinetic energy, and r is a characteristic exponent describing a specific scattering process.

Thermoelectric transport coefficients are more commonly obtained by solving the Boltzmann equation in the relaxation time approximation and expressed in terms of an integral like eqn. (2.4) with the transmission replaced by the so-called transport distribution according to [166]

$$\Sigma(E) = \frac{L^2}{h}M(E)T(E) = \frac{L}{h}M(E)\langle\langle\lambda\rangle\rangle \tag{2.7}$$

A solution of the Boltzmann equation gives [163]

$$\Sigma(E) = \sum_{\vec{k}} \left(\upsilon_x^2 \tau \right) \delta\left(E - E_k \right) \tag{2.8}$$

where τ is the momentum relaxation time. Equation (2.7) relates the solution of the Boltzmann equation in the relaxation time approximation to the Landauer formalism.

By making the definition

$$\left\langle |\upsilon_x| \right\rangle \equiv \frac{\sum_{\vec{k}} |\upsilon_x| \delta\left(E - E_k \right)}{\sum_{\vec{k}} \delta\left(E - E_k \right)} \tag{2.9}$$

eqn. (2.8) can be expressed as

$$\sum\left(E \right) = \frac{\left\langle \upsilon_x^2 \tau \right\rangle}{\left\langle |\upsilon_x| \right\rangle} \left\langle |\upsilon_x| \right\rangle D\left(E \right) = \frac{\left\langle \upsilon_x^2 \tau \right\rangle}{\left\langle |\upsilon_x| \right\rangle} \sum_k |\upsilon_x| \delta\left(E - E_k \right) \tag{2.10}$$

where $D\left(E \right) = \sum_k \delta\left(E - E_k \right)$ is the density of states.

Finally, according to eqn. (2.7), we find

$$M\left(E \right) = \frac{h}{2L} \sum_k |\upsilon_x| \delta\left(E - E_k \right) \tag{2.11}$$

and

$$\left\langle \left\langle \lambda\left(E \right) \right\rangle \right\rangle = 2 \frac{\left\langle \upsilon_x^2 \tau \right\rangle}{\left\langle |\upsilon_x| \right\rangle} \tag{2.12}$$

Equation (2.11) is a well-known result that relates the density of modes in the Landauer formalism to the bandstructure [165,179]. Equation (2.12) is a new results that define an appropriately defined mean-free-path (the mean-free-path for backscattering) so that the Landauer results agree with the Boltzmann equation in the relaxation time approximation. Assuming isotropic energy bands, eqn. (2.12) can be evaluated in one-dimension (1D), two-dimensions (2D), and three-dimensions (3D) to find

$$\left\langle \left\langle \lambda\left(E \right) \right\rangle \right\rangle = 2\upsilon\left(E \right) \tau\left(E \right) \qquad \text{(1D)} \tag{2.13a}$$

$$\left\langle \left\langle \lambda\left(E \right) \right\rangle \right\rangle = \left(\pi/2 \right) \upsilon\left(E \right) \tau\left(E \right) \qquad \text{(2D)} \tag{2.13b}$$

$$\langle\langle\lambda(E)\rangle\rangle = (4/3)\upsilon(E)\tau(E) \qquad \text{(3D)} \qquad (2.13c)$$

In practice, a constant scattering time is often assumed for the Boltzmann equation, but this is hard to justify. In the Landauer approach, a constant mean-free-path simplifies calculations and can be justified in 3D for parabolic bands when the scattering rate is proportional to the density of states.

The discussion above shows that $M(E)$ is essentially the carrier velocity times the density-of-states. If we consider a single parabolic conduction band, $E = \hbar^2 k^2 / 2m^*$, then $M(E)$ for 3D is

$$M(E) = A\frac{m^*_{DOM}}{2\pi\hbar^2}E \qquad (2.14)$$

where the density-of-modes effective mass(m^*_{DOM})is just m^* for a single, spherical band. (Results for 1D and 2D are given in Ref. [166]) For ellipsoidal energy bands, eqn. (2.11) can be evaluated for each equivalent ellipsoid to find $m^*_{DOM} = \sqrt{m^*_y m^*_z}$ with the direction of current flow being along the x-direction. This example shows that *M*(*E*) is related to the density-of-states in the 2D plane transverse to the transport direction. The contributions for each equivalent ellipsoid are then summed. For the conduction band of silicon, the result is $m^*_{DOM} = 2m^*_t + 4\sqrt{m^*_t m^*_l}$ which is 2.04 m_0. Recall that the density of states effective mass is $m^*_{DOS} = 6^{2/3}\left(m_l m_t^2\right)^{1/3} = 1.06m_0$. This example shows that the density-of-modes and density-of-states effective masses can be quite different. The density of states and the density of modes effective mass in the Landuaer approach are analogous to the density of states and the conductivity effective mass in the Boltzmann approach. Finally, for non-parabolic bands with Kane's dispersion relation[180], $E(1+\alpha E) = \hbar^2 k^2 / 2m^*$, $M(E)$ for 3D becomes

$$M(E) = A\frac{m^*}{2\pi\hbar^2}E(1+\alpha E), \qquad (2.15)$$

where α is the non-parabolicity parameter. These analytical results will be our reference against which we compare the numerical results to be presented later.

Two procedures are available to numerically evaluate $M\left(E\right)$. Firstly, $M\left(E\right)$ can be calculated by counting bands for a given bandstructure, because we can express eqn. (2.11) as [179,181]

$$M\left(E\right)=\sum_{k_\perp}\Theta\left(E-E_{k_\perp}\right), \tag{2.16}$$

where Θ is the unit step function and $k_\perp$ refers to *k* states perpendicular to the transport direction (i.e., transverse modes). Equation (2.16) is simply a count of the bands that cross the energy of interest and provides a computationally simple way to obtain *M*(*E*) from a given *E*(*k*). Similar expressions have been used to numerically evaluate the density of modes for phonon transport from a given dispersion relations[182]. A MATLAB® script that implements this calculation for Ge is available[183].

An alternative to counting the number of available bands at a given energy consists of calculating the transmission coefficient through a given structure as function of the injection energy. In the non-equilibrium Green's function formalism[179], $\bar{T}(E)$ is

$$\bar{T}(E)=Tr\left(\Gamma_1 G\Gamma_2 G^\dagger\right) \tag{2.17}$$

where *G* is the retarded Green's function and

$$\Gamma_{1,2}=i(\Sigma_{1,2}-\Sigma_{1,2}{}^\dagger) \tag{2.18}$$

where $\Sigma_{1,2}$ are the contact self-energies. This approach works for bulk thermoelectrics, but it also allows us to obtain the TE parameters for quantum-engineered structures for which the electronic structure may be very different from the bulk.

For our calculations, we have developed a multi-dimensional quantum transport simulator based on different flavors of the nearest-neighbor tight-binding model. It solves Schrödinger equation in the Wave Function (WF) formalism, which in the ballistic limit is equivalent to the Non-equilibrium Green's Function (NEGF), but computationally much more efficient [184]. To obtain the bulk transmission coefficient $\bar{T}(E)$, a small device structure composed of two to three unit cells is constructed, two semi-infinite contacts are attached to both ends of the simulation domain, and electrons and holes are injected and collected from these contacts. This procedure is repeated for different energies and wave vectors so that the entire Brillouin Zone of the considered semiconductor material is spanned. We integrate the resulting transmission coefficient over its momentum-dependence at a given energy to evaluate $\overline{T}(E)$.

To evaluate $M(E)$ beyond the effective mass approximation, an accurate description of the electronic structure is needed. Materials like Si, Ge, or GaAs have been parameterized in the nearest-neighbor tight-binding (TB) model by several groups[185–187] with different levels of approximation (e.g. sp^3s^* [188] and $sp^3d^5s^*$ [187] models) for many years. More exotic materials like Bi_2Te_3 have been parameterized [167,168]. A comparison with energy bands obtained from Density Functional Theory (DFT) shows that a nearest-neighbor $sp^3d^5s^*$ tight-binding approach with spin-orbit coupling is required to capture the essential characteristics of the Bi_2Te_3 bandstructure [168]. Hence, we have extended our quantum transport simulator described above to include the rhombohedral crystal lattice and to calculate transmission coefficients through such structures.

2.3 Results

In this section, we illustrate the techniques discussed in Sec. 2.2 and show how full band calculations are related to effective mass calculations. A few materials that are good illustrations (not necessarily good TE materials) are compared: a) Ge to compare 3 approaches to compute the density of modes - counting bands, NEGF-TB model, effective mass approximation (EMA) – which should all agree rather well since the Ge conduction bands are nearly parabolic, b) Ge valence band to see if we can use an effective mass description for the valence band, c) GaAs to illustrate the effect of non-parabolicity, and d) Bi_2Te_3 because it is commonly used thermoelectric with a more complex bandstructure.

Figure 1 shows the density of modes, $M(E)$ for the Ge conduction band as computed by 3 different approaches. Counting bands gives exactly the same $M(E)$ obtained by NEGF-TB model. As shown in Fig. 2.1, the EMA expression for $M(E)$

(eqn. (2.14)) provides a good fit to the full band calculation near the conduction band edge. Full band calculations of the density of states, $D(E)$ and $M(E)$ for Ge, GaAs, and Bi_2Te_3 are shown in Fig. 2.2. Around the band edge, the linear density of modes ($M(E)$) vs. energy expected from eqn. (2.14) is observed for all materials considered – even for the highly warped valence band. In the bulk, $M(E)$ varies linearly with E because both $D(E)$ and $\upsilon(E)$ are proportional to $\sqrt{E}$. A linear behavior of the "transport distribution" $\Sigma(E)$ vs. E has previously been observed[169], but the transport distribution varies as $D(E)$ times $\upsilon^2(E)$, so it is not expected to be exactly linear when the relaxation time, τ, is assumed to be constant .

To show the relation between full band calculation and the EMA, a "density-of-modes" effective mass (m^*_{DOM}) was extracted from the numerically evaluated $M(E)$ using eqn. (2.14) and compared to the analytical m^*_{DOM} with number of valleys and transport direction being accounted for. The results are listed in Table 2.1. The discrepancy is no larger than 10% for conduction band, while it is about a factor of 2 for valence band.

As shown in Fig. 2.3 for the conduction band of GaAs, a better fit can be obtained when non-parabolicity is accounted for, and the discrepancy between extracted m^*_{DOM} and analytic one reduced from 10% to 2%. As listed in Table 1 and discussed in Sec. 2.2, the "density-of-states" effective masses are clearly different from the density-of-modes effective masses - except for GaAs, where the Gamma valley is the conduction band minimum. Finally, note that although there is no simple relation between the light and heavy hole effective masses and the numerically extracted m^*_{DOM} for the valence band, a constant m^*_{DOM} provides a good fit to $\bar{T}(E)$.

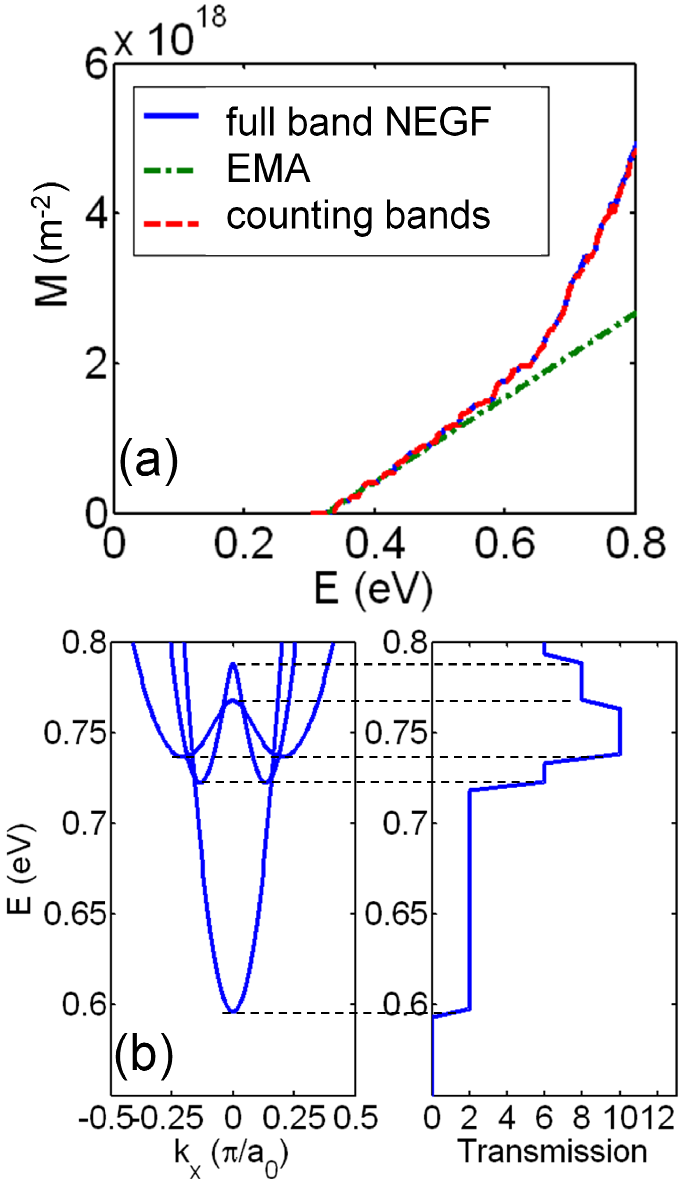

Fig. 2.1. (a) Comparison of the number of modes, $M(E)$, computed by 3 different approaches for Germanium (Ge): NEGF-TB model, Effective Mass Approximation (EMA), and counting bands. The *M(E)* from counting bands (dashed line) is on top of *M(E)* from the NEFG-TB model. (b) Illustration of bands counting method for specific dispersion relation for Ge. Dotted line is guide to eye.

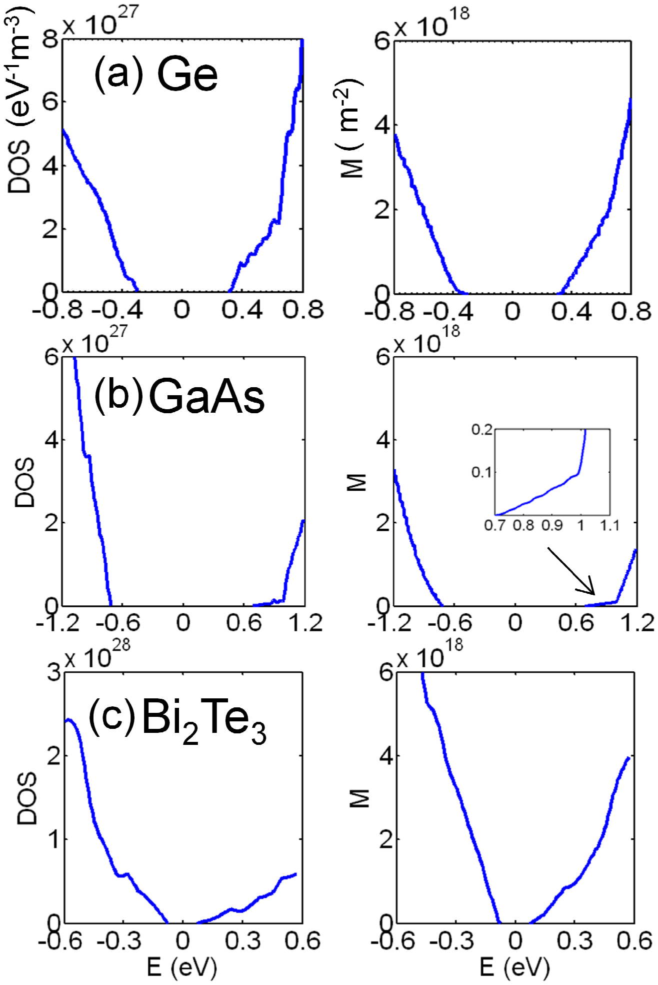

Fig. 2.2. Full band calculations of the density of states (*DOS*) and the number of modes (*M*) for Ge, GaAs, and Bi_2Te_3. The midgap is located at E = 0. The inset in Fig. 2.2(b) shows *M(E)* near the conduction band edge for GaAs.

Table 2.1.

Analytic "density-of-modes" and full band NEGF-TB simulation. For comparison, "density-of-states" effective masses (m^*_{DOS}) are also listed. The transport direction is along the *x* direction. The electron (m^e) and hole effective masses (m^{lh}, m^{hh}) in the device coordinate (*x*, *y*, *z*) are used for analytic effective mass calculations and are given in units of the free electron mass. The 'heavy-hole' effective masses (Ge: 0.35 and GaAs: 0.51) assume spherical symmetry[189,190]. The extracted 'heavy-hole' effective mass for Ge and GaAs has a strong anisotropy (Ge: 0.17 [100], 0.37 [110], 0.53 [111], and GaAs: 0.38 [100], 0.66 [110], 0.84 [111]). CB denotes conduction band and VB denotes valence band. The top three shaded rows are for the conduction bands and generally show good agreement between analytic and numerically extracted values. The bottom three rows for the valence band (VB) generally show a much larger discrepancy. The two columns at the right (enclosed in dashed lines) show that analytic and numerically extracted density-of-states effective masses generally agree reasonably well, but the density-of-states effective masses are typically much lower than the density of modes effective masses.

Material	m^*_{DOM}		m^*_{DOS}	
	Analytic	Extracted	Analytic	Extracted
Ge CB	$4\sqrt{m^e_{yy}m^e_{zz}} = 1.18$	1.24	0.56	0.51
GaAs CB	$m_{yy}=0.066$	0.073	0.066	0.063
Bi_2Te_3 CB	$2\sqrt{m^e_{xx}m^e_{zz}} + 4\sqrt{m^e_{yy}m^e_{zz}} = 1.18$	1.17	0.23	0.28
Ge VB	$m^{lh}_{yy} + m^{hh}_{yy} = 0.37$	1.63	0.35	0.32
GaAs VB	$m^{lh}_{yy} + m^{hh}_{yy} = 0.59$	0.97	0.52	0.39
Bi_2Te_3 VB	$2\sqrt{m^h_{xx}m^h_{zz}} + 4\sqrt{m^h_{yy}m^h_{zz}} = 1.39$	3.53	0.36	0.41

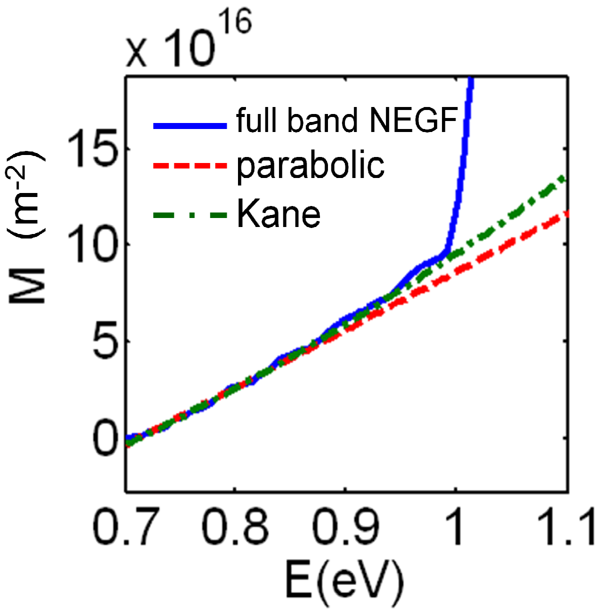

Fig. 2.3. Comparison of fitting based on parabolic dispersion relation with fitting based on Kane dispersion relation. Non-parabolicity parameter α used for GaAs is 0.64[191]. Above 1eV, L valleys contribute to the number of modes in addition to Γ valley.

2.4 Discussion

In this section, thermoelectric properties will be evaluated and interpreted within the Landauer framework. Figure 2.4 compares calculated Seebeck coefficients (S) using eqn. (2.2) to experiments. The results are plotted vs. reduced Fermi level ($\eta_F = \left(E_F - E_C\right)/k_B T$), and we assume that the scattering rate ($1/\tau$) is proportional to the density-of-states, i.e. phonon scattering is dominant[5] , which is equivalent to a constant mean-free-path, λ_0. The Seebeck coefficient (eqn. (2.2)) is independent of λ_0. The results clearly demonstrate that S is nearly independent of electronic band structure (i.e., of m^*_{DOM}). In the effective mass approximation, the Seebeck coefficient in 3D is $S_{3D} = -\left(k_B/q\right)\left(\left(r+2\right)\mathcal{F}_{r+1}\left(\eta_F\right)/\mathcal{F}_r\left(\eta_F\right) - \eta_F\right)$, which depends only on the location of the Fermi level and on r, where r is the characteristic exponent that describes scattering. The Seebeck coefficient depends weakly on electronic structure but more strongly on scattering. Ioffe, for example, pointed out the possibility of making use of ionized impurity scattering (r = 2) to improve S [33].

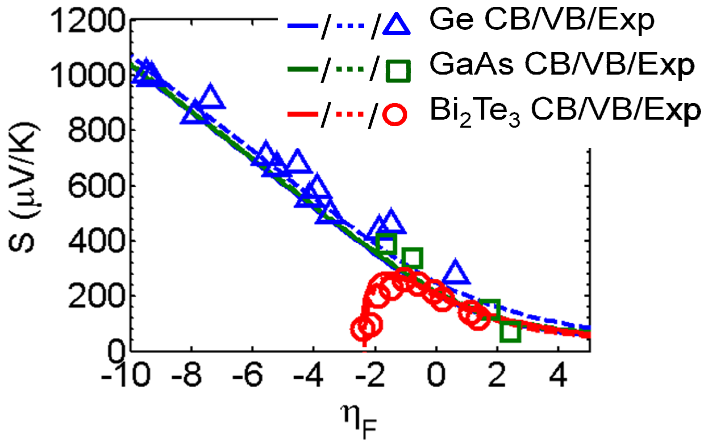

Fig. 2.4. Calculated Seebeck coefficients (S) using eqn. (2) and experiments [4,5,192,193] as a function of reduced Fermi level ($\eta_F = (E_F - E_C)/k_BT$). We assumed that scattering rate ($1/\tau$) is proportional to the density-of-states, i.e. phonon scattering is dominant[5]. The reduction of Seebeck coefficient around $\eta_F = -2$ for Bi_2Te_3 is attributed to the bipolar conduction due to its relatively small bandgap (0.162 eV).

The constant mean-free-path was adjusted to give the best match to experimental data for electrical conductivity (σ) with its corresponding S. This approach is essentially the same as the common approach in which the unknown relaxation time, τ, is treated as a constant [69,168,169,194], which actually turned out to be good approximation even for systems with crystal anisotropy[169,194]. With the best fit λ_0, the power factor ($PF = S^2G$) and electronic thermal conductivity (κ_e) were then evaluated using eqn. (2.1-2.3). The thermoelectric figure of merit, ZT was computed at 300 K using calculated values of PF and κ_e and the experimentally determined the lattice thermal conductivity, κ_l [5]. Figure 2.5 shows well-fitted results for Bi_2Te_3 with $\lambda_0 = 18, 4$ nm for conduction and valence band, respectively. Figure 2.6 compares the calculated PF and ZT vs. Fermi level to experiments for Ge, GaAs and Bi_2Te_3. Calculated results agree well with experiments. (The parameters used in these calculations are summarized in Table

2.2.) These results show that the Landauer approach gives essentially the same accuracy as the BTE approach (although the use of a constant mean-free-path is easier to justify than the use of a constant relaxation time). The Landauer approach has the benefit of being readily extendable to ballistic (e.g. thermionic) and to quantum-engineered structures.

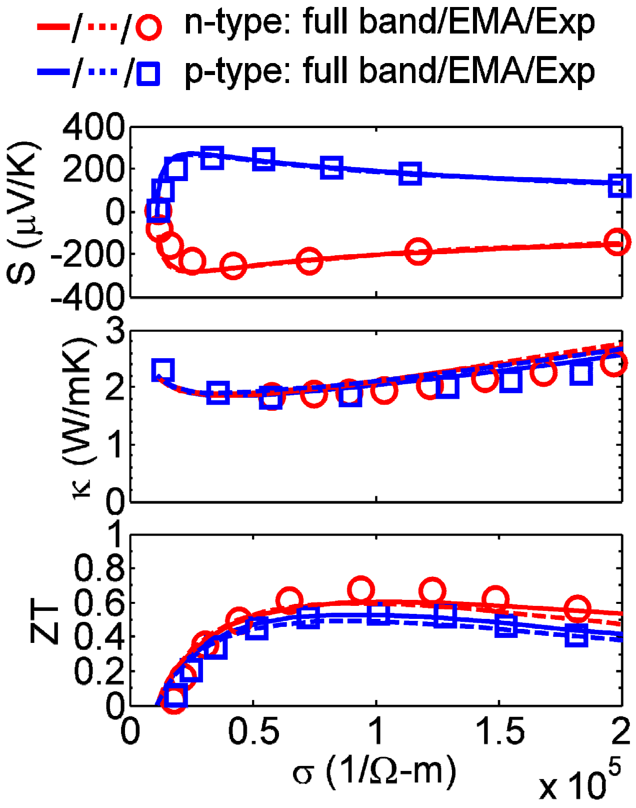

Fig. 2.5. Comparison of the simulated and experimentally[5] measured *S*, *G,* and κ for Bi_2Te_3 assuming a constant mean-free-path, $\lambda_0 = 18, 4\,\mathrm{nm}$ for conduction and valence bands. Thermal conductivity is the sum of the electronic and lattice thermal conductivity. Used parameters are listed in Table 2.2.

Table 2.2.

Summary of parameters used in Figure 2.6: fitted $\lambda_0(nm)$ parameters, experimental lattice thermal conductivity $\kappa_l(Wm^{-1}K^{-1})$. In the power law form of the mean free path, $\langle\langle\lambda(E)\rangle\rangle = \lambda_0\left(E/k_BT\right)^r$, r is 0 since we assumed that phonon scattering is dominant.

Material	λ_0	κ_l
Ge CB/VB	29/9.5	58
GaAs CB/VB	110/39	55
Bi_2Te_3 CB/VB	18/4	1.5

We now consider the effective mass level treatment of this problem. To calculate TE coefficients and analyze measured TE data within the EMA, two effective masses are needed: 1) m^*_{DOM} for $M(E)$ calculation 2) m^*_{DOS} to obtain the reduced Fermi-level ($\eta_F = (E_F - E_C)/k_BT$) from measured carrier concentration. In the EMA,

$$S_{3\mathrm{D}} = -\frac{k_B}{q}\left(\frac{(r+2)\mathcal{F}_{r+1}(\eta_F)}{\mathcal{F}_r(\eta_F)} - \eta_F\right) \tag{2.19}$$

$$G_{3\mathrm{D}} = \lambda_0\frac{2q^2}{h}\frac{m_{DOM}{}^*k_BT}{2\pi\hbar^2}\Gamma(r+2)\mathcal{F}_r(\eta_F) \tag{2.20}$$

$$K_{e,3\mathrm{D}} = \lambda_0 T\left(\frac{k_B}{q}\right)^2\frac{2q^2}{h}\frac{m_{DOM}{}^*k_BT}{2\pi\hbar^2}\Gamma(r+3)\left((r+3)\mathcal{F}_{r+2}(\eta_F) - \frac{(r+2)\mathcal{F}_{r+1}^2(\eta_F)}{\mathcal{F}_r(\eta_F)}\right) \tag{2.21}$$

where $\Gamma(j)$ is the Gamma function, the Fermi-Dirac integral of order j is defined as $\mathcal{F}_j(\eta_F) = 1/\Gamma(j+1)\times\int_0^\infty dx\,x^j/\left(1+e^{x-\eta_F}\right)$ [195], r is the characteristic exponent describing a specific scattering mechanism, and the parameter λ_0 is determined by comparison with experiments. Figures 2.5 and 2.7 show that effective mass theory provides a good agreement with full band atomistic simulation results.

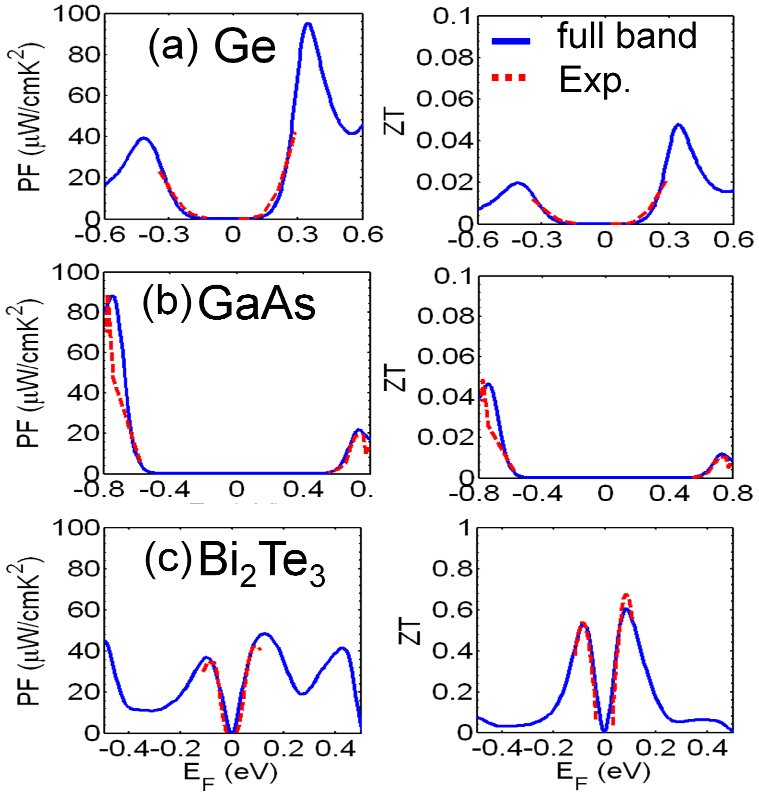

Fig. 2.6. Calculated and measured PF and ZT as function of the Fermi level. Used parameters are listed in Table 2.2.

Because the valence bands are coupled and warped, it is difficult to predict m_{DOM}^* from the values of the heavy- and light- hole effective masses. Indeed, Table 1 shows a large discrepancy between the expected and numerically extracted values. From the Luttinger-Kohn model, the valence band near the Γ point can be expressed as[196],

$$\begin{aligned} E(k)-E_V &= \frac{\hbar^2}{2m_x}\left[\gamma_1 k^2 \pm \sqrt{4{\gamma_2}^2 k^4 + 12({\gamma_3}^2 - {\gamma_2}^2)(k_x^2 k_y^2 + k_y^2 k_z^2 + k_x^2 k_z^2)}\right] \\ &= Ak^2 \pm \sqrt{B^2 k^4 + C^2 (k_x^2 k_y^2 + k_y^2 k_z^2 + k_x^2 k_z^2)} \end{aligned} \tag{2.22}$$

where γ_i are the Luttinger parameters and A, B, and C are constants.

From the definition of density of modes, eqn. (2.11), it is hard to derive analytically the $M(E)$ vs. E relation and then find analytical expression for m_{DOM}^*. But based on the counting bands approach, we can readily see why the extracted m^*_{DOM} is about two times larger than expected one from EMA.

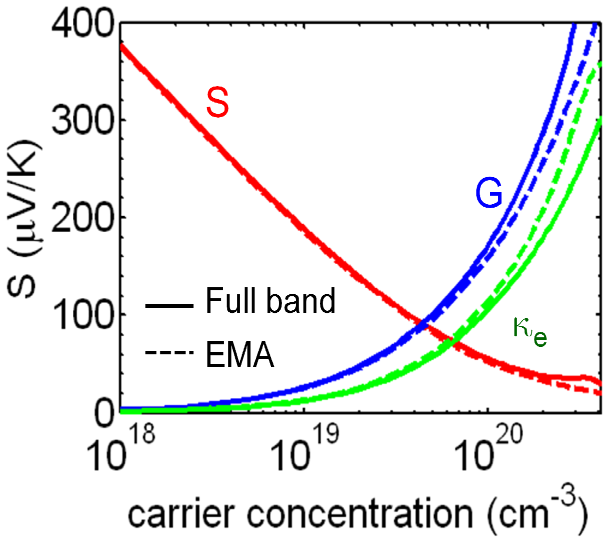

Fig. 2.7. Comparison of EMA with full-band calculation for Ge. On the *y* axis, Seebeck coefficient (*S*), electrical conductivity (*G*) and thermal conductivity by electron(κ_e) are plotted from 0 to 400 μV/K , 0 to 4E6 $\Omega^{-1}m^{-1}$, and 0 to 40 W m^{-1} K^{-1}.

Figure 2.8(a) shows that the conduction band of GaAs is nearly parabolic near the Γ point. According to the counting bands approach, e.g. eqn. (2.16), each band gives one conducting mode for electrons at a specific energy, *E*, due to parabolic behavior of dispersion relation. In other words, effective mass approximation assumes that each band gives one conducting channel for an injected electron having a specific wave vectors and energy *E*. When the bands are nearly parabolic, the analytic m^*_{DOM} agrees well with the m^*_{DOM} extracted from full band calculation, as we can see for the conduction band in Table 1.

If we assume parabolic bands for the valence band (heavy- and light hole) close to the Γ point, the m^*_{DOM} is expressed as $m^*_{DOM} = m_{lh} + m_{hh}$, which is approximately two times less than the value extracted from full band calculation as shown in Table 1. As clearly shown in the Fig. 2.8(b), most of bands for holes (especially for heavy-hole) contribute at least two conducting channels at a specific energy. The parabolic band assumption, however, gives one conducting channel per band and significantly underestimates the density of modes for holes. Warped valence bands provide more conducting modes.

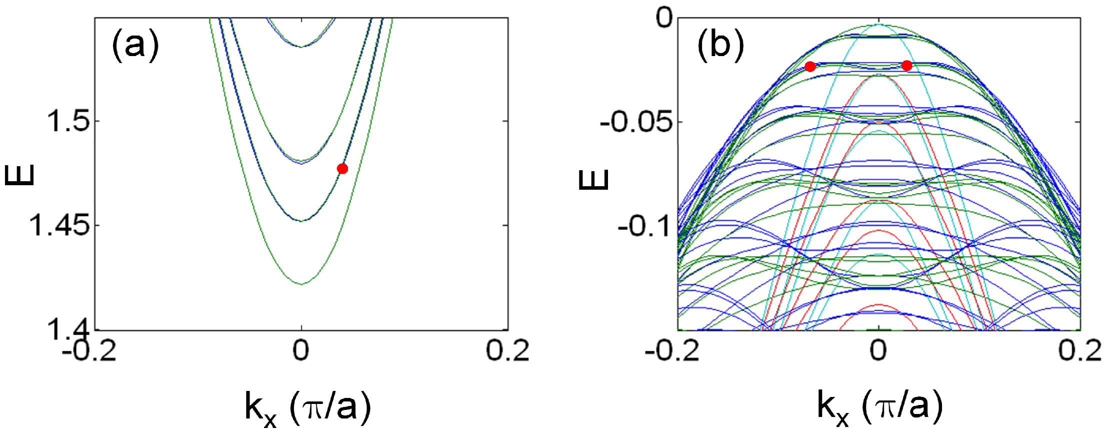

Fig. 2.8. Energy dispersion relation showing the lowest (a) conduction bands and (b) valence bands of GaAs. (y axis ranges from E_C (or E_V) to E_C (or E_V) + $5k_BT$ because $-\partial f_0/\partial E$ spread about $5k_BT$.) Each red dot represents a conducting channels for positive moving electrons at specific energy for an electron moving with a positive velocity. In the valence bands, most of the bands (especially heavy holes) have at least two conducting channels per energy

Using this argument, we may also explain qualitatively the question of why m^*_{DOM} is different between Ge and GaAs even though the valence bands look similar. Including results for Si and InAs valence bands, the hole 'density-of-modes' effective mass, m^*_{DOM} extracted from full band calculations for Si, Ge, GaAs, and InAs are given as, $2.40m_0 > 1.63m_0 > 0.97m_0 > 0.65m_0$, respectively. In eqn. (2.22), the degree of warping can be judged from the values of $(\gamma_3{}^2-\gamma_2{}^2)/\gamma_2{}^2$, which we call the warping parameter. For $\gamma_3=\gamma_2$, eqn. (2.22) yields two parabolic bands (heavy- and light – hole). From the tabulated values of γ_i [196], the calculated warping parameter are 17 > 0.76> 0.62 > 0.20 for Si, Ge, GaAs, and InAs, respectively. This shows that the degree of warping can qualitatively explain the relative magnitude of m_{DOM}^* for Si, Ge, GaAs, and InAs even though the valence band for all those diamond-like materials looks similar. One thing to note is that 6-valley valence band structure of Bi_2Te_3 is another reason for its high m_{DOM}^* .

2.5 Summary and Conclusion

The relation between the so-called transport distribution, which determines the TE coefficients and begins with the BTE, and the transmission obtained from the Landauer approach has been clarified in this chapter. In particular, we showed how the mean-free-path for backscattering in the Landauer approach should be defined so that the Landauer approach is consistent with the BTE in the relaxation time approximation. We also showed that the transmission (transport distribution) is readily obtained from the full band description of the electronic bandstructure of a semiconductor using well-developed techniques - a simple semiclassical band counting method and a quantum mechanical approach. Several example calculations of the transmission and the TE coefficients for representative bulk materials were presented to demonstrate that Landauer approach provides an accurate description of experimentally measured thermoelectric parameters, In practice, the use of a constant mean-free-path in the Landauer approach is easier to justify than the use of a constant relaxation time in the Boltzmann equation. The Landauer approach also provides complementary insight into thermoelectric physics and can be applied to ballistic, quasi-ballistic, and quantum engineered structures. Finally, we showed that an accurate and simple effective mass model can be defined by extracting a "density-of-modes" effective mass from the given full band results. One first computes $M\left(E\right)$ from eqn. (2.16) and then fits the linear portion near the band edge to eqn. (2.14). For accurate results, the fitting should be performed from the band edge to $\approx 5k_BT$ above the maximum expected Fermi level at the highest temperature of operation.

3. LANDAUER VS. BOLTZMANN APPROACH FOR PHONONS

The contents of Chapter 3 have been extracted and revised from the following publication: C. Jeong, S. Datta, and M. Lundstrom, “Landauer vs. Boltzmann and Full Dispersion vs. Debye Model Evaluation of Lattice Thermal Conductivity,” *J. Appl. Phys.*, 109, 073718 (2011).

In this chapter, using a full dispersion description of phonons, the thermal conductivities of bulk Si and Bi_2Te_3 are evaluated using a Landauer approach and related to the conventional approach based on the Boltzmann transport equation. A procedure to extract a well-defined average phonon mean-free-path from the measured thermal conductivity and given phonon-dispersion is presented. The extracted mean-free-path has strong physical significance and differs greatly from simple estimates. The use of simplified dispersion models for phonons is discussed, and it is shown that two different Debye temperatures must be used to treat the specific heat and thermal conductivity (analogous to the two different effective masses needed to describe the electron density and conductivity). A simple technique to extract these two Debye temperatures is presented and the limitations of the method are discussed.

3.1 Introduction

Electron and phonon transport play a critical role in a number of technological applications. They are central to thermoelectric technology, for which performance is determined by the dimensionless figure of merit, *ZT,* which has been limited to ~ 1 [36,47,197] for many years. Recent reports of $ZT > 1$, [36,47,197] have been achieved by using nanostructured materials to suppress the lattice thermal conductivity. Further progress will require careful engineering of both the phonon and electron transport[8,44,62,66,67,69]. Phonon transport also plays an increasingly important role in integrated circuits where the increasing importance of power dissipation, self-heating, and the management of hot spots [198] necessitates electron-thermal co-design. These examples indicate that a unified treatment of electron and phonon transport would be useful.

Diffusive transport has been often described by the Boltzmann transport equation (BTE) and simplifications of it, such as drift-diffusion equation for electrons or Fourier's Law for phonons [128,199]. The Landauer approach[165] provides a simple, physically insightful description of ballistic transport and has been widely used to describe quantized electrical and thermal transport in nanostructures[200–203]. Although not as widely appreciated, the Landauer approach describes diffusive transport as well and provides a simple way to treat the ballistic to diffusive transition. Thermal transport in nanowires has recently been described by a Landauer approach[182], but applications of the Landauer approach to bulk transport have been rare. In a previous chapter[3], we showed a very simple procedure to use the Landauer approach with a full band description of *E(k)* to evaluate thermoelectric transport parameters. In that chapter, we also related the full band calculations to the widely-used effective mass level model and presented a procedure for extracting the two different effective masses (density-of-states and conductivity effective masses) that are needed to evaluate the electron density and the TE transport coefficients.

In this chapter, we extend Ref. [3] to phonons and show how the same very simple procedure can be used to evaluate the lattice thermal conductivity from a full zone description of the phonon dispersion. The main contributions of the chapter consist of presenting a simple technique for extracting a physically meaningful mean-free-path for phonons from the measured thermal conductivity and relating the full dispersion results to the simpler, Debye model for phonon dispersion. Our specific objectives are: 1) to mathematically relate the Landauer expression for the thermal conductivity, κ_{ph} to the more common approach that begins with classical kinetic theory, 2) to show that two different Debye temperatures are needed to accurately evaluate both the specific heat and lattice thermal conductivity with physically meaningful mean-free-paths, 3) to quantitatively examine both electronic performance and thermal performance of bulk silicon (Si) and bismuth telluride (Bi_2Te_3) within the Landauer framework and a full zone description of the phonon dispersion, 4) to present a technique to extract a clearly-defined average phonon mean-free-path for phonon backscattering from the measured thermal conductivity, and 5) to discuss the similarities and differences between electron and phonon transport in terms of the Landauer picture.

The chapter is organized as follows. In Sec. 3.2, we present a brief summary of the Landauer formalism for electron and phonon transport. In Sec. 3.3, the results of full phonon dispersion simulations of the electrical and thermal conductivities of Si and Bi_2Te_3 are presented. A technique to extract a well-defined mean-free-path is presented in Sec. 3.4. We also compare and contrast electron and phonon transport in Sec. 4 and discuss the extraction of the two Debye temperatures that are needed when using simplified models of phonon dispersion to evaluate the specific heat and thermal conductivity. Finally, our conclusions are summarized in Sec. 3.5.

3.2 Approach

The theoretical approach to phonon transport used in this chapter closely follows the approach for electrons as presented in Ref. [3]. In the linear response regime, we can define[166,204]

$$G(E) = \left(\frac{2q^2}{h}\right)\bar{T}_{el}(E) = \frac{A}{L}q^2\Sigma(E) \quad [1/\Omega], \tag{3.1}$$

where

$$\bar{T}_{el}(E) = T_{el}(E)M_{el}(E) = \frac{\lambda_{el}(E)}{\lambda_{el}(E)+L}M_{el}(E) \tag{3.2}$$

is the total transmission for electrons in the Landauer picture[165] with $M_{el}(E)$ being the number of conduction channels at E and T_{el} (E) is the transmission at energy, E, with $\lambda_{el}(E)$ being the mean-free-path for backscattering and L the length of the resistor. Equation (1) also expresses $G(E)$ in terms of the so-called transport distribution, $\Sigma(E)$, which arises when solving the diffusive Boltzmann transport equation (BTE)[204] and is defined as

$$\Sigma(E) = \frac{1}{\Omega}\sum_{\vec{k}} v_x^2(\vec{k})\tau(\vec{k})\delta(E - E(\vec{k})) \tag{3.3}$$

where $\Omega = AL$ and A is the cross-sectional area of the conductor.

Although the approach is more general, in this chapter we restrict our attention to diffusive samples for which $T_{el}(E) \rightarrow \lambda_{el}(E)/L$ and to three dimensional samples for which we write $G(E) = \sigma(E)A/L$, where $\sigma(E)$ is the conductivity. Accordingly, the expressions for conductivity analogous to the conductance in Eq. (3.1) become

$$\sigma(E) = \left(\frac{2q^2}{h}\right)\frac{M_{el}(E)}{A}\lambda_{el}(E) = q^2\Sigma(E) \qquad [1/\Omega\text{-m}], \tag{3.4a}$$

The total electrical conductivity is obtained by integrating $\sigma(E)(-\partial f_0/\partial E)$ over all of the energy channels, and the other thermoelectric coefficients are readily obtained, as described in Ref. [3], where mathematical definitions of $M_{el}(E)$ and $\lambda_{el}(E)$ are also given. For example, the electronic thermal conductivity for zero voltage gradient is obtained as

$$\kappa_0 = \left(\frac{2k_B^2 T_L \pi^2}{3h}\right)\int_{-\infty}^{+\infty}\frac{M_{el}(E)}{A}\lambda_{el}(E)\left(\frac{3}{\pi^2}\left(\frac{E-E_F}{k_B T_L}\right)^2\left(-\frac{\partial f_0}{\partial E}\right)\right)dE \quad [\text{W/m-K}]. \tag{3.4b}$$

Expressions for the lattice thermal conductance, K_{ph}, and lattice thermal conductivity, κ_{ph} analogous to Eq. (3.4b) can be readily obtained and expressed as [200,205]

$$K_{ph}(\omega) = \left(\frac{k_B^2 T_L \pi^2}{3h}\right)\overline{T}_{ph}(\omega) \qquad [\text{W/K}] \tag{3.5a}$$

and in the diffusive limit

$$\kappa_{ph}(\omega) = \left(\frac{k_B^2 T_L \pi^2}{3h}\right)\frac{M_{ph}(\omega)}{A}\lambda_{ph}(\omega) \ [\text{W/m-K}], \tag{3.5b}$$

where n_0 is the Bose-Einstein distribution function, the transmission is $\overline{T}_{ph}(\omega) = T_{ph}(\omega)M_{ph}(\omega)$ and $M_{ph}(\omega)$ is the number of phonon conducting modes (per polarization). The definitions of $T_{ph}(\omega)$ and $M_{ph}(\omega)$ are similar to those for electrons[3]. In 3D, the phonon mean-free-path for backscattering, $\lambda_{ph}(\omega)$ is given as [3]

$$\lambda_{ph}(\omega) = (4/3)\upsilon_{ph}(\omega)\tau_{ph}(\omega) = (4/3)\Lambda(\omega) \tag{3.6}$$

where the pre-factor, 4/3 comes from averaging over angle in 3D, $\upsilon_{ph}(\omega)$ is the spectral phonon group velocity at frequency, ω , $\tau_{ph}(\omega)$ is the phonon momentum relaxation time, and $\Lambda(\omega)$ is the commonly-defined spectral mean free path. Note that the mean-free-path for backscattering, Eq. (3.6), which arises in the Landauer approach, is somewhat longer than the mean-free-path for scattering, Λ . In the appendix, the relation of Eq. (3.5b), the Landauer expression for lattice thermal conductivity, to the conventional expression from kinetic theory is given.

To find the total conductivities, we multiply the energy-resolved quantities by a "window function" and integrate over energy,

$$\sigma = \left(\frac{2q^2}{h}\right)\int_{-\infty}^{+\infty}\frac{M_{el}(E)}{A}\lambda_{el}(E)\left(-\frac{\partial f_0}{\partial E}\right)dE \equiv \left(\frac{2q^2}{h}\right)\langle M_{el}\rangle\langle\langle\lambda_{el}\rangle\rangle \tag{3.7a}$$

$$\begin{aligned}\kappa_{ph} &= \left(\frac{k_B^2 T_L \pi^2}{3h}\right)\int_{-\infty}^{+\infty}\frac{M_{ph}(\omega)}{A}\lambda_{ph}(\omega)\left(\frac{3}{\pi^2}\left(\frac{\hbar\omega}{k_B T_L}\right)^2\left(-\frac{\partial n_0}{\partial(\hbar\omega)}\right)\right)d(\hbar\omega) \\ &\equiv \left(\frac{k_B^2 T_L \pi^2}{3h}\right)\langle M_{ph}\rangle\langle\langle\lambda_{ph}\rangle\rangle\end{aligned} \tag{3.7b}$$

where

$$\langle M\rangle \equiv \int M(x)W(x)\,dx \tag{3.7c}$$

$$\langle\langle\lambda\rangle\rangle \equiv \langle M\lambda\rangle/\langle M\rangle = \int\lambda(x)M(x)W(x)\,dx\Big/\int M(x)W(x)\,dx \tag{3.7d}$$

where $x = E$ for electrons and $x = \hbar\omega$ for phonons and $W(x)$ is a "window" function given by

$$W_{el}(E) = \left(-\frac{\partial f_0}{\partial E}\right) \quad \text{(electrons)} \tag{3.7e}$$

$$W_{ph}(\hbar\omega) = \frac{3}{\pi^2}\left(\frac{\hbar\omega}{k_B T_L}\right)^2\left(-\frac{\partial n_0}{\partial(\hbar\omega)}\right) \quad \text{(phonons)} \tag{3.7f}$$

The electrical conductivity is proportional to the quantum of electrical conductance, $2q^2/h$, and the thermal conductivity to the quantum of thermal conductance, $k_B^2 T_L \pi^2/3h$. The electrical and thermal conductivities are related to these two fundamental parameters and to the number of conducting channels per unit area, the mean-free-paths for backscattering, and to the Fermi-Dirac or Bose-Einstein distributions.

The number of conducting channels is determined by the electronic structure or phonon dispersion of the material. In Ref. [166], we discussed the evaluation of this quantity for electrons in 1D, 2D, and 3D considering a simple, effective mass level model. In Ref. [3], we discussed the evaluation of $M_{el}(E)$ from a full band description of $E(k)$ and its relation to effective mass level models. For phonons, a linear and isotropic phonon dispersion, $\omega = \upsilon_s q$, gives $M_{ph}(\omega)$ and $D_{ph}(\omega)$ as

$$M_{ph}(\omega) = A\left(3\omega^2/4\pi\upsilon_s^{\,2}\right) \qquad \text{(3D)} \qquad (3.8a)$$

$$D_{ph}(\omega) = \Omega\left(3\omega^2/\pi h \upsilon_s^{\,3}\right) \qquad \text{(3D)} \qquad (3.8b)$$

where υ_s is the velocity of sound in the direction of transport, and the factor of 3 comes from 3 branches. In the appendix, corresponding expressions for 1D, 2D, and 3D conductors are given and compared to the expressions for electrons. Our objective in this chapter is to present a simple technique to compute, $M_{ph}(\omega)$ from a given full zone description of the phonon dispersion. Because simple descriptions of phonon dispersions are convenient to use, they find wide applications. The extraction of Debye model parameters from a rigorous evaluation of $M_{ph}(\omega)$ and a discussion of the limitations of the Debye model are, therefore, also important parts of this chapter.

Given a phonon dispersion, $M_{ph}(\omega)$ can be obtained by counting the bands that cross the energy of interest. This method provides a computationally simple way to obtain $M_{ph}(\omega)$ from a given $\omega(q)$ [3,182]. The basic idea is illustrated in Fig. 3.2(a) using a dispersion relation along the transport direction for Si: 1) from 0 to 7.3 *THz,* the $M_{ph}(\omega)$ is three due to two transverse AP modes (TA) and one longitudinal

AP modes (LA), 2) from 7.3 to 12.8 to 15.0 *THz*, we have only one LA and one longitudinal OP modes (LO). 3) from 15.0 to 15.8 *THz*, $M_{ph}(\omega)$ in this case is 3 due to two transverse OP modes (TO) and one LO. To evaluate $M_{ph}(\omega)$, a full band description of phonon dispersion is needed. Several techniques have been reported for computing detailed phonon bandstructure[206,207]. In this work, the full phonon dispersion is calculated by using an interatomic pair potential model within General Utility Lattice Program (GULP)[208].

From the measured thermal conductivity, one can reliably estimate the average mean-free-path from the measured conductivity. From Eq. (3.7b), we can write

$$\langle\langle \lambda_{ph} \rangle\rangle = \frac{\kappa_{ph}}{\frac{k_B^2 T_L \pi^2}{3h} \int_{-\infty}^{+\infty} \frac{M_{ph}(\omega)}{A} \left(\frac{3}{\pi^2} \left(\frac{\hbar\omega}{k_B T_L} \right)^2 \left(-\frac{\partial n_0}{\partial(\hbar\omega)} \right) \right) d(\hbar\omega)} = \frac{\kappa_{ph}}{K_{ph\_BAL}/A} \tag{3.9}$$

where the denominator of Eq. (3.9) is recognized as ballistic thermal conductance per area K_{ph_BAL}/A. Note the units of K_{ph_BAL}/A are *W/m^2-K*, which is different from the units of κ_{ph}, *W/m-K* . Since the numerator in Eq. (3.9) can be measured and the denominator readily evaluated from a known dispersion, reliable estimates of the mean-free-paths can be obtained. The extraction of average electron mean-free-path by similar way has been used to analyze electronic devices[209–211]

Finally, we note that two Debye temperatures are required to evaluate the specific heat and the thermal conductivity properly with the simple Debye model. The use of two Debye temperatures was also found necessary in work on the thermal conductivity of nanowires[182]. The Debye temperature is usually determined to obtain the observed specific heat, which is hereinafter called Debye temperature for the specific heat (Θ_D). The Debye temperature for thermal conductivity (Θ_M) is newly defined and is determined to obtain the correct K_{ph_BAL}. For 3D bulk ballistic conductors with linear phonon dispersion, the specific heat per volume and ballistic thermal conductance per area are expressed as

$$C_{V,3D} = \left(\frac{3 k_B{}^4 T_L{}^3}{2\pi^2 \hbar^3 \upsilon_s{}^3} \right) \int_0^{\Theta_D/T} \frac{x^4 e^x}{\left(e^x - 1\right)^2} dx \tag{3.10a}$$

$$K_{ph\_BAL}/A = \left(\frac{3 k_B{}^4 T_L{}^3}{8\pi^2 \hbar^3 \upsilon_s{}^2} \right) \int_0^{\Theta_M/T} \frac{x^4 e^x}{\left(e^x - 1\right)^2} dx \tag{3.10b}$$

where $x = \hbar\omega / k_B T_L$. Both Θ_D and Θ_M are extracted to match full band results.

3.3 Results

In this section, the phonon thermal conductivity will be evaluated and interpreted within the Landauer framework. Two representative semiconductor materials are compared to examine key factors for good TE materials; Si and Bi_2Te_3. We then compare full band calculations to linear dispersion approximations. A technique to extract a well-defined average mean-free-path is also presented. We show that this mean-free-path has a strong physical significance.

Figures 3.1(a) and 3.1(b) show calculated and measured [212–214] phonon dispersion characteristic along high symmetry directions; the phonon DOS for Si and Bi_2Te_3 are also shown. The Tersoff potential model and Morse potential model are used for Si[215]and Bi_2Te_3[207], respectively. Computed elastic properties with these models show overall good agreement with experiments, indicating that the potential model describe well the harmonic behavior[207,215]. For both materials, it can be seen that the AP modes are well reproduced and OP modes are somewhat overestimated. Because thermal transport is mostly dominated by AP modes, we expect that these full band dispersions will predict the lattice thermal conductivity well. It should be understood that our objective is to describe a general technique and to discuss general features of the solution. More refined treatments of phonon dispersion could be used.

The specific heat per volume (the integral of Eq. (A3)) is calculated and shown in Fig. 3.1(c). As shown in Eq. (A3), the specific heat calculations do not require us to include scattering. In each plot, the solid line is the result with calculated DOS, and the dashed line is the result with the measured DOS. It is seen that two curves are generally in a good agreement for both materials.

Figure 3.2(b) shows full dispersion results and results with a linear dispersion approximation. At low frequency, the linear dispersion approximation provides a good fit to the full band calculation, and it is found that the average sound velocity to fit to full band results for Bi_2Te_3 ($\upsilon_s = 1.74\times10^5$ cm$/s$) is about one third of average sound velocity of Si ($\upsilon_s = 5.32\times10^5$ cm$/s$). The available number of conducting modes is seen to be smaller for Bi_2Te_3 for most of frequency range.

Next, the phonon thermal conductance is evaluated. The ballistic thermal conductance per area for Si and Bi_2Te_3 is calculated as shown in Fig. 3.3. The ballistic thermal conductance is proportional to the effective number of phonon conducting modes, which can be readily obtained from phonon dispersions. Below 30 K, K_{ph_BAL} for Bi_2Te_3 is larger than Si due to the large $M_{ph}(\omega)$ at low frequency. At 300 K, however, K_{ph_BAL} for Si is a factor of 10 larger than K_{ph_BAL} for Bi_2Te_3, which results because the effective number of phonon conducting modes of Bi_2Te_3 is 10 times smaller than that of Si.

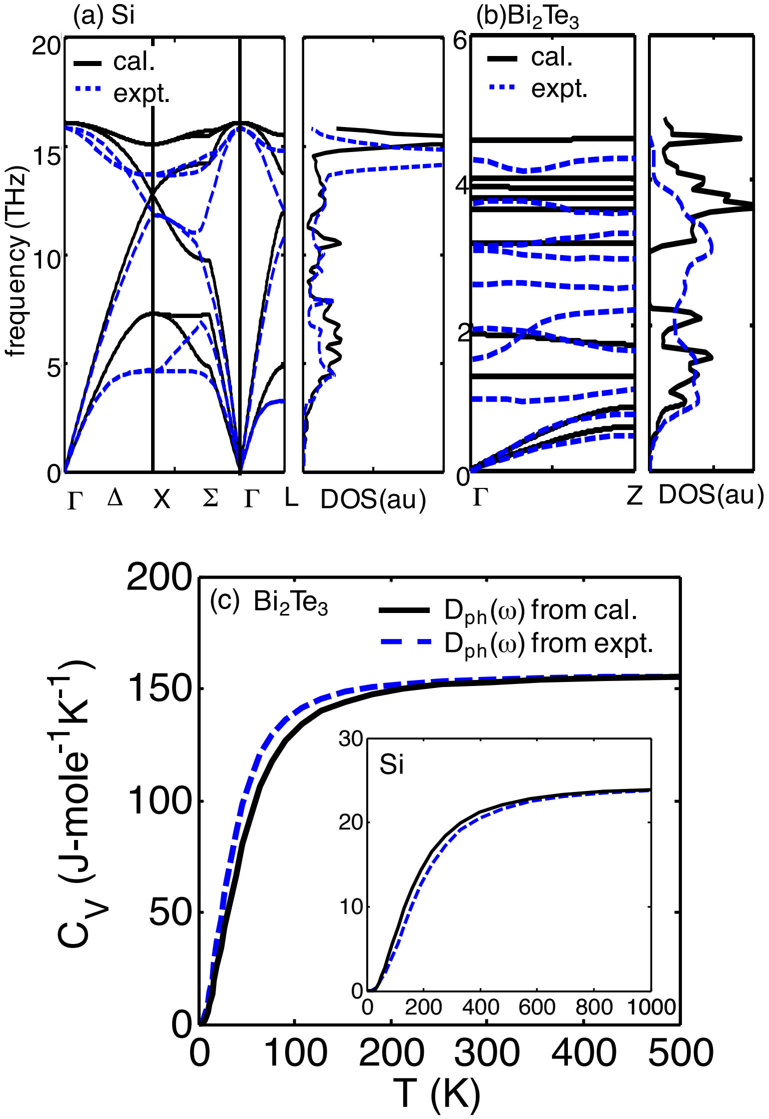

Fig. 3.1. Phonon dispersion along the high symmetry lines and phonon density of states for (a) Si and (b) Bi_2Te_3. (c) Specific heat per volume of Si (Inset) and Bi_2Te_3 . The solid and dashed lines are for the results of calculation and experiments.

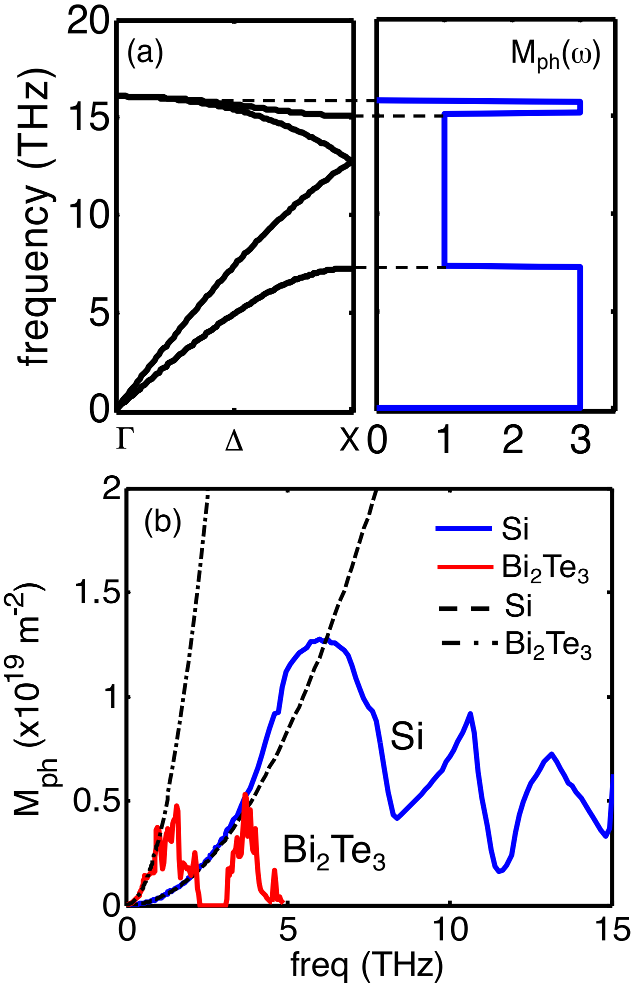

Fig. 3.2. (a) Illustration of bands counting method for specific dispersion relation for Si. Dotted line is guide to eye. (b) Number of phonon modes of Si and Bi_2Te_3. The dashed and dashed-dot lines are the results obtained from the Debye model with the fitted sound velocities of 1.74×10^5 cm/s and 5.32×10^5 cm/s for Si and Bi_2Te_3, respectively.

From Eq. (3.9), the average mean-free-path for backscattering is deduced by taking ratio of the measured thermal conductivity to the ballistic thermal conductance per area. Figure 3.4 shows the extracted $\langle\langle\lambda_{ph}\rangle\rangle$ for Si and Bi_2Te_3. At 300 K, $\langle\langle\lambda_{ph}\rangle\rangle$ for Bi_2Te_3 is 14 nm and for Si, it is 115 nm. To relate extracted $\langle\langle\lambda_{ph}\rangle\rangle$ to expected average $\langle\langle\lambda_{ph}\rangle\rangle$ from the spectral phonon mean-free-path for backscattering $\lambda_{ph}(\omega)$, expressions for $\tau_{ph}(\omega)$ in the relaxation time approximation (RTA) are used for umklapp[24] , point defect[25], and boundary[26] scattering rate: $\tau_u^{-1} = B\omega^2 e^{-C/T}$, $\tau_d^{-1} = D\omega^4$, and $\tau_b^{-1} = \langle \upsilon(\omega)\rangle / (F \cdot l)$, respectively. The parameters to fit extracted $\langle\langle\lambda_{ph}\rangle\rangle$ are $B = 2.8\times10^{-19}$ s/K, $C = 140$ K, $D = 1.32\times10^{-45}$ s^3, $F = 0.4$, $l = 7.16\times10^{-3}$ m for Si and $B = 2.8\times10^{-18}$ s/K, $C = 10$ K, $D = 1.32\times10^{-45}$ s^3, $F\cdot l = 1\times10^{-4}$ m for Bi_2Te_3. As shown in the inset of Fig. 3, experimental thermal conductivity[26,216] and calculations are in a good agreement, which indicate that the extracted $\langle\langle\lambda_{ph}\rangle\rangle$ has strong physical significance.

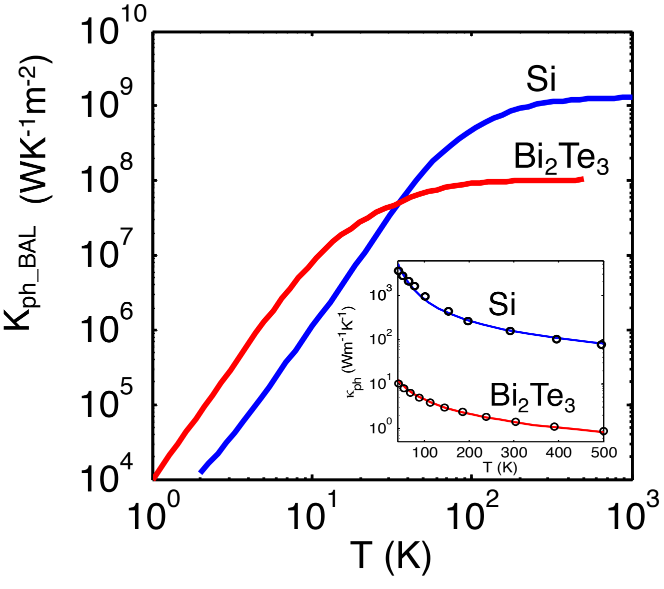

Fig. 3.3. Ballistic thermal conductance per area of Si and Bi_2Te_3 . Insets: lattice thermal conductivity of Si and Bi_2Te_3 . The solid line and symbols are calculated and experimental values, respectively.

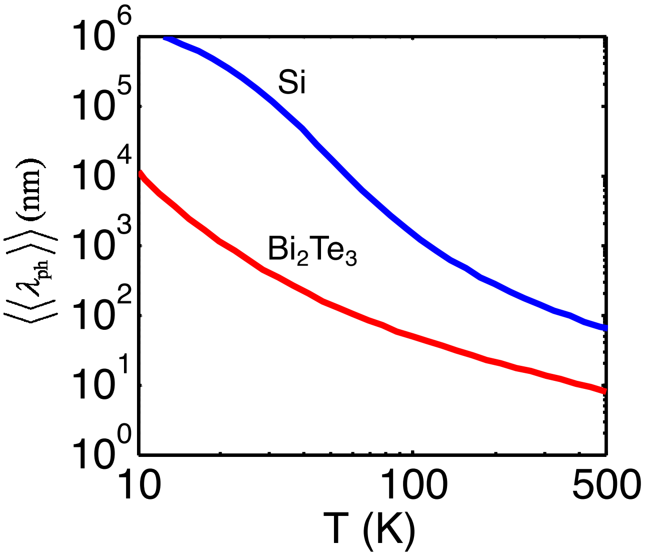

Fig. 3.4. Extracted average mean-free-path of Si and Bi_2Te_3 by taking the ratio of experimental thermal conductivity to ballistic thermal conductance per area.

In the Landauer picture, the low thermal conductivity of Bi_2Te_3 at 300 K is attributed to two factors. First of all, it has an effective number of conduction channels that is ten times smaller than Si, as shown in Fig. 3.3. The different number of conducting channels are related to the different phonon dispersions. On top of that, Bi_2Te_3 has a smaller $\langle\langle \lambda_{ph} \rangle\rangle$ due to umklapp scattering which is a factor of 10 stronger than for Si. Both factors lead to two orders of magnitude reduction in thermal conductivity comparing to Si. For comparison, average electron mean-free-paths at room temperature are 18 nm for Bi_2Te_3 and 13 nm for Si, which are extracted in a similar way from the full band electronic structure [3]. The number of electron conducting modes for Si and Bi_2Te_3 are shown in Fig. 3.7(b). In terms of electronic performance, the effective number of conduction channels and average electron mean-free-path for backscattering are similar for both materials, resulting in similar power factor(S^2G) value.

3.4 Discussion

In this section, we show that average mean-free-path obtained by simple estimates differs by an order of magnitude from that extracted from full phonon dispersion. The use of simplified dispersion model is then discussed.

The simplest conventional approach to estimate bulk mean-free path from a classical kinetic theory is

$$\langle\langle \Lambda \rangle\rangle = 3\kappa_{ph} / C_V \upsilon_s \quad , \tag{3.11}$$

where κ_{ph}, υ_s, and C_V are measured quantities. Using $\upsilon_s = 2.95\times 10^5\ \mathrm{cm}/s$ and C_V = $1.20\times10^6\ J/cm^3\text{-}K$ from Fig. 3.1(b) and (c) for Bi_2Te_3, estimated $\langle\langle \Lambda \rangle\rangle$ at 300 K is 1.2 nm, an order of magnitude smaller than 14 nm extracted from Eq. (3.9). This occurs because the appropriate velocity we should use in Eq. (3.11) is much different from the measured sound velocity ($\upsilon_s = 2.95\times 10^5\ \mathrm{cm}/s$). Equation (A3) can be re-arranged as

$$\kappa_{ph} = \frac{1}{3} C_V \upsilon_{ave} \langle\langle \Lambda \rangle\rangle \tag{3.12}$$

where $\upsilon_{ave}\left(= \int d\left(\hbar\omega\right) C_V(\omega) \upsilon\left(\omega\right) / C_V\right)$ is the appropriate average velocity we should use in Eq. (3.12) and $\langle\langle \Lambda \rangle\rangle \left(= \left(3/4\right) \langle\langle \lambda \rangle\rangle \right)$ is an average mean-free-path for scattering which is different from $\langle\langle \lambda_{ph} \rangle\rangle$ as is seen in Eq. (3.6). At 300 K, $\upsilon_{ave} = 3.40\times 10^4\ \mathrm{cm}/s$, a 5× ~ 9× smaller than either the measured sound velocity ($\upsilon_s = 2.95\times 10^5\ \mathrm{cm}/s$) or the average sound velocity to fit to full band results ($\upsilon_s = 1.74\times 10^5\ \mathrm{cm}/s$). Therefore, prediction of the bulk mean-free path from measured sound velocity in Eq. (3.11) leads to serious errors.

Simple phonon dispersion models are often used to analyze thermoelectric devices. The simplest model is the Debye model (the linear dispersion approximation) with Debye temperature (Θ_D). As mentioned in Sec. 3.2, a Debye temperature for thermal conductivity (Θ_M) must be newly defined to treat the thermal conductivity properly with the simple Debye model. Both Θ_D and Θ_M are extracted to match full band results as shown in Fig. 3.5 (a) for Si and Bi_2Te_3. It can be seen that Θ_M is smaller than Θ_D by 20~50 % depending on materials and the two Debye temperatures are weakly dependent on temperature. For Bi_2Te_3, Fig. 3.5(b) compare the full band and Debye models of $M_{ph}(\omega)$ and $D_{ph}(\omega)$. The Debye cutoff frequencies, $\omega_D (= k_B \Theta_{D,\max} / \hbar)$ and $\omega_M (= k_B \Theta_{M,\max} / \hbar)$ are 3.57 *THz* and 1.93 *THz*, respectively.

Next, the specific heat and thermal conductivity are calculated as shown in Fig. 3.6(a) and the inset of Fig. 3.6(a). Although only the Debye cutoff frequency from the phonon density of states (ω_D) gives the correct specific heat, thermal conductivities obtained from either of the two Debye frequencies, ω_M and ω_D, match well the results using full phonon dispersion. Use of the Debye model with the cutoff frequency, ω_D, however, leads to serious errors in estimating $\langle\langle \lambda_{ph} \rangle\rangle$ — by one order of magnitude as shown in Fig. 3.6(b). The average mean-free-path obtained from Debye model with the cutoff frequency, ω_M is in relatively a good agreement with that obtained by full phonon dispersion because this cutoff frequency gives the correct effective number of conduction channels, i.e. the ballistic thermal conductance per area. The inset of Fig. 6(b), however, shows that the spectral mean-free-path, $\lambda_{ph}(\omega)$ obtained from Debye models doesn't capture exactly the detailed frequency dependence of $\lambda_{ph}(\omega)$ from full phonon dispersion – regardless of choice of cutoff frequency.

The reason that an effective mass description works well for electrons and a Debye model does not works as well for phonon is that the important energy for electrons is near the bottom of the band, but for phonons it is the entire phonon dispersion. Fig. 3.7(a) shows the "window" function for phonons, W_{ph}, and number of phonon conducting modes for Si and Bi_2Te_3. Comparing to the "window" function for electrons, W_{el}, and number of electron conducting modes as shown in Fig. 3.7(b), it can be easily seen that the entire frequency range of full phonon dispersion affect thermal conductivity for Si and Bi_2Te_3. However, only the electron dispersion around the band edges is important. Note that this occurs because of difference between full phonon spectrum and full electronic structure, not because of difference between Fermi-Dirac and Bose-Einstein distribution or between "window" functions, defined by Eqs. (3.7e) and (3.7f). As shown in Fig. 3.7, both "window" functions, W_{ph} and W_{el}, have a width of ~ 5 k_BT_L and the function W_{ph} has similar energy dependence to the so-called Fermi "window" function W_{el}. The integral of window functions for electrons, W_{el} from $-\infty$ to ∞ gives 1, while the integral of W_{ph} from 0 to ∞ is 1. This comparison explains why effective mass approximation (EMA) works well for electron transport[3], and Debye model should be used with caution.

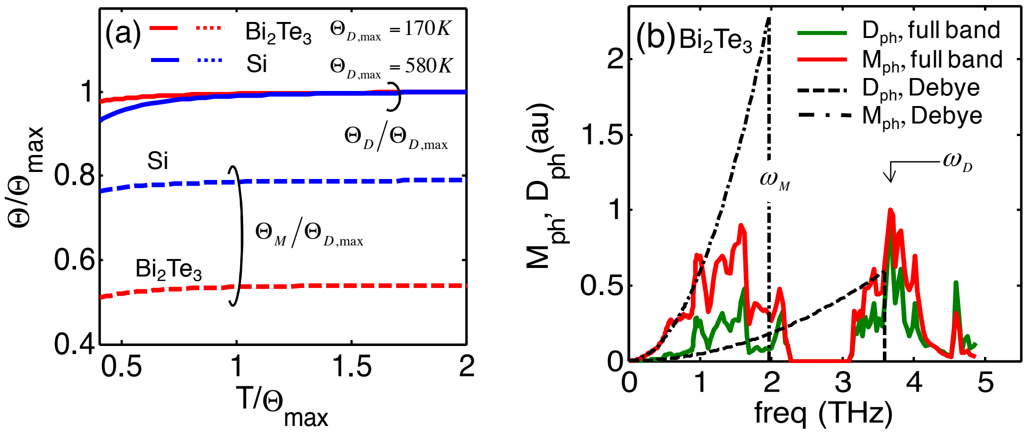

Fig. 3.5. (a) Comparison of Debye temperature for the specific heat (Θ_D) and Debye temperature for thermal conductivity (Θ_M) normalized by maximum Θ_D. (b) Debye model vs. full dispersion for Bi_2Te_3. Red and green solid lines are full band results of number of phonon modes (M_{ph}) and density of states (D_{ph}) in arbitrary units. The dashed-dot and dashed lines are results from Debye approximation at low frequency for M_{ph} and D_{ph}.

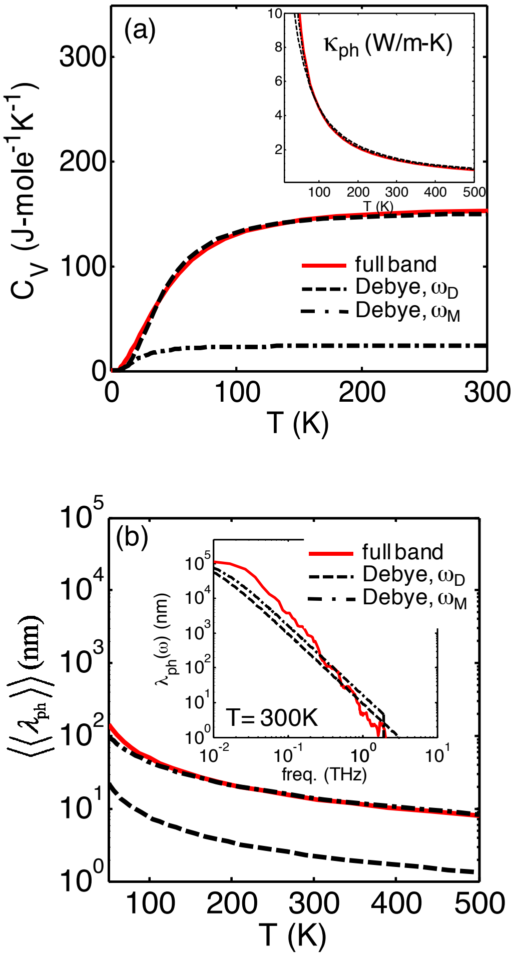

Fig. 3.6. (a) specific heat calculation and (b) extracted average mean-free-path of Bi_2Te_3 for Debye models and full band results. Insets of Fig. 6(a) and Fig. 6(b) are thermal conductivity calculation and spectral mean-free-path for backscattering, respectively. Solid lines: full band results; Dashed and dashed dot lines: Debye approximation.

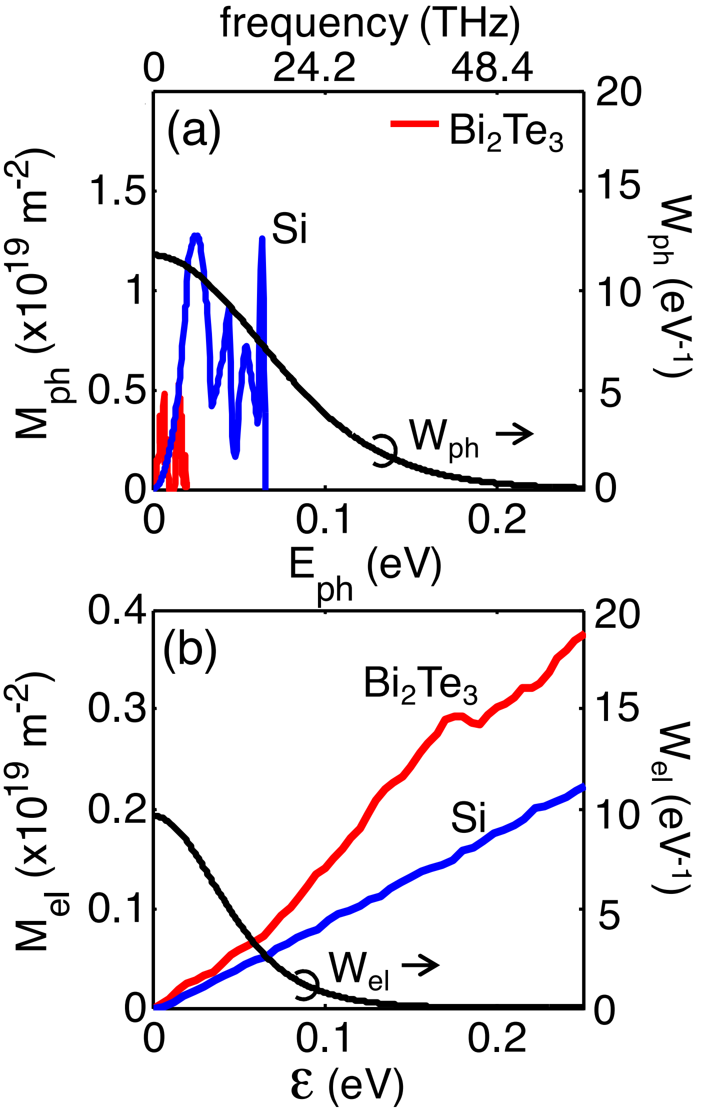

Fig. 3.7. (a) number of phonon conducting modes (M_{ph}) and Eq. (3.7f) at 300 K, (b) number of electron conducting modes (M_{el}) calculated from full band electronic structure and Eq. (3.7e) at 300 K. For horizontal axis, $\varepsilon = E_{el} - E_C$ for number of electron conducting modes and $\varepsilon = E_{el} - E_F$ for a electron "window function" assuming $E_F = E_C$ which is a typical condition for optimum performance.

3.5 Summary and Conclusion

In this chapter, we related the Landauer approach for phonon transport to the more commonly used Boltzmann transport equation approach. Although the Landauer approach applies from the ballistic to diffusive limit and for 1D, 2D, and 3D conductors, we restricted our attention in this chapter to the diffusive limit and to 3D, bulk materials. The common expression for thermal conductance that begins with classical kinetic theory was related to the corresponding Landauer expression. A simple "counting bands" technique for extracting the kernel of the transport integral, $M(E)$, was illustrated. As an example of the technique, we examined the electronic and thermal performance of Si and Bi_2Te_3 using a full band description of phonon dispersion and electronic bandstructure. A simple technique for extracting a physically well defined mean-free-path for phonons was presented. This mean-free-path agrees with a simple estimate from the measured specific heat – as long as the appropriate average velocity obtained from the given phonon dispersion is used. Finally, we discussed the use of simple phonon dispersion models, such as the widely used Debye model for phonon dispersion, which is widely used for device design. We showed that two different Debye temperatures are needed – one to describe the phonon density of states and specific heat and another to describe the distribution of conducting channels, $M(E)$, and the thermal conductivity. The existence of two different Debye temperatures is analogous to the two effective masses needed to describe electron transport, the conductivity and density-of-states effective masses. Using the conductivity Debye temperature and the measured lattice thermal conductivity, a physically meaningful average mean-free-path can be accurately obtained. Finally, we explained why the effective mass model works well for electrons and why the Debye model does not work as well for phonons. Although the conclusion is that simplified phonon models should be used with caution, the simple procedure for evaluating $M(E)$ from the full phonon dispersion provides a practical alternative.

4. THERMAL CONDUCTIVITY OF BULK AND THIN-FILM SILICON: A LANDAUER APPROACH

The contents of Chapter 4 have been extracted and revised from the following manuscript: C. Jeong, S. Datta, and M. Lundstrom, "Thermal Conductivity of Bulk and Thin-Film Silicon: A Landauer Approach," *J. Appl. Phys.*, 111, 093708 (2012)

The question of what fraction of the total heat flow is transported by phonons with different mean-free-paths is addressed using a Landauer approach with a full dispersion description of phonons to evaluate the thermal conductivities of bulk and thin film silicon. For bulk Si, the results reproduce those of a recent molecular dynamic treatment showing that about 50% of the heat conduction is carried by phonons with a mean-free-path greater than about one micrometer. For the in-plane thermal conductivity of thin Si films, we find that about 50% of the heat is carried by phonons with mean-free-paths shorter than in the bulk. When the film thickness is smaller than ~0.2 μm, 50% of the heat is carried by phonons with mean-free-paths longer than the film thickness. The cross-plane thermal conductivity of thin-films, where quasi-ballistic phonon transport becomes important, is also examined. For ballistic transport, the results reduce to the well-known Casimir limit.[141] These results shed light on phonon transport in bulk and thin-film silicon and demonstrate that the Landauer approach provides a relatively simple but accurate technique to treat phonon transport from the ballistic to diffusive regimes.

4.1 Introduction

Recent molecular dynamics (MD) simulations[27] have shown that in bulk silicon (Si) about 50% of the heat is carried by phonons with mean-free-paths (MFPs) greater than about 1 μm – a fact that is surprising and that the authors of Ref. [27] could not explain with a simple, Callaway model with Debye approximation.[217] These results raise similar questions about heat transport in thin Si films. In this paper, we show that a simple Landauer model, essentially a Callaway model with full phonon dispersion, accurately reproduces the results of Ref. [27]. We also show that the same model describes the in-plane thermal conductivity of silicon thin films and find, that about 50% of the heat is carried by phonons with mean-free-paths shorter than in the bulk. When the film thickness is smaller than ~0.2 μm, 50% of the heat is carried by phonons with mean-free-paths longer than the film thickness. Finally, we apply the technique to cross-plane thermal transport in Si. The results shed light on thermal transport in thin Si films and demonstrate that the Landauer approach provides a simple and accurate treatment of lattice thermal conductivity that is useful for analyzing experiments and for designing materials and structures.

The findings of Minnich et al.[27] for bulk Si raise questions about heat conduction in thin Si films and how the heat is carried by phonons with different MFPs. In silicon on insulator (SOI) films, it is well-known that the in-plane thermal conductivity decreases as the film thickness decreases due to the increasing importance of surface roughness scattering.[28–31] The influence of surface roughness is usually modeled by using either a constant [29–31,218,219] or frequency-dependent [28,220] specularity parameter, p, representing the probability of specular phonon boundary scattering. As an example, for perfectly diffusive scattering $p = 0$ and for perfectly specular scattering $p = 1$. The quantitative comparison between the in-plane thermal conductivities with constant and frequency-dependent p suggested that the frequency-dependent model provides a more accurate description for the in-plane thermal conductivity.[221] We show in this paper that with the addition of a model for surface roughness scattering, the Landauer model used for bulk Si also accurately describes in-plane thermal transport. We then use the model to address the question raised by the authors of Ref. [27]: "How do phonons with various mean-free-paths contribute to thermal conduction in thin Si films?"

The measured cross-plane thermal conductivity of thin Si films has been found to be even lower than the in-plane thermal conductivity.[32] In some models,[222–224] the reduction in cross-plane thermal conductivity is modeled with the Boltzmann transport equation (BTE) by including a phonon-boundary scattering time (τ_b), which is assumed to be equal to the average time between "boundary scattering events": $\tau_b = L/(2\upsilon)$, where L is the length of the conductor, and υ the group velocity. Ballistic phonon transport (i.e. no phonon scattering within thin film), which becomes important in cross-plane transport is typically described by an equation of phonon radiative transport (EPRT),[225] which has been developed based on the Boltzmann equation and the analogy between phonons and photons. In the ballistic limit and with the Debye approximation, the EPRT yields a familiar blackbody radiation law for phonons,[123] $q = \sigma\left(T_H^4 - T_C^4\right)$, where σ is the Stefan-Boltzmann constant for phonons. This result has also been derived by Casimir,[141] who treated a perfectly diffusive surface ($p = 0$) as if it absorbed all phonons incident upon it, and reemitted them at a rate depending on the absolute temperature of the surface according to the theory of blackbody radiation. We will show in this paper that the same Landauer approach used to describe diffusive phonon transport can be simply extended to accurately describe ballistic and quasi-ballistic transport.

The Landauer approach is widely-used to treat ballistic electron [165] and phonon [200,205] transport in nanostructures. As recently shown for electrons[3] and phonons,[226] the method can also be applied to diffusive transport in bulk materials. The approach reduces to the BTE for diffusive transport, but is more physically transparent and also provides some computational advantages. Section 4.2 presents a brief summary of the formalism for phonon transport as discussed in detail in Ref. [226]. In Sec. 4.3, results for the thermal conductivity of bulk Si are presented and compared to recent molecular dynamics simulations. In Sec. 4.4, the in-plane and cross-plane thermal conductivities are discussed. Sections 3 and 4 also illustrate a general approach for extracting a well-defined mean-free-path for phonons from measured thermal conductivity data. In Sec. 4.5, we discuss the ballistic limit of phonon transport and relate the Landauer expressions to the well-known Casimir formula.[141] Finally, our conclusions are summarized in Sec. 4.6.

4.2 Approach

This paper is an application of the approach presented in Ref. [226]. The Landauer formula for heat current (I_Q) is expressed as

$$I_Q = \frac{1}{h}\int_0^{\infty} d(\hbar\omega)\left(T_{ph}M_{ph}\right)\hbar\omega\left(n_1 - n_2\right), \tag{4.1a}$$

where T_{ph} is the transmission at a given energy $\hbar\omega$, M_{ph} is the number of conducting channels at a given energy, and n_1 and n_2 are Bose-Einstein distributions for the two contacts across which heat flows.[165] The transmission T_{ph} is given as [165]

$$T_{ph} = \lambda_{ph}(\omega)\big/\left(L + \lambda_{ph}(\omega)\right), \tag{4.1b}$$

where $\lambda_{ph}(\omega)$ is the mean-free-path for backscattering and L the length of the conductor. Equation (4.1a) applies to ballistic limit ($L \quad \lambda_{ph}(\omega)$) for which $T_{ph} = 1$, quasi-ballistic regime ($L \quad \lambda_{ph}(\omega)$) for which $T_{ph} = \lambda_{ph}(\omega)\big/\left(L + \lambda_{ph}(\omega)\right)$ as well as to diffusive limit ($L \quad \lambda_{ph}(\omega)$) for which $T_{ph} = \lambda_{ph}(\omega)\big/L$. In the diffusive limit, it was shown that the Landauer expression for lattice thermal conductivity is essentially equivalent to the conventional expression from BTE.[226] Note that the product $T_{ph}M_{ph}$ is proportional to the "transport distribution" well-known for electrons.[204]

For a small temperature gradient (ΔT), thermal conductance ($K_{ph} = I_Q\big/\Delta T$) is

$$K_{ph} = \left(\frac{k_B^2 T_L \pi^2}{3h}\right)\int_0^{+\infty} d(\hbar\omega)\left(T_{ph}M_{ph}\right)W_{ph}, \tag{4.2a}$$

where $k_B^2 T_L \pi^2\big/3h$ is the quantum of thermal conductance and W_{ph} is a "window function" given by[226]

$$W_{ph}(\hbar\omega) = \frac{3}{\pi^2}\left(\frac{\hbar\omega}{k_B T_L}\right)^2\left(-\frac{\partial n_0}{\partial(\hbar\omega)}\right). \tag{4.2b}$$

The integral of the window function, W_{ph}, from 0 to ∞ is 1, just like the derivative of the Fermi function $(-\partial f_0/\partial E)$ appearing in the expression for electrical conductivity. The thermal conductance, Eq. (4.2a) can be also expressed as

$$K_{ph} = \left(\frac{k_B^2 T_L \pi^2}{3h}\right)\left\langle M_{ph}\right\rangle\left\langle\left\langle T_{ph}\right\rangle\right\rangle, \tag{4.2c}$$

where the average $\langle X \rangle$ for any quantity X is defined as $\langle X \rangle \equiv \int X\, W_{ph} d(\hbar\omega)$ while the average $\langle\langle X \rangle\rangle$ is defined as $\langle M\, X \rangle / \langle M \rangle$. From Eq. (4.2c), the expressions for the lattice thermal conductivity, $\kappa_{ph} = K_{ph}\left(L/A\right)$, can be expressed as

$$\kappa_{ph} = \left(\frac{k_B^2 T_L \pi^2}{3h}\right)\langle M_{ph}/A \rangle \langle\langle \lambda_{ph} \rangle\rangle_{eff}\,, \tag{4.3a}$$

where A is the cross-sectional area of the conductor and $\langle\langle \lambda_{ph} \rangle\rangle_{eff}$ the effective MFP which is given as

$$\langle\langle \lambda_{ph} \rangle\rangle_{eff} = \langle\langle T_{ph} \rangle\rangle L = \left\langle\left\langle \left(\lambda_{ph}^{-1} + L^{-1}\right)^{-1} \right\rangle\right\rangle. \tag{4.3b}$$

From Eq. (4.2c), the ballistic thermal conductance per area K_{ph_BAL}/A can be defined as

$$K_{ph\_BAL}/A = \left(\frac{k_B^2 T_L \pi^2}{3h}\right)\langle M_{ph}/A \rangle, \tag{4.3c}$$

so the thermal conductivity is expressed as

$$\kappa_{ph} = \left(K_{ph\_BAL}/A\right)\langle\langle \lambda_{ph} \rangle\rangle_{eff}\,. \tag{4.3d}$$

Since $\langle M_{ph} \rangle$ and K_{ph_BAL}/A can be readily obtained from the bandstructure, the $\langle\langle \lambda_{ph} \rangle\rangle_{eff}$ can be estimated by taking the ratio of measured κ_{ph} to the K_{ph_BAL}/A . Note that Eqs. (4.3a) and (4.3b) holds for all transport regimes. In the ballistic limit, $L \quad \lambda_{ph}$, $\langle\langle \lambda_{ph} \rangle\rangle_{eff} = L$ and in the diffusive limit, $L \quad \lambda_{ph}$, $\langle\langle \lambda_{ph} \rangle\rangle_{eff} = \langle\langle \lambda_{ph} \rangle\rangle$ with $\langle\langle \lambda_{ph} \rangle\rangle$ being the average MFP in the diffusive limit. In the quasi-ballistic limit, the appropriate effective MFP is given by Eq. (4.3b).

It was shown in Ref. [226] that given an accurate phonon dispersion, $M_{ph}(\omega)$, can be readily computed by a simple numerical technique - the "band counting" method. To evaluate $M_{ph}(\omega)$ in this work, a full band description of phonon dispersion was obtained from the Tersoff [215] interatomic pair potential model within General Utility Lattice Program (GULP).[208] Then it is straightforward to compute K_{ph_BAL}/A.

4.3 Bulk Thermal Conductivity

In this section, the phonon thermal conductivity of bulk Si will be evaluated and compared to a recent MD calculation.[27] Figure 4.1(a) displays the energy-resolved M_{ph}, λ_{ph}, and W_{ph} at 300 K for bulk Si. Note that the entire phonon dispersion participates in conduction since W_{ph} is almost constant. This is in sharp contrast to the case of electrons, in which the important energies are near the bottom of the band. The ballistic thermal conductance, K_{ph_BAL}, is readily evaluated from Eq. (4.3c). By comparing K_{ph_BAL} to the measured conductivity, κ_{ph},[26] the average MFP, $\langle\langle\lambda_{ph}\rangle\rangle$, is readily extracted from Eq. (4.3d). The results in Fig. 4.1b, show that $\langle\langle\lambda_{ph}\rangle\rangle \simeq 135$ nm at $T = 300\ K$. (As will be discussed in Sec. 4.5, when comparing this result to the conventional mean-free-path, l_{ph}, it is important to remember that the Landauer mean-free-path (or mean-free-path for backscattering) is 4/3 times longer.[226])

To examine how heat is conducted by phonons with different mean-free-paths, we need expressions for the spectral phonon mean-free-path for backscattering,[226]

$$\lambda_{ph}(\omega) = (4/3)\upsilon_{ph}(\omega)\tau_{ph}(\omega) = (4/3)l_{ph}(\omega), \tag{4.4}$$

where $\upsilon_{ph}(\omega)$ is the spectral phonon group velocity at frequency ω, $\tau_{ph}(\omega)$ the phonon momentum relaxation time, and $l_{ph}(\omega) = \upsilon_{ph}(\omega)\tau_{ph}(\omega)$. For $\tau_{ph}(\omega)$, the relaxation time approximation (RTA) is used for umklapp scattering,[24] point defect scattering,[25] and crystalline boundary scattering rates[26]: $\tau_u^{-1} = B\omega^2 e^{-C/T}$, $\tau_d^{-1} = D\omega^4$, and $\tau_b^{-1} = \langle\upsilon(\omega)\rangle/(F \cdot l)$, respectively.

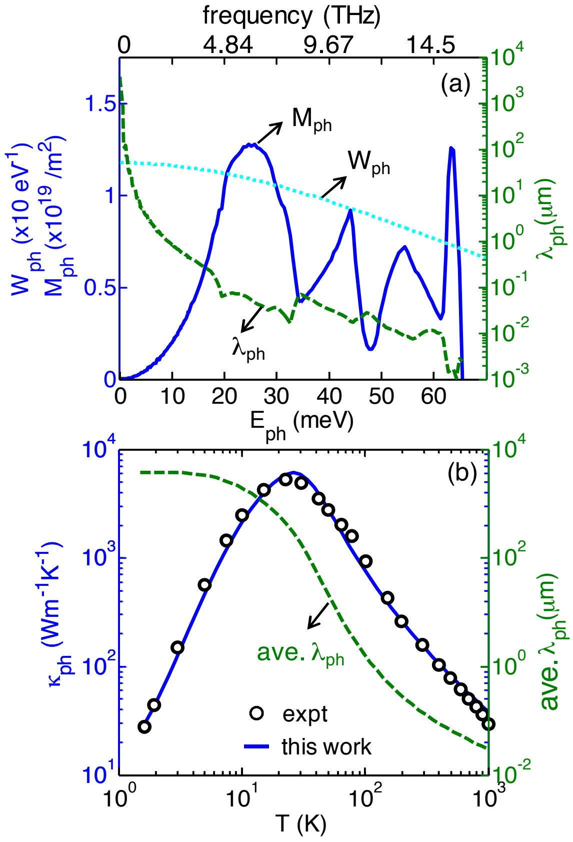

Figure 4.1. (a) For bulk Si, energy-resolved number of conducting channels (M_{ph}), window function (W_{ph}), and the mean-free-path for backscattering (λ_{ph}) are plotted at 300 K. Note that the entire spectrum of M_{ph} participates in conduction since W_{ph} is almost constant. The mean-free-path shows that low-energy acoustic phonons have long λ_{ph} since they don't suffer a lot from umklapp scattering. The spectral λ_{ph} are calculated based on the relaxation time approximation for umklapp scattering,**[24]** point defect scattering,**[25]** and crystalline boundary scattering.**[26]** (b) The thermal conductivity κ_{ph} (left axis) and the average MFP $\langle\langle \lambda_{ph} \rangle\rangle$ (right axis) are plotted as a function of temperature. Experimental results are obtained from Ref. **[26]**. Good agreement between calculation and experiment is observed.

Typical parameters to fit the κ_{ph} *vs*. T for bulk Si are used [226]: $B = 2.8\times10^{-19}$ s/K, $C = 140$ K, $F = 0.4$, and $l = 7.16\times10^{-3}$ m. Parameter $D = 1.32\times10^{-45}$ s^3 is analytically determined from the isotope concentration, so the value given in Ref. [26] is used for bulk Si. Figure 4.1b shows that the resulting fit is excellent. Figure 4.2 shows the cumulative distribution function of thermal conductivity as a function of energy with and without scattering. It can be seen that all energy channels contribute to the ballistic thermal conductance. When scattering is included, however, high energy channels contribute very little to κ_{ph} because high energy phonons have very short MFPs.

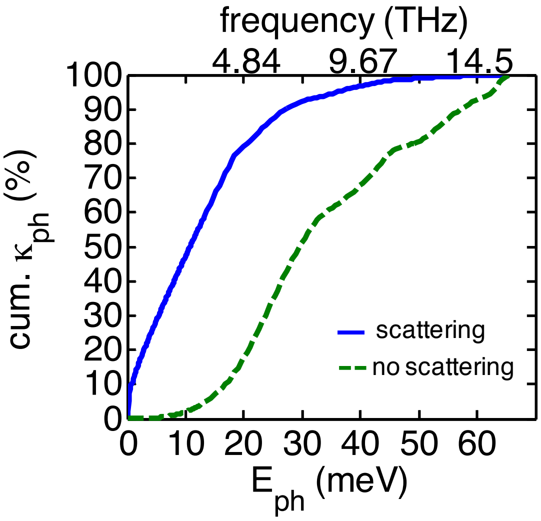

Figure 4.2. The cumulative thermal conductivity, κ_{ph} , as a function of energy is plotted for diffusive (scattering) and ballistic (no scattering) cases. For the ballistic case, all energy channels equally contribute to κ_{ph}. With scattering, low-energy channels mainly contribute to κ_{ph} because high-energy phonons have very short mean-free-paths.

To find how the heat is carried by phonons with different MFPs, the spectral analysis (cumulative κ_{ph} vs. λ_{ph}) is presented in Fig. 4.3. Note that the scattering parameters are adjusted to match measured κ_{ph} vs. T (Fig. 4.1b) rather than to obtain the same MFP distribution as the MD calculations. Our results are in good agreement with the recent MD simulations [27] - ~50% of the heat conduction is attributed to phonons with MFP > ~1 μm. The reason is that the phonons with MFP > ~1 μm are low-energy acoustic phonons near the Brillouin zone center which don't suffer a lot from umklapp scattering, which compensates for the fact that there is a small percentage of low energy channels. As shown in Fig. 4.1b, the average MFP for bulk Si

($\langle\langle \lambda_{ph} \rangle\rangle = \kappa_{ph} / \left(K_{ph\_BAL} / A \right)$) is about 0.135 μm at room temperature. Therefore the commonly used average MFP does not give a clear picture of which phonons carry the heat since the $\langle\langle \lambda_{ph} \rangle\rangle$ includes a significant number of high energy modes with very small MFPs.

To illustrate the effect of phonon dispersion model, two simple approximations of phonon dispersion are assumed. The first is a Debye model, $\omega = \upsilon_s k$, where υ_s is sound velocity and k is a wave vector, and the second is a sine-type dispersion model, $\omega = \omega_0 \sin\left(\pi k / 2k_0 \right)$, where ω_0 is the maximum phonon frequency and k_0 is the Debye cutoff wave vector.[227] As shown in the inset of Fig. 4.3, κ_{ph} vs. temperature computed from the two simple models almost overlap with the results of full phonon dispersion and match well the measured conductivity. But this requires an increase in the *B* parameter for umklapp scattering by a factor of 4.5 for the Debye model and a factor of 3 for the sine-type model. It can be clearly seen that while the simple phonon models can fit the measured thermal conductivity by adjusting fitting parameters, the MFP distribution of the simple models does not agree well with that of MD simulation. Thus, the question of how phonons with different MFPs carry the heat, which is important to know when designing thermoelectric devices, is not correctly addressed by the simple phonon models.

4.4 In-Plane and Cross-Plane Thermal Conductivity for Thin Films

Having verified that a simple Landauer model with full phonon dispersion accurately reproduces the results of MD simulations [27], we turn next to heat transport in thin Si films. For thin Si films, phonon boundary scattering significantly influences the thermal conductivity. In this section, phonon thermal conductivity of thin Si film layers along the in-plane and the cross-pane direction will be evaluated as a function of Si layer thickness.

For in-plane thermal conduction in thin films, we consider the surface roughness of boundaries with a frequency-dependent specularity parameter. The scattering time reduction due to boundary scattering in the thin film has been examined by a solution of the BTE [28,228] and the corresponding MFP of thin film ($\lambda_{ph,thin}$) compared to that of bulk Si ($\lambda_{ph,bulk}$) was given as

$$\lambda_{ph,thin}(\omega)=\lambda_{ph,bulk}(\omega)\left[1-\frac{3(1-p)}{2\delta}\int_{1}^{\infty}\left(\frac{1}{t^{3}}-\frac{1}{t^{5}}\right)\frac{1-\exp(-\delta t)}{1-p\exp(-\delta t)}dt\right], \tag{4.5a}$$

where $\delta=\left(4/3\right)d_{Si}/\lambda_{ph,bulk}$ with d_{Si} being the thickness of Si thin film, and the specularity parameter p is given by[220]

$$p=\exp\left(-\frac{16\pi^{3}\eta_{SOI}^{2}}{\Lambda_{ph}^{2}}\right), \tag{4.5b}$$

where Λ_{ph} is the wavelength of phonon and η_{SOI} is the roughness of surfaces which was estimated to be between 0.2 to 1 *nm* for SOI wafers.[229] To consider the impact of additional imperfections associated with the SOI wafers such as point defects, stacking faults, and dislocations, we use an approximate formula since it is not clear which type of defect is dominant. The same point defect scattering rate formula used for bulk Si ($\tau_{d}^{-1}=D\omega^{4}$) was used except that the pre-factor, *D,* for SOI film is adjusted to fit the experimental thermal conductivity data of SOI film, yielding that the *D* for SOI film is 2× larger than *D* for bulk Si. (Note that for bulk Si we used the parameter $D = 1.32\times10^{-45}\ s^{3}$ analytically determined from the isotope concentration. [26]) Assuming that the length of conductor, L, is much greater than $\lambda_{ph}\left(\omega\right)$, transport is diffusive and $T_{ph}=\lambda_{ph}\left(\omega\right)/L$ in Eq. (4.2a). For these calculations, we retain the bulk phonon dispersions. The results are shown in Fig. 4.4. Previous experimental data are in good agreement with the calculations, and considering point defects produces a better fit to thicker Si layers in SOI.

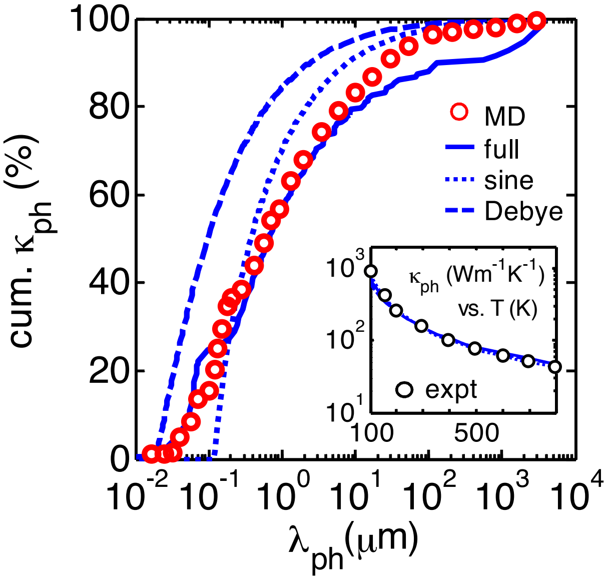

Figure 4.3. We plot the computed cumulative thermal conductivity (κ_{ph}) as a function of the mean-free-path (MFP) for backscattering (λ_{ph}) using three different phonon dispersion models: full phonon dispersion, a sine-type dispersion, and a Debye model. The computed results are compared to the MD simulations obtained from Ref. [[27]]. The MD simulation is plotted while taking into account the difference between a conventional MFP for scattering (l_{ph}) and the MFP for backscattering, i.e. $\lambda_{ph} = (4/3)l_{ph}$. Our results with full phonon dispersion (solid line) is in good agreement with the recent MD simulations,[27] which showed ~50% of the heat conduction is attributed to phonons with MFP > ~1 μm. The MFP distribution is not correctly predicted by a simple sine-type dispersion model (dotted line) or a Debye model (dashed line). Inset: Computed thermal conductivity κ_{ph} vs. temperature is plotted for the three phonon dispersion models and is compared to experiment.[26] Note that regardless of the phonon dispersion model used, we can fit well the experimental data by adjusting scattering parameters.

Next, we examine the cross-plane phonon thermal conductivity of thin Si film layers. For cross-plane thermal transport in thin films of thickness less than ~1 μm, quasi-ballistic transport becomes important. Therefore, the assumption of diffusive transport no longer holds. The cross-plane thermal conductivity is conventionally computed with the BTE by including a phonon-boundary scattering time. For example, $\tau_b = L/(2v)$ [222–224] is commonly used, but the physical significance is unclear. In contrast to the previous work, we have included only scattering processes within the thin film – no interface resistances are considered. In a Landauer picture, we are assuming ideal reflection-less contacts at the top and bottom of the film, so our calculations will provide an upper limit that does not consider the interface resistances that may occur in practice. For the transmission, the expression, $T_{ph} = \lambda_{ph}(\omega) / (L + \lambda_{ph}(\omega))$, is used to describe quasi-ballistic transport.

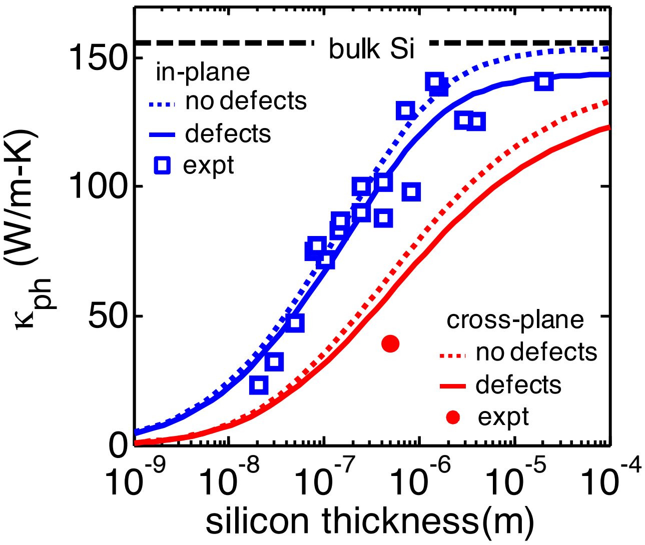

Figure 4.4. Thermal conductivity (κ_{ph}) vs. silicon layer thickness at room temperature is plotted. In-plane experimental data[28–31] and calculations are shown by open squares and by blue lines, respectively. For our calculations, a surface roughness of 0.5 *nm* is used, which is a typical value for SOI wafers. We assume that the point defect scattering rate for SOI wafer is 2× larger than that of bulk Si. The results with the point defects (blue solid line) give a better fit for thicker Si layers. The cross-plane experimental data[32] and calculations are shown by filled circle and by red lines, respectively. It is assumed that the $M_{ph}(\omega)$ for the thin film is the same as that for bulk Si.

Figure 4.4 shows our calculation of the cross-plane thermal conductivity which is defined as $\kappa_{ph} = K_{ph}(L/A)$ compared to a recent experimental observation.[32] In agreement with the one available measurement,[32] our calculations show a much reduced thermal conductivity in the cross-plane. This result occurs even though we have not included possible interface resistances and can be understood from Eq. (4.3a). In the ballistic limit, the effective mean-free-path approaches the thickness of the film. Note that a better fit for the cross-plane measurement could be obtained by increasing the parameter, *D,* in the point defect scattering rate formula (we used the same *D* as for the in-plane calculation, 2× larger than *D* for bulk Si), but the comparison to experiment is clouded by uncertainties in possible interface resistances. Nevertheless, the calculation shows the reduction in thermal conductivity that should be expected for the thin film itself.

Next, we turn to the question of which phonons play the dominant role in the heat conduction in thin films. Figure 4.5 is a plot of $\lambda_{50\%}$ and $\left\langle\left\langle \lambda_{ph} \right\rangle\right\rangle_{eff}$ vs. thickness of thin Si films at room temperature along the in-plane and the cross-plane transport directions. Here, $\lambda_{50\%}$ is the MFP at which the cumulative κ_{ph} is equal to 50%, and the average MFP, $\left\langle\left\langle \lambda_{ph} \right\rangle\right\rangle_{eff}$, is extracted according to Eq. (4.3d). The cross-plane direction displays about 2× smaller $\lambda_{50\%}$ and $\left\langle\left\langle \lambda_{ph} \right\rangle\right\rangle_{eff}$ than the in-plane direction. It can be also seen that $\left\langle\left\langle \lambda_{ph} \right\rangle\right\rangle_{eff}$ is always less than $\lambda_{50\%}$ for the same reason as for the bulk - $\left\langle\left\langle \lambda_{ph} \right\rangle\right\rangle_{eff}$ places too much emphasis on the high energy modes with very small MFPs. However, the difference between $\left\langle\left\langle \lambda_{ph} \right\rangle\right\rangle_{eff}$ and $\lambda_{50\%}$ decreases as the thickness of the thin film decreases. This occurs for both in-plane and cross-plane conduction, but for different reasons. For cross-plane conduction, as the thickness of thin films (i.e. *L* in Eq. (4.1b)) decreases, the transmission T_{ph} in Eq. (4.1b) for phonons with short MFPs increases more rapidly than that for phonons with large MFPs. This results in a decrease of $\lambda_{50\%}$. For in-plane conduction, low-energy acoustic phonons, which have large MFPs ($\lambda_{ph} >\sim 1\ \mu m$) leading to the large $\lambda_{50\%}$ values in the bulk, suffer a lot from boundary scattering in thin films with thickness $< 1\ \mu m$, and therefore the $\lambda_{50\%}$ decreases rapidly with film thickness. Finally, we note that for the in-plane direction, about 50% of the heat conduction is carried by phonons with a mean-free-path greater than the thickness of the thin film when the thickness is smaller than ~0.2 μm.

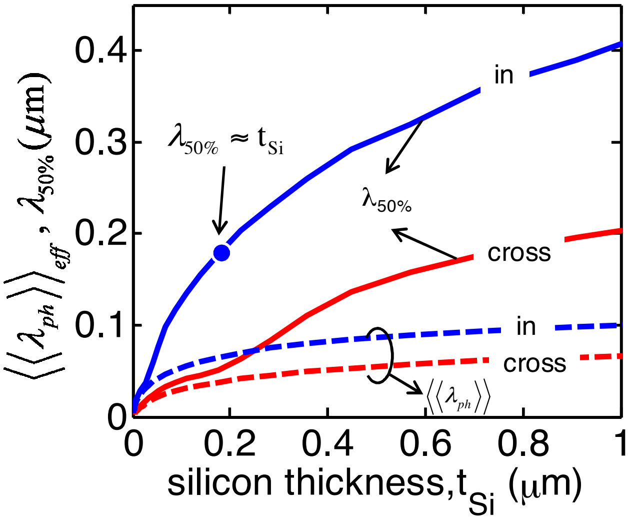

Figure 4.5. Along the in-plane (in) and the cross-plane (cross) transport directions, $\lambda_{50\%}$ and $\langle\langle\lambda_{ph}\rangle\rangle_{eff}$ are plotted as a function of the thickness of the thin Si films at room temperature. Here, $\lambda_{50\%}$ is the mean-free-path (MFP) at which the cumulative thermal conductivity (κ_{ph}) is equal to 50%, and the average MFP, $\langle\langle\lambda_{ph}\rangle\rangle_{eff}$, is obtained from Eq. (4.3d). The cross-plane direction displays about 2× smaller $\lambda_{50\%}$ and $\langle\langle\lambda_{ph}\rangle\rangle_{eff}$ than the in-plane direction. $\langle\langle\lambda_{ph}\rangle\rangle_{eff}$ is always less than $\lambda_{50\%}$ since $\langle\langle\lambda_{ph}\rangle\rangle_{eff}$ places too much emphasis on the high energy modes with very small MFPs. Note that for the in-plane direction, about 50% of the heat conduction is carried by phonons with a mean-free-path greater than the thickness of the thin film when the thickness is smaller than ~0.2 μm (blue symbol).

4.5 Discussion

So far, we have applied the Landauer approach to diffusive transport in bulk materials and thin films along the in-plane direction as well as to quasi-ballistic transport in thin films along the cross-plane direction. Although the BTE with an additional boundary scattering (τ_b) succeeds in modeling the bulk and thin film experiments, including τ_b cannot accurately describe the ballistic limit (i.e. the Casimir limit, $q = \sigma\left(T_H^4 - T_C^4\right)$) for which Majumdar used the equation of phonon radiative transfer

(EPRT).[225] In this section, we show that the Landauer approach reduces to the Casimir limit under the appropriate conditions. We also relate the MFP for backscattering in the Landauer model to the commonly used MFP for scattering and discuss some limitations of the Landauer approach.

In the ballistic limit ($T_{ph} = 1$) and at a temperature much lower than the Debye temperature where $M_{ph}(\omega)$ is given as $M_{ph}(\omega) = A\left(3\omega^2/4\pi\upsilon_s^2\right)$ with υ_s being the velocity of sound. The heat flux (q) can be expressed from Eq. (4.1) for a small temperature gradient (ΔT) as

$$q = \frac{I_Q}{A} = \frac{1}{h}\int_0^\infty d\left(\hbar\omega\right)\left(\frac{3\omega^2}{4\pi\upsilon_s^2}\right)\hbar\omega\left(\frac{dn}{dx}\frac{\partial x}{dT}\Delta T\right), \tag{4.6a}$$

where $n = 1/(e^x - 1)$ and $x \equiv \hbar\omega/k_B T$. Using $\int_0^\infty x^4\left(-dn/dx\right)dx = 4\pi^4/15$, the heat flux of Eq. (4.6a) is given as

$$q = \sigma\Delta\left(T^4\right), \tag{4.6b}$$

where $\sigma = \pi^2 k_B^4/40\hbar^3\upsilon_s^2$ is the Stefan-Boltzmann constant for phonons.[123] This result shows that the Landauer approach correctly reduces to the Casimir result in the ballistic limit with the Debye approximation. Majumdar[225] showed that the Casimir limit can be also obtained from the EPRT and that the use of the Fourier law causes significant errors for conduction across the film. The EPRT, however, does not accurately predict the thermal conductivity reduction for both the in-plane and the cross-plane conduction of Si thin films[222] due to the gray approximation. Finally, note that more generally, for temperatures above the Debye temperature, the ballistic heat flux is $q = \left(K_{ph\_BAL}/A\right)\Delta T$, where the ballistic thermal conductance is given by Eq. (4.3c).

It was also shown from the EPRT[225] with the gray approximation that the Fourier law can be used for all transport regimes if the effective mean-free-path for scattering, $\langle\langle l_{ph}\rangle\rangle_{eff}$, is used instead of the commonly used average MFP for scattering $\langle\langle l_{ph}\rangle\rangle$. According to Eq. (44) in Ref. [225]:

$$\left\langle\left\langle l_{ph}\right\rangle\right\rangle_{eff} = \frac{\left\langle\left\langle l_{ph}\right\rangle\right\rangle}{1+(4/3)\left(\left\langle\left\langle l_{ph}\right\rangle\right\rangle/L\right)}, \tag{4.7a}$$

where the $\left\langle\left\langle l_{ph}\right\rangle\right\rangle$ is the average MFP for scattering that can be obtained from a classical kinetic theory (i.e. $\kappa_{ph} = (1/3)C_V \upsilon_s \left\langle\left\langle l_{ph}\right\rangle\right\rangle$ with C_V being the specific heat). A physical interpretation of Eq. (4.7a), however, was not given: For example, where does the value of 4/3 in the denominator come from? We can easily show that Eq. (4.7a) follows directly from Eq. (4.3b) of the Landauer approach. Using Eq. (4.4) in Eq. (4.7a) to convert from MFP to MFP for backscattering, we find

$$\left\langle\left\langle \lambda_{ph}\right\rangle\right\rangle_{eff} = \left(\frac{1}{\left\langle\left\langle \lambda_{ph}\right\rangle\right\rangle} + \frac{1}{L}\right)^{-1}, \tag{4.7b}$$

which is precisely the Landauer result if we make the gray approximation, $\left\langle\left\langle T_{ph}\right\rangle\right\rangle = \left\langle\left\langle \lambda_{ph}\right\rangle\right\rangle / \left(L + \left\langle\left\langle \lambda_{ph}\right\rangle\right\rangle\right)$.

The value of 4/3 in Eq. (4.7a) comes from the difference between the MFP for scattering and the MFP for backscattering, The usual definition of mean-free-path is the average distance that a carrier travels before scattering. In the Landauer approach, $\lambda_{ph}(\omega)$ is the mean-free-path for backscattering and has a specific meaning; it is the length at which the transmission $T_{ph} = \lambda_{ph}(\omega)/\left(L + \lambda_{ph}(\omega)\right)$ drops to one-half, and the inverse of the $\lambda_{ph}(\omega)$ is interpreted as the probability per unit length that a positive flux is converted into a negative flux. Following the proper definition of $\lambda_{ph}(\omega)$,[3] it can be shown that in 1D, $\lambda_{ph}(\omega) = 2l_{ph}(\omega)$, in 2D, $\lambda_{ph}(\omega) = (\pi/2)l_{ph}(\omega)$, and in 3D, $\lambda_{ph}(\omega) = (4/3)l_{ph}(\omega)$.

We have shown that the Landauer approach provides a simple but physically insightful description of diffusive transport, quasi-ballistic transport, and ballistic transport, but it does have limitations. For example, for problems like cross-plane thermal transport, we made the assumption of ideal contacts (i.e. that are reflection-less and that maintain a near-equilibrium thermal population of phonons.) The role of contacts is problem-specific and should be considered on a case-by-case basis. Problems involving space and time dependent transport and multi-dimensional transport tend to be easier to handle with the Boltzmann equation, but for 1D, steady-state transport, the Landauer approach provides significantly more physical insight as well as computational advantages in computing the transport distribution (or number of channels, $M(\omega)$).

4.6 Summary and Conclusion

In this chapter, we showed that a simple Landauer model in the diffusive limit with a full phonon dispersion reproduces the results of more sophisticated molecular dynamics simulations of phonon transport in bulk Si. For thin Si films, the same approach also accurately describes the measured in-plane (diffusive transport) and cross-plane (quasi-ballistic transport) thermal conductivity, κ_{ph} vs. thickness of the Si layer. The spectral analysis of cumulative thermal conductivity as a function of a mean-free-path (MFP) demonstrates that the commonly used average MFP should be used with caution because it does not convey which phonons mainly contribute to the heat conduction. In the ballistic limit and with the Debye approximation, the Landauer model yields the Casimir limit, the blackbody radiation law for phonons. The results presented here shed new light on phonon transport in Si structures and also show that the Landauer approach provides a simple and useful computational approach that gives new insights into phonon transport from the ballistic to diffusive regimes in both nanostructures and bulk materials.

5. ON THE BEST BANDSTRUCTURE FOR THERMOELECTRIC PERFORMANCE: A LANDAUER PERSPECTIVE

The contents of Chapter 5 have been extracted and revised from the following publication: C. Jeong, R. Kim, and M. Lundstrom, "On the Best bandstructure for thermoelectric performance: A Landaer Perspective," *J. Appl. Phys.* 111, 113707(2012)

In this chapter, the question of what bandstructure produces the best thermoelectric device performance is revisited from a Landauer perspective. We find that a delta-function transport distribution function (TDF) results in operation at the Mahan-Sofo upper limit for the thermoelectric figure-of-merit, *ZT*. We show, however, the upper limit itself depends on the bandwidth (BW) of the dispersion, and therefore a finite BW dispersion produces a higher *ZT* when the lattice thermal conductivity is finite. Including a realistic model for scattering profoundly changes the results. Instead of a narrow band, we find that a broad BW is best. The prospects of increasing *ZT* through high valley degeneracy or by distorting the density-of-states are discussed from a Landauer perspective. We conclude that while there is no simple answer to the question of what bandstructure produces the best thermoelectric performance, the important considerations can be expressed in terms of three parameters derived from the bandstructure – the density-of-states, $D(E)$, the number of channels, $M(E)$, and the mean-free-path, $\lambda(E)$.

5.1 Introduction

The performance of thermoelectric (TE) devices is related to a dimensionless figure of merit, ZT,

$$ZT = \frac{S^2 \sigma T}{\kappa_{ph} + \kappa_{el}}, \tag{5.1}$$

where S is the Seebeck coefficient, σ the electrical conductivity, κ_{ph} the lattice thermal conductivity, and κ_{el} the electronic thermal conductivity. Early work developed TE technology with a figure of merit of about one,[33] but subsequent progress was stalled for several decades. Recent progress has, however, been significant, and there are now several reports of ZT's above one,[230] which have been largely achieved by reducing the lattice thermal conductivity, which dominates the denominator of eqn. (1). Figure 5.1 is a plot of ZT vs. $\kappa_{tot}(=\kappa_{ph}+\kappa_{el})$ for several different TE materials including recent materials with $ZT > 1$.[1–12,15–22] Also shown (dashed line) is the result that would be obtained if the power factor ($S^2\sigma$) of each material were the same as that of silicon. The conclusion is that the performance of a thermoelectric material is largely determined by its thermal conductivity. The power factors of good TE materials are all similar. This raises the question of what controls the magnitude of the power factor and provides an opportunity to further increase ZT by power factor engineering. This paper addresses the question: "How is the electronic structure of a material related to its power factor?"

For conventional TE materials with approximately parabolic energy bands, the power factor is well understood.[231,232] High power factors require high mobility to increase σ, and ionized impurity scattering should dominate to enhance S.[232] In a seminal paper, Mahan and Sofo asked the question: "What shape of a bandstructure would produce the highest thermoelectric performance?" They concluded that materials with a δ-function "transport distribution function," (TDF) would be best.[204] Subsequently, Nishio and Hirano[233] showed that in the absence of thermal conduction by the lattice, a single energy channel leads to "electronic efficiencies" at the Carnot

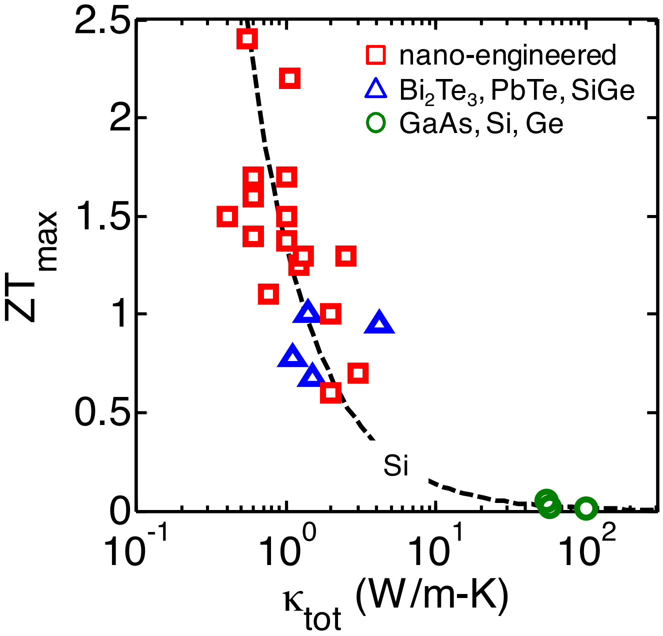

Figure 5.1. The maximum ZT vs. total κ. Conventional semiconductors used in IC industry (circle): Si 300K,[1,2] Ge 300K,[3] GaAs 300K [4]; bulk TE materials used in TE devices (triangles): Bi_2Te_3 300K,[5] $Bi_xSb_{2-x}Te_3$ 300K,[6] $Si_{80}Ge_{20}$ 1275K,[7] PbTe 300K [8]; nano-engineered materials (square): Si nanowire (NW) 300K,[9] Si NW 200K,[10] Bi_2Te_3/Sb_2Te_3 superlattice (SL) 300K,[11] PbTe/PbSeTe quantum dot (QD) SL 300K,[12] Tl-PbTe 773K,[8] $Na_{1-x}Pb_mSb_yTe_{2+m}$ 650K,[15] $Pb_xSn_{1-x}Te$-PbS 642K,[16] $AgPb_mSbTe_{m+2}$ 800K,[17] PbSbTe 700K,[18] p-PbTe-SrTe 800K,[19] Bi_2Te_3 300K,[20] $Bi_xSb_{2-x}Te_3$ 475K,[6] n-$Si_{80}Ge_{20}$ 1275K,[7] Si 1275K,[1] n-LaTe 1273K,[21] n-$Yb_xCo_4Sb_{12+y}$ 800K.[22] The dashed line is the ZT that would be obtained if the power factor of each material were the same as that of silicon.

limit. Similar conclusions were reached by Humphrey and Linke.[234] In a recent paper, Nakpathomkun, *et al*. argued that the power delivered to a load is the important measure of performance and that for such purposes, ZT is not the best figure of merit.[235] Nakpathomkun concluded that the TDF should have a finite bandwidth (BW ~2.25 k_BT) for maximum power output, although the maximum efficiency (for $\kappa_{ph} = 0$) still occurs for a δ-function TDF. The "best bandstructure question" has also been explored recently by Fan *et al*.[236] who concluded that for a normalized TDF (i.e. the area under the TDF vs. energy curve is bounded), the δ-function TDF is best, but for a bounded TDF (the maximum value is limited), a narrow, but finite width of the TDF is best. Very recently, Zhou, *et al*. considered the optimal BW question and concluded that the existence of an optimal BW depends strongly on the scattering model used.[237] Finally, we note the recent experiments reporting improved TE performance in materials with a resonant level[8] and in PbTeSe alloys that display a high degree of valley degeneracy,[238] which increases the density-of-states, $D(E)$, near the Fermi level.

To continue to increase performance of thermoelectric materials, the electronic performance must be enhanced.[230,239] Previous has clarified several of issues, but a number of questions remain:

1) What physical constraints should be placed on the TDF?

   Before we explore the best bandstructure question, the physical constraints to be placed on the TDF must be clarified.

2) How does the BW of the TDF affect TE performance?

   Under what conditions is a δ-function TDF the best and under what conditions is a narrow band the best? When a narrow band is best, what determines the optimum BW? Finally, how do these results relate to Mahan and Sofo's original arguments?

3) How does scattering affect optimum bandstructure?
4) How should the improved performance of materials with a high valley degeneracy[238] or with a resonant energy levels[8] that distort the density-of-states be understood?
5) Is there a best bandstructure for TE performance?

Our goal in this paper is to answer these questions. We use a Landauer approach, which is equivalent to the Boltzmann Transport Equation for crystalline semiconductors in the diffusive limit but has advantages of mathematical simplicity and physical transparency. This is most apparent with regard to the so-called transport distribution, a central quantity in thermoelectric theory[204] whose physical interpretation is unclear. In the Landauer approach, the transport distribution acquires a clear physical interpretation – it is proportional to the number of channels available for conduction times the mean-free-path (MFP) for backscattering, which makes it easy to identify the appropriate physical constraints to place on the TDF.

Following Nakpathomkun, *et al.*[28], we shall assess thermoelectric performance using two different metrics: 1) the maximum thermoelectric efficiency and 2) the maximum power that a thermoelectric generator delivers to a load. The first is of theoretical interest and the second of practical interest. As discussed in the Appendix F, as *ZT* approaches infinity, the maximum thermoelectric efficiency approaches the Carnot efficiency, but the efficiency when the maximum power is delivered to a load approaches one-half of the Carnot limit, the so-called Curzon-Ahlborn limit.[240] Both operating conditions will be considered.

The paper is organized as follows. Section 5.2 summarizes the approach. The expressions presented are those of standard thermoelectric theory with only one difference – the transport distribution is expressed in Landauer form. Section 5.3 is a short discussion of the single energy case (a δ-function TDF). This section sets the stage for understanding the subsequent results and relates this paper to some previous studies. Section 5.4 is a short discussion of one-dimensional (1D) thermoelectrics. The simplicity of the 1D problem provides a clear illustration of how the number of channels for conduction, $M(E)$, is related to the density-of-states, $D(E)$ and allows us to address question 1) above. Question 2) is discussed in Secs. 5.4 and 5.5. Section 5.5 examines how the BW of the dispersion affects TE performance, extending the analysis of Sec. 5.4 to three-dimensional (3D) thermoelectrics. In Sec 5.6, it is shown that the conclusion of Mahan and Sofo is correct, if properly understood. Section 5.7 is a discussion of scattering and addresses question 3), and Secs. 5.8 and 5.9 address question 4). The paper's conclusions are summarized in Sec. 5.10, where our perspective on question 5) is presented.

5.2 Approach

We begin with a brief review of the Landauer approach[164] to TE transport. The TE transport parameters are[3,204]

$$\sigma = \int_{-\infty}^{+\infty} dE \sigma'(E), \tag{5.2a}$$

$$S = \left(\frac{k_B}{q}\right)\int_{-\infty}^{+\infty} dE\left(E - E_F\right)\frac{\sigma'(E)}{\sigma}, \tag{5.2b}$$

$$\kappa_0 = T\left(\frac{k_B}{q}\right)^2 \int_{-\infty}^{+\infty} dE\left(E - E_F\right)^2 \sigma'(E), \tag{5.2c}$$

$$\kappa_{el} = \kappa_0 - S^2\sigma T, \tag{5.2d}$$

where E_F is the Fermi level, and $\sigma'(E)$ is the so-called differential conductivity. For 3D bulk diffusive materials,

$$\begin{aligned} \sigma'(E) &= \frac{2q^2}{h}\left(\frac{M(E)}{A}\right)\lambda(E)\left(-\frac{\partial f_0}{\partial E}\right) \\ &= q^2\Sigma(E)\left(-\frac{\partial f_0}{\partial E}\right), \end{aligned} \tag{5.3}$$

where $2q^2/h$ is the quantum of conductance, $M(E)$ is the number of conducting channels at a given energy, E, A is the cross-sectional area, $\lambda(E)$ is the mean-free-path for backscattering, and f_0 is the Fermi-Dirac distribution. In eqn. (5.3), $\Sigma(E)$ is the so-called transport distribution function (TDF), which arises from a solution to the Boltzmann Transport Equation.[204] The TDF depends on both bandstructure and scattering. In the Landauer approach, $\Sigma(E)$ is proportional to the product of $M(E)$, which depends only on bandstructure and $\lambda(E)$, which depends on bandstructure and the scattering physics. For semiclassical transport in the diffusive limit, the Boltzmann and Landauer approaches are mathematically identical; we use the Landauer approach in this paper because it provides a simple and clear physical interpretation of the TE transport distribution function.

Given a bandstructure, $E(k)$, $M(E)$ is easily obtained by simply counting the bands that cross the energy of interest.[3] For the purposes of this paper, we seek a simple, but realistic bandstructure model that gives $E(k)$ across the entire Brillouin zone (BZ) and for which the BW of the dispersion can be varied from broad to narrow in order to explore the effects of bandwidth on the TE coefficients. A simple, nearest neighbor tight-binding (TB) model,

$$E(k) = 2t_0(1-\cos k_x a) + 2t_0(1-\cos k_y a) + 2t_0(1-\cos k_z a), \tag{5.4}$$

will be used. In eqn. (5.4), $t_0 = \hbar^2/2m_e a^2$ with a and m_e being the lattice constant and the effective electron mass, respectively. The bandwidth (BW) of the electron dispersion is $12t_0$. We change the BW while assuming $a = 5\times 10^{-10}\,\mathrm{m}$, which keeps the total number of states fixed. It is important to note that the TB model gives $E(k)$ across the entire BZ and that we do not assume parabolic energy bands (i.e. $E(k) \neq \hbar^2 k^2/2m_e$). In the case of a large BW, however, only states near the bottom of the band, which is nearly parabolic, are occupied, and we recover the expected results for parabolic energy bands. For the small BW case, however, the TDF approaches a δ-function, and much different results are obtained. Because the TDF is derived from a physically sensible dispersion, no artificial constraints are placed on the TDF.

5.3 Single Energy Case

We begin with a short discussion of the single energy case (a δ-function TDF), which has received a good deal of attention and forms one end of the spectrum of BWs that we will explore. When all the channels are at $E = E_0$, $M(E) = M_0\delta(E-E_0)$, and the differential conductivity becomes $\sigma'(E) = \sigma_0\delta(E-E_0)$. In this case, the thermoelectric coefficients become

$$\sigma = \sigma_0, \tag{5.5a}$$

$$S = \left(-\frac{k_B}{q}\right)\left(\frac{E_0 - E_F}{k_B T}\right), \tag{5.5b}$$

$$\kappa_0 = T\left(\frac{k_B}{q}\right)^2\left(\frac{E_0 - E_F}{k_B T}\right)^2 \sigma_0, \tag{5.5c}$$

$$\kappa_{el} = \kappa_0 - S^2\sigma_0 T = 0. \tag{5.5d}$$

Here, with a constant MFP (λ_0) being assumed, σ_0 is found to be

$$\sigma_0 = \frac{2q^2}{h}\left(\frac{M_0\lambda_0}{k_BT}\right)\frac{e^{\eta_F}}{\left(1+e^{\eta_F}\right)^2}, \tag{5.5e}$$

where $\eta_F = (E_F - E_0)/k_BT$ and $\eta_F \approx \pm 2.4$ for the maximum power factor. The result, (5e), agrees with Mahan and Sofo[204] but not with Zhou *et al.*[237] who found $\sigma_0 = 0$.

For the single energy case, the electronic heat conductivity, κ_{el}, is zero. This occurs because κ_{el} defines the heat flow under open-circuit conditions. If all the current flows at $E = E_0$, then zero current means that no electrons are flowing, so there can be no heat current. For the single energy case,

$$\frac{\kappa_{el}}{\sigma} = LT = 0, \tag{5.5f}$$

which shows that the Lorenz number, *L*, is zero. For a parabolic energy band under strongly degenerate conditions, $L = \left(\pi^2/3\right)\left(k_B/q\right)^2$, but we shall see that as the BW of the dispersion decreases, *L* decreases and approaches eqn. (5.5d) in the limit of zero bandwidth.

5.4 One-dimensional Analysis

Here, we illustrate how the number of conducting channels, $M(E)$, is related to the density-of-states, $D(E)$, by using a simple 1D example that illustrates the physical constraint that should be imposed on the TDF. Figures 2a and 2b show a plot of the 1D dispersion, $E(k) = 2t_0(1-\cos k_x a)$, and the corresponding $D(E)$ for BWs of ~0.1 and ~0.6 *eV*. At a given energy, *E*, the number of states that participate in transport is the number of conducting channels, $M(E)$, which is often referred to as the number of (transverse) modes in analogy with the modes of an electromagnetic waveguide. Given an accurate dispersion, $M(E)$ can be readily computed by counting the bands that cross the energy of interest[3] and is shown in Fig. 5.2c. It can be seen that although the $D(E)$ goes to infinity, $M(E)$ remains bounded, independent of bandwidth. (Zhou *et* *al*.[237] also pointed out that while $D(E) \rightarrow \infty$, $\Sigma(E)$ remains finite.) Note that $\int D(E)dE$ is independent of bandwidth because we fix the total number of states, but it is the peak value of $M(E)$ that is independent of bandwidth, not $\int M(E)dE$. This 1D example demonstrates that the answer to the first question posed in Sec. I is that for a given dispersion, the maximum of $M(E)$ is fixed. Fixing the electrical conductivity when varying the BW[234] or fixing the area under TDF vs. *E*[236] lead to non-physical results.

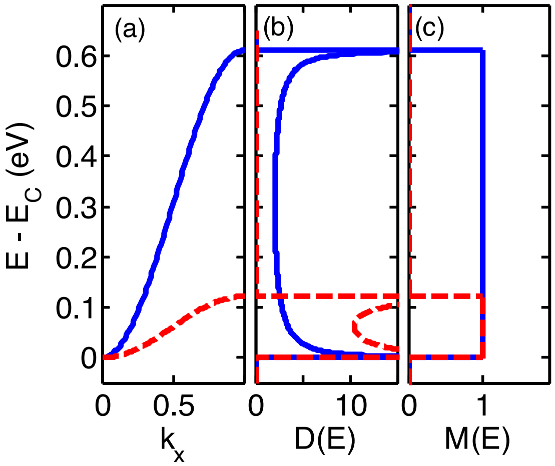

Figure 5.2. (a) The 1D dispersion, $E(k) = 2t_0(1-\cos k_x a)$ with two different bandwidth (BW) of a dispersion, ~0.1 (dashed line) and ~0.6 *eV* (solid line). k_x is displayed in the units of π/a. (b) The corresponding the density-of-states, $D(E)$, in the units of $eV^{-1}nm^{-1}$ and (c) the number of conducting channels, $M(E)$, which represent the number of states that participate in transport at a given energy *E*. Note that although the $D(E)$ goes to infinity, $M(E)$ remains bounded independent of bandwidth.

The counting bands method can be extended to the two-dimensional (2D) and the three-dimensional (3D) cases. The 1D procedure is repeated for each transverse wave vector so that the entire BZ of the material is spanned. The resulting number of conducting channels is integrated over transverse momentum at a given energy to find the

$M(E)$. This method is used next in 3D. Finally, we also note that while not obvious, $M(E)$ is related to the density-of-states according to[3]

$$M(E) = \frac{h}{2}\left\langle \upsilon_x^+(E) \right\rangle D(E), \tag{5.6}$$

where $\left\langle \upsilon_x^+(E) \right\rangle$ is the average velocity in the direction of transport at energy, E, and $D(E)$ is the density of states per spin. The density of states is per unit length in 1D, per unit area in 2D, and per unit volume in 3D. The number of channels is a number in 1D, a number per unit width in 2D and per unit area in 3D, where the width and cross sectional area are normal to the direction of current flow.

5.5 Three-dimensional Analysis: Constant Mean-free-path

In this section, we extend our analysis to 3D and evaluate the TE coefficients at T = 300 K to address question 2). The BW of the dispersion is varied from very narrow to very wide while assuming a constant MFP. Figure 5.3 shows the computed density-of-states, $D(E)$, and number of channels, $M(E)$, for small and large BW dispersions. The $M(E)$ characteristics display a peak value of ~0.6 times the number of atoms in the cross section – independent of bandwidth. As was observed for 1D, the total number of states (area under the $D(E)$ curve) is independent of BW but the area under the $M(E)$ curve depends on BW. Finally, Fig. 5.3 also shows that the parabolic band assumption (dashed line) matches the full-band TB results (solid line) only near the bottom of the band where $D(E) \propto E^{1/2}$ and $M(E) \propto E$.[3]

Next, TE performance for 3D bulk is assessed for two different conditions: 1) the maximum TE efficiency and 2) the maximum power that a thermoelectric generator delivers to a load.[204] The load resistance and the location of the Fermi level are co-optimized in order to extract the maximum efficiency or the maximum power output. For each of the two different operating conditions, the efficiency and power output are calculated as a function of the BW.

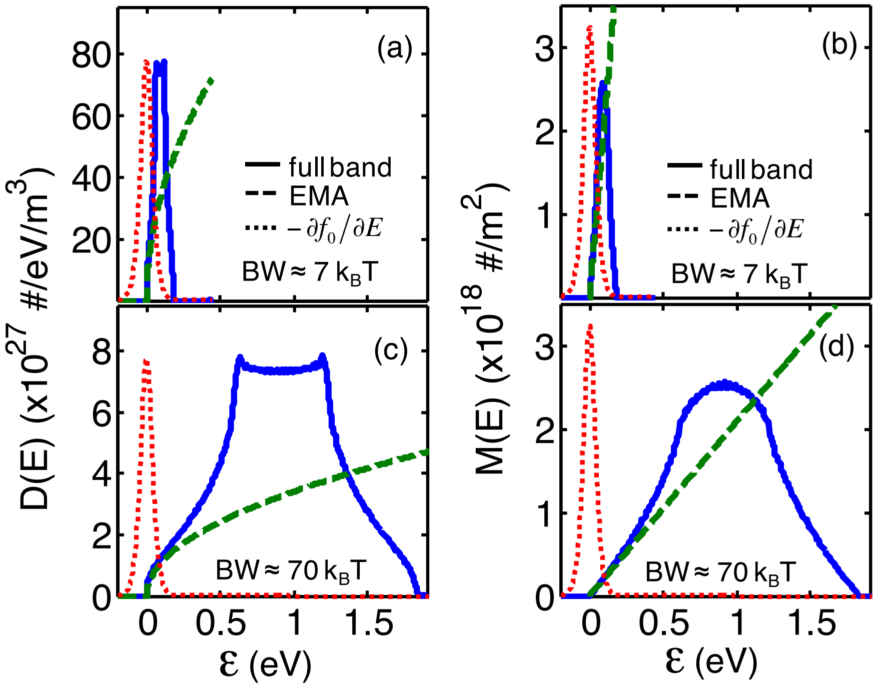

Figure 5.3. (a,c) The 3D density-of-states, $D(E)$, for the narrow and the broad bandwidth (BW) bands. (b,d) The number of conducting channels, $M(E)$, for the narrow and the broad BW bands. Full-band calculations (solid line) are compared to effective mass approximation (EMA, dashed line). Based on the EMA, $D(E) = m_e\sqrt{2m_e(E-E_C)}/2\pi^2\hbar^3$ and $M(E) = m_e(E-E_C)/2\pi\hbar^2$, where E_C is the band edge. Fitted effective masses (m_e) at the bottom of band are $m_e = m_0$ for the broad band and $m_e = 10m_0$ for the narrow band, where m_0 is the electron rest mass. It is seen that the $D(E)$ and the $M(E)$ obtained from parabolic band assumption (dashed line) match well the full-band TB results (solid line) only at the bottom of the band. Dotted line is the arbitrarily normalized " window function", $W = (-\partial f_0/\partial E)$, where f_0 is Fermi-Dirac distributions. For horizontal axis, $\varepsilon = E - E_C$ for $D(E)$ and $M(E)$ and $\varepsilon = E - E_F$ for $W = (-\partial f_0/\partial E)$ where E_F is the Fermi level. We assumes $E_C = E_F$ which is a typical condition for optimum performance.

We first evaluate TE performance for zero lattice thermal conductivity, $\kappa_{ph} = 0$, and the results are shown in Fig. 5.4a where the TE efficiency is normalized by the Carnot efficiency, η_C. For this case, the maximum power output is obtained for a moderate BW band, but the maximum efficiency occurs for a δ-function like narrow band. In agreement with Nakpathomkun,[235] we find that as the TDF (or $M(E)$) approaches a δ-function, the maximum efficiency approaches the Carnot efficiency, but no useful power can be delivered to a load. However, the δ-function TDF does produce a finite power under maximum power conditions with an efficiency of one-half the Carnot efficiency, the Curzon-Ahlborn limit.[240]

Figure 5.4b shows the results with the more realistic case, i.e. a finite κ_{ph} = 0.5 W/m-K, which is about 2~3 times smaller than the lattice thermal conductivity of Bi_2Te_3. In contrast to the case of $\kappa_{ph} = 0$, the maximum efficiency now occurs for a moderate BW, instead of for the narrowest BW. Note that the maximum power occurs for a moderate BW for both zero and finite κ_{ph}. If we repeat the calculations using a smaller (larger) value of κ_{ph}, we find only a slight decrease (increase) in the optimum BW. Next we discuss how the BW affects the four TE transport parameters.

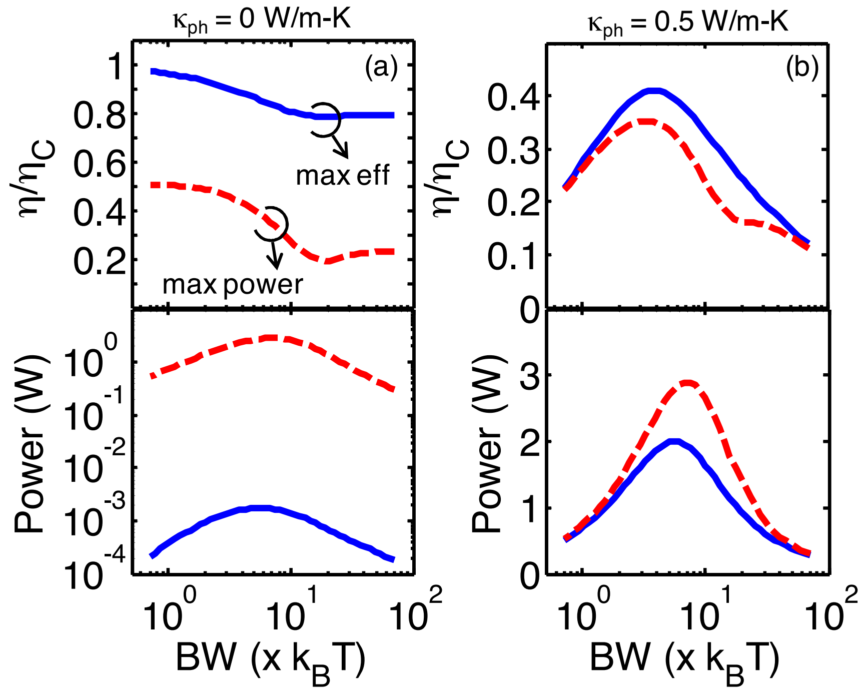

Figure 5.4. Efficiency normalized by Carnot efficiency η_C (upper panel) and power for (a) zero lattice thermal conductivity, $\kappa_{ph} = 0$, and (b) a finite lattice thermal conductivity, $\kappa_{ph} = 0.5$ W/m-K are plotted as a function of the bandwidth (BW). Efficiency and power are evaluated from two different perspectives. Solid line: condition for the maximum thermoelectric efficiency. Dashed line: condition for the maximum power that a thermoelectric generator delivers to a load. The load resistance and the location of the Fermi level are co-optimized in order to extract the maximum efficiency or the maximum power output.

The TE coefficients assuming zero lattice thermal conductivity, $\kappa_{ph} = 0$, are shown in Fig. 5.5. For each value of the BW, we found the optimal location of the Fermi level to maximize *ZT*. As the BW decreases, *ZT* diverges. Therefore, the highest *ZT* and efficiency is obtained for a δ-function like band. As seen in Fig. 5.5b and 5.5c, this occurs mainly because as the BW approaches zero, κ_{el} approaches zero while σ approaches a finite value, eqn. (5.5e), and therefore the Lorenz number, *L*, approaches zero as discussed in Sec. 5.3. For the large BW case, Fig. 5.5b shows that we obtain the expected results for a parabolic energy band, i.e. for large BWs, *L* saturates at a value slightly above 2. Recall that for a parabolic energy band under strongly degenerate conditions, $L/(k_B/q)^2 = \pi^2/3$ and for non-degenerate conditions with a constant MFP, $L/(k_B/q)^2 = 2$. The Wiedemann-Franz "law" states that there is a relation between the electrical conductivity and the electronic component of the thermal conductivity, but the specific value of the *L* depends on bandstructure, scattering, and the location of the Fermi level. As noted by Mahan and Bartkowiak,[241] it should be regarded as a "rule of thumb" rather than a law.

In contrast to the case of $\kappa_{ph} = 0$, Fig. 5.6a shows that the highest *ZT* occurs for a moderate BW when $\kappa_{ph} = 0.5$ W/m-K. As seen in Fig. 5.6b, for this case, the optimum BW for highest *ZT* is mainly determined by the BW dependence of the power factor rather than that of the *L*. Figure 5.6c shows that the BW has a strong effect on σ, but it has a rather small effect on *S*. The stronger variation of σ vs. BW than that of *S* vs. BW explains the shape of the power factor vs. BW characteristic in Fig. 5.6b.

The results shown in Fig. 5.6 can be understood in terms of the width of the Fermi "window function," $(-\partial f_0/\partial E)$, and the distribution of conducting channels, as plotted in Fig. 5.3a. The width of the Fermi window function is a few k_BT, so when the bandwidth of the dispersion is less that this value, σ decreases. The optimum BW for σ occurs when the width of the Fermi window matches the BW of $M(E)$. As the BW of the dispersion increases, the channels are more spread out, so given the finite width of the Fermi window function, a decreasing fraction of the channels can participate in electrical conduction, and σ decreases. Note that the peak of κ_{el} occurs for a somewhat larger BW than that of σ because of the $(E - E_F)^2$ factor in eqns. (5.2d-e).

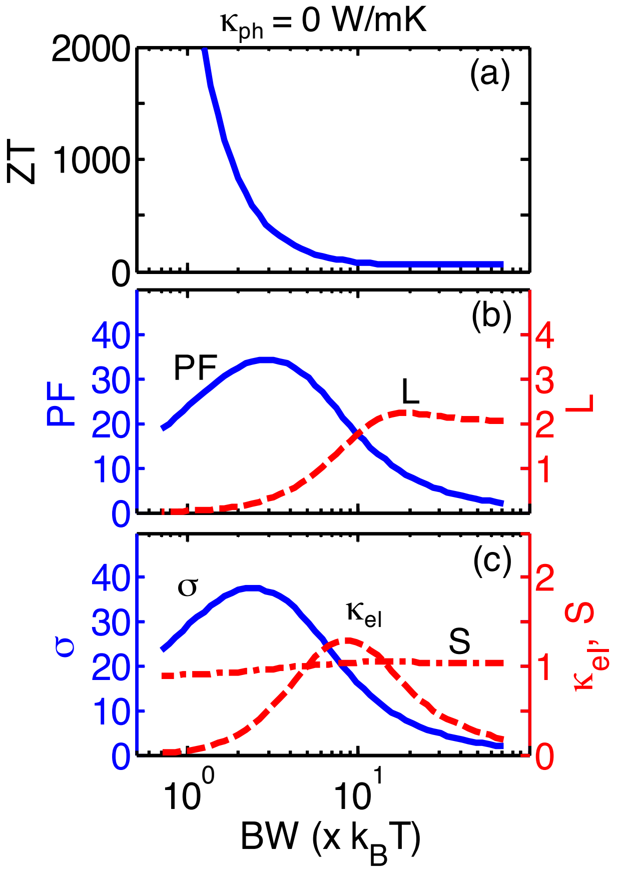

Figure 5.5. For zero lattice thermal conductivity ($\kappa_{ph} = 0$), (a) *ZT*, (b) the power factor (PF) and the Lorenz number (*L*), and (c) the Seebeck coefficient (S), the electrical conductivity (σ) and the electronic thermal conductivity (κ_{el}) are plotted. The units of PF, *L*, *S*, σ, and κ_{el} in the plots are 10^{-6}W/m-K^2, $(k_B/q)^2$, 10^{-3}V/K, $1/\Omega\text{-m}$, and $5\times10^{-5}\text{W/m-K}$, respectively. For each value of the BW, we found the optimal location of the Fermi level to maximize *ZT*. As the BW decreases, the highest *ZT* (i.e. efficiency) is obtained for a delta-function like narrow band. This result occurs mainly because as the BW approaches zero, κ_{el} approaches zero and therefore the *L* approaches zero. Note that the maximum PF still appears at a moderate BW.

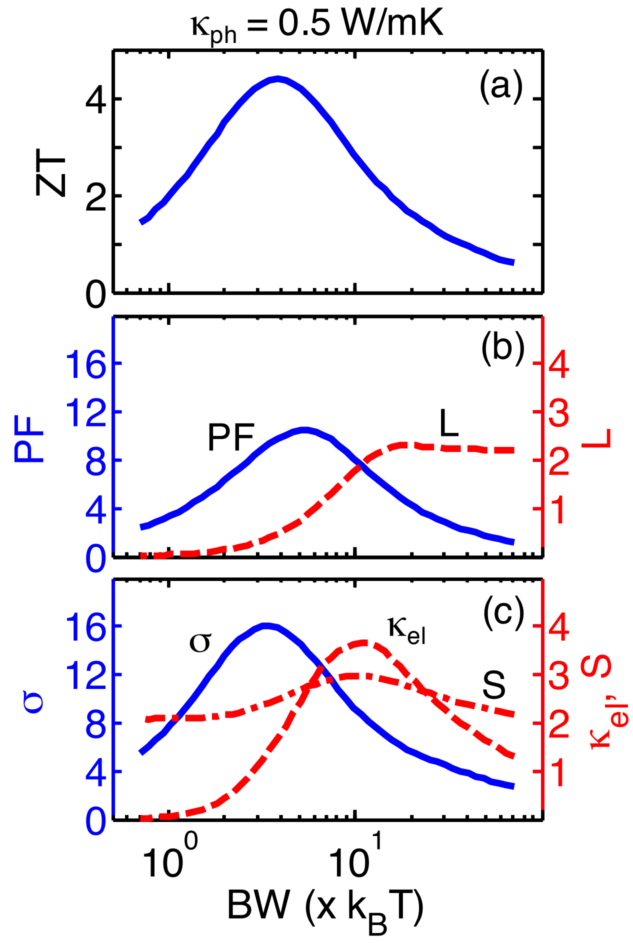

Figure 5.6. For a finite lattice thermal conductivity (κ_{ph} = 0.5 W/m-K), (a) the *ZT*, (b) the power factor (PF) and the Lorenz number (*L*), and (c) the Seebeck coefficient (S), the electrical conductivity (σ) and the electronic thermal conductivity (κ_{el}) are plotted. The units of PF, *L*, *S*, σ, and κ_{el} in the plots are 10^{-3}W/m-K^2, $\left(k_B/q\right)^2$, 10^{-4}V/K, $10^4/\Omega$-m, and 10^{-1}W/m-K, respectively. For each value of the BW, we found the optimal location of the Fermi level to maximize *ZT*. In contrast with the case of $\kappa_{ph}=0$, the highest *ZT* occurs for the moderate BW mainly because of the BW dependence of the power factor. Since the BW has a rather small effect on *S*, the strong variation of σ vs. BW explains the shape of the power factor vs. BW. The optimum BW for σ occurs when the width of the Fermi window matches the width of $M\left(E\right)$.

We have discussed why a δ-function like TDF maximizes the efficiency for $\kappa_{ph}=0$, and why a TDF with a moderate BW of a few k_BT maximizes the efficiency for a finite κ_{ph}. For the maximum power output, however, Fig. 5.4 shows that a moderate BW is best in either case. This occurs because the power output is proportional to the power factor (as discussed in Appendix), and the power factor displays its maximum at a moderate BW regardless of the value of κ_{ph}. Achieving a moderate BW band by coherent transport in a superlattice, however, is not an effective approach because in that case, most of the channels are filtered out. Molecular thermoelectrics is another possibility.[67] This might lead to high efficiency but not to high power, because although molecular levels can be sharp (possibly too sharp), one still needs a large number of channels in a small energy range. Packing molecules closely may broaden the levels and degrade performance.

5.6 The Mahan and Sofo Upper Limit

In previous sections, we have shown that for a constant MFP, a moderate BW (a few k_BT) is best for the practical case of a finite κ_{ph}. This conclusion holds for both the efficiency and the power output when we consider a constant MFP. This fact has been pointed out in previous studies;[204,233–237] we have provided a simple, physical explanation in terms of the need to match the width of the Fermi window to the width of the transport distribution or $M(E)$ and also explained the appropriate physical constraints on the TDF. In this section, we address the question of how these theoretical studies relate to the original arguments.

The Mahan-Sofo upper limit to ZT can be readily obtained by using eqns. (5.1) and (5.2d), from which ZT can be written as

$$ZT = \frac{\kappa_0}{\kappa_{ph}} \times \left(\frac{1 - \kappa_{el}/\kappa_0}{1 + \kappa_{el}/\kappa_{ph}} \right). \tag{5.7a}$$

Since the term in the brackets is always less than 1, it can be seen that

$$ZT \le \frac{\kappa_0}{\kappa_{ph}}, \tag{5.7b}$$

which is the Mahan-Sofo upper limit.[204] Mahan and Sofo[204] also showed that a bandstructure that produces a δ-function TDF (a single energy channel) gives the upper limit. This can be readily understood from the fact that $\kappa_{el} = 0$ for the single energy case, so eqn. (5.7a) shows that the thermoelectric figure of merit reaches its upper limit, $ZT = \kappa_0/\kappa_{ph}$. Figure 5.7 shows the computed upper limit of *ZT* vs. BW of the dispersion (dashed line) along with the computed *ZT* vs. BW (solid line). It can be seen that $ZT \le \kappa_0/\kappa_{ph}$ is always true, and that in agreement with the prediction of Mahan and Sofo,[204] *ZT* approaches its upper limit for the narrowest BW. Although we assumed a constant MFP and a finite κ_{ph}, we find that the conclusion that $ZT \le \kappa_0/\kappa_{ph}$ and $ZT = \kappa_0/\kappa_{ph}$ for δ-function TDF are independent of the specific scattering model and value of κ_{ph}. The important point, however, is that κ_0 depends on the BW, so the upper limit itself depends on BW and shows peak value at a BW of a few k_BT where the maximum *ZT* occurs. The highest *ZT*, therefore, occurs for a BW that results in operation well below the Mahan-Sofo upper limit._

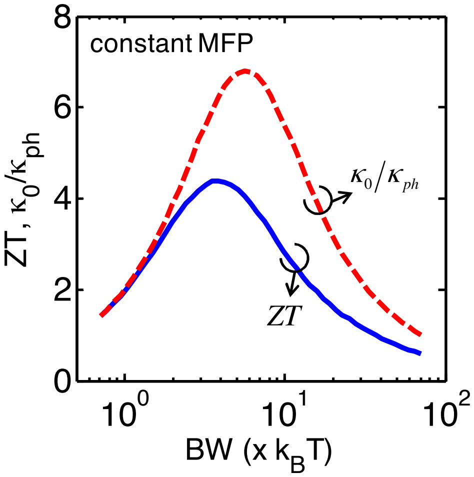

Figure 5.7. For a finite lattice thermal conductivity ($\kappa_{ph} = 0.5$ W/m-K), the *ZT* (solid line) and its upper limit, κ_0/κ_{ph} (dashed line), are plotted as a function of bandwidth (BW). For each assumed bandwidth, the optimal location of the Fermi level is determined to maximize *ZT*. Here a constant mean-free-path is assumed. It can be seen that $ZT \le \kappa_0/\kappa_{ph}$ is always true and the ZT approaches its upper limit for the narrowest BW.

5.7 Role of Scattering

In previous sections we showed that a narrow TDF with a BW of a few k_BT gives the best TE performance. The only exception is that when $\kappa_{ph} = 0$, the maximum efficiency (but not the maximum power delivered to a load) occurs for a δ-function TDF. We also revisited the Mahan-Sofo limit and showed that while the upper limit is obtained for a δ-function TDF, better efficiency can be obtained by operating below the BW dependent upper limit using a TDF with a BW of a few k_BT. These results answer question 2), but before we conclude that a narrow band is best, however, we should realize that our use of the same MFP for all bandwidths is physically unreasonable. One advantage of the Landauer approach is that it separates the TDF into a part that depends only on bandstructure, $M(E)$, and a part that depends both on bandstructure and scattering physics, the MFP. We turn now to the question of how scattering affects TE performance and we shall see that although narrow TDFs have been much discussed,[204,233–237] they are probably not the best for TE performance.

Recent work by Zhou et al.[237] and by the author[242] has examined three models for scattering: 1) the constant mean-free-path discussed here in previous sections, 2) a constant scattering time, and 3) a scattering rate proportional to the density-of-states, $\tau^{-1}(E) = C_{el}D(E)$. The constant MFP can be justified for parabolic energy bands, but it is hard to justify over a wide range of BWs. The constant scattering time is commonly used, but hard to justify under any circumstances. A scattering rate that is proportional to the density-of-states follows directly from Fermi's Golden Rule and should describe acoustic phonon scattering, which typically dominates for good thermoelectrics.

Extensive calculations for the three scattering models have been presented recently,[237,242] so we only review the conclusions here. As discussed in previous sections, for a constant mean-free-path, *ZT* is mostly determined by the BW dependence of σ, which is maximized when the BW of the TDF matches that of the Fermi window function. Similar results are obtained for the constant scattering time case. For the most realistic scattering model, however, it is found that there is no optimum BW.[237,242]

Instead, *ZT* continuously decreases as the BW decreases. The reason is clear in a Landauer picture. According to eqn. (5.3), σ is proportional to the TDF, which is the Landauer picture is proportional to the product of the number of channels, $M(E)$, and the MFP, $\lambda(E)$. As the BW decreases, the number of channels in the Fermi window increases, which should increase the conductivity, but the density of states near the Fermi level also increases, which increases the scattering rate and decreases the MFP. In our isotropic bandstructure model, the smaller BW corresponds to a larger effective mass and smaller velocity. Since the MFP is the product of velocity and scattering time, it decreases faster than $M(E)$ increases so *ZT* decreases as the BW decreases.

In contrast to several previous studies and to the discussion in earlier sections of this paper, which used overly-simplified treatments of scattering, we conclude that for best TE performance, wide (dispersive) bands are the best. This point can also be seen from the expression for the conductivity,

$$\sigma = \int \frac{M(E)}{A} \lambda(E) \left(-\frac{\partial f_0}{\partial E} \right) dE \ . \tag{5.8a}$$

Recall that $M(E) \propto |v_x^+| D(E)$, where $|v_x^+|$ is the average velocity in the direction of transport at energy, E. Recall also that $\lambda(E) \propto |v_x^+| \tau(E)$ and that $1/\tau(E) \propto D(E)$, so eqn. (5.8a) becomes

$$\sigma \propto \int |v_x^+(E)|^2 \left(-\frac{\partial f_0}{\partial E} \right) dE \tag{5.8b}$$

Equation (5.8b) shows that the conductivity is proportional to the square of the average velocity in the Fermi window. High velocities occur for light effective masses (large BWs), so for a realistic model of scattering, we conclude that a wide band, not a narrow band, is best.

5.8 High Valley Degeneracy

The analysis in the previous section showed that it is hard to increase the power factor in a single band by increasing the density-of-states near the Fermi level because of the tradeoff between the number of channels and the mean-free-path. It is generally understood, however, that a high degree of valley degeneracy is beneficial for thermoelectric performance,[33] and recently, this approach has produced significant increases in performance.[238] This leads to the question of how high valley degeneracy affects the power factor.

The benefits of valley degeneracy can be understood with a very simple model. As shown in previous sections, the power factor is mainly controlled by the behavior of the conductivity, σ, and when a realistic model for scattering is assumed (proportional to the density of states), large bandwidths, for which the parabolic band assumption holds, are best. Accordingly, we assume two spherical, parabolic band semiconductors, the first with an effective mass of m_1^* and the second with m_2^*. The first semiconductor has a valley degeneracy of N_{V1}, and the second has only a single valley, i.e. $N_{V2} = 1$. We compare these two semiconductors at the same density of states and ask: how do the power factors of these two semiconductors with the same densities of states compare?

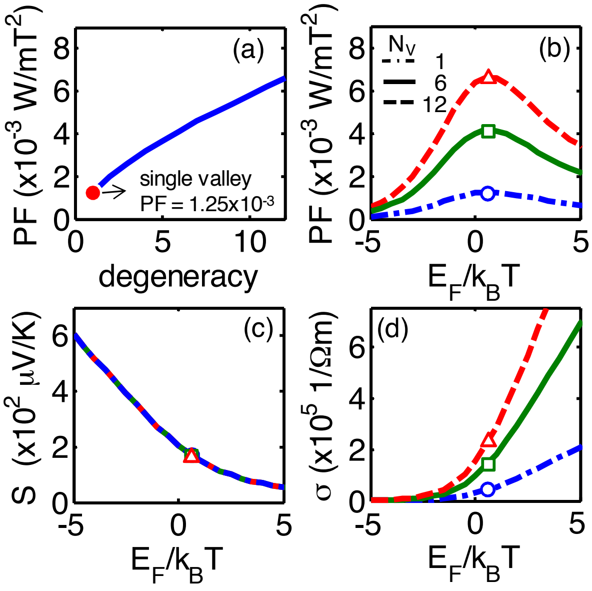

Figure 5.8. (a) The computed power factor vs. valley degeneracy is plotted. (b) The power factor (PF), (c) S, and (d) σ are plotted as a function of Fermi level for three cases of $N_V = 1$, 6, and 12. Symbols represent values at optimal Fermi level. It can be seen that PF of multi-valley semiconductor is improved and that the enhancement is attributed to the increase of σ.

The computed power factor vs. valley degeneracy is plotted in Fig. 5.8a. The calculations assume $m_2^* = m_0$ and that $\tau(E) = C_{el}/D(E)$ with C_{el} selected to produce average MFP ($\langle\langle\lambda\rangle\rangle$) of 10 nm for a single valley. The calculations confirm the expectation that valley degeneracy produces higher performance. For $N_V = 6$, about a factor of 3 increase of the power factor can be achieved in this model multi-valley structure. Figure 5.8b, 8c, and 8d show the power factor, S, and σ as a function of Fermi level for an isotropic single valley ($N_{V2} = 1$) and multi-valley ($N_{V1} = 6$, and $N_{V1} = 12$). It is found that the S vs. E_F characteristics are the same for the three cases, but Fig. 5.8c shows that the conductivity increases with valley degeneracy.

Additional insight into the benefits of valley degeneracy can be gained from Fig. 5.9, which compares $D(E)$, $M(E)$, $\lambda(E)$, and the transport distribution, $M(E)\lambda(E)$ for the three cases. For this calculation, we forced $D(E)$ to be the same in the three cases (Fig. 5.9a), so the scattering times, $\tau(E)$, are also the same. In the multi-valley cases, we combine the contributions of several light mass bands. In an isotropic single valley, the same density-of-states is achieved by increasing the effective mass, which lowers the velocity. As shown in Fig. 5.9b, $M(E)$ is higher for the multiple valley case because $M(E) \propto \upsilon(E)D(E)$. Fig. 5.9c shows that $\lambda(E)$ is also higher for the multiple valley case because $\lambda(E) \propto \upsilon(E)\tau(E)$. Note that with a parabolic band, $\lambda(E)$ is energy-independent. Since the transport distribution is proportional to $M(E)\lambda(E)$, it is considerably higher for the multiple valley case, as shown in Fig. 5.9d. The $\left|\upsilon_x^+(E)\right|^2$ term in eqn. (5.8b) is larger in multi-valley case. Stated another way, $M(E) \propto \upsilon(E)D(E)$ and $\lambda(E) \propto \upsilon(E)\tau(E)$. While $D(E)$ and $\tau(E)$ are the same in the three cases, the velocity is higher in the multi-valley cases, so both $M(E)$ and $\lambda(E)$ are larger when a high density-of-states is obtained by combining light mass valleys.

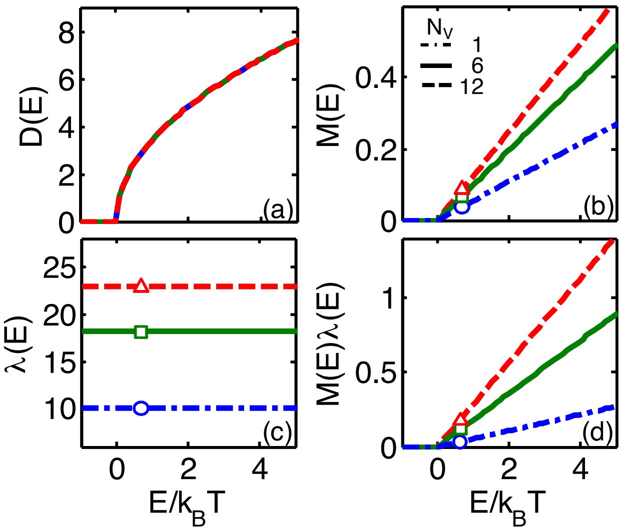

Figure 5.9. (a) Density-of-states ($D(E)$), (b) number of conduction channels ($M(E)$), (c) mean-free-path (MFP) for backscattering ($\lambda(E)$), and (d) $M(E)\lambda(E)$ are plotted for three cases of three cases of $N_V = 1$, 6, and 12. Symbols represent values at optimal Fermi level. $M(E)$ and $\lambda(E)$ are higher for the multiple valley case because $M(E) \propto \upsilon(E)D(E)$ and $\lambda(E) \propto \upsilon(E)\tau(E)$. Since the transport distribution is proportional to $M(E)\lambda(E)$, it is considerably higher for the multiple valley case.

The improved PF for multiple valleys is due to the high conductivity, $\sigma = \left(2q^2/h\right)\langle M\rangle\langle\langle\lambda\rangle\rangle$. The improved power factor is attributed to increases in both the average MFP, $\langle\langle\lambda\rangle\rangle$, and in the number of channels in the Fermi window, $\langle M\rangle$. For example, $\langle M\rangle = 9.5\times10^{16}\ m^{-2}$ and $\langle\langle\lambda\rangle\rangle = 18\ nm$ for the multi-valley case of $N_V = 6$ and $\langle M\rangle = 5.2\times10^{16}\ m^{-2}$ and $\langle\langle\lambda\rangle\rangle = 10\ nm$ for the single valley case.

5.9 Distorted Density of States

Next, we examine the possibility of improving TE performance with a distorted density-of-states, $D(E)$ [8,243,244]. To illustrate the effect of a distorted $D(E)$, we consider a model semiconductor for which the lower band is an isotropic single valley with an effective mass of m_0 and the upper band has an effective mass of $10m_0$. The

$10\times$ larger effective mass induces sharp increase of $D(E)$, which is similar to the effect of a resonant level. We compare the power factor of this semiconductor to that of an isotropic single valley with an effective mass of m_0. Two different scenarios for scattering are considered; the first assumes a constant MFP, $\langle\langle\lambda\rangle\rangle$, with a value of 10 nm. The second scenario assumes that $\tau(E)=C_{el}/D(E)$ with C_{el} selected to produce $\langle\langle\lambda\rangle\rangle$ of 10 nm for an isotropic single valley. In practice, we expect the results to lie between these two limits. We compare TE performance at the optimal location of the Fermi level while varying the band-offset, ΔE_C, between the lower and upper bands.

Figure 5.10a, the computed power factor vs. ΔE_C for the constant MFP case, shows that the best performance is obtained when $\Delta E_C = 0$. The maximum performance is much better than that of the single, small mass valley, and slightly better than that of a single, large mass valley. Figure 5.10b shows that the maximum PF occurs when the Fermi level is located near the bottom of the large mass valley, and Fig. 5.10c shows that a non-monotonic behavior of $S(E_F)$ when $\Delta E_C > 0$ maintains a relatively large maintains a relatively large Seebeck coefficient under degenerate conditions. These results can be understood as show in Fig. 5.11. The density of states for three different valley offsets are shown in Fig. 5.11a, and Fig. 5.11b show the corresponding $M(E)$. The case of $\Delta E_C = 0$ produces the largest M at any energy. Because the MFP is constant (Fig. 5.11c), the transport distribution (which is proportional to $M(E)\lambda(E)$) is largest for all energies for $\Delta E_C = 0$, which leads to the higher power factor. As discussed in Sec. 5.7, however, the assumption of a constant mean free path for this composite band is unrealistic. Next, we discuss the more realistic case where the scattering rate is proportional to the total density-of-states, $\tau(E)=C_{el}/D(E)$. This scattering rate produces a significantly different TDF, which leads to significantly different results.

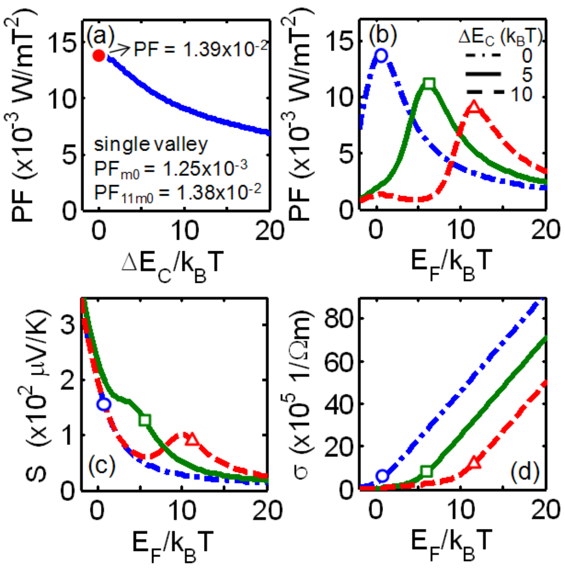

Figure 5.10. (a) For constant mean-free-path (MFP), the power factor (PF) vs. ΔE_C for a material with lower band and upper band, where ΔE_C is the band-offset. Lower band is isotropic single valley with an effective mass of m_0 and upper band has an effective mass of $10m_0$. Note that PFs for single valley with an effective mass of m_0 and $11m_0$ are 1.25×10^{-3} W/mT^2 and 1.38×10^{-2} W/mT^2, respectively. Upper band with heavy effective mass produces higher performance regardless of ΔE_C in comparison to the power factor of a single valley and best performance is obtained when $\Delta E_C = 0$. (b - d) The PF, Seebeck coefficient (*S*), and electrical conductivity (σ) vs. Fermi level for three cases of $\Delta E_C = 0$, 5, and $10k_BT$. Comparing to the case of single valley, it is found that a significant increase in σ lead to improved power factor. Non-monotonic Seebeck coefficient behavior (Fig. 5.10c) maintains large *S* at the degenerate limit. Symbols represent values at optimal Fermi level.

Figure 5.12a shows the computed power factor vs. ΔE_C for the case of $\tau(E) = C_{el}/D(E)$. Also shown is the power factor for a single light mass valley (red circle). As discussed in Sec. 5.7, a single heavy mass valley produces much lower performance. Figure 5.12a shows an enhanced power factor when ΔE_C is larger than about $10k_BT$. For example, about a factor of two increase can be achieved for $\Delta E_C = 15k_BT$. This is in stark contrast to the case of constant MFP for which best performance is obtained with $\Delta E_C = 0$. This behavior occurs because for the case of

$\tau(E) = C_{el}/D(E)$, the increase in $D(E)$ leads to large scattering rates if the upper band with its large $D(E)$ is located within the Fermi window. For $\Delta E_C = 0$, σ is reduced by a factor of ~10 compared to that for the single light mass valley.

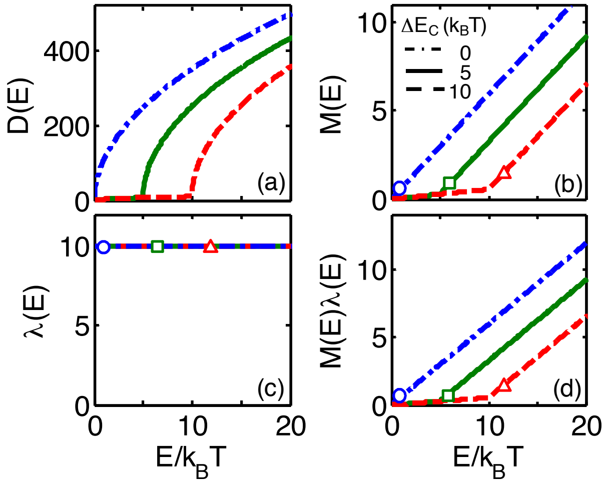

Figure 5.11. (a) Density-of-states ($D(E)$), number of conduction channels ($M(E)$), mean-free-path (MFP) for backscattering ($\lambda(E)$), and $M(E)\lambda(E)$ vs. Fermi level are plotted for three cases of $\Delta E_C = 0$, 5, and $10k_BT$ for constant MFP. Since MFP is constant, the sharp increase of $D(E)$ leads to a sharp increase of $M(E)$ and TDFs (i.e. $M(E)\lambda(E)$). The resulting strong energy dependence of $M(E)\lambda(E)$ produces non-monotonic Seebeck coefficient behavior. Symbols represent values at optimal Fermi level.

Figures 5.12b-12d plot the power factor, S and σ vs. Fermi level for $\Delta E_C = 5,\ 10,$ and $15k_BT$ and show that the improved power factor for $\Delta E_C >\sim 10k_BT$ is mainly attributed to a large σ while maintaining a large S of ~120 $\mu V/K$ at degenerate limit (which is due to the non-monotonic $S(E_F)$ characteristic). For $\Delta E_C = 10k_BT$, $\sigma = 1.88\times10^5\ \Omega^{-1}m^{-1}$ which is about $4\times$ larger than σ for a single light mass valley. It is found that at the optimal Fermi level, σ keeps increasing with ΔE_C because the effective number of conduction channel contributed by the lower band increases for large ΔE_C. In practice, achieving this performance would depend on the ability to dope the semiconductor so that E_F is near ΔE_C.

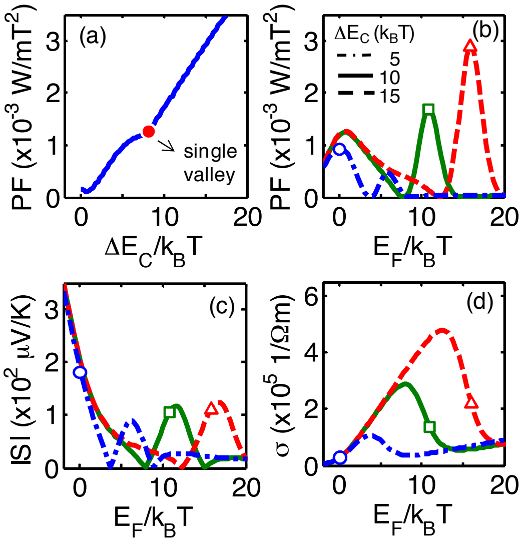

Figure 5.12. (a) The power factor (PF) vs. ΔE_C for a material with lower band and upper band, where ΔE_C is the band-offset. Lower band is isotropic single valley with an effective mass of m_0 and upper band has an effective mass of $10m_0$. Red circles represent the PF for a single valley. The improved PF is obtained for $\Delta E_C >\sim 10k_BT$. (b - d) The PF, Seebeck coefficient (S), and electrical conductivity (σ) vs. Fermi level for three cases of $\Delta E_C = 5$, 10, and $15k_BT$. It can be seen that non-monotonic Seebeck coefficient behavior (Fig. 5.9c) improves S at the degenerate limit. As ΔE_C becomes large, σ at optimal Femi level continues to increase. Therefore, the enhanced power factor is obtained when ΔE_C is larger than about $10k_BT$.

The non-monotonic behavior of $S(E_F)$ is observed for both constant MFP and for $\tau(E) = C_{el}/D(E)$. In fact, for the second case, $S(E_F)$ actually changes sign for $E_F > \Delta E_C$. This can be understood from the $D(E)$, $M(E)$, $\lambda(E)$, and $M(E)\lambda(E)$ characteristics as plotted in Figs. 11 and 13. For constant MFP, the sharp increase of $D(E)$, leads to a sharp *increase* of $M(E)$ and TDF (i.e. $M(E)\lambda(E)$) when the upper bands are available. In contrast, for the second case, the sharp increase of $D(E)$ leads to sharp *decrease* in $\lambda(E)$ and TDF due to large scattering rates when we assume $\tau(E) = C_{el}/D(E)$. From eqn. (5.2b), the Seebeck coefficient in the degenerate limit is given by

$$S = \frac{\pi^2 k_B{}^2 T}{-3q} \frac{d\left(\ln \lambda\left(E\right) M\left(E\right)\right)}{dE}\bigg|_{E=E_F}, \tag{5.9}$$

which is the so-called Mott formula. Consequently, the strong energy dependence of the $M(E)\lambda(E)$ near the edge of the upper band leads to the non-monotonic $S(E_F)$. The drop in $M(E)\lambda(E)$ for the second case, casuses a change in sign of S.

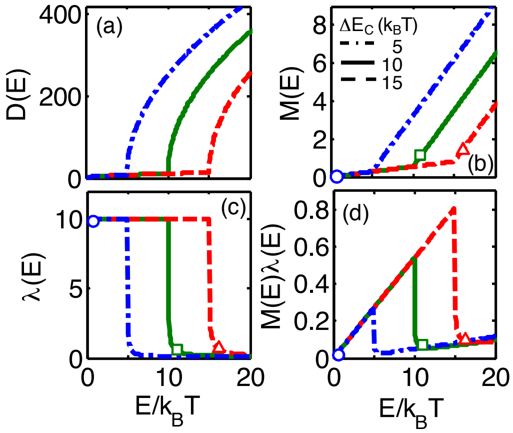

Figure 5.13. Density-of-states ($D(E)$), number of conduction channels ($M(E)$), mean-free-path (MFP) for backscattering ($\lambda(E)$), and $M(E)\lambda(E)$ vs. Fermi level are plotted for three cases of $\Delta E_C = 5$, 10, and $15 k_B T$. The MFP is decreased when upper bands are available. As a result, $M(E)\lambda(E)$ is reduced. The resulting sharp decrease of $M(E)\lambda(E)$ produces non-monotonic Seebeck coefficient behavior.

The simple models considered in this discussion show that we should expect improved TE performance with increasing valley degeneracy. In practice, the valleys may be anisotropic, which provides additional opportunities to increase the number of channels without decreasing the MFP. (Some example calculations are discussed in the Appendix.) We also showed that a semiconductor with a locally distorted $D(E)$ near the Fermi level can display an enhanced power factor through increase of σ and non-monotonic Seebeck coefficient characteristics. Because the distorted $D(E)$ also lowers σ, the increase of power factor only happens when lower and upper bands are engineered in an appropriate way, so the benefits of locally distorted density-of-states should be carefully considered on a case-by-case basis. Finally, these model calculations show how profoundly scattering influences the results underscoring a point recently made by Zhou, et al.,[237] and illustrating how these effects can be understood by interpreting the TDF from a Landauer perspective.

5.10 Summary

In this paper we set out to answer several questions and summarize the answers as follows.

1) What physical constraints should be placed on the TDF?

   The TDF(E) can be written as a product of the number of channel, $M\left(E\right)$ and the mean-free-path, $\lambda\left(E\right)$. Each of these two quantities is well-defined and directly relatable to the underlying electronic bandstructure. For a given dispersion, the maximum of $M\left(E\right)$ is fixed, not the area under $M\left(E\right)$ vs. E.

2) How does the BW of the TDF affect TE performance?

   When the lattice thermal conductivity is zero, a δ-function TDF produces an electronic efficiency at the Carnot limit, but no power can be delivered to a load. For a constant MFP (independent of BW), a narrow TDF maximizes the power delivered to a load – for both zero and finite lattice thermal conductivity. For a finite lattice thermal conductivity, it also maximizes the efficiency. The BW should match the width of the Fermi window. A δ-function TDF produces an *ZT* at the Mahan-Sofo limit, $ZT = \kappa_0 / \kappa_{ph}$, but this upper limit itself depends on the BW, so higher *ZT*s result for higher BWs where operation is below the Mahan-Sofo limit.

3) How does scattering affect optimum bandstructure?

   Scattering profoundly changes these conclusions. If, instead of a constant MFP, we assume that the scattering rate is proportional to the density-of-states, we conclude that a very broad band is better than a narrow band.

4) How should the improved performance of materials with a high valley degeneracy[238] or with a resonant energy levels^8 that distort the density-of-states be understood?

It is best to achieve a high density of states through valley degeneracy with a number of light mass valleys, as opposed to a single heavy mass valley because the higher velocity of the light mass valley increases both $M(E)$ and $\lambda(E)$. Offsetting the valleys in energy can enhance the Seebeck coefficient, but it degrades the conductivity. With a higher upper valley effective mass and the appropriate energy offset, TE performance can be enhanced, but the results are sensitive to the specifics of scattering.

5) Is there a best bandstructure for TE performance?
Although there is no simple answer, the general considerations are clear. Assuming that density-of states scattering dominates, high average velocities in the Fermi window produce the best results, so materials with a small density-of-states are best. The small $D(E)$ helps to increase scattering times. The large velocity times this $D(E)$ gives a significant number of channels for conduction, and the large velocity also increases the MFP.

For more complex thermoelectric performance, materials can be compared in terms of three well-defined physical parameters: 1) the average velocity in the direction of transport, $\left|\upsilon_x^+(E)\right|$, 2) the density-of-states, $D(E)$, and 3) the distribution of channels in energy, $M(E)$. Each of these three parameters can be easily extracted from a bandstructure, $E(k)$. Alternatively, we could express the three parameters as $\upsilon(E)$, $D(E)$, and $\upsilon(E)D(E)$. High velocities lead to long MFPs, low densities-of-states produce long scattering times and long MFPs, and large numbers of channels increase the conductivity. A super linear increase of $M(E)$ is also beneficial for the Seebeck coefficient. As illustrated in the discussion of distorted bandstructures, specific results depend very much on specifics of scattering (e.g. electron-phonon coupling constants, etc.), but these three parameters should provide useful guidance in assessing the performance of materials.

6. EXPLORATION OF POWER FACTOR ENGINEERING APPROACHES

The contents of Chapter 6 have been extracted and summarized from the following two publications: C. Jeong, and M. Lundstrom, "On Electronic Structure Engineering and Thermoelectric Performance," *J. Elec. Mater.,* 40, 738-743 (2011) and C. Jeong, G. Klimeck, and M. Lundstrom, "Computational Study of the Electronic Performance of Cross-Plane Superlattice Peltier Devices," *Mater. Res. Soc. Proc.,* 1314, DOI:10.1557/opl.2011.509 (2011). In this chapter, we address the question of how to engineer the electronic structure to enhance the performance of a thermoelectric material. We examine several different materials and discuss possibilities for enhancing TE performance.

6.1 Introduction

Many efforts have been made to search for materials that maximize the thermoelectric (TE) figure of merit, $ZT = S^2GT/K$, where T is the temperature, S is the Seebeck coefficient, G is the electrical conductance, and K is the thermal conductance, which is the sum of the electronic contribution, K_e, and the lattice thermal conductance, K_l. Most recent improvements in ZT have been achieved by phonon engineering to reduce the lattice thermal conductivity [36,47,197] . The question of how to improve the electronic performance is now an important one [8,44,62,64–67,69].

Significant improvements in S have been predicted and reported for several different materials. For example, an enhanced S has been achieved by engineering the density-of-states (DOS) in the bulk Tl-PbTe [8], and giant Seebeck coefficients have been predicted for nanostructured graphene [66] and for appropriately engineered molecules[67]. These examples all seek to enhance performance by achieving a delta-function like DOS. Also the possibility of enhancing the power factor (S^2G, PF) of TE performance by using SL devices has been studied. For cross-plane transport in SL, it has been predicted that energy filtering will lead to significant increases in *ZT* under a certain condition [72]. Experimentally, researchers have shown the increase in *S* by filtering out low energy electrons, but a limited increase in power factors due to the decrease in electrical conductivity [73–75].

It is still not clear how these materials affects the electronic performance i.e. PF. Since a clear understanding of how electronic structure affects the S and G of a material is essential for developing materials with enhanced power factors (*PF*), we examine a wide variety of thermoelectric (*TE*) materials that have been proposed for enhanced electronic performance: molecules, graphene, composite energy bands, and cross-plane superlattice. Extensive calculations and comparisons for these materials have been done with Landauer approach and a sophisticated quantum transport model, NEMO-1D and are presented in Appendix A and B, so we only review the main points here.

6.2 Molecules, Graphene, and Composite Energy Bands

In order to enhance S, a very sharp energy-dependent transmission or number of conduction M_{el} is desirable near Fermi level. Several ideas to engineer the M_{el} have been proposed: 1) creating Fano resonance [67] (CSW molecule in Fig. 6.1a), 2) periodic graphene PN junction [66] (graphene superlattice in Fig. 6.1b), and 3) a composite energy bands [8] (introducing upper band with a heavy effective mass, $Al_xGa_{1-x}As$ as a model system in Fig. 6.1c). The results for a graphene, graphene SLs, and a molecule are compared with common *TE* semiconductors. As shown in Fig. 6.1d, graphene superlattice (SL), and an CSW molecule device display similar $S(E_F)$ characteristics to common semiconductor materials. The predicted giant *S* for a CSW molecule is actually what is expected from single level model. For a given Fermi level, the 3D bulk results have a somewhat higher *S* than the ideal single level model because in 3D, energy states are spread-out. In the $Al_xGa_{1-x}As$ materials system, however, an increase in *ZT* of 10 times (Fig. 6.1e) is possible because of the non-monotonic *S* behavior (magenta line in Fig. 6.1d), which maintains high *S* at high E_F (i.e. high carrier densities) resulting in high PF.

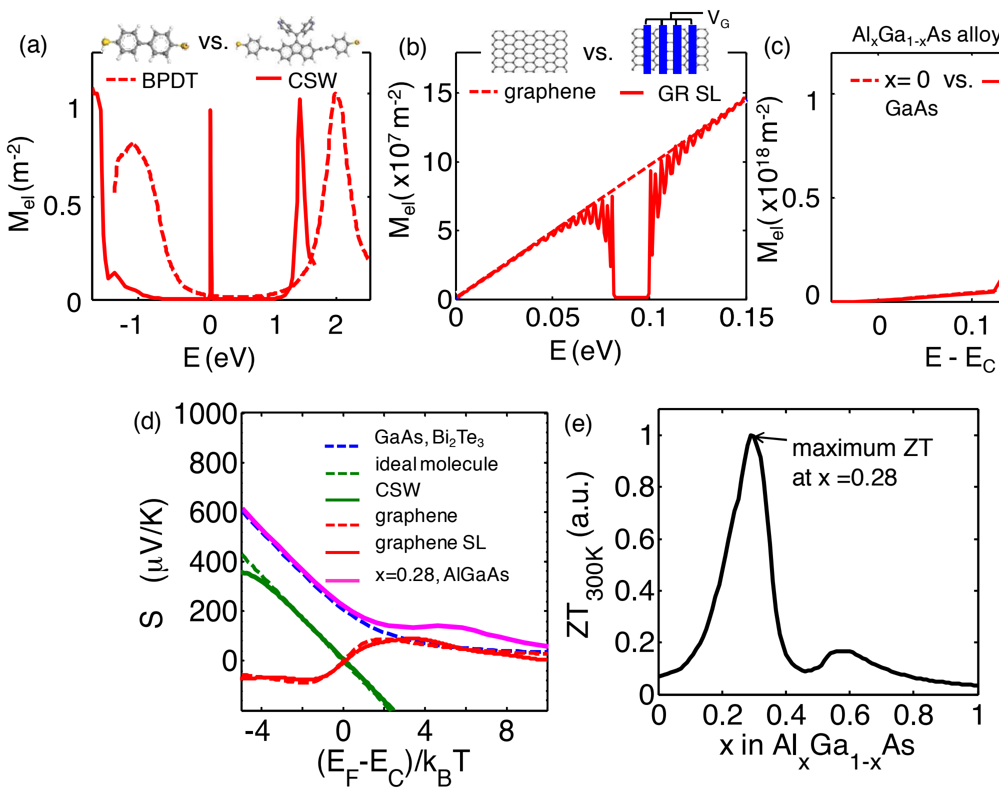

Figure 6.1. (a) The number of conducting channels (M_{el}) for (a) a BPDT vs. a CSW molecules. Engineering the transmission is done by putting side group in the CSW molecule, which creates very sharp Fano resonance. (b) a graphene vs. a graphene superlattice (GR GL). A transmission gap is created by making a periodic graphene PN junction electrostatically. (c) Al content of 0 vs. 0.28 of $Al_xGa_{1-x}As$ alloy. x = 0.28 is the optimal Al content for maximum ZT. All three examples seek to achieve a sharp $M_{el}(E)$. (d) the S vs. E_F for GaAs (x=0 in $Al_xGa_{1-x}As$), Bi_2Te_3, ideal molecule which has a delta-function like M_{el}, CSW molecule, a graphene, a graphene SL and composite bands (x=0.28, $Al_xGa_{1-x}As$). For a given Fermi level, the 3D bulk results have a somewhat higher S than the ideal single level molecule because in 3D, energy states are spread-out. (e) ZT at 300K with respect to Al composition in $Al_xGa_{1-x}As$. At each x, E_F is selected to maximize ZT. The M_{el} is computed from effective mass approximation. The electron mean-free-path is calculated based on the measured mobility. The 10x improvement in ZT is achieved at x=0.28. As shown in Fig. 3c, the band-splitting between a lower band (Gamma) and a upper band (L) is 5~ 7 k_BT and the $M_{el}(E)$ for L band is 20 times steeper than the Gamma band at x=0.28.

6.3 Cross-Plane Superlattice Peltier cooler

The performance of a single barrier and multi barriers (i.e. SL) TE devices are compared (Fig. 6.2a vs. b-c). In addition, the role of SL contacts (Fig. 6.2b) and phase coherence in the SL(Fig. 6.2c) are studied in multi barriers. As shown in Fig. 6.2d-f, our study shows that PF of multi barrier structures is no better than a single barrier TE device. We found that thin barrier, SL contacts and coherency only make energy-depedent transmission less steeper than corresponding bulk materials due to quantum mechanical effects such as tunneling, reflection, and Fabry-Perot type interference which led to 50% reduction in PF comparing to bulk barrier materials which led to 50% reduction in PF comparing to bulk barrier materials.

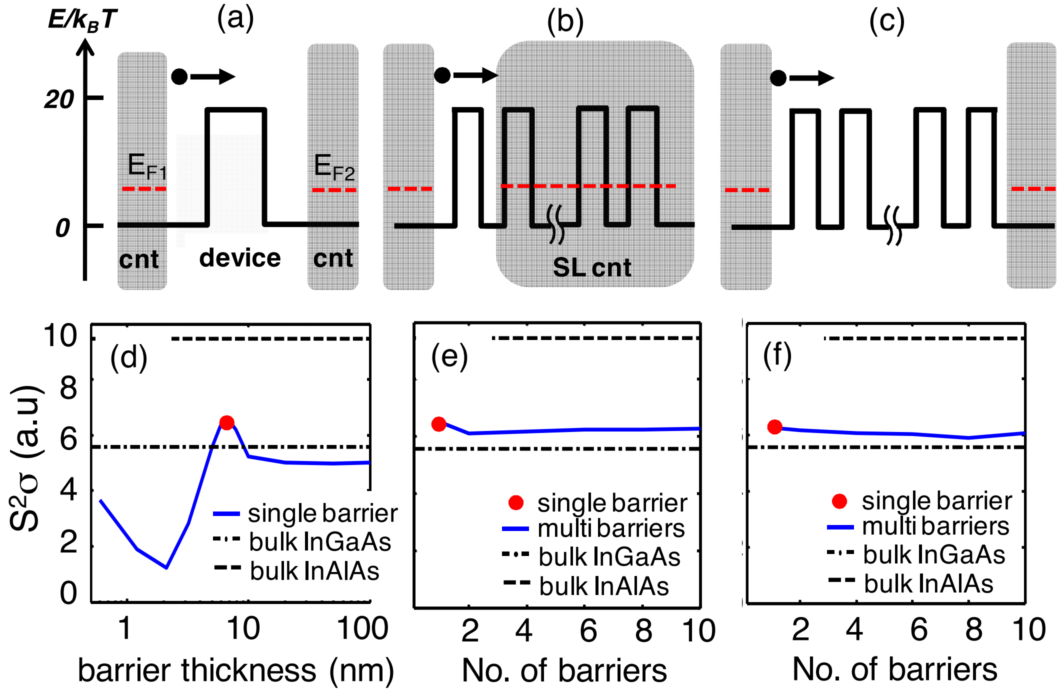

Figure 6.2. Schematic diagrams of test structures and corresponding power factor (PF) are plotted for (a,d) single barrier, (b,e) multi-barriers-1: superlattice (SL) contacts, and (c,f) multi-barriers-2. Barrier is In$_{0.52}$Al$_{0.48}$As. Grayed box represents contact (cnt), where energy relaxation scattering time is assumed to be 50 fs. Solid circle denotes injected electrons from emitter contact. emitter: bulk In$_{0.53}$Ga$_{0.47}$As with 0.044 m_0, barrier: In$_{0.52}$Al$_{0.48}$As with 0.075 m_0, barrier height: 0.51 eV. (d-f) The dashed-dot is the result of bulk In$_{0.53}$Ga$_{0.47}$As and dashed line the result of In$_{0.52}$Al$_{0.48}$As. Red circle symbols in (d-f) denote maximum PF of single barrier device in (d).

6.4 Conclusions

We examined electronic TE performance for several different materials. It was shown that most materials, even those for which giant Seebeck coefficients have been predicted, display a similar monotonic behavior of S vs. E_F that is expected from conventional thermoelectric theory. Using III-V alloy semiconductors as a model system, we demonstrated a promise of composite energy bands because of the non-monotonic S behavior, which maintains high S at high carrier densities resulting in high PF. Our findings show quantitatively how barriers in cross-plane superlattices degrade the electrical performance, i.e. power factor due to quantum mechanical effects, and that PF of multi barrier structures is no better than a single barrier TE device.

7. GRAPHENE AS A TRANSPARENT CONDUCTOR

The contents of Chapter 7 have been extracted and revised from the following publication: C. Jeong, Pradeep Nair, Mohammad Khan, Mark Lundstrom, and Ashraf Alam, “Prospects for Nanowire-doped Polycrystalline Graphene Films for Ultratransparent, Highly Conductive Electrodes,” *Nano Lett.*, 11, 5020 (2011).

In this chapter, we shift our attention to nanocomposite thermoelectric materials and a new approach to model nanocomposite (NC) TE devices is discussed. As a testbed of our model, recent experimental work on polycrystalline graphene is used, and we explain how grain boundaries affect the electronic performance of large-area polycrystalline graphene. We also demonstrate that a composite based on poly-crystalline graphene and a sub-percolating network of metallic nanowires offers a simple and effective route to reduced resistance, while maintaining high optical transmittance. This new approach of ‘percolation-doping by nanowires’ has the potential to beat the transparency-conductivity constraints of existing materials and may be suitable for broad applications in photovoltaics, flexible electronics, and displays.

7.1 Introduction

Since resistivity and transmittance are often fundamentally constrained by the intrinsic properties of a material, developing transparent conducting materials (TCMs) with low sheet resistance (R_S < 10 Ω/sq) and high transmittance (> 90%) has been a persistent challenge. Different metal doped oxides such as indium tin oxide (ITO) are widely used in commercial applications, but a replacement for ITO is desired for the following reasons[245]: 1) the limited availability and high-cost of indium, 2) increasing brittleness with aging, 3) chemical instability under acid or base conditions, 4) poor transmittance in the near infrared [246], and 5) metallic-ion diffusion from ITO into thin barrier layers that results in parasitic leakage.[247] These problems make ITO-based technologies, such as thin-film photovoltaics (PV), touch-screen displays, light emitting diodes, etc., expensive. Various alternative TCMs, such as networks of carbon nanotubes (CNT) [248,249] or metal nanowires (NW) [250,251] and chemical vapor deposited (CVD) polycrystalline graphene (poly-graphene),[252–255] have also been explored. While these potential ITO replacements resolve several practical issues associated with ITO, Fig. 7.1 suggests that their respective R_S-T curves are not significantly different than that of ITO. To understand why, consider the constraints of random CNT or metallic NW networks. To achieve technologically relevant values of R_S < 20 Ω/sq,[250] the density of NWs or CNTs must significantly exceed the percolation threshold for higher sheet conductance;[256] such high density however reduces the transmittance considerably.[250]'[257] Moreover, even with low R_S, the vertical current collection in PV cells is compromised by current crowding at the small-area interface between nanotubes/nanowire electrode and the bulk emitter layer.[256] Graphene provides another intriguing option; *four* layers of CVD graphene, fabricated by a roll-to-roll process, has already shown R_S ~ 30 Ω/sq and T ~ 90 %.[252] Available experimental data,[258] however, suggests that there is a fundamental limitation in sheet resistance and transmittance of thin graphene film and that it may be difficult for poly-crystalline graphene to compete successfully with ITO.[257]

In this Chapter, we use an experimentally calibrated, comprehensive numerical model for electron transport in polycrystalline graphene to conclude that the high resistivity of the film reflects an intrinsic percolation bottleneck of the system in which electrons are periodically trapped in domains formed by high-resistance grain boundaries (GBs). A novel concept which “dopes” poly-graphene with metallic nanowires can overcome this transport bottleneck to achieve T > 90% and R_S < 20 Ω/sq, with performance comparable or better than ITO. To distinguish the effects of doping by metallic NW from those by standard chemical or electrostatic techniques, we define a concept that we call ‘percolation-doping’: a *positive* percolation-doping by metallic nanowires improves conductivity not by increasing the free carrier density, but rather by increasing the number of electronic pathways to bridge the percolation bottleneck. A *negative* percolation doping – in the form of striping of nanotube network – has been previously used in a different context.[259] The continuity of poly-graphene ensures vertical current collection free from current crowding, and a small footprint of nanowires on graphene film ensures that high optical transmittance of single layer graphene is not compromised by percolation-doping.

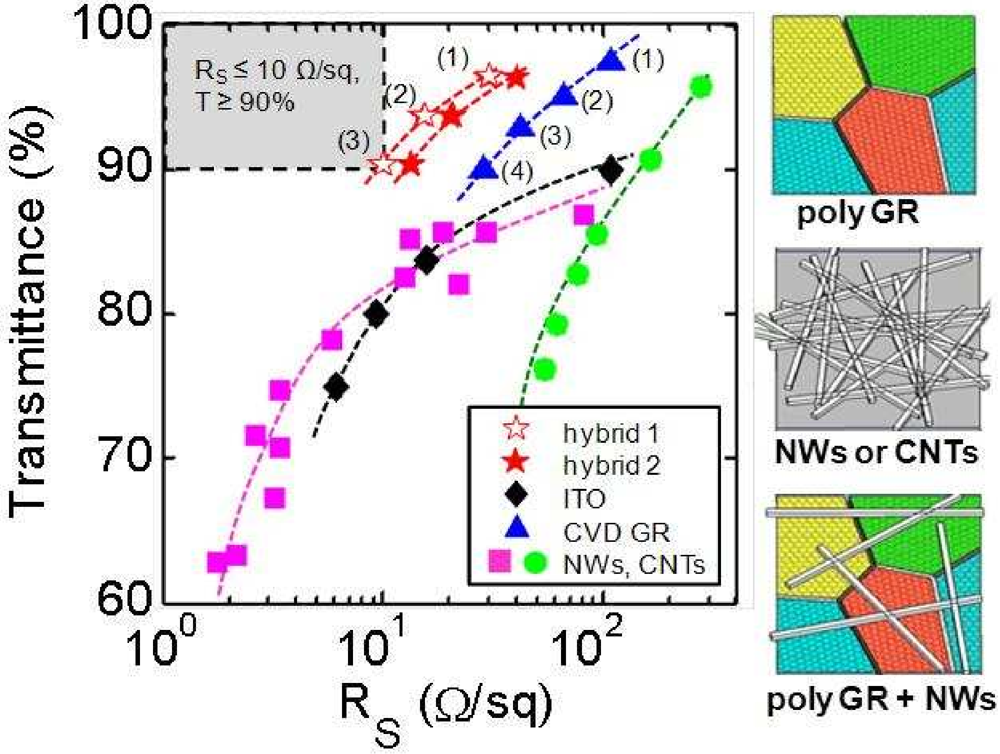

Figure 7.1 Transmittance as a function of sheet resistance (R_S) for polycrystalline graphene grown by chemical vapor deposition (CVD) method,[252] the networks of carbon nanotubes (CNT) [249] and nanowires (NW),[250] ITO,[252] and a hybrid of poly-graphene and NW mesh. The dashed lines are guide to eye. The best reported data are selected from literatures. The data for the hybrid are computed based on the following parameters: the R_S of a single crystalline graphene ~ 30 Ω/sq, the ratio of inter-grain resistance to intra-grain resistance ~ 63, the percentage of high-resistance grain boundary (P_{GB}) = 35%, and geometric aperture of 99% (an average distance between NWs of ~ 10 μm, a line width of 100 nm, and a height of 100 nm) for metal NW mesh with bulk Ag conductivity being assumed. The value in the bracket represents the number of layers for poly-graphene or the hybrid.

The chapter is organized as follows. To explore the origin of high R_S in poly-graphene films, we first construct microstructures of typical poly-graphene films reported in the literature and calculate their corresponding transport properties. Next, we examine quantitatively the impact of GBs on polycrystalline graphene to demonstrate the importance of a percolation bottleneck in these films. Finally, we propose a hybrid of polycrystalline graphene and a metal NW mesh to improve the performance in terms of R_S and T as well as to reduce variations among samples. Finally, we summarize our conclusions.

7.2 Approach

To understand why poly-graphene is so resistive, we use a process model to produce representative structures, an electrical model to compute the sheet resistance, and an optical model to compute the transmittance. The modeling approach is described in detail in the Appendix E. In brief, we begin by synthetically generating polycrystalline graphene samples using Voronoi tessellation.[260] Five types of microstructures (see Fig. 7.2a) of increasing complexity: 1) uniform square grain as a reference, 2) uniform hexagonal grains to approximate films produced by the seeded growth method,[261] 3) perturbed hexagonal grains with Gaussian size distributions, typical of films produced by seeded growth method,[261] 4) random grains with normal size distribution to represent films produced by CVD graphene,[262] and 5) with log-normal size distribution characteristic of CVD graphene.[262,263] The average grain size ($<L_{grain}>$) is ~5 μm, consistent with reported values.[253]'[261] Corresponding grain size distributions are shown in Figure 2b. *Several hundred samples* are prepared for a statistical study of the transport characteristics of the film.

The two key electrical parameters are the resistances of the grains and grain boundaries. In poly-graphene, it is experimentally observed that the ratio of the inter-grain to intra-grain resistance ranges from ~ 1 to ~ 30.[261] Although there might be a distribution of GB resistances as a function of misorientation between neighboring grains, for simplicity in the following discussion, we classify the GBs as either a high-resistance GB or a low-resistance GB. To describe electronic transport through the microstructure, we use a drift-diffusion formulation, i.e., $J = \sigma\left(dV/dx\right) + qD\left(dn/dx\right)$ where J is the current density in A/m, σ_S the sheet conductivity, V the potential, D the diffusion constant, and n_S the sheet carrier concentration. A drift-diffusion formulation is appropriate for this problem because average grain size (~5 μm) is much larger than the typical mean-free path of hundreds of nanometers.[261,210] (A similar drift-diffusion based approach has also been used for CNT networks, with excellent results.[259]) We assume that the charge current is conserved (i.e. no recombination-generation) and solve $\nabla \cdot J = 0 = -\nabla \cdot \left[\sigma \nabla \left(F_n/q\right)\right]$, where F_n is the electrochemical potential.

Within the bulk of the poly-graphene grain, $\sigma = \sigma_0$. The theoretical lower limit of conductivity is 30 Ω/sq, which occurs when only acoustic deformation potential scattering is present. For the conductivity across a GB, we follow a recent theoretical study,[264] which characterizes a high-resistance GB by transport energy gap (E_G) below which charge carriers are perfectly reflected (i.e. $\sigma_{GB}^{(hi)} < \sigma_0$). A low-resistance GB is taken to be being perfectly transparent (i.e. $\sigma_{GB}^{(lo)} \equiv \sigma_0$.) With these three conductivities, i.e., $\sigma_0, \sigma_{GB}^{(lo)}, \sigma_{GB}^{(hi)}$ the transport problem is fully defined. This model with high and low resistance GBs lead to a maze-like morphology landscape through which the electron injected from one contact travels to the other contact, *thereby transforming the problem of transport in poly-crystalline graphene into a percolation problem.*

For a given a microstructure, the finite difference method (FDM) is used to calculate transport properties. Each grain has about 200 nodes. The input parameters used for the FDM calculations are the sheet resistance within the grains, R_{lo} ~30 Ω/sq and the sheet resistance across high-resistance GBs, R_{hi} ~ $63R_{lo}$. (By assuming the lower limit sheet resistance for the grain, R_{lo}, our results establish the best case performance for large area polycrystalline graphene.) The FDM results are compared to a simple "one-node model", for which each grain is represented by only one node, i.e. by four resistors as shown in Figure 7.2a. This one-node model is of practical importance because the resistance, including high- or low-resistance GB in the one-node model, can be easily measured.[261] Finally, we calculate the optical transmittance of the system by (numerically) solving Maxwell equations with Floquet periodic boundary condition.[265] Normal illumination was assumed and the transmittance of both TE and TM waves was calculated for a set of wavelengths spanning the entire solar spectrum.

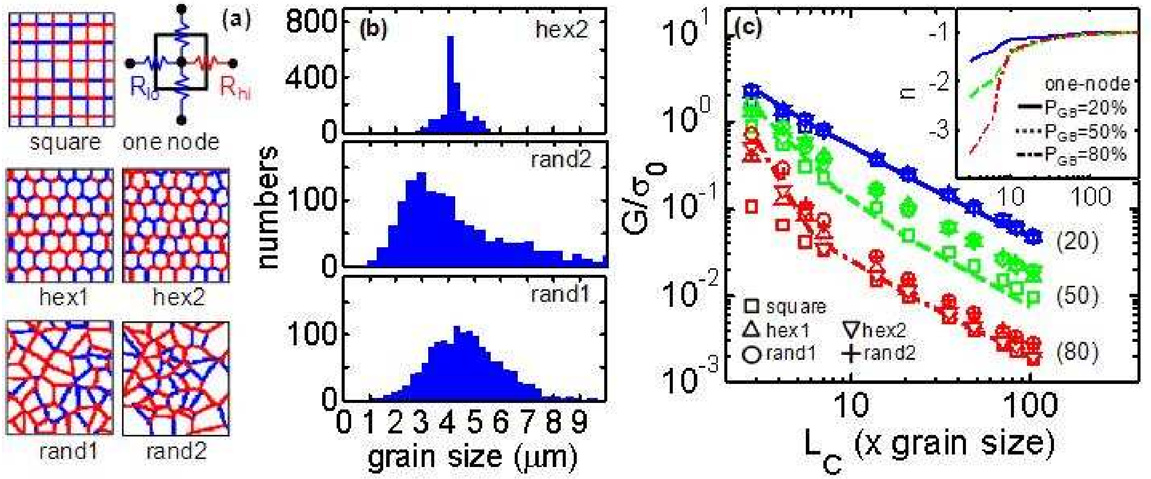

Figure 7.2 (a) Five microstructures generated by Voronoi tessellation for use of finite difference method: uniform square grain (square), uniform hexagonal grain (hex1), perturbed hexagonal grain with normal size distribution (hex2), and random grains with normal size distribution (rand1) and with log-normal size distribution (rand2). The percentage of high-resistance grain boundary is 50%. High- and low- resistance grain boundary are shown by red and by blue line. A grain is shown by white and has about 200 nodes per grain. A schematic diagram for one-model is also shown to explain how the one-node model represents one grain. The sheet resistance across low-resistance grain boundary and the sheet resistance across high resistance grain boundary are denoted as R_{lo} and R_{hi}, respectively. (b) Grain size distributions are shown for perturbed hexagonal grain and two random grains. (c) the normalized conductance vs. sample length for five different microstructures (symbols) and one-node model (solid , dashed, and dashed-dot line) for three different percentage of high-resistance GB (P_{GB} = 20%, 50%, and 80%). Inset: the dependence of the conductance exponent, n, on the sample length, i.e. $G \propto \left(L_C\right)^n$.

7.3 Results

In Fig. 7.2c, we plot the normalized sheet conductance (for five different microstructures) as a function of length for three different percentages of high-resistance GBs (P_{GB} = 20%, 50%, and 80%). The width of the sample is fixed at 7 × average grain size, $<L_{grain}>$ after which the width dependence of the transport properties disappears (as should be the case for large area films). The inset of Fig. 7.2c shows the dependence of the conductance exponent, n, on the length, i.e. $G \propto \left(L_C\right)^n$. If the length is smaller than ~10× average grain size ($<L_{grain}>$), the exponent becomes significantly larger than −1.0, indicating a nonlinear dependence on sample length. Compared to a long sample, there is a higher probability in a short sample that low-resistance GBs and grains form a continuous network between contacts. We are, however, interested in transport in large area (~square meters) poly-graphene appropriate for PV applications, where regardless of P_{GB}, the exponent approaches −1.0 with increasing length. *Remarkably, we find that the grain shape and grain size distributions have little effect on the conductance*. This is because it is the average-size of the grain and the percentage of the high-resistance GBs – not the specific details of grain-size distributions – that dictate the overall transport property of the network.

The plot of normalized conductivity vs. percentage of high-resistance GB shown in Fig. 7.3 is characterized by dramatic suppression of conductivity – even for small increase in P_{GB}. This result can be understood with reference to Fig. 7.4, which interprets the resistance of poly-graphene as a percolation problem defined by high and low resistance GBs. Recall that the percolation threshold for the Voronoi tessellation is (0.667-0.68) [266,267], while that of the hexagonal lattice is 0.6527.[268] Therefore, regardless the specific form of the GB-distribution, when the fraction of high-resistance GB approaches ~0.66 (i.e. $P_{GB} \sim 66\%$), electrons traveling between a pair of contacts must cross one (Stanley's red bonds[269]) or more high-resistance GBs, see Fig. 7.4b. This percolation bottleneck suppresses conductivity exponentially.

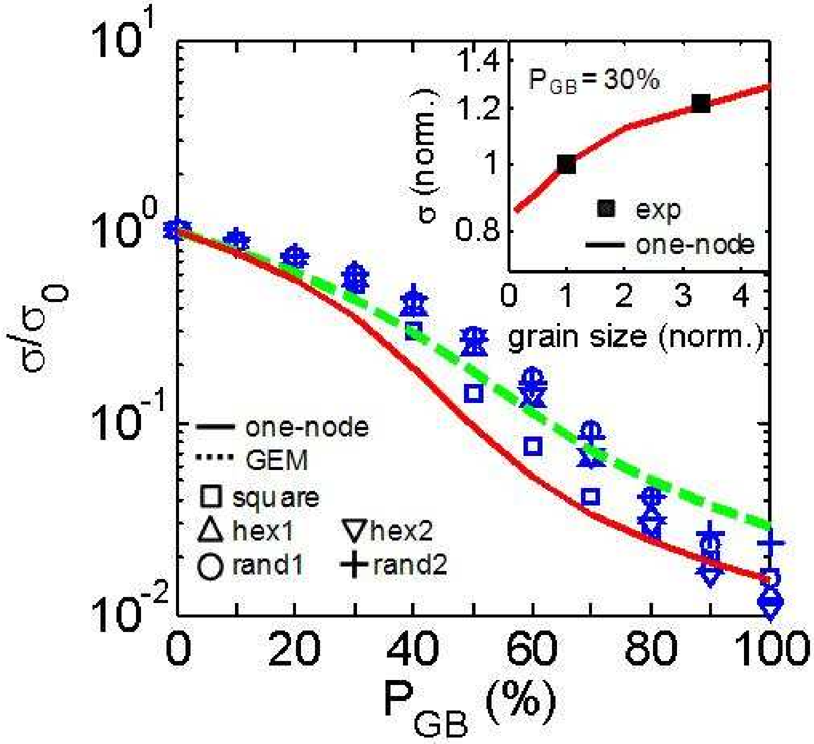

Figure 7.3. For a long sample (L_C ~ 100× average grain size), the dependence of the sheet conductance on the percentage of high-resistance grain boundary (P_{GB}) is plotted. Inset: the computed results for grain size dependence is compared to experiments. [253]

To support this percolation hypothesis quantitatively, we interpret the numerical results by the generalized effective media (GEM) theory.[270,271] The GEM equation is given by

$$f_{GB}\frac{\sigma_{GB}^{1/t}-\sigma^{1/t}}{\sigma_{GB}^{1/t}+A\sigma^{1/t}}+\left(1-f_{GB}\right)\frac{\sigma_0^{1/t}-\sigma^{1/t}}{\sigma_0^{1/t}+A\sigma^{1/t}}=0, \tag{7.1}$$

where f_{GB} is area fraction of grain boundaries, $\sigma_{0(GB)}$ the conductivity of the grain (grain boundary), t a characteristic exponent defined in $\sigma \propto (1-f_{GB}/f_{C,GB})^t$ with $f_{C,GB}$ being the threshold area fraction of GBs, and the constant A is $A = f_{C,GB}/\left(1-f_{C,GB}\right)$. When $\sigma_0/\sigma_{GB}=\infty$, Eq. (4.2) is reduced to a form of percolation equation $\sigma \propto (1-f_{GB}/f_{C,GB})^t$. With $t=1$ and $A=2$, the GEM equation is also reduced to Bruggeman's symmetric effective medium equation.[270] To fit our simulation results, two parameters need to be determined: t and $f_{C,GB}$. We set the bounds for the critical exponent to be from 1.05 to 1.37, typical number for 2D bond percolation,[272,273] while $f_{C,GB}$ is adjusted to fit the data. The relation of $f_{C,GB}$ to $P_{C,GB}$ is $P_{C,GB} = f_{C,GB}(P_{GB}^{100\%} / f_{GB}^{100\%})$, where $f_{GB}^{100\%} \sim 12.6\%$ is the area fraction of GB when $P_{GB} = 100\%$ (in the FDM simulation). The intensity of D bands in the spectroscopic Raman mapping of graphene grains and grain boundaries showed $f_{GB}^{100\%} \sim 10\%$.[261] As shown by dashed line in Figure 7.3, our numerical results for poly-graphene transport are well-reproduced by the GEM equation when $t = 1.05$ and $f_{C,GB} = 8.4 \pm 0.2\%$ corresponding to a percolation threshold of P_{GB}, $P_{C,GB} = 67 \pm 1.6\%$, almost *precisely the value expected from the percolation-hypothesis that interprets poly-graphene transport in terms of percolative transport on Voronoi tessellation*[266,267] *and hexagonal honeycomb lattice*.[268]

Having established the validity of the theory, it can now be used to explain why poly-graphene is so resistive and to extract P_{GB} from experimental data. For example, the inset of Fig. 7.3 compares the computed grain size dependence of sheet conductance to experiments. With the assumption of $R_{hi} \sim 60 R_{lo}$, we find $P_{GB} \approx 30\%$ gives a good match between our model and experiments. For this $P_{GB} < P_{C,GB}$, the effect of grain-boundaries is still significant and percolative transport plays an important role in defining sheet conductivity, with $\sigma/\sigma_0 > 0.2 - 0.3$.

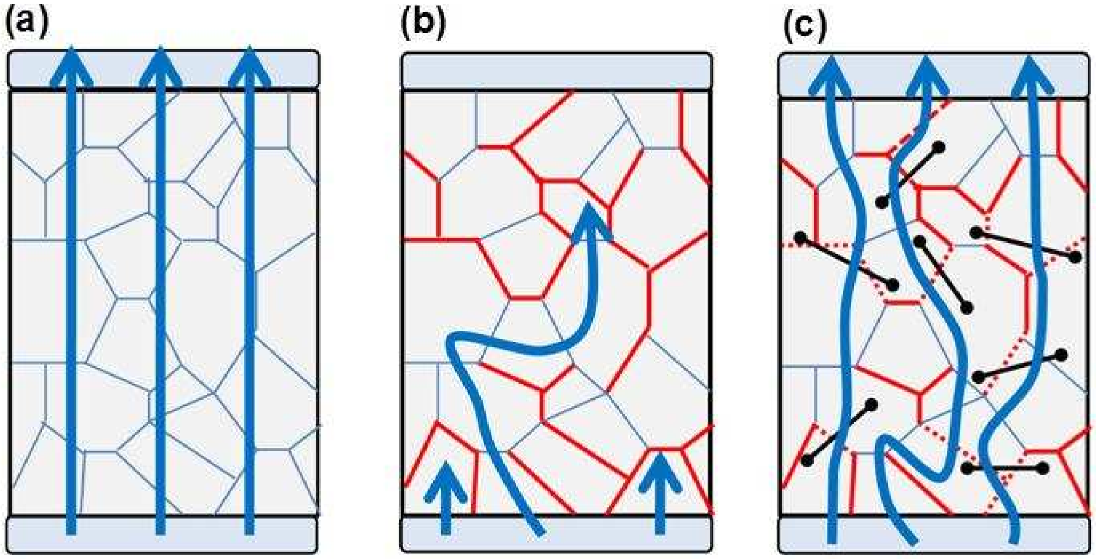

Figure 7.4. The schematic figures to interpret the resistance of poly-graphene as a percolation problem defined by high and low resistance grain boundaries (GB). High-resistance and low-resistance GBs are shown by red and blue line. (a) $P_{GB} = 0\%$ (b) $P_{GB} \sim 60\%$ (c) the concept of 'percolation-doping': doping the polycrystalline graphene by a sparse random mesh of metal NW. Metal NW is represented by black solid line. All arrows indicate current stream.

7.4 Discussion

The results discussed above shows that the key to reduce sheet-resistance of poly-graphene is either by increasing grain-size or by reducing the number of high-resistance grain boundaries Even if the grain-size could be further enlarged by various process techniques,[253]'[261] these grains will be always smaller than the dimension of transparent conductors necessary for PV applications. Most importantly, there is no obvious approach to control the magnitude or the number of high-resistance grain-boundaries by simple process changes. Clearly, a more practical technique to alleviate the influence of high-resistance GBs is needed of graphene electrodes has to be competitive with ITO.

To decrease the influence of high resistance GBs, we propose (see Fig. 7.4c) a novel concept which "dopes" the polycrystalline graphene with a sparse random mesh of metal NWs. The density of these nanowires should be below the percolation threshold, so that NW-NW connectivity is not expected and the NWs themselves do not form a percolating network (Fig. 7.4c, black lines). If the nanowire length is larger than that of the grain, the NWs will cross the grain-boundaries with probability approaching one. If a NW intersects a high-resistance grain-boundary, the GB can no longer inhibit current conduction, so that effective P_{GB} is reduced (see Figure 7.4c). Given the exponential dependence of conductance on P_{GB}, even a modest percolation-doping by metallic NW can dramatically decrease the R_S of poly-graphene films. The following example illustrates our proposition.

To examine the effectiveness of NW doping, consider a poly-graphene film with average grain-size of 5 μm decorated with a random dispersion of ~ 8 μm long, 100nm diameter, Ag nanowires.[250] These Ag NW will bridge the neighboring grains with probability approaching 1. The NW density (ρ_{NW}) is varied from 0 to 100%. We define the 100% coverage when the average distance between NWs is ~ 8-10 μm, so that every other grain – on average – contains a NW. For samples with $\rho_{NW} < 100\%$, the proportional fraction of NWs are randomly removed. Based on a recent measurement,[274] the contact resistance between metal and graphene is $R_C \quad 200\,\Omega \cdot \mu m$. The theoretical lower limit of $R_C \approx 20\,\Omega \cdot \mu m$[275] is obtained by assuming that the work function (W) difference between graphene and silver is about 0.3 eV ($W_{graphene}$ = 4.4 ~ 4.6 eV, W_{Ag} = 4.7 ~ 4.9 eV).[276] The poly-graphene conductivities remain unchanged.

Two dimensional simulation of NW-doped graphene can now be used to calculate the overall conductivity, σ, of the NW-doped poly-graphene film. The results are summarized in Fig. 7.5. The red solid line represents the normalized conductivity of poly-graphene without NW-doping ($\rho_{NW} = 0\%$).From this curve, the best reported sheet resistance of monolayer CVD graphene[252] of 125 Ω/sq translates to $P_{GB} \approx 35\%$ - a typical value. As we increase the NW density, the conductivity increases dramatically – even with a sparse network of only 60% coverage (one NW for every four grains) and relatively poor $R_C \approx 200\,\Omega \cdot \mu m$, the sheet conductance σ begins to approach that of pure single crystalline graphene R_S ~ 30 Ω/sq. Obviously, the conductivity improves further for lower contact resistance (i.e. $R_C \approx 20\,\Omega\cdot\mu m$) as the quasi-percolating NWs begin to carry larger fraction of the current between the contacts and σ reduces below 30 Ω/sq. Given that the sheet resistance of a monolayer of a graphene-NW hybrid, the sheet resistance of 2-3 layers of the NW-doped graphene film is obtained by $R^{n(=2-3)}_{S,hybrid} = R^{1}_{S,hybrid} \big/ n(=2-3)$. This linear dependency of R_S was also observed for roll-to-roll processed CVD graphene.[252] Indeed, as shown in Fig. 7.1, a stack consisting of 2-3 layers of the NW-doped graphene offers sheet resistance approaching 10 Ω/sq – the conductivity target for the potential replacement of ITO.

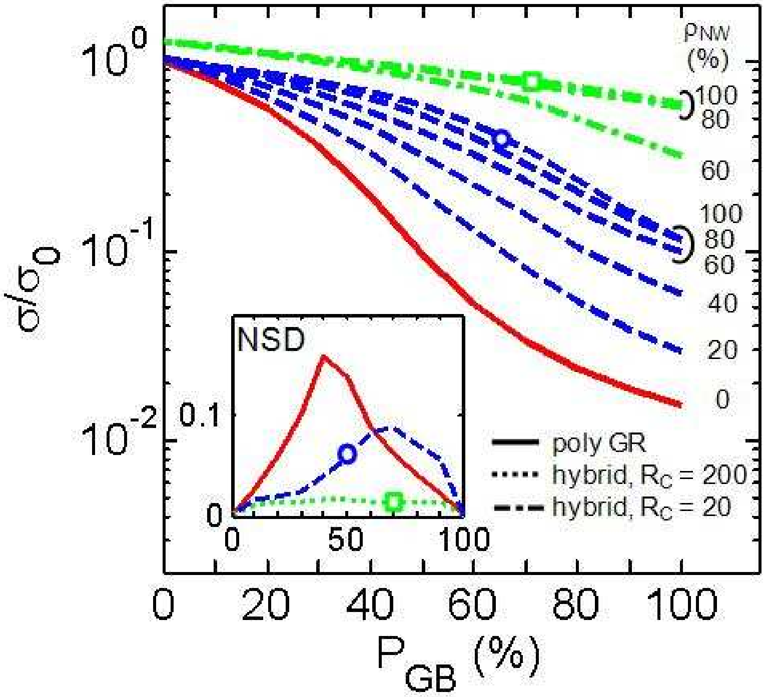

Figure 7.5. For a hybrid of polycrystalline graphene (poly GR) and nanowires (NW) mesh, the sheet conductance vs. the percentage of high-resistance grain boundary (P_{GB}) for two different contact resistance (R_C) are plotted as a function of NW density (ρ_{NW}). At $\rho_{NW} = 100\%$, average distance between NWs is ~10 μm and $\rho_{NW} = 0\%$ represents poly GR. Inset: the normalized standard deviation (NSD) is plotted.

To understand how NW-doping achieves this dramatic improvement, let us consider an illustrative example. In Figure 7.6a-f, we compare the FDM calculation of polycrystalline graphene sample with $P_{GB} \approx 35\%$ to that of hybrid polycrystalline graphene – metal NW in terms of the potential profile. Note that network of metal NWs is sparse enough not to form a continuous percolating path between electrodes. A sharp potential drop at the grain boundaries is observed for poly-graphene samples (See the boxed region in Figure 7.6b and 7.6c), but the impact of high-resistance GBs is significantly suppressed in the hybrid system (Figure 7.6e and 7.6f). This occurs because a sparse metal NW mesh provides a low-resistance path to bypass high-resistance GBs.

It is clear from the discussion above that the sheet conductivity of poly-graphene can be increased by doping it with a small number of Ag NWs, but does the approach compromise optical transmittance? For computational simplicity, we approximate the random NW dispersion with a regularized network (with the same spacing and the same dimensions of NW). Figure 7.6g shows the simulated transmittance for regular grating structures with a period of 10 μm, a line width of 100 nm, and a height of 100 nm, corresponding to a coverage of 100% ($\rho_{NW} = 100\%$). The average transmittance (of the TE and TM modes) exceeds 99%, i.e. $T_{Ag} > 0.99$. Given that the transmittance of monolayer poly-graphene is close to 97.7% as well, a graphene-NW composite is expected to achieve $T = T_{graphene} \times T_{Ag} \sim 0.96$. As shown in Figure 7.1, even with 2-3 layers of graphene, $T = \left(T_{graphene} \times T_{Ag}\right)^{n(=2-3)} > 0.90$ is obtained.

These R_S and T values of NW-doped poly-graphene suggest significant improvement of the tradeoff between R_S and T for the NW-doped poly-graphene as compared to conventional TCMs. There is an additional improvement: the NW-doped graphene also has reduced statistical variation in sheet resistance compared to pure poly-graphene films. The inset of Fig. 7.5 shows the normalized standard deviation (NSD) computed for polycrystalline graphene and the hybrid with $R_C \approx 200$ and $20\,\Omega \cdot \mu m$ as a function of P_{GB}. For a polycrystalline graphene, the maximum NSD is about 0.15, which means about 15% variation in sheet resistance among the samples. The inset figure shows that NSD values for the hybrid with $R_C \approx 200\,\Omega \cdot \mu m$ is significantly improved. For $P_{GB} \approx 35\%$, an 4× reduction of NSD is achieved. It is clear that a metal NW mesh can suppress variation.

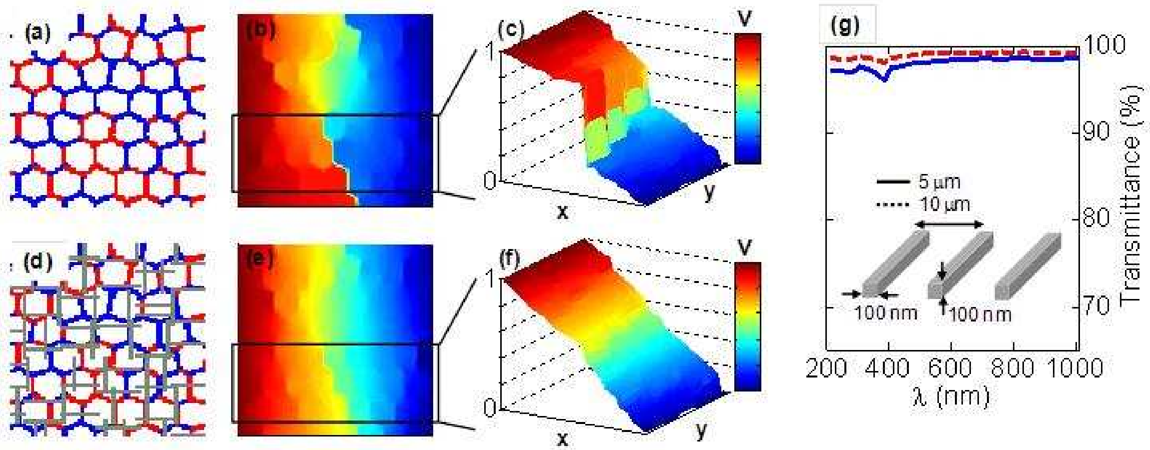

Figure 7.6. (a) A polycrystalline graphene sample with perturbed hexagonal grain for $P_{GB} = 35\%$. High-resistance and low-resistance grain boundaries (GB) are shown by red and blue line, respectively. (d) hybrid polycrystalline graphene – network of metal NW (gray solid line). (b, c, e, f) Corresponding potential profile are plotted for comparison. All potential data are normalized. The contact resistance between graphene and metal NW is assumed to be $200\,\Omega \cdot \mu m$. (g) The simulated transmittance vs. wavelength data for regular grating structures with a period of 5 and 10 μm, a line width of 100 nm, and a height of 100 nm. The average transmittance for the TE and TM mode are considered here.

Very recently, the concept of a metal NW-graphene composite has been experimentally demonstrated.[277] The experimental results are promising, but the two approaches are quite different. Zhu, et al., use graphene to enhance the performance of a metallic grid defined by top-down photolithography with spacing much larger than grain-sizes; the graphene provides a continuous conductive surface for the metallic grid. In contrast, we propose to randomly disperse a thin, sub-percolating network of metallic tubes to enhance the performance of a graphene conductor by opening up new conducting channels through high-resistance GBs. Our assumptions that (i) the net transmission can be expressed as a product of transmittance of individual layers and that (ii) a highly conducting metal grid can change the effective sheet resistivity of graphene from kΩ/sq to ~100 Ω/sq are clearly demonstrated by Fig. 7.2c and Table 1 of Ref. [34]. The two approaches have different trade-offs. The metallic grid-based approach may provide lower sheet resistance, while the NW-doped graphene-based approach being proposed here may provide greater flexibility and transmission.

7.5 Conclusions

In this study, the impact of the microstructure on electrical performance of the large-area polycrystalline graphene has been numerically explored based on experimentally reported parameters such as grain shape, grain size, statistical distributions, and grain and grain boundary resistances. The numerical results show that the grain shape and its grain size distribution do not substantially affect the electronic performance, but the grain size and the percentage of high-resistance grain boundaries play important roles. We propose a novel concept of NW-doping of poly-graphene by Ag NWs to beat the transparency-conductivity constraint of pure poly-graphene or pure NW networks. Our results show that both the sheet resistance and its variation can be significantly improved by using the hybrid without a loss of transmittance. These results should inspire new experiments in search of novel alternatives to TCOs.

8. CONCULSIONS AND FUTURE WORK

In this thesis, we presented comprehensive theoretical and simulational studies for nanoscale electronic and thermoelectric devices. The main accomplishments of this thesis are the following:

1) In Chapter 2, using a full band description of electronic bandstructure, the Landauer approach to diffusive transport was mathematically related to the solution of the Boltzmann transport equation, and expressions for the thermoelectric parameters in both formalisms were presented. Quantum mechanical and semiclassical techniques to obtain from a full description of the bandstructure, $E(k)$, the density of modes in the Landauer approach or the transport distribution in the Boltzmann solution were compared and thermoelectric transport coefficients were evaluated. Several example calculations for representative bulk materials were presented, and the full band results were related to the more common effective mass formalism. Finally, given a full $E(k)$ for a crystal, a procedure to extract an accurate, effective mass level description was presented.

2) In Chapter 3, using a full dispersion description of phonons, the thermal conductivities of bulk Si and Bi_2Te_3 were evaluated using a Landauer approach and related to the conventional approach based on the Boltzmann transport equation. A procedure to extract a well-defined average phonon mean-free-path from the measured thermal conductivity and given phonon-dispersion was presented. The extracted mean-free-path had strong physical significance and differed greatly from simple estimates. The use of simplified dispersion models for phonons was discussed, and it was shown that two different Debye temperatures must be used to treat the specific heat and thermal conductivity (analogous to the two different effective masses

needed to describe the electron density and conductivity). A simple technique to extract these two Debye temperatures was presented, and the limitations of the method were discussed.

3) In Chapter 4, the question of what fraction of the total heat flow in bulk and thin-film Si is transported by phonons with different mean-free-paths was addressed using a Landauer approach with a full dispersion description of phonons. For bulk Si, the results reproduced those of a recent molecular dynamic treatment showing that about 50% of the heat conduction is carried by phonons with a mean-free-path greater than about one micrometer. For the in-plane thermal conductivity of thin Si films, we found that the 50% point occurs at even shorter mean-free-paths. When the film thickness is smaller than ~$0.2\,\mu m$, 50% of the heat is carried by phonons with mean-free-paths longer than the film thickness. The cross-plane thermal conductivity of thin-films, where quasi-ballistic phonon transport becomes important, was also examined. For ballistic transport, the results reduced to the well-known Casimir limit [141]. These results shed light on phonon transport in bulk and thin-film silicon and demonstrated that the Landauer approach provides a relatively simple but accurate technique to treat phonon transport from the ballistic to diffusive regimes.

4) In Chapter 5, the question of what bandstructure produces the best thermoelectric device performance was revisited from a Landauer perspective. We found that a delta-function transport distribution function (TDF) results in operation at the Mahan-Sofo upper limit for the thermoelectric figure-of-merit, *ZT*. We showed, however, that the upper limit itself depends on the bandwidth (BW) of the dispersion, and therefore a finite BW dispersion produces a higher *ZT* when the lattice thermal conductivity is finite. Including a realistic model for scattering profoundly changes the results. Instead of a narrow band, we found that a broad BW is best. The prospects of increasing *ZT* through high valley degeneracy or by distorting the density-of-states were discussed

from a Landauer perspective. We concluded that while there is no simple answer to the question of what bandstructure produces the best thermoelectric performance, the important considerations can be expressed in terms of three parameters derived from the bandstructure – the density-of-states, $D(E)$, the number of channels, $M(E)$, and the mean-free-path, $\lambda(E)$.

5) In Chapter 6, we addressed the question of how to engineer the electronic structure to enhance the performance of a thermoelectric material. We examined electronic TE performance for several different materials. It was shown that most materials, even those for which giant Seebeck coefficients have been predicted, display a similar monotonic behavior of S vs. E_F that is expected from conventional thermoelectric theory. Using III-V alloy semiconductors as a model system, we demonstrated a promise of composite energy bands because that display a non-monotonic S vs. E_F behavior, which maintains high S at high carrier densities resulting in high PF. Our findings showed quantitatively how barriers in cross-plane superlattices degrade the electrical performance, i.e. power factor due to quantum mechanical effects, and that PF of multi barrier structures is no better than a single barrier TE device.

6) In Chapter 7, we shifted our attention to nanocomposite thermoelectric materials and a new approach to model nanocomposite (NC) TE devices was discussed. As a testbed of our model, recent experimental work on polycrystalline graphene was used. The effect of grain boundaries on the electronic performance of large-area polycrystalline graphene was investigated. We also demonstrated that a composite based on poly-crystalline graphene and a sub-percolating network of metallic nanowires offers a simple and effective route to reduced resistance while maintaining high transmittance. This new approach of ‘percolation-doping by nanowires’ has the potential to beat the transparency-conductivity constraints of existing materials and may

be suitable for broad applications in photovoltaics, flexible electronics, and displays.

There are a few possible directions to extend this work.

1) In Chapter 7, we developed computational framework for modeling the electronic performance of the polycrystalline materials that accounts for the distribution of grain boundaries (GBs) and grain sizes obtained from process simulation. For future work, a modeling of thermoelectric properties will be required to optimize the performance of nanocomposites (NC). The work in Chapters 3 and 4 can be extended to treat phonon transport in NCs. In particular, a simple phenomenological model is necessary to treat energy relaxation inside grain and evaluate Seebeck coefficient properly, which could be done using the previous results with non-equilibrium Green's function, as presented in Ref. [278].

2) While it is well known that GB properties and the grain statistics determine the performance of the NC TE devices, the microstructure-performance connection has generally been empirical. This is because grain and GB statistics are only known for specific instances, and there is no physical model that can predict the performance of NCs as a function of grain and GB statistics. Therefore, it will be worthwhile to develop a new NC modeling tool that is informed by the process-specific distribution of grains and GBs and associated electrical and thermal parameters of grains and GBs. A key strategy will be to use numerical simulation to identify the critical parameters for the performance and examine distinct classes of grain and interfacial microstructures such as the NCs with embedded nanoinclusions or lamellar structures obtained from thermal processing methods. The model will enable us to find a strategy to enhance bulk TE performances using various types of microstructures and to design NCs in short cycle times by reducing the parameter space to be explored by design-of-experiments (DOE) experiments.

3) Once the microstructure-aware modeling tool is sufficiently advanced, the output of physics-based process simulation of sintering, nucleation/growth, and spinodal decomposition would be directly transferred to the device modeling tools for a process-device co-modeling of grain- and GBs-influenced performances of TE devices. Such integrated capabilities are needed to investigate unexplored problems such as effects of process condition such as annealing on device performance and to predict long-term reliability.

LIST OF REFERENCES

LIST OF REFERENCES

[1] S.K. Bux, R.G. Blair, P.K. Gogna, H. Lee, G. Chen, M.S. Dresselhaus, R.B. Kaner, and J.-P. Fleurial, "Nanostructured Bulk Silicon as an Effective Thermoelectric Material," *Advanced Functional Materials*, vol. 19, 2009, pp. 2445–2452.

[2] L. Weber and E. Gmelin, "Transport properties of silicon," *Applied Physics A: Materials Science & Processing*, vol. 53, 1991, pp. 136–140.

[3] C. Jeong, R. Kim, M. Luisier, S. Datta, and M. Lundstrom, "On Landauer versus Boltzmann and full band versus effective mass evaluation of thermoelectric transport coefficients," *Journal of Applied Physics*, vol. 107, 2010, p. 023707.

[4] G. Homm, P.J. Klar, J. Teubert, and W. Heimbrodt, "Seebeck coefficients of n-type (Ga,In)(N,As), (B,Ga,In)As, and GaAs," *Applied Physics Letters*, vol. 93, Jul. 2008, pp. 042107–3.

[5] H. j Goldsmid, *Thermoelectric Refrigeration*, Plenum Press, 1964.

[6] Y. Ma, Q. Hao, B. Poudel, Y. Lan, B. Yu, D. Wang, G. Chen, and Z. Ren, "Enhanced Thermoelectric Figure-of-Merit in p-Type Nanostructured Bismuth Antimony Tellurium Alloys Made from Elemental Chunks," *Nano Letters*, vol. 8, 2008, pp. 2580–2584.

[7] X.W. Wang, H. Lee, Y.C. Lan, G.H. Zhu, G. Joshi, D.Z. Wang, J. Yang, A.J. Muto, M.Y. Tang, J. Klatsky, S. Song, M.S. Dresselhaus, G. Chen, and Z.F. Ren, "Enhanced thermoelectric figure of merit in nanostructured n-type silicon germanium bulk alloy," *Applied Physics Letters*, vol. 93, 2008, p. 193121.

[8] J.P. Heremans, V. Jovovic, E.S. Toberer, A. Saramat, K. Kurosaki, A. Charoenphakdee, S. Yamanaka, and G.J. Snyder, "Enhancement of Thermoelectric Efficiency in PbTe by Distortion of the Electronic Density of States," *Science*, vol. 321, Jul. 2008, pp. 554–557.

[9] A.I. Hochbaum, R. Chen, R.D. Delgado, W. Liang, E.C. Garnett, M. Najarian, A. Majumdar, and P. Yang, "Enhanced thermoelectric performance of rough silicon nanowires," *Nature*, vol. 451, Jan. 2008, pp. 163–167.

[10] A.I. Boukai, Y. Bunimovich, J. Tahir-Kheli, J.-K. Yu, W.A. Goddard III, and J.R. Heath, “Silicon nanowires as efficient thermoelectric materials,” *Nature*, vol. 451, Jan. 2008, pp. 168–171.

[11] R. Venkatasubramanian, E. Siivola, T. Colpitts, and B. O’Quinn, “Thin-film thermoelectric devices with high room-temperature figures of merit,” *Nature*, vol. 413, Oct. 2001, pp. 597–602.

[12] T.C. Harman, P.J. Taylor, M.P. Walsh, and B.E. LaForge, “Quantum Dot Superlattice Thermoelectric Materials and Devices,” *Science*, vol. 297, Sep. 2002, pp. 2229–2232.

[13] T. Harman, M. Walsh, B. laforge, and G. Turner, “Nanostructured thermoelectric materials,” *Journal of Electronic Materials*, vol. 34, May. 2005, pp. L19–L22.

[14] G.S. Nolas, M. Kaeser, R.T. Littleton IV, and T.M. Tritt, “High figure of merit in partially filled ytterbium skutterudite materials,” *Applied Physics Letters*, vol. 77, 2000, pp. 1855–1857.

[15] P.F.P. Poudeu, J. D’Angelo, A.D. Downey, J.L. Short, T.P. Hogan, and M.G. Kanatzidis, “High Thermoelectric Figure of Merit and Nanostructuring in Bulk p-type Na1−xPbmSbyTem+2,” *Angewandte Chemie International Edition*, vol. 45, Jun. 2006, pp. 3835–3839.

[16] J. Androulakis, C.-H. Lin, H.-J. Kong, C. Uher, C.-I. Wu, T. Hogan, B.A. Cook, T. Caillat, K.M. Paraskevopoulos, and M.G. Kanatzidis, “Spinodal Decomposition and Nucleation and Growth as a Means to Bulk Nanostructured Thermoelectrics: Enhanced Performance in Pb1-xSnxTe−PbS,” *Journal of the American Chemical Society*, vol. 129, 2007, pp. 9780–9788.

[17] K.F. Hsu, S. Loo, F. Guo, W. Chen, J.S. Dyck, C. Uher, T. Hogan, E.K. Polychroniadis, and M.G. Kanatzidis, “Cubic AgPbmSbTe2+m: Bulk Thermoelectric Materials with High Figure of Merit,” *Science*, vol. 303, Feb. 2004, pp. 818–821.

[18] J.R. Sootsman, H. Kong, C. Uher, J.J. D’Angelo, C.-I. Wu, T.P. Hogan, T. Caillat, and M.G. Kanatzidis, “Large Enhancements in the Thermoelectric Power Factor of Bulk PbTe at High Temperature by Synergistic Nanostructuring,” *Angewandte Chemie International Edition*, vol. 47, Oct. 2008, pp. 8618–8622.

[19] K. Biswas, J. He, Q. Zhang, G. Wang, C. Uher, V.P. Dravid, and M.G. Kanatzidis, “Strained endotaxial nanostructures with high thermoelectric figure of merit,” *Nature Chemistry*, vol. 3, Jan. 2011, pp. 160–166.

[20] M.G. Kanatzidis, “Nanostructured Thermoelectrics: The New Paradigm?†,” *Chemistry of Materials*, vol. 22, Feb. 2010, pp. 648–659.

[21] A.F. May, J.-P. Fleurial, and G.J. Snyder, “Thermoelectric performance of lanthanum telluride produced via mechanical alloying,” *Physical Review B*, vol. 78, 2008, p. 125205.

[22] H. Li, X. Tang, Q. Zhang, and C. Uher, “Rapid preparation method of bulk nanostructured Yb[sub 0.3]Co[sub 4]Sb[sub 12 + y] compounds and their improved thermoelectric performance,” *Applied Physics Letters*, vol. 93, Dec. 2008, pp. 252109–3.

[23] C.J. Vineis, T.C. Harman, S.D. Calawa, M.P. Walsh, R.E. Reeder, R. Singh, and A. Shakouri, “Carrier concentration and temperature dependence of the electronic transport properties of epitaxial PbTe and PbTe/PbSe nanodot superlattices,” *Physical Review B*, vol. 77, Jun. 2008, p. 235202.

[24] M. Asen-Palmer, K. Bartkowski, E. Gmelin, M. Cardona, A.P. Zhernov, A.V. Inyushkin, A. Taldenkov, V.I. Ozhogin, K.M. Itoh, and E.E. Haller, “Thermal conductivity of germanium crystals with different isotopic compositions,” *Physical Review B*, vol. 56, Oct. 1997, p. 9431.

[25] P.G. Klemens, “The Scattering of Low-Frequency Lattice Waves by Static Imperfections,” vol. A68, 1955, p. 1113.

[26] M.G. Holland, “Analysis of Lattice Thermal Conductivity,” *Physical Review*, vol. 132, Dec. 1963, p. 2461.

[27] A.J. Minnich, M.S. Dresselhaus, Z.F. Ren, and G. Chen, “Bulk nanostructured thermoelectric materials: current research and future prospects,” *Energy & Environmental Science*, vol. 2, 2009, pp. 466–479.

[28] M. Asheghi, M.N. Touzelbaev, K.E. Goodson, Y.K. Leung, and S.S. Wong, “Temperature-dependent thermal conductivity of single-crystal silicon layers in SOI substrates,” *Journal of heat transfer*, vol. 120, 1998, p. 30.

[29] M. Asheghi, Y.K. Leung, S.S. Wong, and K.E. Goodson, “Phonon-boundary scattering in thin silicon layers,” *Applied Physics Letters*, vol. 71, 1997, pp. 1798–1800.

[30] Y.S. Ju and K.E. Goodson, “Phonon scattering in silicon films with thickness of order 100 nm,” *Applied Physics Letters*, vol. 74, May. 1999, pp. 3005–3007.

[31] W. Liu and M. Asheghi, “Thermal conduction in ultrathin pure and doped single-crystal silicon layers at high temperatures,” *Journal of applied physics*, vol. 98, 2005, p. 123523.

[32] P.E. Hopkins, C.M. Reinke, M.F. Su, R.H. Olsson, E.A. Shaner, Z.C. Leseman, J.R. Serrano, L.M. Phinney, and I. El-Kady, “Reduction in the Thermal

Conductivity of Single Crystalline Silicon by Phononic Crystal Patterning," *Nano Lett.*, vol. 11, 2010, pp. 107–112.

[33] A.F. Ioffe, *Semiconductor Thermoelements and Thermoelectric Cooling*, Infosearch Limitied, 1957.

[34] S. Datta, *Lecture 4: Maxwell's demon: Energy from information*, 2010.

[35] M. Lundstrom, *ECE 656 Lecture 8: Thermoelectric Effects*, 2009.

[36] G.J. Snyder and E.S. Toberer, "Complex thermoelectric materials," *Nat Mater*, vol. 7, Feb. 2008, pp. 105–114.

[37] *Thermoelectrics Handbook Macro to Nano-Structured Materials (Ed: D. M.Rowe)*, Boca Raton, FL: Taylor&Francis, 2006.

[38] L.E. Bell, "Cooling, Heating, Generating Power, and Recovering Waste Heat with Thermoelectric Systems," *Science*, vol. 321, Sep. 2008, pp. 1457–1461.

[39] *Thermoelectrics Handbook Macro to Nano-Structured Materials (Ed: D. M.Rowe)*, Boca Raton, FL: Taylor&Francis, 2006.

[40] K. Matsubara and M. Matsuura, *Thermoelectrics Handbook Macro to Nano-Structured Materials (Ed: D. M.Rowe)*, Boca Raton, FL: Taylor&Francis, 2006.

[41] I. Chowdhury, R. Prasher, K. Lofgreen, G. Chrysler, S. Narasimhan, R. Mahajan, D. Koester, R. Alley, and R. Venkatasubramanian, "On-chip cooling by superlattice-based thin-film thermoelectrics," *Nat Nano*, vol. 4, 2009, pp. 235–238.

[42] A. Shakouri, "Nanoscale Thermal Transport and Microrefrigerators on a Chip," *Proceedings of the IEEE*, vol. 94, 2006, pp. 1613–1638.

[43] G.J. Snyder, M. Soto, R. Alley, D. Koester, B. Conner, and N.T. Solutions, "Hot spot cooling using embedded thermoelectric coolers," *2006 IEEE Twenty-Second Annual IEEE Semiconductor Thermal Measurement and Management Symposium*, 2006, pp. 135–143.

[44] A. Bentien, S. Johnsen, G.K.H. Madsen, B.B. Iversen, and F. Steglich, "Colossal Seebeck coefficient in strongly correlated semiconductor FeSb2," *EPL (Europhysics Letters)*, vol. 80, 2007, p. 17008.

[45] M. Lundstrom, *ECE 656 Lecture 9: Coupled Current Equations*, 2009.

[46] J. Fairbanks, "The Growth Potential of Thermoelectrics," San Diego, CA, USA: 2009.

[47] A. Majumdar, “MATERIALS SCIENCE: Enhanced: Thermoelectricity in Semiconductor Nanostructures,” *Science*, vol. 303, Feb. 2004, pp. 777–778.

[48] M.D. Ulrich, P.A. Barnes, and C.B. Vining, “Comparison of solid-state thermionic refrigeration with thermoelectric refrigeration,” *Journal of Applied Physics*, vol. 90, 2001, p. 1625.

[49] G.J. Snyder and T.S. Ursell, “Thermoelectric Efficiency and Compatibility,” *Physical Review Letters*, vol. 91, Oct. 2003, p. 148301.

[50] L.D. Hicks and M.S. Dresselhaus, “Thermoelectric figure of merit of a one-dimensional conductor,” *Physical Review B*, vol. 47, 1993, pp. 16631–16634.

[51] L.D. Hicks and M.S. Dresselhaus, “Effect of quantum-well structures on the thermoelectric figure of merit,” *Physical Review B*, vol. 47, May. 1993, p. 12727.

[52] M. Christensen, A.B. Abrahamsen, N.B. Christensen, F. Juranyi, N.H. Andersen, K. Lefmann, J. Andreasson, C.R.H. Bahl, and B.B. Iversen, “Avoided crossing of rattler modes in thermoelectric materials,” *Nat Mater*, vol. 7, Oct. 2008, pp. 811–815.

[53] L.D. Hicks, T.C. Harman, X. Sun, and M.S. Dresselhaus, “Experimental study of the effect of quantum-well structures on the thermoelectric figure of merit,” *Physical Review B*, vol. 53, Apr. 1996, p. R10493.

[54] Woochul Kim, S. Singer, A. Majumdar, J. Zide, A. Gossard, and A. Shakouri, “Role of nanostructures in reducing thermal conductivity below alloy limit in crystalline solids,” *Thermoelectrics, 2005. ICT 2005. 24th International Conference on*, 2005, pp. 9–12.

[55] W. Kim, S.L. Singer, A. Majumdar, D. Vashaee, Z. Bian, A. Shakouri, G. Zeng, J.E. Bowers, J.M.O. Zide, and A.C. Gossard, “Cross-plane lattice and electronic thermal conductivities of ErAs: InGaAs/ InGaAlAs superlattices,” *Applied Physics Letters*, vol. 88, 2006, p. 242107.

[56] X. Sun, S.B. Cronin, J. Liu, K.L. Wang, T. Koga, M.S. Dresselhaus, and G. Chen, “Experimental study of the effect of the quantum well structures on the thermoelectric figure of merit in Si/Si1-xGex system,” *Thermoelectrics, 1999. Eighteenth International Conference on*, 1999, pp. 652–655.

[57] G. Joshi, H. Lee, Y. Lan, X. Wang, G. Zhu, D. Wang, R.W. Gould, D.C. Cuff, M.Y. Tang, M.S. Dresselhaus, G. Chen, and Z. Ren, “Enhanced Thermoelectric Figure-of-Merit in Nanostructured p-type Silicon Germanium Bulk Alloys,” *Nano Letters*, vol. 8, Dec. 2008, pp. 4670–4674.

[58] L. Shi, D. Li, C. Yu, W. Jang, D. Kim, Z. Yao, P. Kim, and A. Majumdar, “Measuring Thermal and Thermoelectric Properties of One-Dimensional

Nanostructures Using a Microfabricated Device," *Journal of Heat Transfer*, vol. 125, Oct. 2003, pp. 881–888.

[59] A. Balandin and K.L. Wang, "Significant decrease of the lattice thermal conductivity due to phonon confinement in a free-standing semiconductor quantum well," *Physical Review B*, vol. 58, 1998, pp. 1544–1549.

[60] S.G. Walkauskas, D.A. Broido, K. Kempa, and T.L. Reinecke, "Lattice thermal conductivity of wires," *Journal of Applied Physics*, vol. 85, 2009, pp. 2579–2582.

[61] W. Kim, J. Zide, A. Gossard, D. Klenov, S. Stemmer, A. Shakouri, and A. Majumdar, "Thermal Conductivity Reduction and Thermoelectric Figure of Merit Increase by Embedding Nanoparticles in Crystalline Semiconductors," *Physical Review Letters*, vol. 96, Feb. 2006, pp. 045901–4.

[62] T. Koga, X. Sun, S.B. Cronin, and M.S. Dresselhaus, "Carrier pocket engineering to design superior thermoelectric materials using GaAs/AlAs superlattices," *Applied Physics Letters*, vol. 73, Nov. 1998, pp. 2950–2952.

[63] T. Koga, S.B. Cronin, M.S. Dresselhaus, J.L. Liu, and K.L. Wang, "Experimental proof-of-principle investigation of enhanced Z[sub 3D]T in (001) oriented Si/Ge superlattices," *Applied Physics Letters*, vol. 77, 2000, pp. 1490–1492.

[64] D. Bilc, S.D. Mahanti, E. Quarez, K.-F. Hsu, R. Pcionek, and M.G. Kanatzidis, "Resonant States in the Electronic Structure of the High Performance Thermoelectrics AgPbmSbTe2+m: The Role of Ag-Sb Microstructures," *Physical Review Letters*, vol. 93, 2004, p. 146403.

[65] A.F. May, D.J. Singh, and G.J. Snyder, "Influence of band structure on the large thermoelectric performance of lanthanum telluride," *Physical Review B*, vol. 79, Apr. 2009, p. 153101.

[66] D. Dragoman and M. Dragoman, "Giant thermoelectric effect in graphene," *Applied Physics Letters*, vol. 91, Nov. 2007, pp. 203116–3.

[67] C.M. Finch, V.M. Garcia-Suarez, and C.J. Lambert, "Giant thermopower and figure of merit in single-molecule devices," *Physical Review B (Condensed Matter and Materials Physics)*, vol. 79, Jan. 2009, pp. 033405–4.

[68] T. Koga, X. Sun, S.B. Cronin, and M.S. Dresselhaus, "Carrier pocket engineering applied to ``strained'' Si/Ge superlattices to design useful thermoelectric materials," *Applied Physics Letters*, vol. 75, Oct. 1999, pp. 2438–2440.

[69] T. Thonhauser, T.J. Scheidemantel, J.O. Sofo, J.V. Badding, and G.D. Mahan, "Thermoelectric properties of Sb_ {2} Te_ {3} under pressure and uniaxial stress," *Physical Review B*, vol. 68, 2003, p. 85201.

[70] T. Borca-Tasciuc, W. Liu, J. Liu, T. Zeng, D.W. Song, C.D. Moore, G. Chen, K.L. Wang, M.S. Goorsky, and T. Radetic, "Thermal conductivity of symmetrically strained Si/Ge superlattices," *SUPERLATTICES AND MICROSTRUCTURES*, vol. 28, 2000, pp. 199–206.

[71] D.A. Polvani, J.F. Meng, N.V. Chandra Shekar, J. Sharp, and J.V. Badding, "Large Improvement in Thermoelectric Properties in Pressure-Tuned p-Type Sb1.5Bi0.5Te3," *Chem. Mater.*, vol. 13, May. 2001, p. 2068.

[72] L.W. Whitlow and T. Hirano, "Superlattice applications to thermoelectricity," *Journal of Applied Physics*, vol. 78, 1995, p. 5460.

[73] W. Kim, J. Zide, A. Gossard, D. Klenov, S. Stemmer, A. Shakouri, and A. Majumdar, "Thermal Conductivity Reduction and Thermoelectric Figure of Merit Increase by Embedding Nanoparticles in Crystalline Semiconductors," *Physical Review Letters*, vol. 96, Feb. 2006, p. 045901.

[74] J.M.O. Zide, D. Vashaee, Z.X. Bian, G. Zeng, J.E. Bowers, A. Shakouri, and A.C. Gossard, "Demonstration of electron filtering to increase the Seebeck coefficient in In[sub 0.53]Ga[sub 0.47]As/In[sub 0.53]Ga[sub 0.28]Al[sub 0.19]As superlattices," *Physical Review B (Condensed Matter and Materials Physics)*, vol. 74, Nov. 2006, pp. 205335–5.

[75] J.P. Heremans, C.M. Thrush, and D.T. Morelli, "Thermopower enhancement in lead telluride nanostructures," *Physical Review B*, vol. 70, 2004, p. 115334.

[76] *Thermoelectrics Handbook Macro to Nano-Structured Materials (Ed: D. M.Rowe)*, Boca Raton, FL: Taylor&Francis, 2006.

[77] H.J. Ryu, Z. Aksamija, D.M. Paskiewicz, S.A. Scott, M.G. Lagally, I. Knezevic, and M.A. Eriksson, "Quantitative Determination of Contributions to the Thermoelectric Power Factor in Si Nanostructures," *Physical Review Letters*, vol. 105, Dec. 2010, p. 256601.

[78] *Thermoelectrics Handbook Macro to Nano-Structured Materials (Ed: D. M.Rowe)*, Boca Raton, FL: Taylor&Francis, 2006.

[79] P. Sun, N. Oeschler, S. Johnsen, B.B. Iversen, and F. Steglich, "Huge Thermoelectric Power Factor: FeSb2 versus FeAs2 and RuSb2," *Applied Physics Express*, vol. 2, 2009, p. 091102.

[80] P. Sun, N. Oeschler, S. Johnsen, B.B. Iversen, and F. Steglich, "FeSb[sub 2]: Prototype of huge electron-diffusion thermoelectricity," *Physical Review B (Condensed Matter and Materials Physics)*, vol. 79, Apr. 2009, pp. 153308–4.

[81] Y. Wang, N.S. Rogado, R.J. Cava, and N.P. Ong, “Spin entropy as the likely source of enhanced thermopower in NaxCo2O4,” *Nature*, vol. 423, May. 2003, pp. 425–428.

[82] G.D. Mahan, “Thermionic refrigeration,” *Journal of Applied Physics*, vol. 76, Oct. 1994, pp. 4362–4366.

[83] G.D. Mahan and L.M. Woods, “Multilayer Thermionic Refrigeration,” *Physical Review Letters*, vol. 80, 1998, pp. 4016–4019.

[84] G. Mahan, B. Sales, and J. Sharp, “Thermoelectric materials: New approaches to an old problem,” *Physics Today*, vol. 50, 1997, pp. 42–47.

[85] A. Shakouri, C. LaBounty, J. Piprek, P. Abraham, and J.E. Bowers, “Thermionic emission cooling in single barrier heterostructures,” *Applied Physics Letters*, vol. 74, 1999, p. 88.

[86] D.K. Schroder, *Semiconductor material and device characterization*, John Wiley and Sons, 2006.

[87] *Thermoelectrics Handbook Macro to Nano-Structured Materials (Ed: D. M.Rowe)*, Boca Raton, FL: Taylor&Francis, 2006.

[88] T.C. Harman, “Special Techniques for Measurement of Thermoelectric Properties,” *Journal of Applied Physics*, vol. 29, Sep. 1958, pp. 1373–1374.

[89] H. Iwasaki, S. Yokoyama, T. Tsukui, M. Koyano, and H.H. and S. Sano, “Evaluation of the Figure of Merit of Thermoelectric Modules by Harman Method,” *Japanese Journal of Applied Physics*, vol. 42, 2003, pp. 3707–3708.

[90] R. Singh, Z. Bian, G. Zeng, J. Zide, J. Christofferson, H. Chou, A. Gossard, J. Bowers, and A. Shakouri, “Transient Harman Measurement of the Cross-plane ZT of InGaAs/InGaAlAs Superlattices with Embedded ErAs Nanoparticles,” *MATERIALS RESEARCH SOCIETY SYMPOSIUM PROCEEDINGS*, Warrendale, Pa.; Materials Research Society; 1999, 2006, p. 123.

[91] M.S. Dresselhaus, G. Chen, M.Y. Tang, R.G. Yang, H. Lee, D.Z. Wang, Z.F. Ren, J.P. Fleurial, and P. Gogna, “New directions for low-dimensional thermoelectric materials,” *Advanced Materials*, vol. 19, 2007, pp. 1043–1053.

[92] D.L. Medlin and G.J. Snyder, “Interfaces in bulk thermoelectric materials: A review for Current Opinion in Colloid and Interface Science,” *Current Opinion in Colloid & Interface Science*, vol. 14, Aug. 2009, pp. 226–235.

[93] G. Chen, “Thermal conductivity and ballistic-phonon transport in the cross-plane direction of superlattices,” *Physical Review B*, vol. 57, Jun. 1998, p. 14958.

[94] *Thermoelectrics Handbook (Ed: D. M.Rowe)*, Boca Raton, FL: Taylor&Francis, 1995.

[95] H.J. Goldsmid, *Introduction to thermoelectricity*, Springer Verlag, 2009.

[96] B. Poudel, Q. Hao, Y. Ma, Y. Lan, A. Minnich, B. Yu, X. Yan, D. Wang, A. Muto, D. Vashaee, X. Chen, J. Liu, M.S. Dresselhaus, G. Chen, and Z. Ren, "High-Thermoelectric Performance of Nanostructured Bismuth Antimony Telluride Bulk Alloys," *Science*, vol. 320, May. 2008, pp. 634–638.

[97] W. Xie, J. He, H.J. Kang, X. Tang, S. Zhu, M. Laver, S. Wang, J.R.D. Copley, C.M. Brown, Q. Zhang, and T.M. Tritt, "Identifying the Specific Nanostructures Responsible for the High Thermoelectric Performance of (Bi,Sb)2Te3 Nanocomposites," *Nano Letters*, vol. 10 (9), 2010, pp. 3283–3289.

[98] H. Lee, D. Vashaee, D.Z. Wang, M.S. Dresselhaus, Z.F. Ren, and G. Chen, "Effects of nanoscale porosity on thermoelectric properties of SiGe," *Journal of Applied Physics*, vol. 107, 2010, p. 094308.

[99] A. Minnich, H. Lee, X. Wang, G. Joshi, M. Dresselhaus, Z. Ren, G. Chen, and D. Vashaee, "Modeling study of thermoelectric SiGe nanocomposites," *Physical Review B*, vol. 80, Oct. 2009.

[100] H. Li, X. Tang, Q. Zhang, and C. Uher, "High performance In[sub x]Ce[sub y]Co[sub 4]Sb[sub 12] thermoelectric materials with in situ forming nanostructured InSb phase," *Applied Physics Letters*, vol. 94, 2009, p. 102114.

[101] Y. Lan, A.J. Minnich, G. Chen, and Z. Ren, "Enhancement of Thermoelectric Figure-of-Merit by a Bulk Nanostructuring Approach," *Advanced Functional Materials*, vol. 20, 2010, pp. 357–376.

[102] K. Kishimoto, M. Tsukamoto, and T. Koyanagi, "Temperature dependence of the Seebeck coefficient and the potential barrier scattering of n-type PbTe films prepared on heated glass substrates by rf sputtering," *Journal of Applied Physics*, vol. 92, Nov. 2002, pp. 5331–5339.

[103] K. Kishimoto and T. Koyanagi, "Preparation of sintered degenerate n-type PbTe with a small grain size and its thermoelectric properties," *Journal of Applied Physics*, vol. 92, 2002, pp. 2544–2549.

[104] L.-D. Zhao, B.-P. Zhang, W.-S. Liu, and J.-F. Li, "Effect of mixed grain sizes on thermoelectric performance of Bi[sub 2]Te[sub 3] compound," *Journal of Applied Physics*, vol. 105, Jan. 2009, pp. 023704–6.

[105] A. Popescu, L.M. Woods, J. Martin, and G.S. Nolas, "Model of transport properties of thermoelectric nanocomposite materials," *Physical Review B*, vol. 79, May. 2009, p. 205302.

[106] J. Zhou, X. Li, G. Chen, and R. Yang, “Semiclassical model for thermoelectric transport in nanocomposites,” *Physical Review B*, vol. 82, 2010, p. 115308.

[107] G. Wilde, *Nanostructured materials*, Elsevier, 2009.

[108] J.-P. Fleurial, “Lecture 3: Selection and Evaluation of Materials for Thermoelectric Applications,” *SCT-93 Short Course on Thermoelectrics*, Yokohama-shi, Japan: International Thermoelectric Society, 1993.

[109] J.R. Sootsman, R.J. Pcionek, H. Kong, C. Uher, and M.G. Kanatzidis, “Strong Reduction of Thermal Conductivity in Nanostructured PbTe Prepared by Matrix Encapsulation,” *Chemistry of Materials*, vol. 18, Oct. 2006, pp. 4993–4995.

[110] M. Zhou, J.-F. Li, and T. Kita, “Nanostructured AgPbmSbTem+2 System Bulk Materials with Enhanced Thermoelectric Performance,” *Journal of the American Chemical Society*, vol. 130, Apr. 2008, pp. 4527–4532.

[111] B.A. Cook, M.J. Kramer, J.L. Harringa, M.-K. Han, D.-Y. Chung, and M.G. Kanatzidis, “Analysis of Nanostructuring in High Figure-of-Merit Ag1–xPbmSbTe2+m Thermoelectric Materials,” *Advanced Functional Materials*, vol. 19, 2009, pp. 1254–1259.

[112] B. Poudel, Q. Hao, Y. Ma, Y. Lan, A. Minnich, B. Yu, X. Yan, D. Wang, A. Muto, D. Vashaee, X. Chen, J. Liu, M.S. Dresselhaus, G. Chen, and Z. Ren, “High-Thermoelectric Performance of Nanostructured Bismuth Antimony Telluride Bulk Alloys,” *Science*, vol. 320, May. 2008, pp. 634–638.

[113] M. Groeber, S. Ghosh, M.D. Uchic, and D.M. Dimiduk, “A framework for automated analysis and simulation of 3D polycrystalline microstructures.: Part 1: Statistical characterization,” *Acta Materialia*, vol. 56, Apr. 2008, pp. 1257–1273.

[114] M. Groeber, S. Ghosh, M.D. Uchic, and D.M. Dimiduk, “Developing a robust 3-D characterization-representation framework for modeling polycrystalline materials,” *JOM Journal of the Minerals, Metals and Materials Society*, vol. 59, 2007, pp. 32–36.

[115] M.A. Schneider, M. Wenderoth, A.J. Heinrich, M.A. Rosentreter, and R.G. Ulbrich, “Current transport through single grain boundaries: A scanning tunneling potentiometry study,” *Applied Physics Letters*, vol. 69, 1996, p. 1327.

[116] T.-H. Kim, X.-G. Zhang, D.M. Nicholson, B.M. Evans, N.S. Kulkarni, B. Radhakrishnan, E.A. Kenik, and A.-P. Li, “Large Discrete Resistance Jump at Grain Boundary in Copper Nanowire,” *Nano Letters*, vol. 10, 2010, pp. 3096–3100.

[117] D.G. Cahill, K. Goodson, and A. Majumdar, “Thermometry and Thermal Transport in Micro/Nanoscale Solid-State Devices and Structures,” *Journal of Heat Transfer*, vol. 124, Apr. 2002, pp. 223–241.

[118] H.-K. Lyeo, A.A. Khajetoorians, L. Shi, K.P. Pipe, R.J. Ram, A. Shakouri, and C.K. Shih, “Profiling the Thermoelectric Power of Semiconductor Junctions with Nanometer Resolution,” *Science*, vol. 303, Feb. 2004, pp. 816–818.

[119] N. Chen, F. Gascoin, G.J. Snyder, E. Muller, G. Karpinski, and C. Stiewe, “Macroscopic thermoelectric inhomogeneities in (AgSbTe[sub 2])[sub x](PbTe)[sub 1 - x],” *Applied Physics Letters*, vol. 87, Oct. 2005, pp. 171903–3.

[120] J.Y.W. Seto, “The electrical properties of polycrystalline silicon films,” *Journal of Applied Physics*, vol. 46, 1975, p. 5247.

[121] A.F. Mayadas and M. Shatzkes, “Electrical-Resistivity Model for Polycrystalline Films: the Case of Arbitrary Reflection at External Surfaces,” *Physical Review B*, vol. 1, Feb. 1970, p. 1382.

[122] C.R. Tellier and A.J. Tosser, “Thermoelectric power of metallic films in the Mayadas-Shatzkes model,” *Thin Solid Films*, vol. 41, Mar. 1977, pp. 161–166.

[123] E.T. Swartz and R.O. Pohl, “Thermal boundary resistance,” *Reviews of Modern Physics*, vol. 61, Jul. 1989, p. 605.

[124] D.J. Bergman and O. Levy, “Thermoelectric properties of a composite medium,” *Journal of Applied Physics*, vol. 70, 1991, p. 6821.

[125] D.J. Bergman and L.G. Fel, “Enhancement of thermoelectric power factor in composite thermoelectrics,” *Journal of Applied Physics*, vol. 85, Jun. 1999, pp. 8205–8216.

[126] I. Webman, J. Jortner, and M.H. Cohen, “Thermoelectric power in inhomogeneous materials,” *Physical Review B*, vol. 16, 1977, p. 2959.

[127] O. Levy and D.J. Bergman, “Scaling behaviour of the thermopower in a two-component composite near a percolation threshold,” *Journal of Physics A: Mathematical and General*, vol. 25, 1992, p. 1875.

[128] M. Lundstrom, *Fundamentals of carrier transport*, Cambridge Univ Pr, 2000.

[129] X. Zhou, S.B. Chiah, and K.Y. Lim, “A compact deep-submicron MOSFET gds model including hot-electron and thermoelectric effects,” *Solid-State Electronics*, vol. 48, 2004, pp. 2125–2131.

[130] K.P. Pipe, R.J. Ram, and A. Shakouri, “Bias-dependent Peltier coefficient and internal cooling in bipolar devices,” *Physical Review B*, vol. 66, 2002, p. 125316.

[131] W.Y. Zhou, Y.B. Liou, and C. Huang, "Steady-state and transient heat responses in AlGaAs/GaAs HBTs," *Solid-State Electronics*, vol. 38, May. 1995, pp. 1118–1120.

[132] S.V. Faleev and F. Leonard, "Theory of enhancement of thermoelectric properties of materials with nanoinclusions," *Physical Review B*, vol. 77, Jun. 2008, p. 214304.

[133] M. Zebarjadi, K. Esfarjani, A. Shakouri, J.-H. Bahk, Z. Bian, G. Zeng, J. Bowers, H. Lu, J. Zide, and A. Gossard, "Effect of nanoparticle scattering on thermoelectric power factor," *Applied Physics Letters*, vol. 94, 2009, p. 202105.

[134] R. Yang and G. Chen, "Thermal conductivity modeling of periodic two-dimensional nanocomposites," *Physical Review B*, vol. 69, May. 2004, p. 195316.

[135] M.-S. Jeng, R. Yang, D. Song, and G. Chen, "Modeling the Thermal Conductivity and Phonon Transport in Nanoparticle Composites Using Monte Carlo Simulation," *Journal of Heat Transfer*, vol. 130, Apr. 2008, pp. 042410–11.

[136] A.S. Henry and G. Chen, "Spectral phonon transport properties of silicon based on molecular dynamics simulations and lattice dynamics," *Journal of Computational and Theoretical Nanoscience*, vol. 5, 2008, pp. 141–152.

[137] A. Minnich and G. Chen, "Modified effective medium formulation for the thermal conductivity of nanocomposites," *Applied Physics Letters*, vol. 91, 2007, p. 073105.

[138] W. Zhang, T.S. Fisher, and N. Mingo, "Simulation of Interfacial Phonon Transport in Si--Ge Heterostructures Using an Atomistic Green's Function Method," *Journal of Heat Transfer*, vol. 129, Apr. 2007, pp. 483–491.

[139] C. Bera, M. Soulier, C. Navone, G. Roux, J. Simon, S. Volz, and N. Mingo, "Thermoelectric properties of nanostructured Si[sub 1 - x]Ge[sub x] and potential for further improvement," *Journal of Applied Physics*, vol. 108, Dec. 2010, pp. 124306–8.

[140] A. Khitun, K.L. Wang, and G. Chen, "Thermoelectric figure of merit enhancement in a quantum dot superlattice," *Nanotechnology*, vol. 11, 2000, p. 327.

[141] H.B.G. Casimir, "Note on the conduction of heat in crystals," *Physica*, vol. 5, 1938, pp. 495–500.

[142] D.J. Singh, "Theoretical Considerations for Finding New Thermoelectric Materials," *MATERIALS RESEARCH SOCIETY SYMPOSIUM PROCEEDINGS*, Warrendale, Pa.; Materials Research Society; 1999, 2002, pp. 15–22.

[143] K.F. Hsu, S. Loo, F. Guo, W. Chen, J.S. Dyck, C. Uher, T. Hogan, E.K. Polychroniadis, and M.G. Kanatzidis, “Cubic AgPbmSbTe2+m: Bulk Thermoelectric Materials with High Figure of Merit,” *Science*, vol. 303, Feb. 2004, pp. 818–821.

[144] S. Ohta, T. Nomura, H. Ohta, M. Hirano, H. Hosono, and K. Koumoto, “Large thermoelectric performance of heavily Nb-doped SrTiO[sub 3] epitaxial film at high temperature,” *Applied Physics Letters*, vol. 87, 2005, pp. 092108–3.

[145] D.A. Broido and T.L. Reinecke, “Thermoelectric figure of merit of quantum wire superlattices,” *Applied Physics Letters*, vol. 67, Jul. 1995, pp. 100–102.

[146] O. Rabina, Y.-M. Lin, and M.S. Dresselhaus, “Anomalously high thermoelectric figure of merit in Bi[sub 1 - x]Sb[sub x] nanowires by carrier pocket alignment,” *Applied Physics Letters*, vol. 79, Jul. 2001, pp. 81–83.

[147] P. Martin, Z. Aksamija, E. Pop, and U. Ravaioli, “Impact of Phonon-Surface Roughness Scattering on Thermal Conductivity of Thin Si Nanowires,” *Physical Review Letters*, vol. 102, Mar. 2009, pp. 125503–4.

[148] T. Markussen, A.-P. Jauho, and M. Brandbyge, “Electron and phonon transport in silicon nanowires: Atomistic approach to thermoelectric properties,” *Physical Review B (Condensed Matter and Materials Physics)*, vol. 79, Jan. 2009, pp. 035415–7.

[149] N. Mingo, “Thermoelectric figure of merit and maximum power factor in III--V semiconductor nanowires,” *Applied Physics Letters*, vol. 84, Apr. 2004, pp. 2652–2654.

[150] M.P. Singh and C.M. Bhandari, “Thermoelectric properties of bismuth telluride quantum wires,” *Solid State Communications*, vol. 127, Sep. 2003, pp. 649–654.

[151] E.B. Ramayya, D. Vasileska, S.M. Goodnick, and I. Knezevic, “Thermoelectric Properties of Silicon Nanowires,” *Nanotechnology, 2008. NANO ’08. 8th IEEE Conference on*, 2008, pp. 339–342.

[152] I. Bejenari and V. Kantser, “Thermoelectric properties of the bismuth telluride nanowires in the constant-relaxation-time approximation,” *Phys. Rev. B*, vol. 78, 2008, pp. 115322–12.

[153] Y.-M. Lin, X. Sun, and 2 Dresselhaus1, “Theoretical investigation of thermoelectric transport properties of cylindrical Bi nanowires,” *Physical Review B*, vol. 62, 2000, p. 4610.

[154] T.T.M. Vo, A.J. Williamson, V. Lordi, and G. Galli, “Atomistic Design of Thermoelectric Properties of Silicon Nanowires,” *Nano Letters*, vol. 8, Apr. 2008, pp. 1111–1114.

[155] L.D. Hicks, T.C. Harman, and M.S. Dresselhaus, “Use of quantum-well superlattices to obtain a high figure of merit from nonconventional thermoelectric materials,” *Applied Physics Letters*, vol. 63, Dec. 1993, pp. 3230–3232.

[156] G. Wang and T. Cagin, “Electronic structure of the thermoelectric materials Bi[sub 2]Te[sub 3] and Sb[sub 2]Te[sub 3] from first-principles calculations,” *Physical Review B (Condensed Matter and Materials Physics)*, vol. 76, 2007, pp. 075201–8.

[157] V. Rawat, “Growth and characterization of metal-semiconductor nitride multilayers and superlattices for solid state thermionic energy conversion,” Purdue University, 2008.

[158] D. Vashaee and A. Shakouri, “Improved Thermoelectric Power Factor in Metal-Based Superlattices,” *Physical Review Letters*, vol. 92, 2004, p. 106103.

[159] J.O. Sofo and G.D. Mahan, “Thermoelectric figure of merit of superlattices,” *Applied Physics Letters*, vol. 65, 1994, p. 2690.

[160] X.B. Zhao, X.H. Ji, Y.H. Zhang, T.J. Zhu, J.P. Tu, and X.B. Zhang, “Bismuth telluride nanotubes and the effects on the thermoelectric properties of nanotube-containing nanocomposites,” *Applied Physics Letters*, vol. 86, Feb. 2005, pp. 062111–3.

[161] Ming-Shan Jeng, Ronggui Yang, and Gang Chen, “Monte Carlo simulation of thermoelectric properties in nanocomposites,” *Thermoelectrics, 2005. ICT 2005. 24th International Conference on*, 2005, pp. 21–26.

[162] Hohyun Lee, Dezhi Wang, Wenzhong Wang, Zhifeng Ren, B. Klotz, M.Y. Tang, Ronggui Yang, P. Gogna, J.-P. Fleuiral, M.S. Dresselhaus, and Gang Chen, “Thermoelectric properties of Si/Ge nano-composite,” *Thermoelectrics, 2005. ICT 2005. 24th International Conference on*, 2005, pp. 269–271.

[163] G.D. Mahan and J.O. Sofo, *The best thermoelectric*, National Acad Sciences, 1996.

[164] R. Landauer, vol. 1, 1957, p. 223.

[165] S. Datta, *Electronic Transport in Mesoscopic Systems*, Cambridge University Press, 1997.

[166] R. Kim, S. Datta, and M.S. Lundstrom, “Influence of dimensionality on thermoelectric device performance,” *Journal of Applied Physics*, vol. 105, Feb. 2009, pp. 034506–6.

[167] P. Pecheur and G. Toussaint, “Electronic structure and bonding in bismuth telluride,” *Physics Letters A*, vol. 135, Feb. 1989, pp. 223–226.

[168] S. Lee and P. von Allmen, "Tight-binding modeling of thermoelectric properties of bismuth telluride," *Applied Physics Letters*, vol. 88, Jan. 2006, pp. 022107–3.

[169] T.J. Scheidemantel, C. Ambrosch-Draxl, T. Thonhauser, J.V. Badding, and J.O. Sofo, "Transport coefficients from first-principles calculations," *Physical Review B*, vol. 68, 2003, p. 125210.

[170] S. Katsuki, "The Band Structure of Bismuth Telluride," *Journal of the Physical Society of Japan*, vol. 26, 1969, pp. 58–64.

[171] P.M. Lee and L. Pincherle, "The Electronic Band Structure of Bismuth Telluride," *Proceedings of the Physical Society*, vol. 81, 1963, pp. 461–469.

[172] S.K. Mishra, S. Satpathy, and O. Jepsen, "Electronic structure and thermoelectric properties of bismuth telluride and bismuth selenide," *JOURNAL OF PHYSICS CONDENSED MATTER*, vol. 9, 1997, pp. 461–470.

[173] S.J. Youn and A.J. Freeman, "First-principles electronic structure and its relation to thermoelectric properties of Bi2Te3," *Physical Review B*, vol. 63, Feb. 2001, p. 085112.

[174] M. Kim, A.J. Freeman, and C.B. Geller, "Screened exchange LDA determination of the ground and excited state properties of thermoelectrics: Bi2 Te3," *Physical Review B*, vol. 72, Jul. 2005, p. 035205.

[175] B.-L. Huang and M. Kaviany, "Ab initio and molecular dynamics predictions for electron and phonon transport in bismuth telluride," *Physical Review B (Condensed Matter and Materials Physics)*, vol. 77, Mar. 2008, pp. 125209–19.

[176] S.-G. Kim, I.I. Mazin, and D.J. Singh, "First-principles study of Zn-Sb thermoelectrics," *Physical Review B*, vol. 57, Mar. 1998, p. 6199.

[177] U. Sivan and Y. Imry, "Multichannel Landauer formula for thermoelectric transport with application to thermopower near the mobility edge," *Physical Review B*, vol. 33, Jan. 1986, p. 551.

[178] C.R. Proetto, "Thermopower oscillations of a quantum-point contact," *Physical Review B*, vol. 44, Oct. 1991, p. 9096.

[179] S. Datta, *Quantum Transport*, Cambridge University Press, 2005.

[180] E.O. Kane, "Band structure of indium antimonide," *Journal of Physics and Chemistry of Solids*, vol. 1, Jan. 1957, pp. 249–261.

[181] S. Datta, *ECE 495N Lecture 26: Ballistic Conductance*, http://nanohub.org/resources/5725, 2008.

[182] N. Mingo, "Calculation of Si nanowire thermal conductivity using complete phonon dispersion relations," *Physical Review B*, vol. 68, 2003, p. 113308.

[183] C. Jeong, *Calculating number of modes from given E-k dispersion*, http://nanohub.org/resources/7382, 2009.

[184] M. Luisier, A. Schenk, W. Fichtner, and G. Klimeck, "Atomistic simulation of nanowires in the sp[sup 3]d[sup 5]s[sup *] tight-binding formalism: From boundary conditions to strain calculations," *Physical Review B (Condensed Matter and Materials Physics)*, vol. 74, Nov. 2006, pp. 205323–12.

[185] J.M. Jancu, F. Bassani, F. Della Sala, and R. Scholz, "Transferable tight-binding parametrization for the group-III nitrides," *Applied Physics Letters*, vol. 81, 2002, p. 4838.

[186] G. Klimeck, F. Oyafuso, T.B. Boykin, R.C. Bowen, and P. von Allmen, "Development of a nanoelectronic 3-D (NEMO 3-D) simulator for multimillion atom simulations and its application to alloyed quantum dots," *CMES-Computer Modeling in Engineering and Sciences(1526-1492)*, vol. 3, 2002, pp. 601–642.

[187] T.B. Boykin, G. Klimeck, and F. Oyafuso, "Valence band effective-mass expressions in the sp 3 d 5 s* empirical tight-binding model applied to a Si and Ge parametrization," *Phys. Rev. B*, vol. 69, 2004, p. 115201.

[188] P. Vogl, H.P. Hjalmarson, and J.D. Dow, "Semi-empirical tight-binding theory of the electronic structure of semiconductors.," *J. Phys. Chem. Sol.*, vol. 44, 1983, pp. 265–378.

[189] J.S. Blakemore, "Semiconducting and other major properties of gallium arsenide," *Journal of Applied Physics*, vol. 53, Oct. 1982, pp. R123–R181.

[190] E.G.S. Paige, *The electrical conductivity of germanium*, Heywood, 1964.

[191] A.M. Anile and V. Romano, "Non parabolic band transport in semiconductors: closure of the moment equations," *Continuum Mechanics and Thermodynamics*, vol. 11, Oct. 1999, pp. 307–325.

[192] T.H. Geballe and G.W. Hull, "Seebeck Effect in Germanium," *Physical Review*, vol. 94, Jun. 1954, p. 1134.

[193] H.P.R. Frederikse, "Thermoelectric Power of Germanium below Room Temperature," *Physical Review*, vol. 92, 1953, pp. 248–252.

[194] P.B. Allen, W.E. Pickett, and H. Krakauer, "Anisotropic normal-state transport properties predicted and analyzed for high-Tc oxide superconductors," *Physical Review B*, vol. 37, May. 1988, p. 7482.

[195] R. Kim and M. Lundstrom, *Notes on Fermi-Dirac Integrals (3rd Edition)*, http://nanohub.org/resources/5475, 2008.

[196] K.W. Böer, *Survey of Semiconductor Physics: Electrons and other particles in semiconductors*, Wiley, 2002.

[197] G. Chen, M.S. Dresselhaus, G. Dresselhaus, J.P. Fleurial, and T. Caillat, "Recent developments in thermoelectric materials," *International Materials Reviews*, vol. 48, 2003, p. 45.

[198] E. Pop, S. Sinha, and K.E. Goodson, "Heat generation and transport in nanometer-scale transistors," *Proceedings of the IEEE*, vol. 94, 2006, pp. 1587–1601.

[199] G. Chen, *Nanoscale energy transport and conversion: a parallel treatment of electrons, molecules, phonons, and photons*, Oxford University Press, USA, 2005.

[200] D.E. Angelescu, M.C. Cross, and M.L. Roukes, "Heat transport in mesoscopic systems," *Superlattices and Microstructures*, vol. 23, Mar. 1998, pp. 673–689.

[201] B.J. Van Wees, H. Van Houten, C.W.J. Beenakker, J.G. Williamson, L.P. Kouwenhoven, D. Van der Marel, and C.T. Foxon, "Quantized conductance of point contacts in a two-dimensional electron gas," *Physical Review Letters*, vol. 60, 1988, pp. 848–850.

[202] D.A. Wharam, T.J. Thornton, R. Newbury, M. Pepper, H. Ahmed, J.E.F. Frost, D.G. Hasko, D.C. Peacock, D.A. Ritchie, and G.A.C. Jones, "One-dimensional transport and the quantisation of the ballistic resistance," *Journal of Physics C: solid state physics*, vol. 21, 1988, p. L209.

[203] L.G.C. Rego and G. Kirczenow, "Quantized Thermal Conductance of Dielectric Quantum Wires," *Physical Review Letters*, vol. 81, Jul. 1998, p. 232.

[204] G.D. Mahan and J.O. Sofo, "The best thermoelectric," *Proceedings of the National Academy of Sciences of the United States of America*, vol. 93, Jul. 1996, pp. 7436–7439.

[205] N. Mingo, "Calculation of Si nanowire thermal conductivity using complete phonon dispersion relations," *Physical Review B*, vol. 68, 2003, p. 113308.

[206] B.-L. Huang and M. Kaviany, "Ab initio and molecular dynamics predictions for electron and phonon transport in bismuth telluride," *Physical Review B*, vol. 77, Mar. 2008, p. 125209.

[207] B. Qiu and X. Ruan, "Molecular dynamics simulations of lattice thermal conductivity of bismuth telluride using two-body interatomic potentials," *Physical Review B*, vol. 80, Oct. 2009, p. 165203.

[208] J.D. Gale and A.L. Rohl, “The general utility lattice program (GULP),” *Molecular Simulation*, vol. 29, 2003, pp. 291–341.

[209] J.-Y. Park, S. Rosenblatt, Y. Yaish, V. Sazonova, H. Üstünel, S. Braig, T.A. Arias, P.W. Brouwer, and P.L. McEuen, “Electron−Phonon Scattering in Metallic Single-Walled Carbon Nanotubes,” *Nano Letters*, vol. 4, Mar. 2004, pp. 517–520.

[210] K.I. Bolotin, K.J. Sikes, J. Hone, H.L. Stormer, and P. Kim, “Temperature-Dependent Transport in Suspended Graphene,” *Physical Review Letters*, vol. 101, 2008, pp. 096802–096804.

[211] Changwook Jeong, D.A. Antoniadis, and M.S. Lundstrom, “On Backscattering and Mobility in Nanoscale Silicon MOSFETs,” *Electron Devices, IEEE Transactions on*, vol. 56, 2009, pp. 2762–2769.

[212] P.A. Temple and C.E. Hathaway, “Multiphonon Raman Spectrum of Silicon,” *Physical Review B*, vol. 7, Apr. 1973, p. 3685.

[213] H. Rauh, R. Geick, H. Kohler, N. Nucker, and N. Lehner, “Generalized phonon density of states of the layer compounds Bi2Se3, Bi2Te3, Sb2Te3 and Bi2 (Te0. 5Se0. 5) 3,(Bi0. 5Sb0. 5) 2Te3,” *Journal of Physics C: Solid State Physics*, vol. 14, 1981, p. 2705.

[214] J.O. Jenkins, J.A. Rayne, and R.W. Ure, “Elastic Moduli and Phonon Properties of Bi_{2} Te_{3},” *Physical Review B*, vol. 5, Apr. 1972, p. 3171.

[215] J. Tersoff, “Modeling solid-state chemistry: Interatomic potentials for multicomponent systems,” *Physical Review B*, vol. 39, Mar. 1989, p. 5566.

[216] P.A. Walker, “The Thermal Conductivity and Thermoelectric Power of Bismuth Telluride at Low Temperatures,” *Proceedings of the Physical Society*, vol. 76, Jul. 1960, pp. 113–126.

[217] J. Callaway, “Model for Lattice Thermal Conductivity at Low Temperatures,” *Physical Review*, vol. 113, Feb. 1959, p. 1046.

[218] P. Chantrenne, J.L. Barrat, X. Blase, and J.D. Gale, “An analytical model for the thermal conductivity of silicon nanostructures,” *Journal of Applied Physics*, vol. 97, 2005, p. 104318.

[219] Y.F. Zhu, J.S. Lian, and Q. Jiang, “Re-examination of Casimir limit for phonon traveling in semiconductor nanostructures,” *Applied Physics Letters*, vol. 92, 2008, p. 113101.

[220] J.M. Ziman, *Electrons and phonons: the theory of transport phenomena in solids*, Oxford University Press, New York,, 1960.

[221] M. Maldovan, “Micro to nano scale thermal energy conduction in semiconductor thin films,” *Journal of Applied Physics*, vol. 110, 2011, p. 034308.

[222] D.P. Sellan, E.S. Landry, J.E. Turney, A.J.H. McGaughey, and C.H. Amon, “Size effects in molecular dynamics thermal conductivity predictions,” *Physical Review B*, vol. 81, 2010, p. 214305.

[223] D.P. Sellan, J.E. Turney, A.J.H. McGaughey, and C.H. Amon, “Cross-plane phonon transport in thin films,” *Journal of Applied Physics*, vol. 108, 2010, p. 113524.

[224] A.J.. McGaughey, E.S. Landry, D.P. Sellan, and C.H. Amon, “Size-dependent model for thin film and nanowire thermal conductivity,” *Applied Physics Letters*, vol. 99, 2011, pp. 131904–131904–3.

[225] A. Majumdar, “Microscale heat conduction in dielectric thin films,” *ASME Transactions Journal of Heat Transfer*, vol. 115, 1993, pp. 7–16.

[226] C. Jeong, S. Datta, and M. Lundstrom, “Full dispersion versus Debye model evaluation of lattice thermal conductivity with a Landauer approach,” *Journal of Applied Physics*, vol. 109, Apr. 2011, pp. 073718–8.

[227] C. Dames and G. Chen, “Theoretical phonon thermal conductivity of Si/Ge superlattice nanowires,” *Journal of Applied Physics*, vol. 95, Jan. 2004, pp. 682–693.

[228] E.H. Sondheimer, “The mean free path of electrons in metals,” *Advances in Physics*, vol. 1, 1952, pp. 1–42.

[229] W.P. Maszara, “Silicon-On-Insulator by Wafer Bonding: A Review,” *Journal of the Electrochemical Society*, vol. 138, 1991, p. 341.

[230] J.R. Sootsman, D.Y. Chung, and M.G. Kanatzidis, “New and Old Concepts in Thermoelectric Materials,” *Angewandte Chemie International Edition*, vol. 48, Nov. 2009, pp. 8616–8639.

[231] H.J. Goldsmid, “Principles of thermoelectric devices,” *British Journal of Applied Physics*, vol. 11, 1960, p. 209.

[232] G.D. Mahan, “Good Thermoelectrics,” *Solid State Physics*, Academic Press, 1997, pp. 81–157.

[233] Y. NISHIO and T. HIRANO, “Methods of improving the efficiency of thermoelectric energy conversion and characteristic energy range of carriers,” *Japanese journal of applied physics*, vol. 36, pp. 5181–5182.

[234] T.E. Humphrey and H. Linke, “Reversible Thermoelectric Nanomaterials,” *Physical Review Letters*, vol. 94, Mar. 2005, pp. 096601–4.

[235] N. Nakpathomkun, H.Q. Xu, and H. Linke, “Thermoelectric efficiency at maximum power in low-dimensional systems,” *Physical Review B*, vol. 82, Dec. 2010, p. 235428.

[236] Z. Fan, H.-Q. Wang, and J.-C. Zheng, “Searching for the best thermoelectrics through the optimization of transport distribution function,” *Journal of Applied Physics*, vol. 109, Apr. 2011, pp. 073713–6.

[237] J. Zhou, R. Yang, G. Chen, and M.S. Dresselhaus, “Optimal Bandwidth for High Efficiency Thermoelectrics,” *Physical Review Letters*, vol. 107, Nov. 2011, p. 226601.

[238] Y. Pei, X. Shi, A. LaLonde, H. Wang, L. Chen, and G.J. Snyder, “Convergence of electronic bands for high performance bulk thermoelectrics,” *Nature*, vol. 473, May. 2011, pp. 66–69.

[239] B.C. Sales, “Critical overview of recent approaches to improved thermoelectric materials,” *International journal of applied ceramic technology*, vol. 4, 2007, pp. 291–296.

[240] F.L. Curzon, “Efficiency of a Carnot engine at maximum power output,” *American Journal of Physics*, vol. 43, 1975, p. 22.

[241] G.D. Mahan and M. Bartkowiak, “Wiedemann--Franz law at boundaries,” *Applied Physics Letters*, vol. 74, Feb. 1999, pp. 953–954.

[242] C. Jeong, R. Kim, and M. Lundstrom, “On the Best Bandstructure for Thermoelectric Performance,” *arXiv:1103.1274v1*, 2011.

[243] J.-H. Lee, J. Wu, and J.C. Grossman, “Enhancing the Thermoelectric Power Factor with Highly Mismatched Isoelectronic Doping,” *Physical Review Letters*, vol. 104, Jan. 2010, p. 016602.

[244] C. Jeong and M. Lundstrom, “On Electronic Structure Engineering and Thermoelectric Performance,” *Journal of Electronic Materials*, vol. 40, May. 2011, pp. 738–743.

[245] Y.H. Hu, H. Wang, and B. Hu, “Thinnest Two-Dimensional Nanomaterial—Graphene for Solar Energy,” *ChemSusChem*, vol. 3, 2010, pp. 782–796.

[246] L. Hu, D.S. Hecht, and G. Grüner, “Infrared transparent carbon nanotube thin films,” *Appl. Phys. Lett.*, vol. 94, 2009, pp. 081103–081105.

[247] S. Dongaonkar, J.D. Servaites, G.M. Ford, S. Loser, J. Moore, R.M. Gelfand, H. Mohseni, H.W. Hillhouse, R. Agrawal, and M.A. Ratner, "Universality of non-Ohmic shunt leakage in thin-film solar cells," *J. Appl. Phys.*, vol. 108, 2010, pp. 124509–124517.

[248] B. Chandra, A. Afzali, N. Khare, M.M. El-Ashry, and G.S. Tulevski, "Stable Charge-Transfer Doping of Transparent Single-Walled Carbon Nanotube Films," *Chem. Mater.*, vol. 22, 2010, pp. 5179–5183.

[249] H.-Z. Geng, K.K. Kim, K.P. So, Y.S. Lee, Y. Chang, and Y.H. Lee, "Effect of Acid Treatment on Carbon Nanotube-Based Flexible Transparent Conducting Films," *J. Am. Chem. Soc.*, vol. 129, Jun. 2007, pp. 7758–7759.

[250] J.-Y. Lee, S.T. Connor, Y. Cui, and P. Peumans, "Solution-Processed Metal Nanowire Mesh Transparent Electrodes," *Nano Lett.*, vol. 8, Feb. 2008, pp. 689–692.

[251] H. Wu, L. Hu, M.W. Rowell, D. Kong, J.J. Cha, J.R. McDonough, J. Zhu, Y. Yang, M.D. McGehee, and Y. Cui, "Electrospun metal nanofiber webs as high-performance transparent electrode," *Nano Lett.*, vol. 10, 2010, pp. 4242–4248.

[252] S. Bae, H. Kim, Y. Lee, X. Xu, J.-S. Park, Y. Zheng, J. Balakrishnan, T. Lei, H. Ri Kim, Y.I. Song, Y.-J. Kim, K.S. Kim, B. Ozyilmaz, J.-H. Ahn, B.H. Hong, and S. Iijima, "Roll-to-roll production of 30-inch graphene films for transparent electrodes," *Nat. Nanotechnol.*, vol. 5, 2010, pp. 574–578.

[253] X. Li, C.W. Magnuson, A. Venugopal, J. An, J.W. Suk, B. Han, M. Borysiak, W. Cai, A. Velamakanni, and Y. Zhu, "Graphene films with large domain size by a two-step chemical vapor deposition process," *Nano Lett.*, vol. 10, 2010, pp. 4328–4334.

[254] X. Li, W. Cai, J. An, S. Kim, J. Nah, D. Yang, R. Piner, A. Velamakanni, I. Jung, E. Tutuc, S.K. Banerjee, L. Colombo, and R.S. Ruoff, "Large-Area Synthesis of High-Quality and Uniform Graphene Films on Copper Foils," *Science*, vol. 324, Jun. 2009, pp. 1312 –1314.

[255] K.S. Kim, Y. Zhao, H. Jang, S.Y. Lee, J.M. Kim, K.S. Kim, J.-H. Ahn, P. Kim, J.-Y. Choi, and B.H. Hong, "Large-scale pattern growth of graphene films for stretchable transparent electrodes," *Nature*, vol. 457, Feb. 2009, pp. 706–710.

[256] N. Pimparkar, M. Chowalla, and M.A. Alam, "Device optimization for organic photovoltaics with CNT networks as transparent electrode," *Proc. IEEE Photovoltaic Specialists Conference, 33rd, 2008*, pp. 1–4.

[257] S. De, P.J. King, P.E. Lyons, U. Khan, and J.N. Coleman, “Size Effects and the Problem with Percolation in Nanostructured Transparent Conductors,” *ACS Nano*, vol. 4, Dec. 2010, pp. 7064–7072.

[258] S. De and J.N. Coleman, “Are There Fundamental Limitations on the Sheet Resistance and Transmittance of Thin Graphene Films?,” *ACS Nano*, vol. 4, May. 2010, pp. 2713–2720.

[259] N. Pimparkar, Q. Cao, J.A. Rogers, and M.A. Alam, “Theory and practice of ‘striping’ for improved on/off ratio in carbon nanonet thin film transistors,” *Nano Research*, vol. 2, 2009, pp. 167–175.

[260] A. Okabe, B. Boots, K. Sugihara, and S.N. Chiu, *Spatial tessellations*, John Wiley and Sons, 2000.

[261] Q. Yu, L.A. Jauregui, W. Wu, R. Colby, J. Tian, Z. Su, H. Cao, Z. Liu, D. Pandey, and D. Wei, “Control and characterization of individual grains and grain boundaries in graphene grown by chemical vapour deposition,” *Nature Materials*, vol. 10, 2011, pp. 443–449.

[262] P.Y. Huang, C.S. Ruiz-Vargas, A.M. van der Zande, W.S. Whitney, M.P. Levendorf, J.W. Kevek, S. Garg, J.S. Alden, C.J. Hustedt, Y. Zhu, J. Park, P.L. McEuen, and D.A. Muller, “Grains and grain boundaries in single-layer graphene atomic patchwork quilts,” *Nature*, vol. 469, Jan. 2011, pp. 389–392.

[263] P. Nemes-Incze, K.J. Yoo, L. Tapaszto, G. Dobrik, J. Labar, Z.E. Horvath, C. Hwang, and L.P. Biro, “Revealing the grain structure of graphene grown by chemical vapor deposition,” *Applied Physics Letters*, vol. 99, 2011, pp. 023104–923106.

[264] O.V. Yazyev and S.G. Louie, “Electronic transport in polycrystalline graphene,” *Nat Mater*, vol. 9, Oct. 2010, pp. 806–809.

[265] “COMSOL multiphysics user’s guide,” p. Multiphysics and Simulation Software: COMSOL. http://www.comsol.com/.

[266] H.-P. Hsu and M.-C. Huang, “Percolation thresholds, critical exponents, and scaling functions on planar random lattices and their duals,” *Physical Review E*, vol. 60, Dec. 1999, pp. 6361–6370.

[267] A.M. Becker and R.M. Ziff, “Percolation thresholds on two-dimensional Voronoi networks and Delaunay triangulations,” *Physical Review E*, vol. 80, Oct. 2009, pp. 041101–041108.

[268] M.F. Sykes and J.W. Essam, “Exact critical percolation probabilities for site and bond problems in two dimensions,” *Journal of Mathematical Physics*, vol. 5, 1964, pp. 1117–1127.

[269] R. Pike and H.E. Stanley, "Order propagation near the percolation threshold," *Journal of Physics A: Mathematical and General*, vol. 14, 1981, pp. L169–L177.

[270] D.S. McLachlan, M. Blaszkiewicz, and R.E. Newnham, "Electrical Resistivity of Composites," *Journal of the American Ceramic Society*, vol. 73, 1990, pp. 2187–2203.

[271] E. Rossi, S. Adam, and S. Das Sarma, "Effective medium theory for disordered two-dimensional graphene," *Physical Review B*, vol. 79, Jun. 2009, pp. 245423–245429.

[272] J.P. Straley, "Critical exponents for the conductivity of random resistor lattices," *Physical Review B*, vol. 15, Jun. 1977, pp. 5733–5737.

[273] D.J. Frank and C.J. Lobb, "Highly efficient algorithm for percolative transport studies in two dimensions," *Physical Review B*, vol. 37, Jan. 1988, pp. 302–307.

[274] A. Hsu, H. Wang, K.K. Kim, J. Kong, and T. Palacios, "Impact of Graphene Interface Quality on Contact Resistance and RF Device Performance," *Electron Device Letters, IEEE*, vol. 32, 2011, pp. 1008–1010.

[275] D. Berdebes, T. Low, Y. Sui, J. Appenzeller, and M. Lundstrom, "Substrate Gating of Contact Resistance in Graphene Transistors," *arXiv:1103.5773v2*, Mar. 2011.

[276] G. Giovannetti, P.A. Khomyakov, G. Brocks, V.M. Karpan, J. van den Brink, and P.J. Kelly, "Doping Graphene with Metal Contacts," *Physical Review Letters*, vol. 101, Jul. 2008, pp. 026803–026806.

[277] Y. Zhu, Z. Sun, Z. Yan, Z. Jin, and J.M. Tour, "Rational Design of Hybrid Graphene Films for High-Performance Transparent Electrodes," *ACS Nano*, vol. 5, Jul. 2011, pp. 6472–6479.

[278] R. Kim and M.S. Lundstrom, "Computational study of energy filtering effects in one-dimensional composite nano-structures," *Journal of Applied Physics*, vol. 111, Jan. 2012, pp. 024508–024508–9.

[279] M. Lundstrom, *ECE 656 Lecture 17: BTE and Landauer*, http://nanohub.org/resources/7509, 2009.

[280] H. Fritzsche, "A general expression for the thermoelectric power," *Solid State Communications*, vol. 9, Nov. 1971, pp. 1813–1815.

[281] *Properties of Aluminium Gallium Arsenide*, London: IEE, INSPEC, 1993.

[282] M. Lundstrom, *ECE 656 Lecture 4: Density of States - Density of Modes*, http://nanohub.org/resources/7349, 2009.

[283] A.K. Saxena and K.S. Gurumurthy, “Scattering parameters from an analysis of the hall electron mobility in Ga1-xAlxAs alloys,” *Journal of Physics and Chemistry of Solids*, vol. 43, 1982, pp. 801–808.

[284] M.W. Cresswell and J.P. McKelvey, “Minority-Carrier Mobility in p-Type Germanium Under High Uniaxial Stress,” *Physical Review*, vol. 144, Apr. 1966, p. 605.

[285] M. Lundstrom, *Fundamentals of Carrier Transport*, Cambridge University Press, 2000.

[286] R.C. Newman, “The upper limits of useful n- and p-type doping in GaAs and AlAs,” *Materials Science and Engineering B*, vol. 66, Dec. 1999, pp. 39–45.

[287] G.D. Mahan and L.M. Woods, “Multilayer Thermionic Refrigeration,” *Physical Review Letters*, vol. 80, May. 1998, p. 4016.

[288] G. Klimeck, R. Lake, R.C. Bowen, W.R. Frensley, and T.S. Moise, “Quantum device simulation with a generalized tunneling formula,” *Applied Physics Letters*, vol. 67, 1995, pp. 2539–2541.

[289] R. Kim, C. Jeong, and M.S. Lundstrom, “On momentum conservation and thermionic emission cooling,” *Journal of Applied Physics*, vol. 107, 2010, p. 054502.

[290] N.W. Ashcroft and N.D. Mermin, *Solid State Physics*, Brooks Cole, 1976.

[291] P.E. Phelan, “Application of Diffuse Mismatch Theory to the Prediction of Thermal Boundary Resistance in Thin-Film High-T[sub c] Superconductors,” *Journal of Heat Transfer*, vol. 120, Feb. 1998, pp. 37–43.

[292] A.D. Rollett, D. Saylor, J. Fridy, B.S. El-Dasher, A. Brahme, S.B. Lee, C. Cornwell, and R. Noack, “Modeling Polycrystalline Microstructure in 3D,” *AIP Conference Proceedings*, IOP INSTITUTE OF PHYSICS PUBLISHING LTD, 2004, pp. 71–77.

[293] A.C.E. Reid, R.C. Lua, R.E. Garcia, and V.R. Coffman, “Modelling microstructures with oof2,” *International Journal of Materials and Product Technology*, vol. 35, 2009, pp. 361–373.

[294] C.H. Rycroft, “VORO++: a three-dimensional voronoi cell library in C++.,” *Chaos (Woodbury, NY)*, vol. 19, 2009, p. 041111.

[295] M. Groeber, S. Ghosh, M.D. Uchic, and D.M. Dimiduk, “A framework for automated analysis and simulation of 3D polycrystalline microstructures. Part 2: Synthetic structure generation,” *Acta Materialia*, vol. 56, Apr. 2008, pp. 1274–1287.

[296] *Qhull code for convex hull, Delaunay triangulation, Voronoi diagram, and half space intersection about a point*, http://www.qhull.org/, .

[297] *Triangle: A two-dimensional quality mesh generator and Delaunay triangulator*,, http: //www.cs.cmu.edu/~quake/triangle.html, .

[298] C.H. Rycroft, "Multiscale modeling in granular flow."

[299] *Voro++ library for the computation of three dimensional Voronoi cells*, http://math.lbl.gov/voro++/, .

APPENDICES

A. ON ELECTRONIC STRUCTURE ENGINEERING AND THERMOELECTRIC PERFORMANCE

In this appendix A, we address the question of how to engineer the electronic structure to enhance the performance of a thermoelectric material. We examine several different materials and show that all of them, even those for which giant Seebeck coefficients have been predicted, display a value that is expected from conventional thermoelectric theory. For molecular thermoelectrics, we show that the detailed lineshape plays an important role. Finally, using III-V alloy semiconductors as a model system, we explore the role of electronic structure on the Seebeck coefficient, electrical conductivity, and power factor. In the process, some general guidelines for engineering the electronic component of thermoelectric performance are identified.

A.1 Introduction

The dimensionless figure of merit, $ZT = S^2GT/K$, is the primary material parameter governing the maximum thermoelectric (*TE*) efficiency, where *T* is the temperature, *S* is the Seebeck coefficient, *G* is the electrical conductance, and *K* is the thermal conductance, which is the sum of the electronic contribution, K_e, and the lattice thermal conductance, K_l. For a single, parabolic band material, the Fermi level (E_F) is positioned near the bottom of conduction band due to the balance between *S* and *G*. Most recent improvements in *ZT* have been achieved by phonon engineering to reduce the lattice thermal conductivity [36,47,197] . The question of how to improve the electronic performance is now an important one [8,44,62,64–67,69].

Significant improvements in *S* have been predicted and reported for several different materials. For example, an enhanced *S* has been achieved by engineering the density-of-states (DOS) in the bulk Tl-PbTe[8], LAST [$(PbTe)_{1-x}(AgSbTe_2)_x$] system[64],

$La_{3-x}Te_4$[65], and giant Seebeck coefficients have been predicted for nanostructured graphene[66] and for appropriately engineered molecules[67]. These examples all seek to enhance performance by achieving a delta-function like DOS. A clear understanding of how electronic structure affects the *S* and *G* of a material is essential for developing materials with enhanced power factors (*PF*) and is the subject of this chapter.

In this appendix, we:

1) Examine a wide variety of thermoelectric (*TE*) materials for which large Seebeck coefficients have been predicted.
2) Demonstrate that the Seebeck coefficient for each of them can be explained within the conventional, single particle framework and show that most materials display similar *S* vs. E_F characteristics.
3) Show for molecular thermoelectrics, that the detailed shape of the transmission plays an important role.
4) Use $Al_xGa_{1-x}As$ as a model system to explore the role of electronic structure and significant enhancement in electronic performance are observed due to non-monotonic behavior of $S(E_F)$.
5) Present general guidelines to enhance the electronic performance of *TE* devices.

A.2 Approaches

Our approach, based on the Landauer formalism, is equivalent to the conventional Boltzmann transport equation (BTE) approach[204], but, it adds physical insight and is applicable to quantum-engineered structures as well as to bulk materials[3,279].

We begin with a brief review of conventional thermoelectric theory and the Landauer formalism. According to conventional thermoelectric theory[280], integrating the contributions of each energy channel, we find the total *S* as

$$S = \left(\frac{k_B}{q}\right)\int_{-\infty}^{+\infty}\left(\frac{E - E_F}{k_B T}\right)\frac{G(E)}{G}dE \tag{A.1}$$

This expression can be alternatively expressed as

$$S = -\frac{\left(E_C - E_F + \Delta_n\right)}{qT} \tag{A.2}$$

with

$$\Delta_n = \int_{-\infty}^{+\infty} (E - E_C)\frac{G(E)}{G}dE \tag{A.3}$$

where Δ_n represents average energy of charge carriers above the conduction band edge (E_C). This expression suggests that all materials should display similar S vs. E_F characteristics within a framework of conventional *TE* theory, and bandstructure effect only affects Δ_n. For an ideal single channel, $\Delta_n = 0$, while for non-degenerate materials with parabolic energy bands and a constant mean-free-path (mfp), $\Delta_n = 2k_BT$.

To evaluate the Seebeck coefficient, we need to calculated *G(E)*. Within the Landauer formalism, *G(E)* is given as[3]

$$G(E) = \frac{2q^2}{h}\bar{T}(E)\left(-\frac{\partial f_0}{\partial E}\right) \tag{A.4}$$

with

$$\bar{T}(E) = T(E)M(E), \tag{A.5}$$

being the transmission, and $M(E)$ the number of conducting channels. For a conductor of length, L, and mfp for backscattering, $\langle\langle\lambda(E)\rangle\rangle$, $T(E)$ is given as

$$T(E) = \langle\langle\lambda(E)\rangle\rangle / L \tag{A.6}$$

in the diffusive limit. For some common scattering mechanisms, $\langle\langle\lambda(E)\rangle\rangle$ can be expressed in power law form as $\langle\langle\lambda(E)\rangle\rangle = \lambda_0 (E/k_BT)^r$, where λ_0 is a constant, E is the kinetic energy, and r is a characteristic exponent describing a specific scattering process. If we consider a single parabolic conduction band, $E = \hbar^2k^2/2m^*$, then $M(E)$ for 3D is

$$M(E) = A\frac{m^*_{DOM}}{2\pi\hbar^2}(E - E_C) \tag{A.7}$$

where the density-of-modes effective mass, m^*_{DOM} is just m^* for a single, spherical band. For ellipsoidal energy bands, m^*_{DOM} for each equivalent ellipsoid is $\sqrt{m^*_y m^*_z}$ with the direction of current flow being along the x-direction [3]. Procedures for evaluating *M(E)* from the full band electronic dispersion have been given in Ref. [3]

To explore how the electronic structure can be engineered to enhance performance, three *TE* devices are examined:

1) Graphene superlattice [66] for which a 30 mV/*K* Seebeck coefficient was predicted. $\bar{T}(E)$ is evaluated using transfer matrix method .
2) Single molecular device[67], in which the engineering of transmission gives rise to huge increase in *S*. $\bar{T}(E)$ is taken from the original paper.
3) $Al_xGa_{1-x}As$, ternary materials such as $Al_xGa_{1-x}As$, $Al_xGa_{1-x}Sb$, $Al_xIn_{1-x}As$, and $GaAs_{1-x}P_x$, which are good examples to illustrate the effect of the electronic structure on *TE* coefficients because
    - the band-splitting, *ΔE,* and effective masses for Γ, L, and X valleys depend on Al composition [281]
    - the effective masses of L and X valleys are ~ 10 times larger than the effective mass of Γ valley.
    - At x = 0.42, all valleys are degenerate, and the thermal conductivity is minimum, 5 and 10 times smaller than the thermal conductivity for GaAs and AlAs, respectively.

A.3 Results

Our goal is to discuss, in a single particle framework, how electronic structure can be engineered to enhance the electronic component of *TE* performance.

Figure A.1a shows the transmission of an infinite graphene sheet and a graphene superlattice (SL)[66]. The transmission for a graphene is linearly proportional to energy[282]. Since graphene is a zero gap material, there is a sizable contribution from valence band. Therefore, the expected maximum *S* (S_{max}) is only about 100 μV/K. To enhance the Seebeck coefficient, a transmission gap is created by making a periodic graphene PN junction electrostatically, as shown in Fig. A.1a[66]. The S is evaluated by full integral formula, Eq. A.1 rather than simplified Mott formula. Figure A.1b compares the S vs. E_F characteristics of graphene and a graphene SL. It turns out that the predicted 30 mV/K at 300 K is a mathematical artifact caused by the inappropriate use of the Mott formula and that the superlattice is no better than graphene.

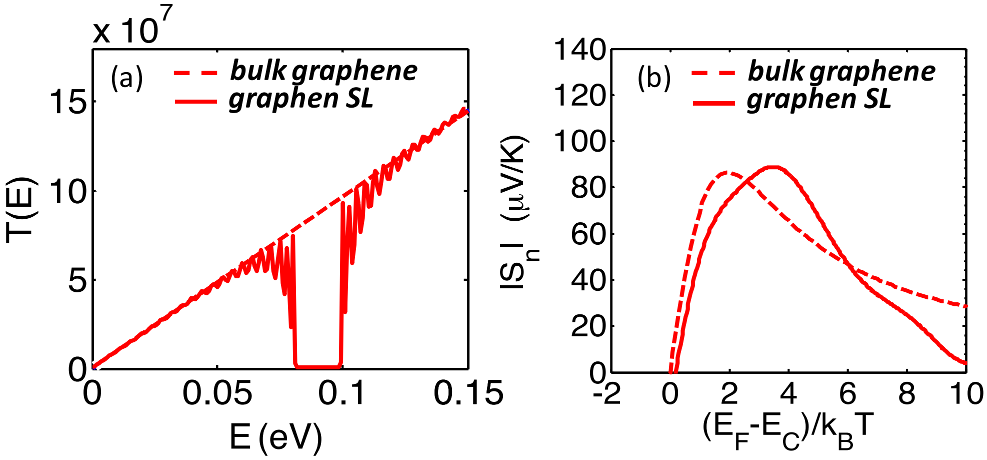

Figure A.1 For graphene and a graphene SL (a) the transmission (b) the S vs. E_F characteristics

A significant enhancement in S in single molecule devices was also predicted by engineering transmission as shown in Fig. A.2a[67]. Figure A.2a shows the transmission for a BPDT molecule, for which S_{max} is found to be ~ 10 μV/K. This low value is attributed to the relatively flat transmission near the Fermi level, which is in the LUMO-HOMO bandgap region. In order to enhance S, a very sharp transmission is desirable near Fermi level. Engineering the transmission is done by putting side group in the CSW molecule, which creates very sharp Fano resonance[67]. In the Fig. A.2b, the results of BPDT and CSW molecules are compared. Comparing to BPDT, CSW shows a huge improvement in S.

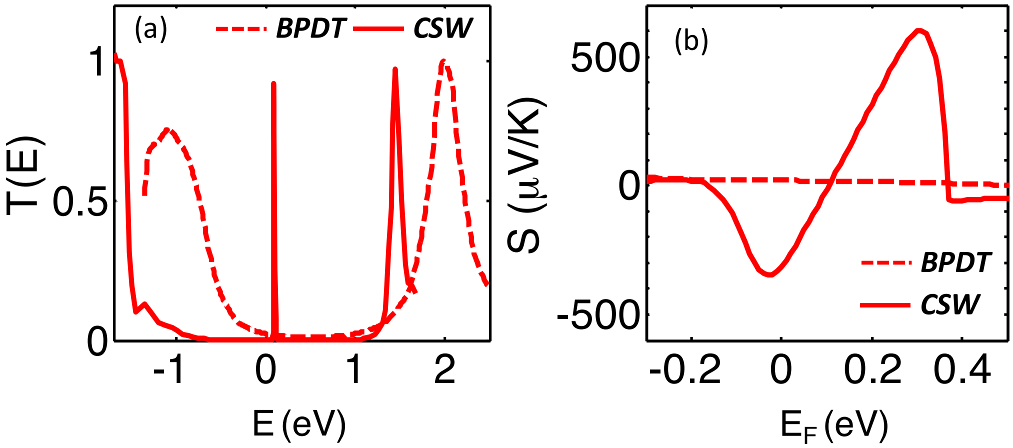

Figure A.2 For a BPDT molecule and a CSW molecule, (a) the transmission (b) the *S* vs. E_F

A.4 Discussion

Questions that will be addressed are

1) How close are the results for graphene SLs and single molecules to common *TE* semiconductors? Can all be understood within the traditional thermoelectric theory?
2) Why does the Seebeck coefficient for the CSW molecule with the sharp transmission deviate from the single level model?
3) How can the electronic structure be engineered for maximum *TE* performance?

The results for a graphene, graphene SLs, and a single molecule are compared with common *TE* semiconductors as shown in Fig. A.3. Nano-structured graphene SLs, and an appropriately engineered molecule device display similar $S(E_F)$ characteristics to common semiconductor materials, as is expected from Eq. A.2. The predicted giant *S* for a CSW molecule is actually what is expected from single level model. For a given Fermi level, the 3D bulk results have a somewhat higher *S* than the ideal single level model because in 3D, energy states are spread-out.

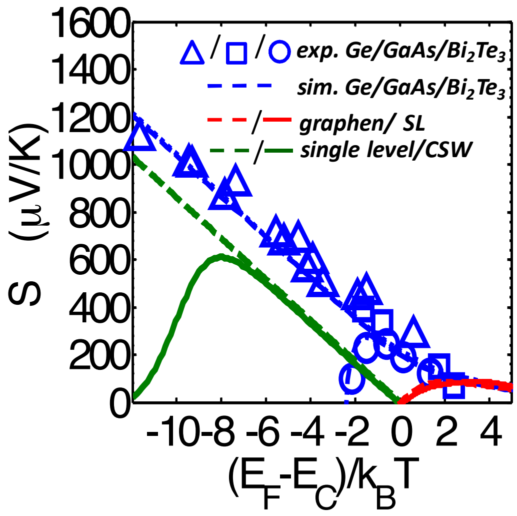

Figure A.3 The results for graphene, graphene SL, and a single molecule are compared with common *TE* semiconductors.

It is interesting that *S* for the CSW molecule deviates from a single level model when E_F is far below the level. The actual Seebeck coefficient is reduced below what we expect from single level model by a factor of 30, though the CSW molecule has a very sharp transmission which almost look like ideal delta function as shown in Fig. A.2a. This is because the CSW molecule transmission has a finite linewidth with a shape that is actually described by a Lorentzian model where transmission is proportional to E^2. This energy dependency is important because most of the charge and heat flow occurs at the Fermi Level, not at the position of transmission peak when E_F is far below the level. In the single level model, however, all charge and heat should flow at the single channel, no matter where the Fermi level is sitting in. To illustrate the importance of detailed shape of transmission, we compare the results for Gaussian shaped and Lorentzain shaped transmissions, as shown in Fig. A.4. The results for a Gaussian lineshape, shown in the dashed line, follows exactly single level model even with large standard deviation value. The Seebeck coefficient for a Lorentzian lineshape, however, shows degradation from single level model, and the maximum Seebeck coefficient depends on the value of the standard deviation.

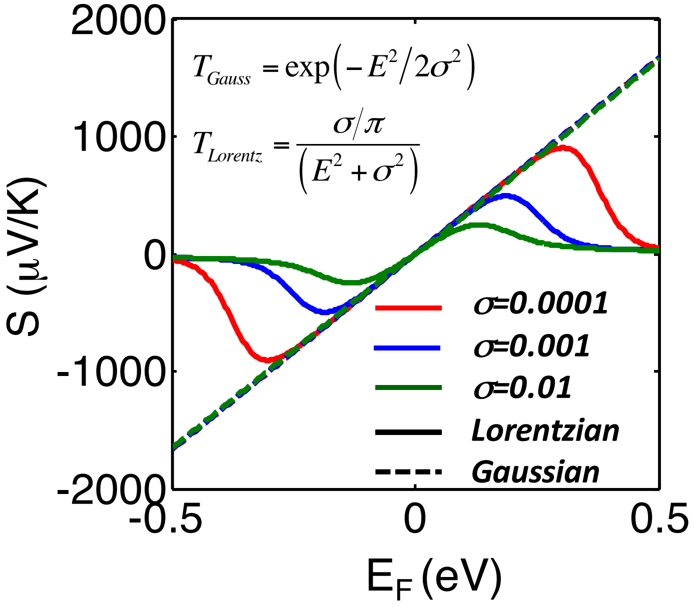

Figure A.4 Comparison of the results for Gaussian shaped and Lorentzian shaped transmission with respect to standard deviation (σ).

Since all materials examined so far display similar Seebeck coefficient behavior, it is essential to consider other approaches for enhancing *S* by electronic structure engineering. Using ideas similar to those of Ref. [8], it will be shown that enhancing the electronic component of *TE* performance is possible even in common semiconductors such as $Al_xGa_{1-x}As$ just by changing composition of Al.

For varying composition of Al, relevant parameters are taken from Ref. [281], and linear interpolation is used for unknown parameters. Although the scattering parameters generally depend on the location of Fermi level, the average mfp, $\langle\langle\lambda(E)\rangle\rangle$, is assumed to be energy-independent, λ_0 , because calculations with the constant λ_0 approximation[3] turned out to be in good agreement with experiments over wide range of doping densities (or E_F level) for common semiconductors. (Others have found similarly good agreement with experimental data by solving the BTE in the constant relaxation time approximation [168,169]). As shown in Fig. A.5, calculations with a constant mean-free-path (black dashed line), match well experiments over the range of E_F of interest, and it also captures well the maximum value of the *PF*. The constant λ_0 is estimated as follows. Firstly, λ_i for each valley i, is calculated using the 3D expression for mfp for backscattering[3].

$$\lambda_i = \frac{4}{3}\upsilon_T\tau_i = \frac{4}{3}\sqrt{\frac{2m_c^* k_B T}{\pi q^2}}\mu_i \tag{A.8}$$

with μ_i and m_c^* being the experimentally determined mobility and the conductivity effective mass, respectively[283]. The overall λ_0 is estimated by weighting λ_i in each valley by the electron population density of i th valley, n_i [284].

$$\lambda_0 = \sum_{i\ valley} n_i\lambda_i \Big/ \sum_{i\ valley} n_i \tag{A.9}$$

Figure A.5 compares the calculation of *ZT* for GaAs (x=0 in $Al_xGa_{1-x}As$) with best fitted λ_0 and Eq. A.9. Although Eq. A.9 underestimates the experimental results by about 50 %, this doesn't affect the comparison of $Al_xGa_{1-x}As$ alloy to pure GaAs and AlAs. The comparisons are the subject of this study. It is also assumed that upper limit of doping density is 5×10^{18} cm^{-3}.

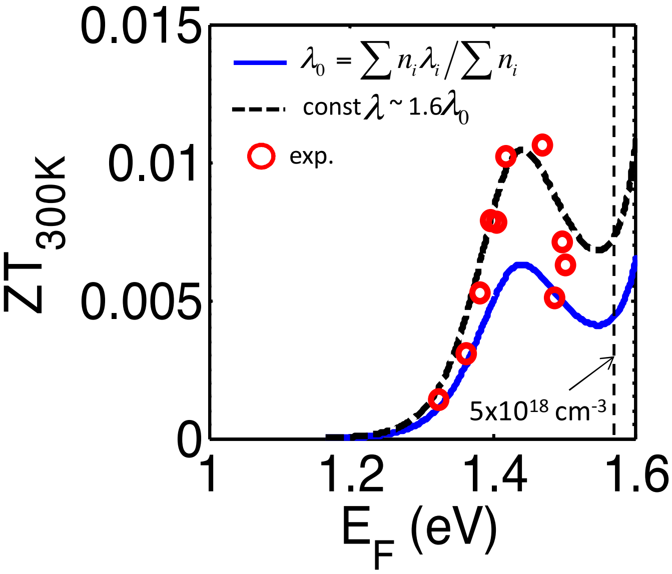

Figure A.5 Calculation of *ZT* for GaAs (x=0 in $Al_xGa_{1-x}As$) with best fitted λ_0 and Eq. 9 is compared to experimental results[4].

For each Al composition, the optimum position of Femi level (doping density) is determined for maximum *ZT*. The resulting optimum *TE* parameters (*S*, *G*, *K*, *PF*, *ZT*) are shown in Figure A.6. Comparing to GaAs (x = 0), a 5 times enhancement in *PF* and 10 times enhancement in *ZT* are predicted at x = 0.28 and 0.29, respectively. Interestingly, maximum *ZT* is not achieved at Al concentration of 0.42 where all valleys are degenerate and the thermal conductivity is minimum. When x ≥ 0.06, the optimum doping density for maximum *ZT* is the maximum allowed doping of 5×10^{18} cm^{-3}, which causes *S* (*G*) suddenly to decrease (increase) at x = 0.06 . The reason why *S* (*G*) gradually increases (decreases) at x $\geqslant$ 0.06 is that non-monotonic behavior of *S* vs. E_F is noticeable as shown in Fig. A.7b and A.7c.

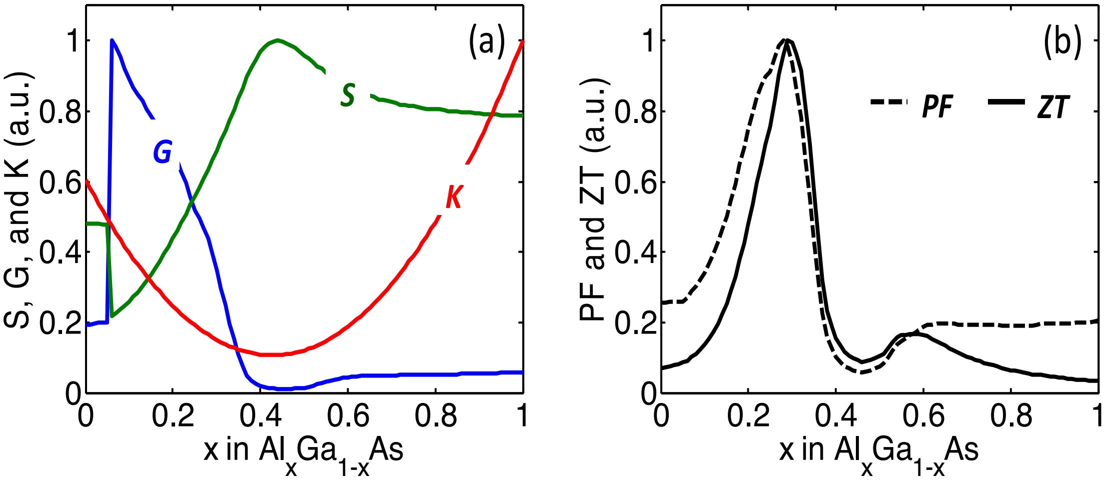

Figure A.6 (a) optimum *S*, *G*, and *K* (b) *PF* and *ZT* with respect to Al composition

Figure A.7 shows *S*, *G* and *PF* vs. Fermi level for Al composition of 0, 0.17, 0.28 and 0.42. For pure GaAs (x=0), a conventional monotonic *S*(E_F) is observed up to $E_F = 5k_BT$ at which the Seebeck coefficient starts increasing again with E_F due to contribution of L valley. Also the optimum doping density is below the maximum allowed doping 5×10^{18} cm^{-3}. At x=0.17 and x=0.28, the non-monotonic *S*(E_F) characteristic becomes prominent, giving rise to high *S* and *PF* at the degenerate limit, whereas the totally degenerate condition (x=0.42) doesn't show enhancement in *PF* mainly due to low mobility. This non-monotonic *S* was also reported in bulk Tl-PbTe[8]. Note that the upper limit of doping density, shown in the dashed line, is the optimum doping density for maximum *PF* at x=0.17, x=0.28, and x=0.42.

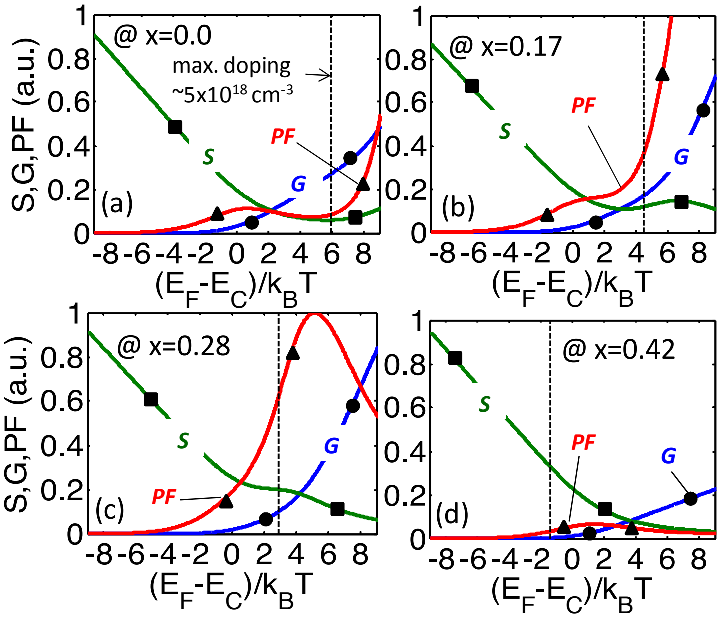

Figure A.7 *S*, *G* and *PF* vs. Fermi level for Al composition of (a) 0, (b) 0.17, (c) 0.28 and (d) 0.42.

The DOS at x=0.17 and x=0.28 are shown in Fig. A.8. The band-splitting (ΔE) between Γ and L is 5~ 7 k_BT and the effective density-of-states mass (m^*_{DOS}) and density-of-modes mass (m^*_{DOM}) for L valley are 7 and 20 times larger than the Γ valley, respectively. The L-valley with heavy effective mass is analogous to the resonant states in bulk Tl-PbTe[8]. To find a general guideline for effective mass ratio (m_2^*/m_1^*) between lower (m_1^*) and upper valley (m_2^*) and band-splitting (ΔE) to achieve maximum *PF*, two simple parabolic bands case are studied. Unlike $Al_xGa_{1-x}As$, in this simple model, the effective mass ratio and band-splitting (ΔE) can be varied without constraint.

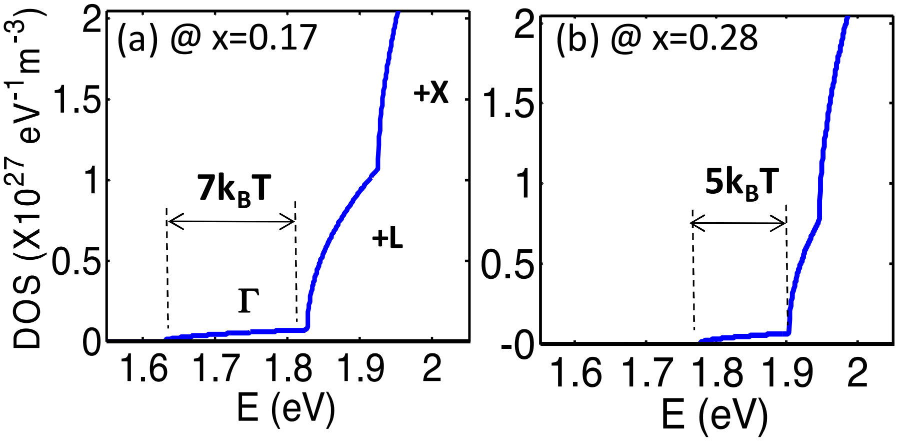

Figure A.8 Density-of -states at (a) x=0.17 and (b) x=0.28.

Calculation of the maximum *PF* for the simple two band model are shown in Fig. A.9a, where the results are normalized by the maximum *PF* obtained for one band case. Similar to the case of $Al_xGa_{1-x}As$ with x = 0.28, an increase in *PF* of about 5 times is achieved when m_2^*/m_1^* =10 and ΔE~$5k_BT$. As shown in Fig. A.9b, a non-monotonic *S* vs. E_F behavior is also observed at maximum *PF* condition.

Figure A.10 shows under which condition non-monotonic *S* occurs. The band splitting between two bands is kept at $5k_BT$ and then we examine the effects of effective mass of upper band on *S* vs. E_F characteristics. Non-monotonic behavior of *S* starts appearing when the effective mass ratio is larger than 5 as shown in Fig. A.10a. In the Fig. A.10b, the band splitting varies with m_2^*/m_1^* kept at 10. In the case where the band splitting is above $4k_BT$, non-monotonic behavior of *S* is observed. When two bands are very close, their *S* follows conventional thermoelectric theory.

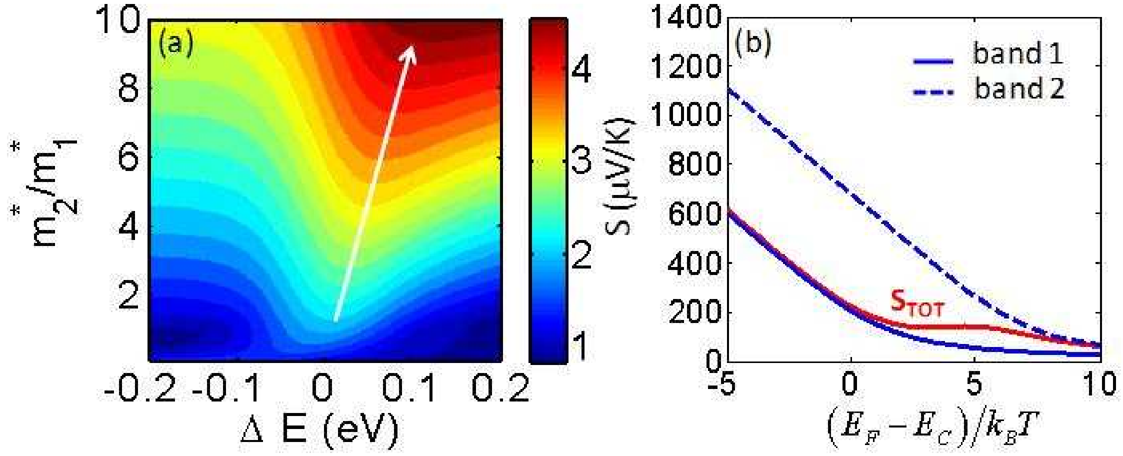

Figure A.9 (a) calculation of maximum *PF* for the simple two band model which is normalized by the maximum *PF* obtained for one band case. (b) S vs. E_F characteristics at maximum *PF* condition.

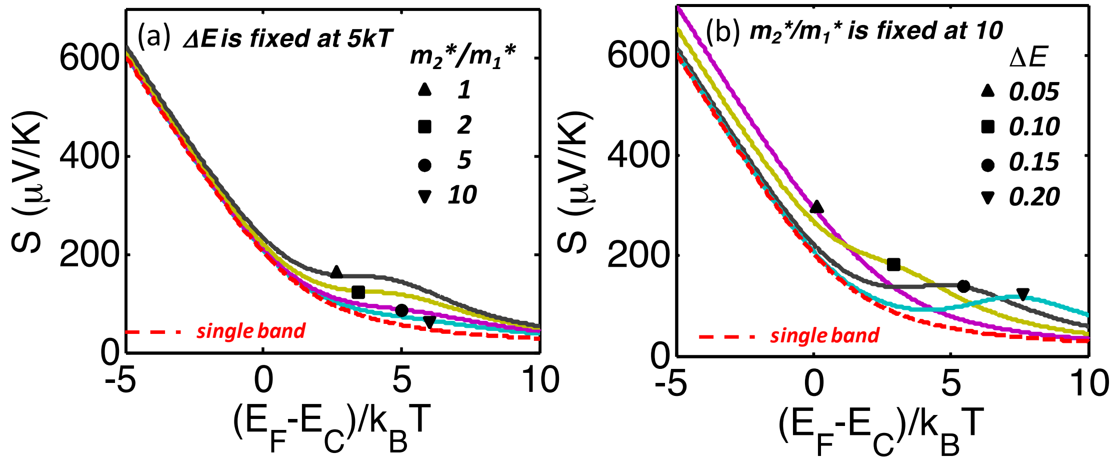

Figure A.10 S vs. E_F characteristics (a) with the band splitting kept at $5k_BT$ (b) with m_2^*/m_1^* kept at 10.

Generally the higher m_2^*/m_1^* is, the better *PF* because the higher m_2^*/m_1^* is desirable for non-monotonic $S(E_F)$. For maximum *PF*, a certain amount of band splitting (ΔE) needs for both non-monotonic $S(E_F)$ and the suppression of scattering, which is due to the fact that our model assumes the scattering rates increase with the DOS. This is the case of the phonon dominated scattering and scattering from delta-function like perturbing potential such as defects[285]. Considering typical doping limit[286], the optimum band-splitting might be an order of $5k_BT$.

A.5 Summary and Conclusion

In summary, it was shown in this appendix that most materials display a similar monotonic behavior of S vs. E_F, but for molecular thermoelectrics, the detailed lineshape of the transmission plays an important role. In the $Al_xGa_{1-x}As$ materials system, an increase in PF of 5 times and in ZT of 10 times is possible because of the non-monotonic S behavior, which maintains high S at high carrier densities resulting in high PF. This result is similar to the behavior reported for bulk Tl-PbTe [8]. The increase only happens when multiple bands are engineered in an appropriate way. General guidelines for electronic structure engineering are as follows: 1) an upper band with a heavy m^* (equivalently, sharp resonant states) are needed, and 2) the minimum of the upper band must be about $5k_BT$ above the lower, dispersive band. The appropriate bandstructure may be achieved with an alloy of the proper composition, as discussed in this appendix, by the introduction of resonant states, as discussed in [4], or by proper strain engineering.

B. COMPUTATIONAL STUDY OF THE ELECTRONIC PERFORMANCE OF CROSS-PLANE SUPERLATTICE PELTIER DEVICES

In this appendix B, we use a state-of-the-art non-equilibrium quantum transport simulation code, NEMO-1D, to address the device physics and performance benchmarking of cross-plane superlattice Peltier coolers. Our findings show quantitatively how barriers in cross-plane superlattices degrade the electrical performance, i.e. power factor. The performance of an $In_{0.53}Ga_{0.47}As/In_{0.52}Al_{0.48}As$ cross-plane SL Peltier cooler is lower than that of either a bulk $In_{0.53}Ga_{0.47}As$ or bulk $In_{0.52}Al_{0.48}As$ device, mainly due to quantum mechanical effects. We find that a cross-plane SL device has a Seebeck coefficient vs. conductance tradeoff that is no better than that of a bulk device. The effects of tunneling and phase coherence between multi barriers are examined. It is shown that tunneling, SL contacts, and coherency only produce oscillatory behavior of Seebeck coefficient vs. conductance without a significant gain in PF. The overall TE device performance is, therefore, a compromise between the enhanced Seebeck coefficient and degraded conductance.

B.1 Introduction

The dimensionless figure of merit, $ZT = S^2GT/K$, is the primary material parameter governing the maximum thermoelectric (TE) efficiency. Here T is the temperature, S is the Seebeck coefficient, G is the electrical conductance, and K is the thermal conductance, which is the sum of the electronic contribution, K_e, and the lattice thermal conductance, K_{ph}. Most recent improvements in ZT have been achieved by phonon engineering to reduce the lattice thermal conductivity [36,47,197]. One way is to use thin film superlattices (SLs), which has led to significant reduction in the lattice thermal conductivity and, therefore, enhanced TE performance [11]. The possibility of enhancing the electronic component (S^2G, power factor: PF) of TE performance by using

SL devices has been studied. First quantitative calculations for in-plane direction in SLs were done by Hicks and Dresselhaus in 1993 [51,155] and showed promising results. For cross-plane transport in SL, it has been predicted that energy filtering will lead to significant increases in *ZT* under a certain condition [72]. A single barrier and multi-layer thermionic refrigeration were proposed [85,287]. Experimentally, researchers have shown the increase in *S* by filtering out low energy electrons, but a limited increase in power factors due to the decrease in electrical conductivity [73–75].

Although there have been a number of studies, it is still not clear how a SL affects the electronic performance i.e. PF. This work explores the physics of transport in a single barrier and multi barriers (i.e. SL) TE devices using a sophisticated quantum transport model, NEMO-1D. A clear understanding of how barriers affect the PF is essential for developing a single barrier or multi barriers TE device with enhanced PF and is the objective of this appendix.

B.2 Approach

In the linear response regime, the Landauer expressions for electronic transport properties such as G, S, and K_e are expressed as

$$G = \left(\frac{2q^2}{h}\right) I_0 \qquad [1/\Omega] \tag{B.1}$$

$$S = \left(-\frac{k_B}{q}\right)\frac{I_1}{I_0} \qquad [\mathrm{V/K}] \tag{B.2}$$

$$K_e = \left(\frac{2k_B^2 T}{h}\right)\left\{I_2 - \frac{I_1^{\,2}}{I_0}\right\} \quad [\mathrm{W/K}], \tag{B.3}$$

where

$$I_j = \int_{-\infty}^{+\infty} \left(\frac{E-E_F}{k_B T_L}\right)^j \overline{T}_e(E)\left(-\frac{\partial f_0}{\partial E}\right) dE \tag{B.4}$$

with

$$\overline{T}_e(E) = T_e(E) M_e(E) \tag{B.5}$$

being the transmission, and $M_e(E)$ the number of electron conducting modes. In this study, $\bar{T}_e(E)$ is evaluated with the NEMO tool [288], which was originally developed to simulate resonant tunneling devices (RTDs) by the non-Equilibrium Green's Function (NEGF) approach and rigorously consider quantum mechanical (QM) reflection and interferences and contacts with phenomenological energy relaxation model. In this study we assume conductors with $T_e\left(E\right)=1$, i.e. ballistic transport. Quantum mechanical effects like quantum reflections, tunneling, and interferences are included in $M_e(E)$. An $In_{0.53}Ga_{0.47}As/In_{0.52}Al_{0.48}As$ is considered as a model structure and an effective mass model is used in NEMO. To begin with, we examine the hetero-junction and then a single barrier is studied with varying barrier thickness to evaluate quantitatively the effect of tunneling. Then, the effects of multi barriers are studied. - First, the effect of "SL contacts" and second, the effects of phase coherency between SL periods. Sketches of test structures are shown in Fig. B.1.

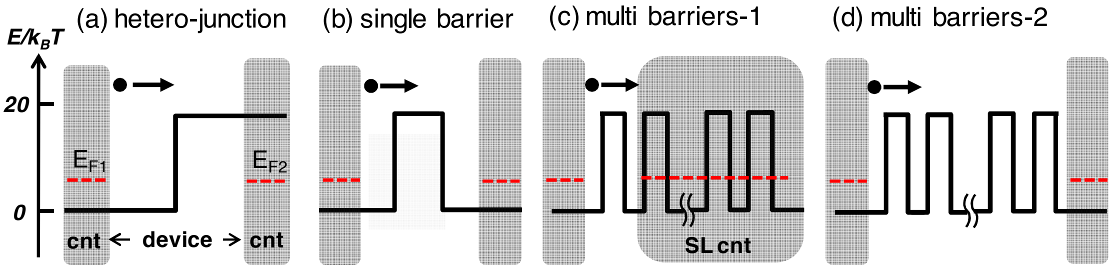

Figure B.1. Schematic diagrams of test structure of numerical experiments. (a) hetero-junction, (b) single barrier (c) multi-barriers-1: SL contacts and (d) multi-barriers-2. Barrier is $In_{0.52}Al_{0.48}As$. Grayed box represents contact (cnt), where energy relaxation scattering time is assumed to be 50 fs. Solid circle denotes injected electrons from emitter contact. emitter: bulk $In_{0.53}Ga_{0.47}As$ with 0.044 m_0, barrier: $In_{0.52}Al_{0.48}As$ with 0.075 m_0, barrier height, Φ_B : 0.51 eV.

B.3 Results And Discussion

B.3.1. Hetero-junction and Single barrier

A previous theoretical study [289] suggested a simple general rule in a semiclassical picture that given a transmissions (number of conducting modes) in the emitter and the barrier, the smaller one determines overall transmission at the hetero-junction. As shown in Fig. B2(a), the semiclassical transmission (blue solid line) of the hetero-junction is the lower of transmission of bulk $In_{0.53}Ga_{0.47}As$ and that of bulk $In_{0.52}Al_{0.48}As$. For the most of energy range, the overall transmission is determined by barrier because of its lower number of conducting modes. NEMO simulations at the hetero-junction were compared to the semiclassical transmission. It is seen that the slope of NEMO $\overline{T}_e(E)$ becomes shallower than semiclassical one due to QM reflection at the junction interface. The inset of Fig. B2(a) is contour plot of NEMO transmission at hetero-junction as a function of longitudinal energy (x-axis) and transverse energy (y-axis). Note that transmission is close to one even when incident longitudinal energy is less than barrier height or close to zero. This occurs because of transverse momentum and total energy conservation condition at the interface. In the case of homo-junction, however, the transmission is independent of the transverse energy which is not shown here. In comparison to the hetero-junction, the transmission for the single barrier with barrier thickness of 20 nm (thick enough to suppress tunneling current) is smaller due to Fabry-Perot type interference. Therefore, it can be easily predicted that QM evaluation of transmission gives worse electrical conductance than semiclassical approach. In addition, the weak energy dependence of transmission produces a small S from Eq. (B.2). Overall S vs. G tradeoff and PF vs. E_F are shown in Fig. 3(a) and 4(a). It is seen that PF of a single barrier is about 50% of bulk $In_{0.52}Al_{0.48}As$ and no better than hetero-junction and bulk $In_{0.53}Ga_{0.47}As$.

Next, the effect of tunneling is quantitatively evaluated in a single barrier. Figure 2(b) shows the transmission for barrier thickness of 6, 21, 70 and 100 Å. As the barrier thickness gets smaller, i.e., tunneling contribution is dominant, the overall curve is reduced to $\overline{T}_e(E)$ of bulk $In_{0.53}Ga_{0.47}As$ and energy dependency of $\overline{T}_e(E)$ becomes weak. The results of S vs. G tradeoff and PF vs. barrier thickness are shown in Fig. 3(b) and 4(b). In Fig. 4(b), comparing to thick barrier case (ex: 200 Å), it can be seen that PF generally decreases with thickness down to 21 Å and then increase again to value of bulk $In_{0.53}Ga_{0.47}As$. However, the behavior of PF from 200 down to 21 Å shows local maximum of PF at thickness of 70 Å, which is in contrast to the conventional notion that electrons should not tunnel through barriers for maximum cooling performance.

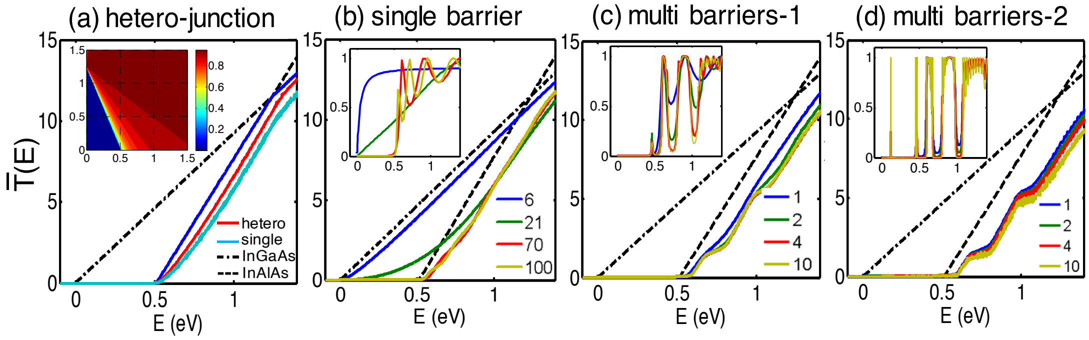

Figure B.2. Transmission results: (a) semi-classical (blue) for hetero-junction vs. QM calculation for hetero-junction (red) and single barrier (light blue). Barrier thickness is 200 Å (b) single barrier. Barrier thickness: 6, 21, 70, 100 Å (c) multi-barriers-1 (no. of barriers in SL contacts): 1, 2, 4, 10, and (d) multi-barriers-2 (no. of barriers in device region): 1, 2, 4, 10. The dashed dot is bulk $In_{0.53}Ga_{0.47}As$ and dashed line is $In_{0.52}Al_{0.48}As$. Insets: (a) contour plot of transmission at hetero junction as a function of longitudinal energy (x-axis) and transverse energy (y-axis), (b-d) transmission (y-axis) vs. total energy (x-axis, in *eV*) plot when transverse energy is zero.

The 15% improvement in comparison to thick barrier case is attributed to the delicate interplay between S and G as shown in Fig. B3(b): This behavior results from non-monotonic behavior of S vs. E_F due to non-negligible tunneling current. It can be understood from the two band model: $S_{tot} = \left(S_1G_1 + S_2G_2\right)/\left(G_1 + G_2\right)$, where $S_1 = -\left(\Phi_B - E_F + \Delta_{n1}\right)/qT$ and $S_2 = -\left(-E_F + \Delta_{n2}\right)/qT$ are S of thick barrier ($In_{0.52}Al_{0.48}As$) and bulk emitter ($In_{0.53}Ga_{0.47}As$), respectively and are weighted by thermionic emission over the barrier, G_1 and tunneling current, G_2. Bandstructure and QM effects affect the value of Δ_n. At the fixed $E_F > 0$, it is seen that absolute value of S_1 is larger than S_2. At the barrier thickness of 70 Å, S_{tot} at low E_F is same as S_2 because high barrier height ($\Phi_B - E_F$) suppress G_1 and dominant current is G_2. However, S_{tot} becomes S_1 at high E_F due to $G_1 > G_2$. Transition from small S_2 to large S_1 gives oscillatory behavior of S_{tot} vs. E_F (or S vs. G as shown in Fig. B3(b)). The location of local maximum of S_{tot} depends on barrier thickness: local maximum of S_{tot} vs. E_F moves toward lower E_F as barrier becomes thick. Though this behavior enhances PF slightly, tunneling generally degrades the electronic performance.

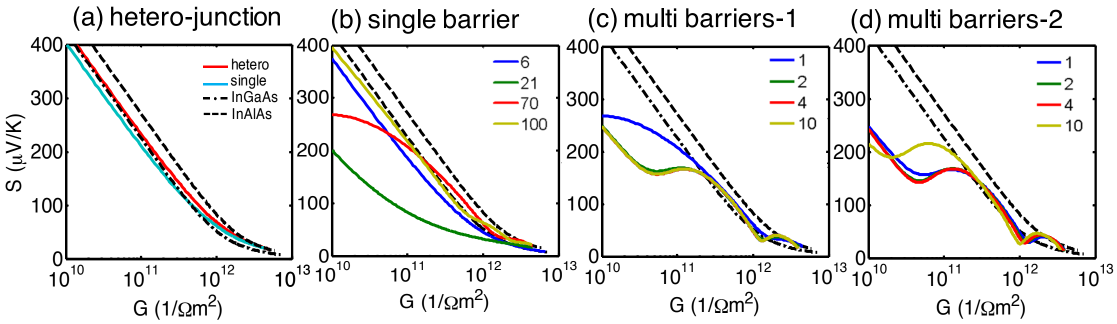

Figure B.3. S vs. G trade-off: (a) dashed dot is bulk $\mathrm{In_{0.53}Ga_{0.47}As}$, dashed line is $\mathrm{In_{0.52}Al_{0.48}As}$ and semiclassical results for hetero-junction, red solid line is NEMO calculation for hetero-junction, and light blue line is NEMO calculation for single barrier with barrier thickness of 200 Å (b) single barrier. Barrier thickness: 6, 21, 70, 100 Å (c) multi-barriers-1, no. of barriers in SL cnts + a single barrier device: 1, 2, 4, 10, and (d) multi-barriers-2, no. of barriers in device region: 1, 2, 4, 10. The dashed dot is bulk $\mathrm{In_{0.53}Ga_{0.47}As}$ and dashed line is $\mathrm{In_{0.52}Al_{0.48}As}$.

B.3.2. Multi Barriers

Firstly, the effect of "SL contacts" is studied to see if there is possibility to enhance the PF of a single barrier TE device when it is the first period of SL as shown in Fig. B.1(c). A single period of SL is composed of $\mathrm{In_{0.53}Ga_{0.47}As}$ (50 Å)/ $\mathrm{In_{0.52}Al_{0.48}As}$ (70 Å). As shown in the inset of Fig. B.2(c), SL contacts produces mini-bands, though they are not sharply defined because strong phase relaxation is assumed ($\tau = 5 \times 10^{-14}$ s). The effects of SL contacts saturates as the number of periods increase from 2 periods of SLs to 9 periods of SLs in the contact (total no. of barrier is 10). The $\overline{T}_e(E)$ for SL contacts is no better than a single barrier case, resulting in poor PF as shown in Fig. B.4(c).

Next, we examine how phase coherency between the SL periods affects the performance. The device region is extended from 1 barrier to 10 barriers. Increasing coherency between SL periods makes more sharply defined mini-bands, resulting in a step-like $\overline{T}_e(E)$ curve, as shown Fig. B.2(d). It is also seen that $\overline{T}_e(E)$ becomes shallow as coherency become stronger. Therefore, this leads to no improvement in PF as shown in

Fig. B.4(d) though the step shaped $\overline{T}_e(E)$ (or mini-bands) leads to oscillatory S behaviors as shown in Fig. B.3(c) and (d).

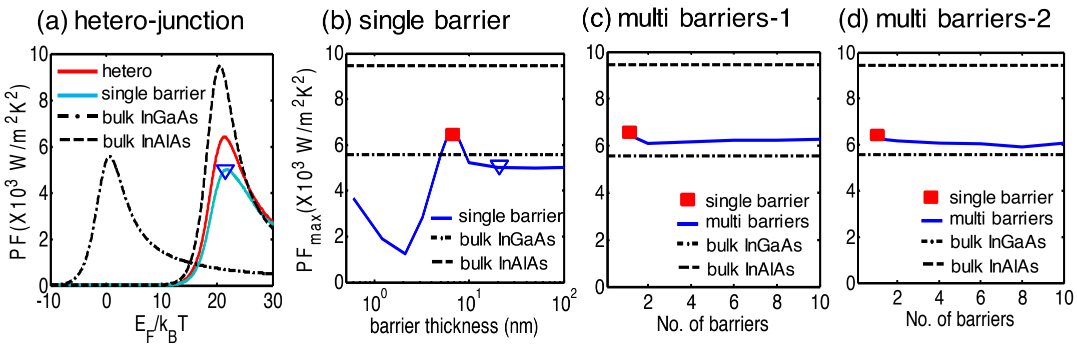

(a) hetero-junction

(b) single barrier

(c) multi barriers-1

(d) multi barriers-2

Figure B.4. (a) PF vs. E_F results: dashed dot is bulk $In_{0.53}Ga_{0.47}As$, dashed line is $In_{0.52}Al_{0.48}As$ and semi-classical results for hetero-junction, red solid line is NEMO calculation for hetero-junction, and light blue line is NEMO calculation for single barrier with barrier thickness of 200 Å (b) maximum PF (PF_{max}) of single barrier with respect to barrier thickness: 6, 21, 70, 100 Å (c) PF_{max} of multi barriers-1, no. of barriers in SL cnts + a single barrier device: 1, 2, 4, 10, and (d) PF_{max} of multi barriers-2, no. of barriers in device region: 1, 2, 4, 10. The dashed dot and dashed lines in (b)-(d) represents PF_{max} of bulk $In_{0.53}Ga_{0.47}As$ and $In_{0.52}Al_{0.48}As$ in (a), respectively. Square symbols in (c) and (d) denotes PF_{max} of corresponding single barrier device in (b).

B.4 Conclusions

We examined Peltier cooling in semiconductor SL devices. Quantum transport simulations for hetero-junction and single barrier show that transmission degrades due to QM effects which led to 50% reduction in PF comparing to bulk barrier materials. In addition, the role of SL contacts and phase coherence in the SL are studied in multi barriers. Our study shows that PF of multi barrier structures is no better than a single barrier TE device. Tunneling, SL contacts and coherency produces oscillatory behavior in the S vs. G tradeoff, in contrast to conventional monotonic decreasing behavior, but we found no gain in PF. The effect of electrostatic self-consistency, scattering, and SL structure design are under study.

C. NUMBER OF CONDUCTING CHANNELS FOR 1D, 2D, AND 3D.

To relate Eq. (3.5b), the Landauer expression for lattice thermal conductivity, to the conventional expression from kinetic theory, we write the number of phonon conduction channels per area, $M'_{ph}(\omega)$, as [3]

$$M'_{ph}(\omega) = (h/4)\upsilon(\omega)D'_{ph}(\omega) , \tag{C.1}$$

where $D'_{ph}(\omega) \equiv (1/\Omega)\sum_{q}\delta(\hbar\omega - \hbar\omega_q)$ is the phonon density of states (DOS) per polarization per volume. Using Eqs. (3.6) and (3.7), Eq. (3.5b) the phonon thermal conductivity can be written in the conventional form [217,290] as

$$\kappa_{ph} = \frac{1}{3}\int_{-\infty}^{+\infty} d(\hbar\omega)C_V(\omega)\upsilon_{ph}(\omega)\Lambda_{ph}(\omega) \tag{C.2}$$

with $C_V(\omega)$ being the specific heat per unit volume

$$C_V(\omega) = k_B{}^2 T_L D_{ph}(\omega)\left(\frac{\hbar\omega}{k_B T_L}\right)^2\left(-\frac{\partial n_0}{\partial(\hbar\omega)}\right). \tag{C.3}$$

Next, for both electron and phonon, the number of conduction channels is defined as[3]

$$M(E) = \frac{h}{2L}\sum_{k}|\upsilon_x|\delta(E - E_k) \tag{C.4}$$

Assuming parabolic dispersion for electron ($E - \varepsilon_1 = \hbar^2 k^2/2m_e$), corresponding expression for the number of conduction channels per spin per valley for 1D, 2D, and 3D conductors are given as[166]

$$M_{el}(E) = \Theta(E - \varepsilon_1) \qquad \text{(1D)} \tag{C.5a}$$

$$M_{el}(E) = W\frac{\sqrt{2m_e(E - \varepsilon_1)}}{\pi\hbar} \qquad \text{(2D)} \tag{C.5b}$$

$$M_{el}\left(E\right) = A\frac{m_e}{2\pi\hbar^2}\left(E - E_C\right) \quad \text{(3D)} \qquad \text{(C.5c)}$$

where Θ is the unit step function, ε_1 is the bottom of the first subband, m_e is the electron effective mass, E_C is the conduction band edge and *W* and *A* are the width and the area of the 2D and 3D conductors, respectively. For phonons with linear and isotropic dispersion approximation, $\omega = \upsilon_s q$, $M_{ph}\left(\omega\right)$ per polarization is given as

$$M_{ph}\left(\omega\right) = \Theta\left(\omega\right) \quad \text{(1D)} \qquad \text{(C.6a)}$$

$$M_{ph}\left(\omega\right) = W\left(\omega/\pi\upsilon_s\right) \quad \text{(2D)} \qquad \text{(C.6b)}$$

$$M_{ph}\left(\omega\right) = A\left(\omega^2/4\pi\upsilon_s^{\ 2}\right) \quad \text{(3D)} \qquad \text{(C.6c)}$$

where υ_s is the velocity of sound.

D. DIFFUSIVE MISMATCH MODEL FROM LANDAUER APPROACH

In a Landauer approach, heat current from side 1 to side 2 is

$$I_{Q,1\to 2} = \frac{\hbar\omega}{h}\int d\left(\hbar\omega\right)\left[T_{1\to 2}\left(\omega\right)M_1\left(\omega\right)n_1 - T_{2\to 1}\left(\omega\right)M_2\left(\omega\right)n_2\right] \tag{D.1}$$

where T_i and M_i is the transmission and the number of conduction channels at side *i* and n_i is Bose-Einstein distributions at side *i*. For an interface in thermal equilibrium, $I_{Q,1\to 2} = 0$ in Eq. (D.1) or

$$T_{1\to 2}\left(\omega\right)M_1\left(\omega\right)n_1 = T_{2\to 1}\left(\omega\right)M_2\left(\omega\right)n_2 \tag{D.2}$$

In thermal equilibrium, $T_{L,1} = T_{L,2} = T_L$ and $n_1 = n_2$. Therefore,

$$T_{1\to 2}\left(\omega\right) = T_{2\to 1}\left(\omega\right)M_2\left(\omega\right)/M_1\left(\omega\right) \tag{D.3}$$

The DMM model assumes a diffusive scattering at interface, resulting in the phonons forgetting where they came from except for their energy [291]. So, transmission from material 1 to 2 at the interface is assumed to be same as reflection at the interface from material 2 to 1.

$$T_{1\to 2}\left(\omega\right) = R_{2\to 1}\left(\omega\right) = 1 - T_{2\to 1}\left(\omega\right) \qquad ` \tag{D.4}$$

From Eqs. (D.3) and (D.4), we can solve for $T_{1\to 2}\left(\omega\right)$:

$$T_{1\to 2}\left(\omega\right) = M_2\left(\omega\right)/\left(M_1\left(\omega\right) + M_2\left(\omega\right)\right) \tag{D.5}$$

According to Ref. [3] , number of modes are defined as

$$M\left(E\right) = \frac{h}{2L}\sum_k \left|\upsilon_x\right|\delta\left(E - E_k\right) \tag{D.6}$$

so, Eq. (D.5) becomes

$$T_{1\to 2}\left(\omega\right) = \left\langle\left|\upsilon_{x,2}\right|\right\rangle D_2\left(\omega\right)/\left(\left\langle\left|\upsilon_{x,1}\right|\right\rangle D_1\left(\omega\right) + \left\langle\left|\upsilon_{x,2}\right|\right\rangle D_2\left(\omega\right)\right) \qquad ` \tag{D.7}$$

where $D(E)=\sum_{k}\delta(E-E_k)$ is the density of states and $\langle|\upsilon_x|\rangle$, the velocity for transport direction, is defined as

$$\langle|\upsilon_x|\rangle \equiv \sum_{\vec{k}}|\upsilon_x|\delta(E-E_k)\Big/\sum_{\vec{k}}\delta(E-E_k) \tag{D.8}$$

Therefore, Eq. (D.5) is essentially same as the results in the DMM.

E. MODELING APPROACH FOR NANOCOMPOSITES

E.1 Introduction

To explore the thermoelectric (TE) performance of polycrystalline materials, it is essential to model transport on the micro/macro scale with physics-based input from the nano scale. Such modeling efforts, however, have been rare for this problem. Conventional modeling efforts to understand the electronic and thermal properties are done with a variety of techniques with most of the emphasis being on microscopic modeling including: 1) Boltzmann transport equation (BTE) for electrons [99,105,106,132,133] and phonons [134], 2) Monte Carlo (MC) simulations [135], 3) Molecular dynamic (MD) simulations [136], 4) modified effective medium theory [137], and 5) non-equilibrium Green's function (NEGF) method [138]. The current models, however, ignore the statistics of grains and GBs and their associated properties as well as their configurations in three dimensions (3D). Therefore, microstructure-aware modeling informed by macroscopic properties is required.

For this problem, we first need to generate the microstructure. Many different methods for constructing 3D grain microstructures have been used. We can start with images from existing microstructures, which have a clear physical meaning. A limited number of two dimensional (2D) samples, however, yield uncertainties in the reconstruction of the 3D structure, although many properties such as grain size, its topology, its orientation are given [113]. Another way is simulation of microstructures based on physics [292,293]. This method enables us to simulate how the grain network evolves with respect to process and operation condition, which are expected to have important implications for macro properties such as reliability. Microstructure simulation, however, needs a lot of computational resources. Synthetic generation of microstructures like Voronoi tessellation [260,294,295] is also popular because it is computationally simple and efficient.

In this work, we first synthetically generated a polycrystalline structure using Voronoi tessellation method, which enables us to control the statistics of grain and GBs. We used a simple model for grains and GBs along with a Landauer approach for transport. A Landauer approach for homogeneous materials has previously been considered by Kim et al. [166] within an effective mass context. Extensions of the Landauer approach to full band electron and phonon dispersions have been discussed by Jeong et al. [3]. We will use their methods to illustrate key consideration in TE transport in polycrystalline type TECs. We compute the transmission of the polycrystalline TECs and compare the TE performance of the TECs in comparison to that of the single crystalline TECs. Our specific objectives are: 1) to quantitatively examine electronic performance for polycrystalline thin film TECs, 2) to present a technique to extract a energy resolved transmission for the inhomogeneous NCs, 3) to discuss the similarities and differences between NC and composite energy bands in terms of the transmission engineering, and 4) to discuss percolation phenomena in energy space.

This chapter is organized as follows. In Sec. E.2, we present our approach to construct the microstructure. In Sec. E.3, we describe our approach to calculate transport properties.

E.2 Generating the Physical Structure

This section describes the Voronoi tessellation scheme for generating microstructure. We synthetically generate 2D microstructure using Voronoi tessellation which can be easily extended to 3D. The concept of the Voronoi tessellation was originally proposed by Georgy Voronoi in 1907 [260]. In the simplest case, we are given a set of points in the plane, which are the Voronoi sites. Each site, *s*, has a Voronoi cell consisting of all points closer to *s* than to any other site. The segments of the Voronoi diagram are all the points in the plane that are equidistant to the two nearest sites as shown in Fig. E.1a. This method is essentially same as the method to construct Wigner–Seitz primitive cell (the first Brillouin zone) for the Bravais lattice (the reciprocal lattice). The statistics of output Voronoi cells such as shape and size depends on the input parameters such as pattern and number of Voronoi sites. For a complete discussion, the reader should refer to the book by Okabe et al. [260].

There are already several software projects and libraries that compute the Voronoi tessellation because the Voronoi diagram has many applications across science in problems that involve allocating space between a group of objects. The software package QHull [296] can compute Voronoi diagrams in arbitrary numbers of dimensions, making use of an indirect projection method; Matlab's Voronoi routines make use of this package. Another program is Triangle [297], which is most well-known for mesh generation via the Delaunay triangulation, but it also computes the Voronoi tessellation. However, this code is specific to two-dimensional computations [298]; Voro++ is an open source software library for the computation of three dimensional Voronoi cells [298,299]. In this preliminary study, we used Voro++.

Figure E.1b, c, d, and e shows constructed 2D microstructures with respect to number probability of high-angle grain boundaries (HAGBs) which is shown by black solid lines. For a given probability of HAGBs, the grain boundaries are categorized into HAGBs and low-angle grain boundaries (LAGBs), randomly. In this study, microstructure with 50% HAGBs is used, and average grain size is about 12 nm. Most of nanograins for Si and Si_xGe_{1-x} NC are in the 10 - 30nm range[101].

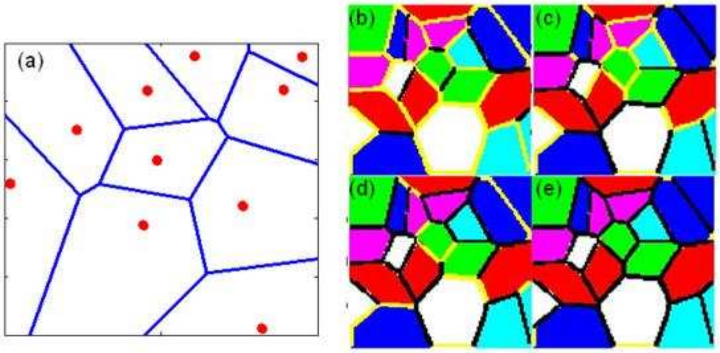

Figure E.1 (a) the Voronoi diagram of a random set of points in the plane shown by red dots (all points lie within the image), (b)-(e) 2D microstructure generated by Voronoi tessellation. The number probability of HAGBs (shown by black solid line) for (b), (c), (d), and (e) are 25, 50, 75, and 100%, respectively. In this study, microstructure with 50% HAGBs is used – i.e. (c).

E.3 Modeling Electron Transport

This section describes the mesh structure and the finite difference scheme for solving the transport equation for polycrystalline TECs. Given a microstructure, we define a uniform square grid structure for the use of finite difference method to calculate transport properties in non-homogenous materials. In this preliminary study, we used a grid size of $N = 100$ in each direction.

For illustrative purpose, we first consider charge current with the voltage gradient only. To solve charge (particle) current, we assumed that particle fluxes are conserved (i.e. no recombination-generation);

$$0 = \nabla \cdot \vec{J} = \nabla \cdot \left(\sigma \vec{E} \right) = -\nabla \cdot \left(\sigma \nabla V \right) \tag{E.1a}$$

The 2D finite difference mesh for a device is given in Fig. E.2a. For a node (i, j), Eq. (E.1a) can be discretized as follows,

$$\begin{aligned} 0 &= g_{i,j}^{i-1,j}(V_{i,j} - V_{i-1,j}) + g_{i,j}^{i+1,j}(V_{i,j} - V_{i+1,j}) + g_{i,j}^{i,j-1}(V_{i,j} - V_{i,j-1}) + g_{i,j}^{i,j+1}(V_{i,j} - V_{i,j+1}) \\ &= -g_{i,j}^{i,j-1}V_{i,j-1} - g_{i,j}^{i-1,j}V_{i-1,j} + g_{i,j}^{i,j}V_{i,j} - g_{i,j}^{i+1,j}V_{i+1,j} - g_{i,j}^{i,j+1}V_{i,j+1} \end{aligned} \tag{E.1b}$$

where g_m^n is the local conductivity between a node m and a neighboring node n. A node (i, j) is numbered as m which is given as $(j\text{-}1)N + i$. We can write linear equations for all N^2 nodes which can be rewritten as a matrix form:

$$\begin{bmatrix} \\ BC \\ \\ \end{bmatrix}_{N^2 \times 1} = \begin{bmatrix} \\ G \\ \\ \end{bmatrix}_{N^2 \times N^2} \begin{bmatrix} \\ V \\ \\ \end{bmatrix}_{N^2 \times 1}, \tag{E.1c}$$

where the matrix *[BC]* has the information on the boundary conditions, and the conductivity matrix *[G]* is a large sparse matrix. For a node m ,

$$\begin{bmatrix} \\ \\ BC_m \\ \\ \\ \end{bmatrix} = \begin{bmatrix} & & & & & & \\ \cdots & -g_m^{m-N} & \cdots -g_m^{m-1} & g_m^m & -g_m^{m+1}\cdots & -g_m^{m+N} & \cdots \\ & & & & & & \end{bmatrix} \begin{bmatrix} \vdots \\ V_{m-N} \\ \vdots \\ V_{m-1} \\ V_m \\ V_{m+1} \\ \vdots \\ V_{m+N} \\ \vdots \end{bmatrix} \qquad \text{(E.1d)}$$

Because two voltages are known for two sides connected to electrodes (i.e., the Dirichlet boundary condition), BC_m and corresponding local conductivity are given by

$$BC_m = V_{high}\ (V_{low}) \quad \text{for } i = 1\ (N), \quad \text{where } m = (j\text{-}1)N + i\ , \qquad \text{(E.1e)}$$

$$g_m^m = 1 \qquad \text{for } i = 1 \text{ or } N \qquad \text{(E.1f)}$$

Zero flux boundary conditions (i.e. Neumann boundary condition) are applied for the other two sides (i.e. j = 1 and N), and BC_m and local conductivity for this condition are given by

$$BC_m = 0 \qquad \text{for } j = 1 \text{ or } N\ , \quad \text{where } m = (j\text{-}1)N + i\ , \qquad \text{(E.1g)}$$

$$g_m^m = 1\ , \text{and} \quad g_m^{m+N}\,(g_m^{m-N}) = -1 \qquad \text{for } j = 1\ (N) \qquad \text{(E.1h)}$$

Otherwise, BC_m and local conductivity, g_m^n, are given by

$$BC_m = 0 \quad \text{for } 1 < i,j < N, \quad \text{where} \quad m = (j\text{-}1)N + i\ , \qquad \text{(E.1i)}$$

$$g_m^n = \left(\sigma_m + \sigma_n\right)/2 \qquad \text{for } m \neq n, \text{and} \quad g_m^m = \sum_{n \neq m} g_m^n \qquad \text{(E.1j)}$$

The voltage vector, *[V],* is obtained by using left matrix division in Matlab (i.e., *[V] = [G]\[BC]*). Finally the current flux J of a composite systems is computed from $J = \sum_j \sigma_{1,j}\left(V_{1,j} - V_{2,j}\right)/h$, and the effective conductivity σ_{NC} is evaluated from $J = \sigma_{NC}\left(V_{high} - V_{low}\right)/L$.

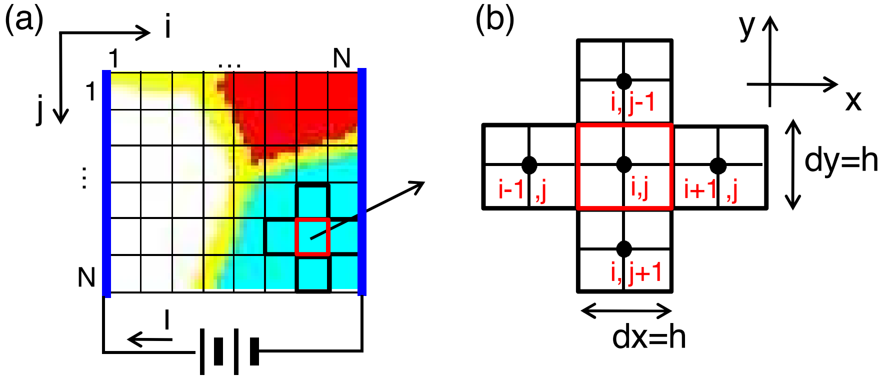

Figure E.2 (a) schematic diagram of 2D finite difference mesh ($N \times N$ grids, $N = 100$, grid size = 1 nm). (b) grid points around element (i, j)

A general equation for charge current including temperature gradient is given as

$$0 = \nabla \cdot \vec{J} = -\nabla \cdot \left[\sigma \nabla V - \left[S\sigma \right] \nabla T \right], \tag{E.2a}$$

where $[S\sigma]$ is the Seebeck coefficient times conductivity, which could be integrated values as well as energy resolved values. The boundary conditions for temperature gradient are the same as those for voltage gradient. The charge (particle) conservation equations should be valid at each energy in near equilibrium to satisfy Eq. (E.2a). This will be checked in Sec. E.3. The corresponding heat current equations are expressed as

$$0 \neq \nabla \cdot \overrightarrow{J_Q} = -\sum_{j} \left[T_{ave} \left[S\sigma \right] \nabla V - \kappa_0 \nabla T \right], \tag{E.2b}$$

where κ_0 is the electronic thermal conductivity for zero voltage gradient. In contrast to a previous work [126], which assumed energy flux conservation, carriers are assumed to absorb and dissipate energy through electron-phonon interactions in this study – i.e. the energy relaxation length << grain size. The heat current is evaluated using voltage and temperature information obtained from Eq. (E.2a). In principle, Eqs. (E.2a) and (E.2b) need to be solved self-consistently because the electrical properties such as σ, S, and κ_0 also depend on temperature. We may assume that the temperature gradient is not large and therefore the electrical properties are not dependent on temperature.

F. THE MAXIMUM POWER CONDITION AND THE MAXIMUM EFFICIENCY CONDITION

For the maximum power condition and the maximum efficiency condition, we will find the power delivered to the load resistance and the efficiency. The power delivered to the load,

$$P_{Load} = I^2 R_{Load} \tag{F.1}$$

where I is the current flow due to temperature gradient and is expressed as

$$I = \frac{S\Delta T}{R + R_{Load}} \tag{F.2}$$

where R is the resistance of thermoelectric devices. So Eq. (F.1) becomes

$$P_{Load} = \left(\frac{S\Delta T}{R + R_{Load}} \right)^2 R_{Load} \tag{F.3}$$

Equation (F.3) can be expressed as

$$P_{Load} = \frac{S^2 \Delta T^2}{R} \frac{M}{\left(1 + M\right)^2} \tag{F.4}$$

where M is the ratio of the resistance of R_{Load} to R, $M \equiv R_{Load}/R$. The efficiency is given by

$$\eta = \frac{P_{Load}}{W_{in}} = \frac{I^2 R_{Load}}{ST_h I + K_{tot}\left(T_h - T_c\right)} \tag{F.5}$$

where W_{in} is the total heat flow from hot side.

The maximum power condition, $R_{Load} = R$

First, it can be seen from Eqs. (F.3) or (F.4) that the power is the maximum for $R_{Load} = R$ and the maximum power $P^{\dagger}_{Load}$ is given by

$$P_{Load}^{\dagger} = \frac{S^2}{4R}\Delta T^2 = PF\frac{\Delta T^2}{4} \tag{F.6}$$

with $PF = S^2/R$ being the power factor. The power delivered to the load for this condition is a function of PF, not ZT. Under this condition, the current is obtained to be $I = S\Delta T/2R$ from Eq. (F.2). Inserting this current into Eq. (F.5), the efficiency under the maximum power condition is given by

$$\begin{aligned} \eta^{\dagger} &= \frac{\left(S\Delta T/2R\right)^2 R}{ST_h\left(S\Delta T/2R\right) + K_{tot}\Delta T} \\ &= \frac{Z\Delta T}{2ZT_{hot} + 4} \\ &= \frac{Z}{\left(2Z + 4/T_{hot}\right)}\frac{\Delta T}{T_{hot}} \end{aligned} \tag{F.7}$$

where $Z = S^2/\left(RK_{tot}\right)$. The efficiency is a function of Z.

The maximum efficiency condition, $R_{Load} = R\sqrt{1+ZT}$

We can maximize the efficiency in Eq. (F.5) when $M \equiv R_{Load}/R$ is given by

$$M = \sqrt{1+ZT}\ , \tag{F.8}$$

Under this condition, the maximum efficiency is obtained from Eq. (F.5) to be

$$\eta^{*} = \left\{\frac{\sqrt{1+ZT} - 1}{\sqrt{1+ZT} + T_{cold}/T_{hot}}\right\}\frac{\Delta T}{T_{hot}}. \tag{F.9}$$

This is the same as Eq. (F.7). This efficiency is also a function of Z. Under the maximum efficiency condition (i.e. $R_{Load} = R\sqrt{1+ZT}$), the power delivered to the load P_{Load}^{*} is obtained from Eq. (F.3),

$$\begin{aligned} P^{*}_{Load} &= \left(\frac{S\Delta T}{R + R\sqrt{1+ZT}} \right)^2 R\sqrt{1+ZT} \\ &= \left(\frac{S^2 \Delta T^2}{R} \right) \frac{\sqrt{1+ZT}}{\left(1+\sqrt{1+ZT}\right)^2} \\ &= P^{\dagger}_{Load} \frac{4\sqrt{1+ZT}}{\left(1+\sqrt{1+ZT}\right)^2} \end{aligned} \tag{F.10}$$

where we also used Eq. (F.6). P^{*}_{Load} is a function of Z as well as PF since $P^{\dagger}_{Load}$ is a function of PF. In addition, we can see that $P^{*}_{Load} \leq P^{\dagger}_{Load}$ always holds because $4\sqrt{1+ZT} \leq \left(1+\sqrt{1+ZT}\right)^2$. Now we have the efficiency (Eqs. (F.7) and (F.9)) and the power (Eqs. (F.6) and (F.10)) under both conditions.

G. THE EFFECT OF ANISOTROPIC BAND

To illustrate the effect of anisotropic valleys in a multi-valley materials, we consider multi-valley materials with a valley degeneracy of $N_V = 6$. For ellipsoidal bands, the degree of anisotropy (*k*) is represented by the ratio of the longitudinal effective mass (m_l^*) to transverse effective mass (m_t^*), i.e. $k = m_l^* / m_t^*$. We compare an anisotropic multi-valley material to a single valley material with an effective mass of m_2^* at the same density of states. It is found that anisotropic multi-valleys produces higher performance than isotropic multi-valleys. This occurs mainly because a larger degree of anisotropy (i.e. larger k) leads to increases in $\langle\langle \lambda \rangle\rangle$ and $\langle M \rangle$ (i.e. enhanced power factor).

The results can be understood in a following way. With the same density-of-states,

$$N_V \left(\left(m_l^* m_t^{*2} \right)^{1/3} \right)^{3/2} = \left(m_2^* \right)^{3/2} \tag{G.1}$$

or

$$m_2^* = N_V^{2/3} \left(m_l^* m_t^{*2} \right)^{1/3}. \tag{G.2}$$

For each equivalent ellipsoidal bands, the number of conduction channels is the density-of-states in the 2D plane transverse to the transport direction[3] (i.e. $\sqrt{m_l^* m_t^*}$). The MFP for backscattering is proportional to velocity times scattering time. The velocity is proportional to $1 / \sqrt{m_t^*}$ but the scattering times are the same if we make the physically reasonable assumption that the scattering rate is proportional to the density-of-states. From eqn. (G.1) or (G.2), the ratio of σ for anisotropic multi-valley (σ_1) to that for isotropic single valley (σ_2) is

$$\frac{\sigma_1}{\sigma_2} \approx \frac{M_1}{M_2} \times \frac{\lambda_1}{\lambda_2} = \frac{N_V \sqrt{m_t^* m_l^*}}{m_2^*} \times \left(\frac{m_2^*}{m_t^*} \right)^{1/2} = N_V^{2/3} k^{1/3}. \tag{G.3}$$

Equation (G.3) reduces to an isotropic case at $k = 1$. The simple models considered here show that we should expect improved power factor with increasing valley degeneracy and with the degree of anisotropy. Also note that the conductivity of the multiband semiconductor depends more strongly on valley degeneracy than on the degree of anisotropy.

VITA

VITA

Changwook Jeong received the B.S. and M.S. degrees in Material Science and engineering from Seoul National University, Seoul, Korea, in 1999 and 2001, respectively. From 2003 to 2007, he worked at Samsung Electronics and involved in the development of non-volatile high density memories such as Magnetoresistive RAM and Phase-Change RAM. He is currently working toward the Ph.D. degree in Electrical and Computer Engineering in the School of Electrical and Computer Engineering, Purdue University, West Lafayette, IN. His current research interests include nanosacle device physics and devices for energy conversion.